

**PREPARATION OF HYDROXYAPATITE/SILK
PROTEIN THIN FILM IMPLANT SURFACES,
INVESTIGATION OF THEIR
MICROSTRUCTURAL PROPERTIES AND MODEL
PROTEIN INTERACTIONS**

**A Thesis Submitted to
the Graduate School of Engineering and Sciences of
İzmir Institute of Technology
in Partial Fulfillment of the Requirements for the Degree of**

DOCTOR OF PHILOSOPHY

in Chemical Engineering

**by
Selçuk ÖZCAN**

**July 2009
İZMİR**

We approve the thesis of **Selçuk ÖZCAN**

Prof. Dr. Muhsin ÇİFTÇİOĞLU
Supervisor

Prof. Dr. Mustafa GÜDEN
Committee Member

Assoc. Prof. Dr. Oğuz BAYRAKTAR
Committee Member

Assoc. Prof. Dr. Funda TIHMINLIOĞLU
Committee Member

Assoc. Prof. Dr. Mustafa TOPARLI
Committee Member

13 July 2009

Prof. Dr. Devrim BALKÖSE
Head of the Department of
Chemical Engineering

Prof. Dr. Hasan BÖKE
Dean of the Graduate School of
Engineering and Sciences

ACKNOWLEDGEMENTS

The author wishes to express his deepest gratitude and sincere regards to Professor Dr. Muhsin Çiftçiođlu for his guidance and encouragement throughout this work, which is not alone confined to the supervision of a Ph.D. degree study, but rather encompassing the overhaul of incitements for a prolific and profound life time scientific endeavor.

The author is indebted to Assoc. Prof. Dr. Ođuz Bayraktar for his guidance and suggestions, providing part of the experimental material, and facilitating the use of Bioreaction Engineering Laboratory facilities of Izmir Institute of Technology; without which this work would not have been completed.

The author wishes to express his sincere thanks to Prof. Dr. Mustafa Guden for his invaluable advice and suggestions, and providing part of the experimental material.

The author wishes to express his gratitude to Assoc. Prof. Dr. Sedat Akkurt for his ever kindly encouragement, and contributions in terms of coworked publications.

The author wishes to express his gratitude to Prof. Dr. Muhsin Çiftçiođlu, Assoc. Prof. Dr. Sedat Akkurt, Assist. Prof. Dr. Erol Őeker, Assist. Prof. Dr. Turgut Battal, Assist. Prof. Dr. Sileyman Tarı, Assist. Prof. Dr. Gnlur Erciyes for their enlightening and excellent teaching.

The author wishes to express his sincere gratitude to Prof. Dr. Semra lklü, Prof. Dr. Devrim Balköse, and Dr. Muzaffer Sipahiođlu for their kindly encouragement throughout this study.

The author wishes to express his special thanks to Rukiye Çiftçiođlu, Deniz ŐimŐek, the Center for Material Research staff for their understanding, friendly cooperation, and support which has been indeed instrumental for the completion of the experimental part of this study.

Financial support from the Research Fund of Izmir Institute of Technology, for part of this research project, is gratefully acknowledged.

ABSTRACT

PREPARATION OF HYDROXYAPATITE/SILK PROTEIN THIN FILM IMPLANT SURFACES, INVESTIGATION OF THEIR MICROSTRUCTURAL PROPERTIES AND MODEL PROTEIN INTERACTIONS

Biocompatible hydroxyapatite (HAp) coatings of load bearing metallic in vivo hard tissue implants act as local scaffolds for enhanced osteoconduction, providing fast bone apposition and cementless fixation. In this study, in an attempt to exploit the potential of hydroxyapatite as a carrier of bone morphogenetic proteins for post operative accelerated healing, and implant durability, the tailored microstructural properties, and protein adsorption capabilities of thin film hydroxyapatite implant surfaces were investigated.

A novel particulate sol method was used to fabricate HAp thin films on bioinert glass, and Ti6Al4V substrates by dip and spin coating. The microstructural characterization of the thin films was carried out by SEM/EDX, AFM, XRD, and FTIR, and their surface roughness, Vickers hardness and adhesion strength were determined. The effects of silk fibroin and sericin thin film layers on the HAp film microstructure, and model protein (bovine serum albumin, BSA) adsorption behavior (by the size exclusion HPLC method) were investigated.

The minimum threshold solid content of the suspensions was determined as 15% by weight for a continuous HAp film structure. The silk sericin and fibroin intermediate layers drastically improved homogeneity of the HAp layer. The BSA adsorption of the glass/sericin/commercial-HAp film was $2.6 \mu\text{g}/\text{cm}^2$, more than twice of the glass/commercial-HAp, and glass/sericin/dry-milled-HAp films, evidencing the effectiveness of surface micro/nano topographical structure as well as chemical structure. The XRD patterns of spin coated commercial-HAp films on Ti6Al4V pointed out to a particular crystal orientation which increased the positive degree of cooperativity between HAp and proteins during adsorption or deposition.

ÖZET

HİDROKSİAPATİT/İPEK PROTEİN İNCE FİLM İMPLANT YÜZEYLERİ HAZIRLANMASI, MİKROYAPISAL ÖZELLİKLERİNİN VE MODEL PROTEİN ETKİLEŞİMLERİNİN İNCELENMESİ

Metal yük taşıyıcı sert doku implant cihazları üzerindeki biyouyumlu hidroksiapatit (HAp) kaplamalar lokal olarak yüzey üzerinde kemik dokusu oluşumunu hızlandırıp çimentosuz bağlanma sağlar. Hidroksiapatitin ameliyat sonrası iyileşme hızının artmasını ve implant ömrünün uzamasını sağlayan kemik dokusu oluşturucu proteinleri (BMP) taşıma potansiyelini kullanabilme amacıyla ince film HAp mikroyapıları geliştirilip, yüzeyde protein tutma kapasiteleri incelenmiştir.

HAp ince filmler, geliştirilen bir partikül sol metodu ve daldırma ve spin kaplama teknikleri ile biyoinert camlar ve Ti6Al4V alaşımlar üzerinde oluşturulmuştur. Filmlerin mikroyapıları SEM/EDX, AFM, XRD, ve FTIR yöntemleri ile incelenmiş ve yüzey pürüzlülükleri, Vickers sertlikleri ve yüzeye tutunma mukavemetleri tespit edilmiştir. İpek fibroin ve sericin protein film ara tabakalarının, üzerlerine kaplanan ince film hidroksiapatitin mikroyapısına ve model protein olarak kullanılan “bovine serum albumin (BSA)”i yüzeyde tutabilme davranışına, etkileri incelenmiştir.

Boşluksuz HAp film oluşumu için suspansiyonların minimum katı içeriği ağırlıkça %15 olarak tespit edilmiştir. İpek sericin ve fibroin ara tabakaları HAp filmlerin homojenliğini büyük ölçüde arttırmıştır. Cam/sericin/ticari-HAp filmin BSA adsorpsiyonu $2.6 \mu\text{g}/\text{cm}^2$ olarak tespit edilmiştir ve cam/ticari-HAp ve cam/sericin/kuru-öğütülmüş-HAp filmlerin adsorpsiyonlarının iki mislinden fazladır. Buda adsorpsiyonda yüzey mikro/nano topoğrafik yapısının, kimyasal yapı kadar etkili olabildiğine işaret etmektedir. Ti6Al4V altlık üzerinde spin kaplama yöntemi ile oluşturulan ticari-HAp filmlerin, yüzeye tutunma veya birikme sırasında HAp ile protein arasındaki pozitif kooperativite derecesini arttıracak yönde, belirli bir yönelmeye sahip kristal yüzeyi oluşturduğu, X- ışınları-kırınımı yöntemi ile tespit edilmiştir.

TABLE OF CONTENTS

LIST OF FIGURES	ix
LIST OF TABLES.....	xix
LIST OF ABBREVIATIONS.....	xx
CHAPTER 1. INTRODUCTION.....	1
CHAPTER 2. BONE HISTOLOGY, PHYSIOLOGY, CALCIUM AND PHOSPHATE METABOLISM.....	4
2.1. Overview of Bone Anatomy and Histology	4
2.1.1. Cortical Bone Structure	7
2.1.2. Trabecular Bone Structure.....	12
2.2. Overall Calcium and Phosphate Intake and Excretion Cycles	15
2.3. Bone Physiology.....	20
2.3.1. Structure of Collagen.....	20
2.3.2. Structure of Hydroxyapatite.....	23
2.3.3. Mechanism of Bone Production	24
2.3.4. Remodeling of Bone	26
2.3.5. Hormonal Control of Extracellular Fluid Levels of Calcium and Phosphate, and Their Deposition to and Resorption from the Bone	29
CHAPTER 3. BIOMEDICAL IMPLANTS	37
3.1. Overview of Biomedical Implants.....	37
3.2. Polymeric Implant Materials	42
3.3. Metallic Implant Materials.....	44
3.4. Ceramic Implant Materials	51
3.4.1. Almost Inert Crystalline Bioceramics.....	51
3.4.2. Porous Ceramics	54
3.4.3. Bioactive Glasses and Glass Ceramics	55

3.4.4. Calcium Phosphate Ceramics	57
3.5. Composite Implant Materials.....	59
CHAPTER 4. PREPARATION OF HYDROXYAPATITE THIN FILMS.....	60
4.1. Plasma Spray Hydroxyapatite Coating.....	60
4.2. Sol-Gel Routes for Thin Film Preparation.....	64
4.3. Particulate Sols	72
4.4. Sol-Gel Methods for Hydroxyapatite Coating.....	73
CHAPTER 5. HYDROXYAPATITE-PROTEIN INTERACTIONS	76
5.1. Hydroxyapatite-Silk Protein Interactions	76
5.2. The Effect and Delivery of Growth Factor and Cytokine Affinity for Bone Fracture and Peri-Implant Healing	80
5.3. BSA Adsorption onto Hydroxyapatite.....	83
5.4. Hydroxyapatite-Protein Interactions by Molecular Modeling.....	86
CHAPTER 6. EXPERIMENTAL.....	93
6.1. Materials	93
6.2. Methods	94
6.2.1. Hydroxyapatite Powder Dispersion, and Characterization.....	94
6.2.2. Preparation of Hydroxyapatite/Silk Protein Thin Films by Dip Coating.....	96
6.2.3. Bovine Serum Albumin and Collagen Adsorption on Thin Films	98
6.2.4. Electrochemical Anodization of Ti6Al4V	99
6.2.5. Preparation of Titania/Hydroxyapatite Thin Films by Spin Coating.....	99
6.2.6. Characterization of Thin Films	100
6.2.6.1. Microstructural Characterization	100
6.2.6.2. Mechanical Characterization	101
6.2.7. Molecular Modeling Methods	102
CHAPTER 7. RESULTS AND DISCUSSION.....	103
7.1. Hydroxyapatite Powder Dispersion, and Characterization.....	103

7.2. Particulate Sol Route Hydroxyapatite/Silk Protein Thin Film	
Surface Interactions	117
7.3. Enhanced Model Protein Adsorption of Silk Protein/ Hydroxyapatite Thin Films	156
7.4. Microstructural and Mechanical Properties of Titania/ Hydroxyapatite Films on Ti6Al4V Substrates	190
7.5. The Surface Electrostatic Potential Distribution of Hydroxyapatite by Molecular Modeling.....	242
CHAPTER 8. CONCLUSIONS AND RECOMMENDATIONS	253
REFERENCES	258

LIST OF FIGURES

Figure	Page
Figure 2.1. Schematic of partially sectioned humerus or arm bone	5
Figure 2.2. Schematic of blood supply to bone	6
Figure 2.3. Schematic haversian system (osteons) in compact bone and trabeculae in cancellous bone.....	6
Figure 2.4. Osteons (haversian system).....	9
Figure 2.5. The woven bone forming in a fracture callus.....	9
Figure 2.6. Photomicrograph of plexiform bone tissue	10
Figure 2.7. An interference contrast micrograph of haversian system showing osteon, lamellae and lacunae	11
Figure 2.8. Schematic lamellar substructures in osteon, and their cross sectional pictures under polarized light	11
Figure 2.9. A model of crystal plate orientation regulated by collagen fibrils.....	12
Figure 2.10. Trabecular (cancellous) bone level 1 structure.....	13
Figure 2.11. Trabecular (cancellous or spongy) bone trabecular packets and level 2 structure. The bony space contains the bone marrow	14
Figure 2.12. Organizational levels of cortical and trabecular bone	14
Figure 2.13. Overall calcium intake and excretion in the body	16
Figure 2.14. Distribution of calcium forms in blood plasma.....	16
Figure 2.15. Effect of increasing vitamin D ₃ intake on the plasma concentration of 25-hydroxycholecalciferol	17
Figure 2.16. Effect of plasma calcium ion concentration on the plasma concentration of 1,25-dihydroxycholecalciferol.....	18
Figure 2.17. Conversion of vitamin D ₃ to active forms and its role in controlling the plasma calcium concentration.....	19
Figure 2.18. Tropocollagen triple helix (madras helix)	22
Figure 2.19. Plan and side views of the hydroxyapatite structure	23
Figure 2.20. Schematic of periosteal and intraosseous osteoblasts	26
Figure 2.21. Induced stem cell differentiation into preosteoblasts.....	27
Figure 2.22. Schematic of osteoclast with villus like projections on the ruffled border	28

Figure 2.23. Histological structure of a parathyroid gland.....	30
Figure 2.24. Approximate changes in calcium and phosphate concentrations during the 5 hours of parathyroid hormone infusion.....	31
Figure 2.25. The approximate relation of plasma concentrations of parathyroid hormone and calcitonin with plasma calcium concentration.....	36
Figure 3.1. Schematic illustration of biocompatibility	40
Figure 3.2. A schematic illustration of probability of failure versus implant period for hip joint replacements	41
Figure 3.3. Yield strength to density ratio of some metallic implant materials.....	47
Figure 3.4. Part of phase diagram of Ti-Al-V (at 4 w% V).....	49
Figure 3.5. Optical micrograph of a chemically etched α - β Ti6Al4V alloy.....	49
Figure 3.6. Sequence of interfacial reactions involved in forming tissue-bioactive implant bond	56
Figure 3.7. The phase diagram for CaO and P ₂ O ₅ under 500 mmHg water partial pressure	58
Figure 4.1. Schematic cross-section of non-transferred DC arc plasma spray gun.....	60
Figure 4.2. A view of the internal workings of a DC arc plasma gun	61
Figure 4.3. Energy content vs. gas temperature for a DC thermal plasma operating with different plasma gases.....	61
Figure 4.4. Schematic model of the thermal decomposition of a spherical hydroxyapatite particle	62
Figure 4.5. Sequence of events a to f occurring during deposition of a supersonically accelerated semi-molten hydroxyapatite particle impinging.....	63
Figure 4.6. Schematic of the steady state sol-gel dip coating process depicting structural development of a gel film.....	66
Figure 4.7. Schematic of the stages of the dip coating	67
Figure 4.8. Stages of the batch spin-coating process.....	68
Figure 4.9. An inorganic route for the preparation of particulate sol hydroxyapatite coatings.	74
Figure 4.10. An organic route without the presence of any dense particles >1nm for the preparation of hydroxyapatite particles.....	74
Figure 5.1. In the sericin structure Serine and Threonine linkage sequences in the crystal domain forming β -sheet aggregates	77
Figure 5.2. Schematic of the extracellular and intracellular BMP signaling pathways	82

Figure 5.3. The schematic representation of HAp-protein surface interactions	84
Figure 7.1. Change in the tapped apparent density of the c-HAp powder as a function of dry milling time in tungsten carbide mill	103
Figure 7.2. Hydroxyapatite powder SEM images.....	104
Figure 7.3. Particle size distribution of c-HAp powder (7.6%) dispersed with ultrasound and the dispersant was hydropalate (2%).....	105
Figure 7.4. Particle size distribution of c-HAp powder (7.6%) dispersed with ultrasound and the dispersant was calgon (1%).....	105
Figure 7.5. Particle size distribution of c-HAp powder (7.6%) dispersed with liquid nitrogen quenching (single and double), wet ball milling with zirconia balls, followed by ultrasound, and with 2% hydropalate as dispersant.	107
Figure 7.6. Particle size distribution of c-HAp powder (7.6%) dispersed with thermal shock (from 450 C powder quenched in ambient T water), followed by ultrasound, and with 2% hydropalate as dispersant.....	107
Figure 7.7. Particle size distribution of c-HAp powder (7.6%) dispersed with liquid nitrogen quenching (single and double), fast propeller mixing, followed by ultrasound, and with 1% calgon as dispersant	108
Figure 7.8. Particle size distribution of c-HAp powder (30%) dispersed with liquid nitrogen quenching (double), wet ball milling with zirconia balls, followed by ultrasound, and with 2% hydropalate as dispersant.....	109
Figure 7.9. Particle size distribution of c-HAp powder (30%) dispersed with liquid nitrogen quenching (double), wet ball milling with zirconia balls, followed by ultrasound, and with 1% calgon as dispersant.....	110
Figure 7.10. Particle size distribution of c-HAp powder(30%) dispersed with liquid nitrogen quenching (double), wet ball milling with zirconia balls, followed by ultrasound, and with 3% fructose as dispersant.....	110
Figure 7.11. pH versus 1.0 N acid solution volume added obtained by autotitrator for (a) c-HAp powder suspension, (b) p-HAp powder suspension.....	112
Figure 7.12. pH versus zeta potential for (a) c-HAp powder suspensions, (b) m-HAp powder suspensions	113
Figure 7.13. Number mean particle size distributions of HAp suspensions as a function of pH, measured by zeta sizer (without any dispersant).....	116
Figure 7.14. Number mean particle size distributions HAp suspensions as a function of hydropalate 64 ratio (organic dispersant), measured by zeta sizer.....	116

Figure 7.15. The SEM images of c-HAp coating on glass substrates by dip coating in 1.0% solid content suspension.....	117
Figure 7.16. The SEM images of m-HAp coating on glass substrates by dip coating in 1.0% solid content suspension.....	118
Figure 7.17. The SEM images of the coatings on glass substrates prepared by 5 times dip coating in the 1% c-HAp powder.....	119
Figure 7.18. The SEM images of the coatings on glass substrates prepared by 5 times dip coating in the 1% m-HAp powder	120
Figure 7.19. The SEM images of the c-HAp coatings on the glass substrates prepared by 15% solid content sol by dip coating.....	122
Figure 7.20. The AFM images of the c-HAp coated on the glass substrates prepared by 15% solid content sol by dip coating.....	123
Figure 7.21. The SEM images of the m-HAp coatings on the glass substrates prepared by 15% solid content sol, by dip coating.....	125
Figure 7.22. The AFM images of the m-HAp coatings on the glass substrates prepared by 15% solid content sol by dip coating.....	127
Figure 7.23. The SEM images of the m-HAp coated on the glass substrates prepared by 25% solid content sol by dip coating.....	129
Figure 7.24. The SEM images of the thin films prepared with 15% c-HAp suspension after the heat treatment at 560°C, for 30 min.....	131
Figure 7.25. The SEM images of the thin films prepared with 15% m-HAp suspension after the heat treatment at 560°C, for 30 min.....	132
Figure 7.26. The SEM images of the thick film prepared with 25% m-HAp suspension, after the heat treatment at 560°C, for 30 min.....	133
Figure 7.27. (a) Grazing incidence XRD pattern of the glass/c-HAp thin film, (b) the same film heat treated at 560°C for 30 min	134
Figure 7.28. (a) Grazing incidence XRD pattern of the glass/m-HAp thin film, (b) the same film heat treated at 560°C for 30 min	134
Figure 7.29. FTIR spectrum of bulk commercial hydroxyapatite (c-HAp) powder.....	135
Figure 7.30. (a) The FTIR spectrum of the glass/c-HAp thin film, (b) the same film heat treated at 560°C for 30 min.....	135
Figure 7.31. (a) The FTIR spectrum of the glass/m-HAp thin film, (b) the same film heat treated at 560°C for 30 min.....	135
Figure 7.32. The FTIR spectra of sericin and fibroin films on glass substrates	136

Figure 7.33. The SEM images of the sericin film on glass substrate	137
Figure 7.34. The AFM images of the sericin film on glass	138
Figure 7.35. The SEM images of the fibroin film on glass	139
Figure 7.36. The AFM images of the fibroin film on glass substrate.....	140
Figure 7.37. The SEM images of the c-HAp films (with 15% solid content suspension) on the glass/sericin substrate.....	142
Figure 7.38. The AFM images of the c-HAp films (with 15% solid content suspension) on the glass/sericin substrate.....	143
Figure 7.39. The SEM images of the m-HAp films (with 15% solid content suspension) on the glass/sericin substrate.....	144
Figure 7.40. The AFM images of the m-HAp films (with 15% solid content suspension) on the glass/sericin substrate.....	145
Figure 7.41. The SEM images of the c-HAp films (with 15% solid content suspension) on glass/fibroin substrate	147
Figure 7.42. The AFM images of the c-HAp films (with 15% solid content suspension) on glass/fibroin substrate	148
Figure 7.43. The SEM images of the m-HAp films (with 15% solid content suspension) on the glass/fibroin substrate	150
Figure 7.44. The AFM images of the m-HAp films (with 15% solid content suspension) on the glass/fibroin substrate	151
Figure 7.45. (a), (b), (c) The SEM images of the c-HAp films (with 11% solid content suspension) on glass/fibroin substrate.....	153
Figure 7.46. (a), (b), (c) The SEM images of the m-HAp films (with 11% solid content suspension) on glass/fibroin substrate.....	153
Figure 7.47. (a) glass/sericin/c-HAp, (b) glass/sericin/m-HAp, (c) glass/fibroin/ c-HAp, (d) glass/fibroin/m -HAp thin film structures after heat treatment at 560°C	154
Figure 7.48. BSA particles adsorbed on glass surface.....	156
Figure 7.49. The AFM image of the BSA adsorption on fibroin film.....	157
Figure 7.50. The AFM image of the BSA adsorption on sericin film.....	159
Figure 7.51. The AFM image of adsorbed BSA on c-HAp film on glass substrate	161
Figure 7.52. The AFM images of adsorbed BSA on m-HAp film on glass substrate	163
Figure 7.53. The AFM images of adsorbed BSA on glass/fibroin/c-HAp film.....	166
Figure 7.54. The AFM images of adsorbed BSA on glass/fibroin/m-HAp.....	168

Figure 7.55. The AFM images of adsorbed BSA on glass/sericin/c-HAp	170
Figure 7.56. The AFM images of adsorbed BSA on glass/sericin/m-HAp	172
Figure 7.57. The AFM image of the collagen type I adsorption on glass surface	174
Figure 7.58. The AFM image of the collagen type I adsorption on fibroin film	175
Figure 7.59. The AFM image of the collagen adsorption on sericin film	176
Figure 7.60. The AFM image of adsorbed collagen type I on c-HAp film on glass substrate	179
Figure 7.61. The AFM image of adsorbed collagen type I on m-HAp film on glass substrate	180
Figure 7.62. The AFM images of adsorbed collagen type I on glass/fibroin/c-HAp film	181
Figure 7.63. The AFM images of adsorbed collagen type I on glass/fibroin/m-HAp film	182
Figure 7.64. The AFM images of adsorbed collagen type I on glass/sericin/c-HAp film	183
Figure 7.65. The AFM images of adsorbed collagen type I on glass/sericin/m-HAp film	185
Figure 7.66. Calibration curve for BSA analysis by size exclusion HPLC; total peak area versus concentration	187
Figure 7.67. BSA adsorption on glass (blank), glass/c-HAp, glass/m-HAp, glass/sericin/c-HAp, and glass/sericin/m-HAp substrates, reported as decrease in BSA concentration versus time	188
Figure 7.68. BSA adsorbed quantity on glass/m-HAp film as a function of time	188
Figure 7.69. BSA adsorbed quantity on glass/sericin/m-HAp film as a function of time	189
Figure 7.70. BSA adsorbed quantity on glass/sericin/c-HAp film as a function of time	189
Figure 7.71. The glycerol/water ratio (weight %) for constant current of 15 mA as a function of voltage for electrochemical anodization of Ti6Al4V	190
Figure 7.72. The surface roughness, R_q , of the Ti6Al4V alloy as it was, and as anodized at various voltages versus surface finish (grinding grit)	191
Figure 7.73. Surface hardness (HV) of the Ti6Al4V alloy with respect to surface finish grit and anodization voltage	192

Figure 7.74. Ti6Al4V alloy surface hardness versus anodization voltage averaged over surface roughness; the alloy (without anodization) is shown as 0 volt	192
Figure 7.75. The SEM images of the 20 V anodized, 1200 grit grinded Ti6Al4V alloy (a), (b) general view, (c) crest region, (d) trough region	193
Figure 7.76. The EDX analysis of 20 V anodized, 1200 grit grinded Ti6Al4V alloy (a) crest region, (b) trough region	194
Figure 7.77. The EDX analysis of 1200 grit grinded Ti6Al4V alloy anodized at (a) 60 V, (b) 120 V, (c) 240 V, (d) 400 V	194
Figure 7.78. Ti/O ratio of the anodized 1200 grit grinded alloys versus anodization voltage	195
Figure 7.79. The Vickers hardness versus Ti/O atomic ratio of the 1200 grit grinded alloys anodized at various voltages	195
Figure 7.80. The XRD patterns of 1200 grit grinded alloys anodized at various voltages	196
Figure 7.81. The SEM images of 1200 grit grinded Ti6Al4V alloy anodized at (a), (b) 60V, (c), (d) 120 V, (e), (f) 240 V, and (g), (h) 400 V	198
Figure 7.82. The SEM images of the Ti6Al4V alloy substrate (1200 grit)/ c-TiO ₂ (H ₂ O suspension, 1 layer), spin coated, heat treated at 360°C	200
Figure 7.83. The SEM images of the Ti6Al4V alloy substrate (180 grit)/ c-TiO ₂ (EtOH suspension, 3 layers), spin coated, heat treated at 360°C	201
Figure 7.84. The SEM images of the Ti6Al4V alloy substrate (1200 grit)/ c-TiO ₂ (H ₂ O suspension, 1 layer), spin coated, heat treated at 850°C	202
Figure 7.85. The SEM images of the Ti6Al4V alloy substrate (180 grit)/ c-TiO ₂ (EtOH suspension, 3 layers), spin coated, heat treated at 850°C	203
Figure 7.86. The XRD patterns of (a) Degussa P25 TiO ₂ powder, (b) 1200 grit Ti6Al4V alloy, (c) 1200 grit Ti6Al4V/c-TiO ₂ (1 layer, H ₂ O suspension) heat treated at 850°C, (d) 180 grit Ti6Al4V/c-TiO ₂ (3 layers, EtOH suspension) heat treated at 850°C	205
Figure 7.87. The SEM images of the Ti6Al4V alloy substrate (1200 grit)/c-HAp (H ₂ O suspension, 1 layer), spin coated, heat treated at 360°C	208
Figure 7.88. The SEM images of the Ti6Al4V alloy substrate (1200 grit)/c-HAp (H ₂ O suspension, 1 layer), spin coated, heat treated at 850°C	209

Figure 7.89. The SEM images of the Ti6Al4V alloy substrate (1200 grit)/c-HAp (EtOH suspension, 1 layer), spin coated, heat treated at 360°C	210
Figure 7.90. The SEM images of the Ti6Al4V alloy substrate (1200 grit)/c-HAp (EtOH suspension, 1 layer), spin coated, heat treated at 700°C	211
Figure 7.91. The SEM images of the Ti6Al4V alloy substrate (1200 grit)/c-HAp (EtOH suspension, 1 layer), spin coated, heat treated at 850°C	212
Figure 7.92. The SEM images of the Ti6Al4V alloy substrate (1200 grit)/c-HAp (H ₂ O suspension, 3 layers), spin coated, heat treated at 700°C	213
Figure 7.93. The SEM images of the Ti6Al4V alloy substrate (1200 grit)/c-HAp (H ₂ O suspension, 3 layers), spin coated, heat treated at 850°C	214
Figure 7.94. The XRD patterns of (a) c-HAp powder, (b) 180 grit Ti6Al4V alloy/c-HAp (3 layers, EtOH suspension) film heat treated at 360°C, (c) 180 grit Ti6Al4V/c-HAp (3 layers, EtOH suspension) film heat treated at 700°C.....	217
Figure 7.95. The XRD patterns of (a) 1200 grit Ti6Al4V alloy/c-HAp (1 layer, H ₂ O suspension) film heat treated at 360°C, (b) 1200 grit Ti6Al4V/c-HAp (1 layer, H ₂ O suspension) film heat treated at 700°C, (c) 1200 grit Ti6Al4V/c-HAp (1 layer, H ₂ O suspension) heat treated at 850°C	219
Figure 7.96. The SEM images of the Ti6Al4V alloy substrate (1200 grit) anodized at 20 V/c-HAp (EtOH suspension, 3 layers), spin coated, heat treated at 850°C.....	222
Figure 7.97. The SEM images of the Ti6Al4V alloy substrate (1200 grit) anodized at 60 V/c-HAp (EtOH suspension, 3 layers), spin coated, heat treated at 850°C.....	223
Figure 7.98. The SEM images of the Ti6Al4V alloy substrate (1200 grit)/c-TiO ₂ (H ₂ O suspension, 3 layers)/c-HAp (H ₂ O suspension, 1 layer), spin coated, heat treated at 360°C	224
Figure 7.99. The SEM images of the Ti6Al4V alloy substrate (1200 grit)/c-TiO ₂ (H ₂ O suspension, 3 layers)/c-HAp (H ₂ O suspension, 1 layer), spin coated, heat treated at 850°C	225
Figure 7.100. The SEM images of the Ti6Al4V alloy substrate (1200 grit)/c-TiO ₂ (H ₂ O suspension, 2 layers)/c-HAp (H ₂ O suspension, 3 layers), spin coated, heat treated at 850°C	226

Figure 7.101. The XRD pattern of the film Ti6Al4V (1200 grit)/c-TiO ₂ (H ₂ O suspension, 1 layer)/c-HAp (H ₂ O suspension, 1 layer), heat treated at 850°C	227
Figure 7.102. The surface roughness, R _q , of the Ti6Al4V alloy (1200 grit grinded)/c-TiO ₂ as a function of coated TiO ₂ thickness	228
Figure 7.103. The surface roughness, R _q , of the Ti6Al4V alloy (1200 grit grinded)/c-HAp as a function of heat treatment temperature	229
Figure 7.104. The surface roughness, R _q , of the (a) anodized Ti6Al4V alloy/c-HAp (H ₂ O suspension, 3 layers), (b) anodized Ti6Al4V alloy/c-HAp (EtOH suspension, 3 layers), heat treated at 850°C as a function of voltage.....	230
Figure 7.105. The surface roughness, R _q , Ti6Al4V alloy/c-TiO ₂ /c-HAp as a function of intermediate TiO ₂ layers coated	231
Figure 7.106. The surface hardness (HV) of the Ti6Al4V alloy/c-TiO ₂ as a function of coated TiO ₂ thickness (coated layers)	232
Figure 7.107. The surface hardness (HV) of the Ti6Al4V alloy/c-HAp as a function of heat treatment temperature (a) the hardness at 850°C as the apparent hardness values, (b) the detailed hardness values up to 700°C	233
Figure 7.108. The surface hardness (HV) of the Ti6Al4V alloy/c-TiO ₂ /c-HAp as a function of TiO ₂ thickness (coated layers)	234
Figure 7.109. The dilatometric curves of the pellets prepared from the bulk powders of c-TiO ₂ , c-HAp, homogeneous mixture of c-TiO ₂ and c-HAp, layered c-TiO ₂ /c-HAp.....	236
Figure 7.110. The adhesion strength (by tensile test) of Ti6Al4V (1200 grit)/c-TiO ₂ (H ₂ O suspension, 2 layers) as a function of temperature.....	236
Figure 7.111. The adhesion strength (by scratch test) of the Ti6Al4V (180g)/c-TiO ₂ (EtOH suspension), heat treated at 850°C, as a function of TiO ₂ thickness (coated layers)	237
Figure 7.112. The adhesion strength (by tensile test) of the Ti6Al4V/c-HAp with various substrate surface finish (grit), suspending medium, and HAp thickness (coated layers) as a function of heat treatment temperature	238
Figure 7.113. The adhesion strength (by scratch test) of the Ti6Al4V (180 grit)/c-HAp (EtOH suspension, 1 layer) as a function of heat treatment temperature	238

Figure 7.114. The adhesion strength (by tensile test) of the anodized Ti6Al4V (1200 grit)/c-HAp (H ₂ O suspension, 3 layers) heat treated at 850°C as a function of anodization voltage	240
Figure 7.115. The adhesion strength (by tensile test) of Ti6Al4V substrate/c-TiO ₂ (H ₂ O suspension, 2 layers)/c-HAp, with various substrate surface finish (grit), and suspending medium, as a function of temperature	240
Figure 7.116. The adhesion strength (by scratch test) of the 180 grit Ti6Al4V substrate/c-TiO ₂ (EtOH suspension)/c-HAp (EtOH suspension, 3 layers), heat treated at 850°C as a function of TiO ₂ thickness (coated layers)	241
Figure 7.117. Hydroxyapatite unit cell; the color codes for axis are: a=red, b=green, c=blue; the color codes for atoms are: Ca=Khaki, P=orange, O=red, H=white	244
Figure 7.118. Hydroxyapatite crystal structure with 9 unit cells: (a), (b) ax3, bx3, cx1, (b) viewed through c-axis, (c), (d) ax1, bx3, cx3	245
Figure 7.119. Solid and transparent views of the electrostatic potential mapped on the electron isodensity surface of 0.0004 e/Bohr ³	246
Figure 7.120. Solid and transparent views of the electrostatic potential mapped on the electron isodensity surface of 0.0004 e/Bohr ³	247
Figure 7.121. Solid and transparent views of the ESP mapped on the electron isodensity surface of 0.0004 e/Bohr ³ of two unit cells of HAp crystal, ax2, bx1, cx1, through	248
Figure 7.122. Solid and transparent views of the ESP mapped on the electron isodensity surface of 0.0004 e/Bohr ³ of two unit cells of HAp crystal, ax1, bx2, cx1, through	249
Figure 7.123. Solid and transparent views of the ESP mapped on the electron isodensity surface of 0.0004 e/Bohr ³ of two unit cells of HAp crystal, ax1, bx1, cx2, through	250
Figure 7.124. The ESP distribution of NaCl crystal of two unit cells mapped on the isovalue electron density surface of 0.0004 isovalue with maximum potential values as ±0.05897 hartree	251
Figure 7.125. Solid views of the ESP mapped on various electron isodensity surfaces unit cells of HAp.....	251
Figure 7.126. Electrostatic potential surface versus electron isodensity surface for one and two unit cells of hydroxyapatite crystal	252

LIST OF TABLES

<u>Table</u>	<u>Page</u>
Table 2.1. Bone structural organization.....	7
Table 3.1. The possible host tissue responses to implant material	38
Table 3.2. Classification of implant materials	40
Table 3.3. Surgical use of implant materials	41
Table 3.4. Effect of implantation on polymers	44
Table 3.5. Composition of 316L stainless steel surgical implants.....	45
Table 3.6. Mechanical properties of stainless steel surgical implants.....	45
Table 3.7. Chemical compositions of Co-based alloys.....	46
Table 3.8. Mechanical properties of Co-based alloys.....	46
Table 3.9. Chemical composition of pure titanium	48
Table 3.10. Chemical composition of wrought Ti alloys	48
Table 3.11. Chemical composition of Ti6Al4V alloys.....	48
Table 3.12. Mechanical properties of pure titanium.....	49
Table 3.13. Mechanical properties of wrought Ti alloys.....	50
Table 3.14. Mechanical properties of Ti6Al4V	50
Table 3.15. Mechanical properties of dense Al ₂ O ₃ and ZrO ₂ based ceramics in comparison to CoCr ally and cortical bone	54
Table 7.1. Geometry Optimization Job.....	242

LIST OF ABBREVIATIONS

BSA	: Bovine serum albumin
BML	: Bovine milk lactoferrin
BMP	: Bone morphogenetic protein
c-Hap	: Hydroxyapatite from commercial source
e	: electron charge
Fg	: Fibrinogen
HHT	: Human holo-transferrin
IEP	: Iso electric point
LSZ	: Lysozyme
m-Hap	: Dry milled hydroxyapatite powder
PBS	: Phosphate buffer solution
PZC	: Point of zero charge
SBF	: Simulated body fluid
TGF- β	: Transforming growth factor-beta superfamily
ζ	: Zeta potential

CHAPTER 1

INTRODUCTION

The formation of hydroxyapatite in vivo as the mineral constituent of bone and teeth tissue is closely related to the physiology of calcium and phosphate metabolism in vertebrates. The intricate hormonal control (parathyroid hormone and calcitonin with the combined effect of vitamin D₃) mechanisms of osteoblastic and osteoclastic activities, including the feedback control of calcium and phosphate extracellular fluid levels, regulate the deposition and resorption of calcium phosphate (CaP) compounds in the bone (Guyton 1991). The embodiment of hard tissue implants to the host bone tissue is achieved through morphological fixation, osteoconduction, osseointegration, or time regulated resorption, with healing accelerated osteoinductively, governed by the closely related biological and chemical processes. The intended permanent or transitory anchorage of the implant in the living tissue with a minimal foreign body reaction, for proper biofunctioning, and without premature failure, is engineered by material development, design, and strict quality assured manufacturing (Winn, et al. 1998).

Biocompatible mineral coatings of CaP allow metallic materials to be employed as in vivo hard tissue implants. They act as local scaffolds for enhanced osteoconduction by osteogenic cell proliferation and differentiation on the implant surface (osteinduction) resulting in ingrowth of the surrounding hard tissue. Hydroxyapatite (HAp), $\text{Ca}_{10}(\text{PO}_4)_6(\text{OH})_2$, has been experimentally confirmed to be one of the best implant coating materials for post operative fast bone apposition and cementless mechanical fixation based on the concerted dynamic resorption-precipitation-bone substitution in vivo processes. Plasma sprayed HAp is the most widely employed industrial method for bioactive CaP coatings. However, there is a general tendency to develop new routes for hydroxyapatite coatings on implant materials due to the fact that coatings produced by the plasma spraying have a number of disadvantages, namely, inhomogeneous chemical composition and crystallinity, formation of in vivo fast dissolving unfavorable phases (α -tricalcium phosphate, tetracalcium phosphate, oxyhydroxyapatite, calcium oxide, and amorphous phases), thermal and amorphous to crystalline phase transformation stress cracking, and

delamination or even detachment of the coating layer (Heimann 2006, Best, et al. 2008, Radin, et al. 1993, Cirilli, et al. 1997). Sputter coating (Torrise and Foti 1993), pulsed laser deposition (Gyorgi 2004), electrophoresis (Raja, et al. 2005, Zhitomirsky 2000, Albayrak, et al. 2007), electrochemical deposition (Ban and Maruno 1998), thermal substrate method (Kuroda, et al. 2001), aerosol-gel method (Manso-Silvan, et al. 2003), biomimetic formation (Varma 1999, Liu 2002), and sol-gel deposition (Kim 2004, Gan and Pilliar 2004, Cavalli, et al. 2001) are among the other techniques. Hydroxyapatite thin film coatings prepared by sol-gel methods have attracted much attention due to the inherent advantages of being chemically and physically homogeneous and pure, capability of tailoring chemical composition, porosity, pore size and surface roughness, besides the relative simplicity of the method.

The favorable interactions between hydroxyapatite, and silk fibroin and sericin in the biomimetic nucleation and crystal growth of hydroxyapatite deposits, were experimentally observed (Kong, et al. 2004, Takeuchi, et al. 2005). The aspartate, arginine, glutamate residues are arranged in polar clusters in the β -sheet structure of fibroin, inducing a surface charge distribution due to the hydroxyl, carboxyl, and carbonyl groups, that have an affinity for calcium ions, providing local concentrations of Ca^{2+} leading to nucleation of HAp crystals. HAp is deposited in the form of tiny crystals on fibroin due to the regular surface arrangement of nucleation sites distributed on a molecular scale. In the β -sheet structure of sericin, 10% of the carboxyl groups are arranged perpendicular to the plane of the sheet, providing a periodic distribution of charged surface sites which induces electrostatic affinity for Ca^{2+} ions leading to HAp nucleation and crystal growth.

Fracture or peri-implant healing involves interactions between the critical physical, molecular, and cellular elements inducing the sequence of events, potentially osteogenic cell recruitment, attachment, expansion, differentiation, and bone tissue generation. Cytokines and bone morphogenetic proteins (BMPs) from the disrupted matrix, and from degranulation of platelets in the hemorrhage zone signal and guide the marrow derived osteogenic cell populations including vascular pericytes, stromal cells and mesenchymal stem cells (MSCs) to migrate to the damaged site. MSCs are converted to preosteogenic cells on the site, which in turn transformed into osteoblastic, chondroblastic, or fibroblastic differentiated cell lineages. The technology to use CaP compound coatings as BMPs carrier is under development by imparting enhanced affinity between hydroxyapatite and proteins (Winn, et al. 1998, Bansal, et al.

2005). In these studies bovine serum albumin (BSA) is used as model protein to mimic the behavior of BMPs. Hydroxyapatite was shown to strongly adsorb proteins, for example BSA by calcium ions, and lysozyme by phosphate ions (Kandori, et al. 1998). HAp affinity can be imparted to proteins by chemical modifications (e.g. through thiol-labile disulfide linkages) (Winn, et al. 1998). The surface topography of the hydroxyapatite was shown to be as important as the chemistry for protein adsorption.

In this study, hydroxyapatite film implant surfaces were prepared by a particulate sol route. A variety of particle dispersion techniques were used to prepare HAp colloidal suspensions. Preparation of thin films of HAp with the colloidal suspensions on bioinert glass surfaces by dip coating method was investigated. The microstructure of the films was characterized by SEM, AFM, XRD and FTIR. The effects of the intermediate silk fibroin and silk sericin coatings on the formation and surface topography of HAp films were determined. The model protein (BSA) adsorption capabilities of the various hydroxyapatite surfaces were investigated comparatively. The HAp films were prepared on Ti6Al4V surfaces by a particular sol spin coating method. TiO₂ intermediate layers of controlled, variable thickness were incorporated. The surface roughness and Vickers hardness of the surfaces, and the adhesion strength of the films were determined.

CHAPTER 2

BONE HISTOLOGY, PHYSIOLOGY, CALCIUM AND PHOSPHATE METABOLISM

The formation of bone and teeth is closely connected with the physiology of calcium and phosphate metabolism, the function of vitamin D and the regulatory functions of the parathyroid hormone and calcitonin. In order to assess the physiological details, a brief overview of bone anatomy and histology is provided. A more detailed physiology-structure-function analysis is elaborated in conjunction with the physiology of bone formation.

2.1. Overview of Bone Anatomy and Histology

Bones in human (and other mammals) can be classified into three groups on the basis of general shape: short, flat and long (or tubular). Tarsals, carpals, and vertebral bodies are examples of short bones, and are approximately equiaxed in shape. Flat and tubular bones are marked with one dimension much longer or shorter than the other two; cranial vault, scapula, wing of ileum are formed by large flat bones, while lamina of vertebra constitutes an example of small flat bones. Humerus, ulna, radius, metacarpals, femur, tibia, fibula, metatarsals, and phalanges are tubular long bones with expanded metaphysis and epiphysis parts at the either end of diaphyseal shaft. In Figure 2.1a partially sectioned arm bone (humerus) is shown schematically.

Bones are also classified into two types on the basis of minute microstructure and especially on porosity. The cortical (compact) bone is the denser type with a porosity of 5-10%. It is found in the shaft of long bones and forms the outer shell around the cancellous bone. Approximately 80% of the total bone mass is comprised by the cortical bone. The trabecular (cancellous or spongy) bone is the porous type with a porosity of 50-90%. It is found in the end sections of long bones (proximal epiphysis, distal epiphysis, metaphysis), in short bones like vertebrae, and in flat bones like pelvis.

The bone consists of a central fatty and hematopoietic marrow that is supported by hard tissue and surrounded by periosteum. It is a dynamic structure which is

continually being absorbed and deposited by cellular activity and hence numerous nutrients, and metabolic waste are being carried in and out of the site. This material transport is achieved through the circulation of blood within the bone by nutrient artery, periosteal, epiphyseal, metaphyseal arteries, capillaries (Figure 2.2), haversian capillaries (Figure 2.3), and the corresponding veins. Marrow is a source of bone cells, and blood vessels in marrow form an essential part of the blood circulation in the bone.

Both the cortical and trabecular bone structures are examined in four organizational levels based on the size scale summarized in Table 2.1 (Martin and Burr 1998).

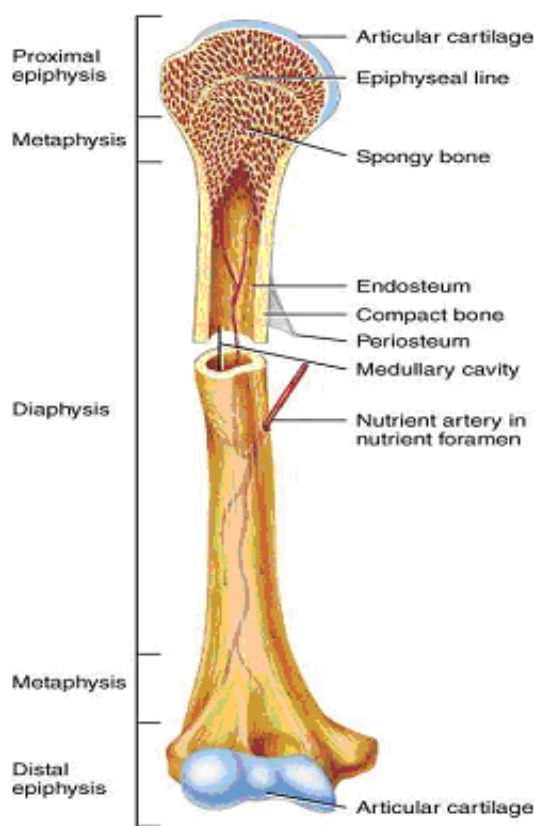


Figure 2.1. Schematic of partially sectioned humerus or arm bone (an example of a long bone from shoulder to elbow) illustrating the anatomic macro relation (level 0) of the trabecular and compact bone structures. (Source: Shashidhar 2006)

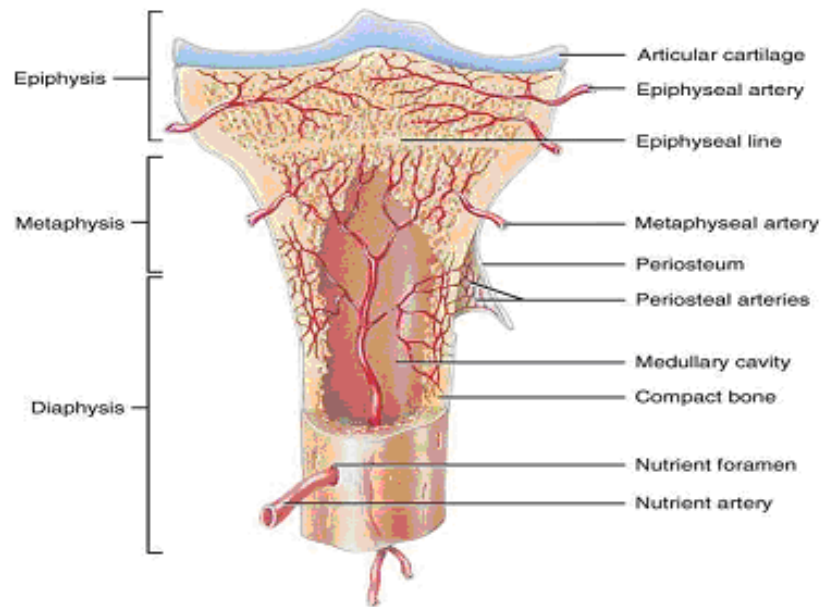


Figure 2.2. Schematic of blood supply to bone.
(Source: Shashidhar 2006)

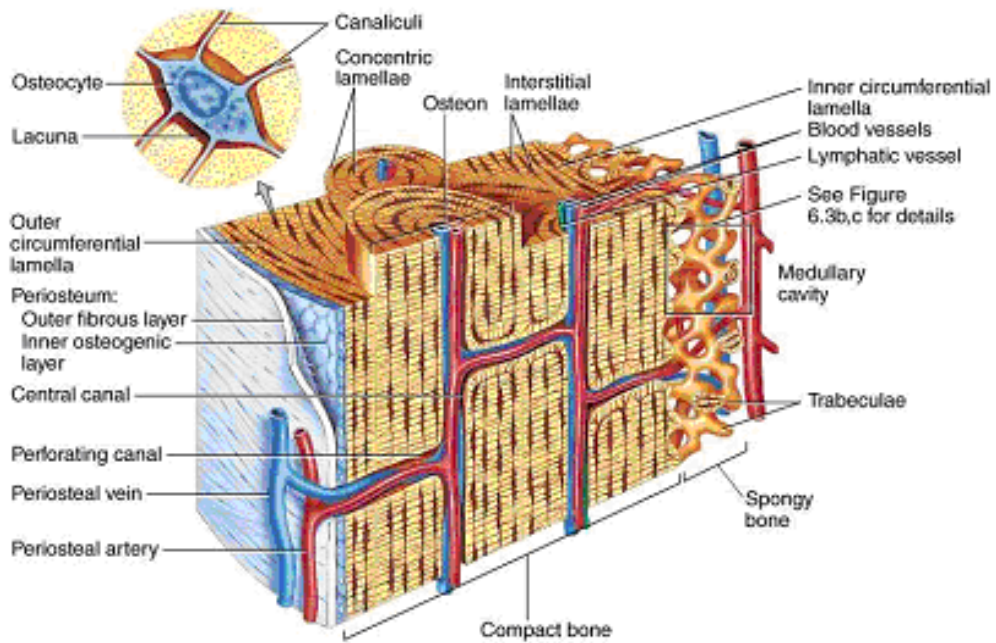


Figure 2.3. Schematic haversian system (osteons) in compact bone and trabeculae in cancellous bone. (Source: Shashidhar 2006)

Table 2.1. Bone structural organization
(Source: Martin and Burr 1998)

Level	Cortical Structure	Size Range	Trabecular Structure	Size Range
0	Macro structure	>3 mm	Macro structure	>3 mm
1	Primary osteons Secondary osteons Woven tissue Plexiform tissue Interstitial tissue	100-300 μm	Primary trabeculae Secondary trabeculae Trabecular packets	75-200 μm
2	Lamellae Lacunae Cement lines Canaliculi	3-20 μm	Lamellae Lacunae Cement lines Canaliculi	1-20 μm
3	Collagen-mineral composite	1-600 nm	Collagen-mineral composite	1-400 nm

2.1.1. Cortical Bone Structure

In general, the bone has a very limited strain resistance, and is a brittle, micro cracking solid. **The level 0 macro structure of cortical bone** provides the effective stiffness, toughness, and strength as a solid material. **The first organizational level of cortical bone** defines four types of cortical bone tissue as follows.

Primary Osteonal Cortical Bone Tissue: The predominant structure found in the first level cortical structure is osteon (also termed haversian system in honor of Clopton Havers who published his work in 1691), which consists of concentric cylinders termed lamellae with a central canal (haversian canal) in which blood capillaries and nerve fibers run through. In general, osteons are aligned parallel to the long axis of bone. The primary bone structures are formed on cartilage where previously bone tissue does not exist. The osteons in the primary bone tissue are smaller compared to the secondary osteons, do not contain as many lamella, and the vascular channels (haversian channels) are smaller in diameter, and hence, it is hypothesized that primary osteonal cortical bone is mechanically stronger than secondary osteonal cortical bone (Martin and Burr 1998).

Secondary Osteonal Cortical Bone Tissue: The osteons in the secondary cortical bone tissue are formed by continual absorption by osteoclasts (large phagocytic, multinucleated cells), and continual deposition by osteoblasts (active bone forming

cells) of the bone tissue, a process known as remodeling of bone. The osteoclasts eat out a tunnel in the bone tissue for a period of 3 weeks, at the end of which osteoclasts disappear and the tunnel is invaded by osteoblasts. New bone is laid down in staggered concentric layers of lamellae on the inner surfaces of cavity until the bone begins to encroach on the blood vessels supplying the area, and the haversian canal thereby is formed which is what remains of the original cavity (Guyton 1991). The diameter of the secondary osteons ranges in 200 to 300 μm , while the diameter of haversian canals ranges in 50 to 90 μm , incorporating the blood capillaries of typically 15 μm in diameter (Martin and Burr 1998). The haversian canals, and hence, osteons are connected to each other and the periosteum by oblique channels termed volkmann's canals. The spaces between the separate osteons are occupied by interstitial lamellae which are formed by pre-existing osteons that have since been reabsorbed. Figure 2.3 and Figure 2.4 shows the osteons and the related secondary level structures in the haversian system.

Woven-Fibered Cortical Bone: Woven bone is a disorganized and loose arrangement of third level bone structure of collagen type I, but highly mineralized, and is the type of bone that can be formed all new without the need of any existing cartilage or bone tissue. The woven bone does not contain any organized structures such as osteons. It is often found in the skeletons of fast growing youngsters and in the skeletons of adults only in the case of trauma or disease. Especially fracture of a bone activates a large osteoblastic activity and woven bone tissue is laid down very fast forming the fracture callus. Because of the disorganized collagen fiber structure and higher mineralization, the woven bone is relatively stiffer and more brittle (Christel, et al. 1981). Figure 2.5 shows a picture of woven bone.

Plexiform Cortical Bone Tissue: Plexiform bone comprises of vascular plexus contained within lamellar bone sandwiched by woven bone. Its grows in consequent perpendicular and parallel patterns to the outer bone surface forming brick like structures 125 μm wide. Plexiform bone tissue has a larger surface area compared to other cortical bone tissue giving way to faster formation of tissue, and increasing the stiffness and strength in short time. Therefore, this type of cortical bone tissue is found mostly in rapidly growing large animals like cow or sheep. However, due to its brick like structure it can hardly arrest crack propagation, and hence is not common in active

species such as dogs and humans. Photomicrographs of plexiform bone tissue are shown in Figure 2.6.

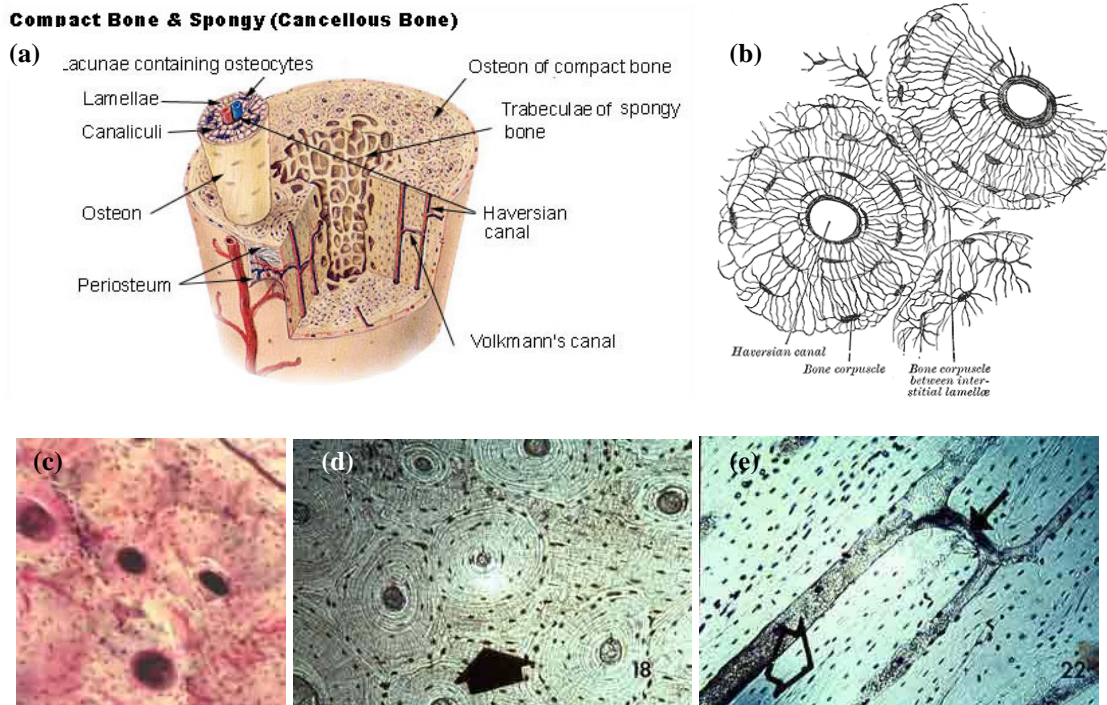


Figure 2.4. Osteons (haversian system), (a) schematic of compact bone and cancellous bone showing a protruded osteon, (b) schematic of cross sectional osteonal tissue, (c), (d) histological views of compact bone transverse cross sections, (e) histological view of compact bone, longitudinal cross section. (Source: (a) Histology-World-1 2008, (b) Histology-World-2 2008, (c), (d), (e) Univ. Michigan Eng. 2008)

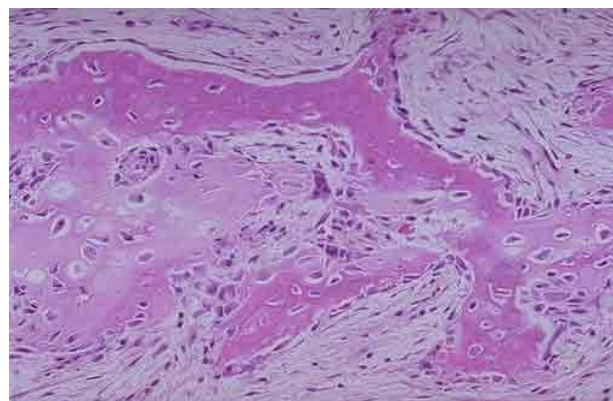


Figure 2.5. The woven bone forming in a fracture callus. (Source: Univ. Michigan Eng. 2008)

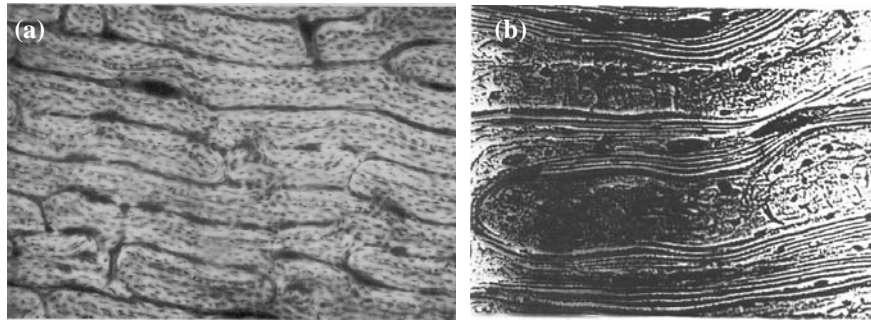


Figure 2.6. (a) Photomicrograph of plexiform bone tissue, (b) same type of tissue showing the sandwiched structure of the lamellar and woven bone tissue. (Source: Martin and Burr 1998)

The second organizational level of cortical bone consists of the structural elements: lamellae, lacunae, canaliculi, cement lines, volkmann's canals, and plexus which form osteonal, plexiform and interstitial bone tissue (the woven bone tissue contains no discernable second level structures). These structures are shown in Figure 2.3, 2.4a, and 2.7. The osteons are comprised of concentric *lamellae*, which are 3 to 7 μm layers arranged around the central haversian canal. The collagen fibers in a lamella run parallel to each other but their orientation across separate lamellae are different as evidenced by the separate refraction patterns of the polarized light in Figure 2.7. The fiber density at the border between adjacent lamellae is lower accounting for the distinctive appearance of an osteon. While the osteoblasts are laying the organic matrix of mainly collagen fibers termed osteoid they become entrapped in the osteoid forming holes in the structure called *lacunae*. The trapped cells are termed osteocytes. The sizes of lacunae range in 10 to 20 μm , which is related to the original osteoblast size. *Canaliculi* are small tunnels connecting lacunae and incorporating the cytoplasmic processes of osteocytes. Therefore, they provide a network of nutrients and metabolic waste exchange, and of osteocytic communication of stress states in the tissue, which is crucial in the bone adaptation. Osteons are separated from each other by *cement lines* through which collagen fibers and canaliculi do not cross. The cement lines are products of bone remodeling process occurring at the front where bone absorption stops and deposition starts. Cement lines do not contain collagen fibers and are highly mineralized compared to the surrounding tissue, and are 1 to 5 μm in thickness. It was suggested that they serve to arrest crack propagation, and absorb energy (Schaffler, et al. 1987).

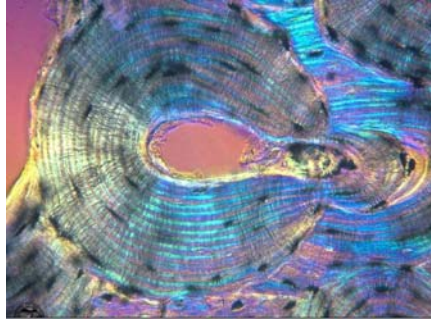


Figure 2.7. An interference contrast micrograph of haversian system showing osteon, lamellae and lacunae. (Source: Univ. Michigan Eng. 2008)

The third organizational level of cortical bone is separated into two basic types: lamellar and woven. Each type consists of type I collagen fiber-mineral (hydroxyapatite) composite.

The lamellar bone (osteonal, and plexiform bone tissue) is laid down in an organized pattern. The collagen fibers within the same lamella are predominantly parallel to each other while the orientation of the fibers on the adjacent lamella is at an angle that may change up to 90° (Ascenzi, et al. 1986). Three types of osteons were identified according to their lamellar substructures as shown in Figure 2.8.

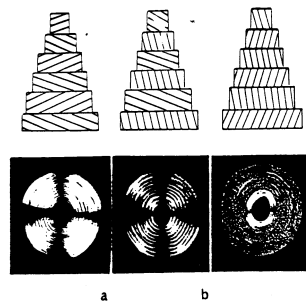


Figure 2.8. Schematic lamellar substructures in osteon, and their cross sectional pictures under polarized light (a) type T, (b) type A, (c) type L. (Source: Martin and Burr 1998)

Type T lamellar substructure contains fiber bundles which are parallel to the plane of section or perpendicular to the osteonal axis. These bundles reflect the polarized light, hence appear as light circles. In type A osteon the fibers at adjacent lamellae are oriented perpendicular to one another appearing as dark and light circles

under polarized light. Type L osteon contains fiber bundles oriented as parallel to the osteonal axis hence are not able to reflect polarized light appearing dark.

There are a number of other models suggested for collagen fiber orientation within cortical bone lamellae. Among these are twisted plywood model (Giraud-Guille 1988), and random oriented alternating dense and loose packed fibers lamellar model (Marotti and Muglia 1988). The light and dark pattern of circles under polarized light were attributed to the alternating loosely and densely packed fibers, respectively. The model also suggests that osteoblasts lay down collagen fibers in an intertwined mesh.

Collagen fibrils of 3 μm in length, and roughly 50 nm in diameter are packed together to form collagen fibers. While the fibrils are being packed, distinct or contiguous gaps of sizes 0.37 μm long and 15 nm wide are formed, within which the mineral crystals (predominantly hydroxyapatite and other CaP compounds) are deposited. The crystal sizes are given as 40 nm long, 10 nm wide, and 1-3 nm thick (Guyton 1991), whereas the crystal plates formed by these crystallites are 500 nm long, 250 nm wide, and 20-30 nm thick. Naturally the orientation of the type I collagen fibers determine the orientation of the crystal plates. Figure 2.9 shows a model of mineral deposition oriented by collagen fibers. The molecular and crystal structures of collagen and hydroxyapatite will be elaborated in sections 2.3.1, and 2.3.2, respectively.

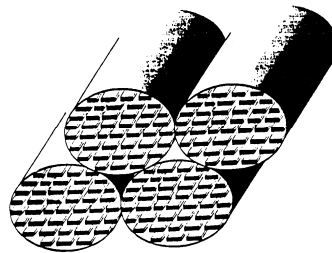


Figure 2.9. A model of crystal plate orientation regulated by collagen fibrils.
(Source: Weiner and Traub 1992)

2.1.2. Trabecular Bone Structure

The level 0 macro structure of trabecular bone serves to distribute and dissipate energy from articular contact loads. Such a major mechanical property is achieved by being 70% porous by volume on the average and having a surface area to volume ratio of around 20 mm^2/mm^3 (as compared to 2.5 mm^2/mm^3 in cortical bone).

The basic structural entities at level 1 are trabeculae which are rod or plate like structures as seen in Figure 2.10. Trabeculae are in general maximum 200 μm thick and 1 mm long without a central channel and any blood capillary. In exceptional cases a trabecula can be so thick as to contain a central channel with a blood vessel (vascular channel). The trabecular packets reside within the secondary trabecula which are the products of bone remodeling (bone reformation by cellular resorption and apposition). The bone marrow is contained within the trabecular bone spaces. The typical trabecular packet has a crescent shape, and is about 50 μm thick, and 1 mm long as shown in Figure 2.11.

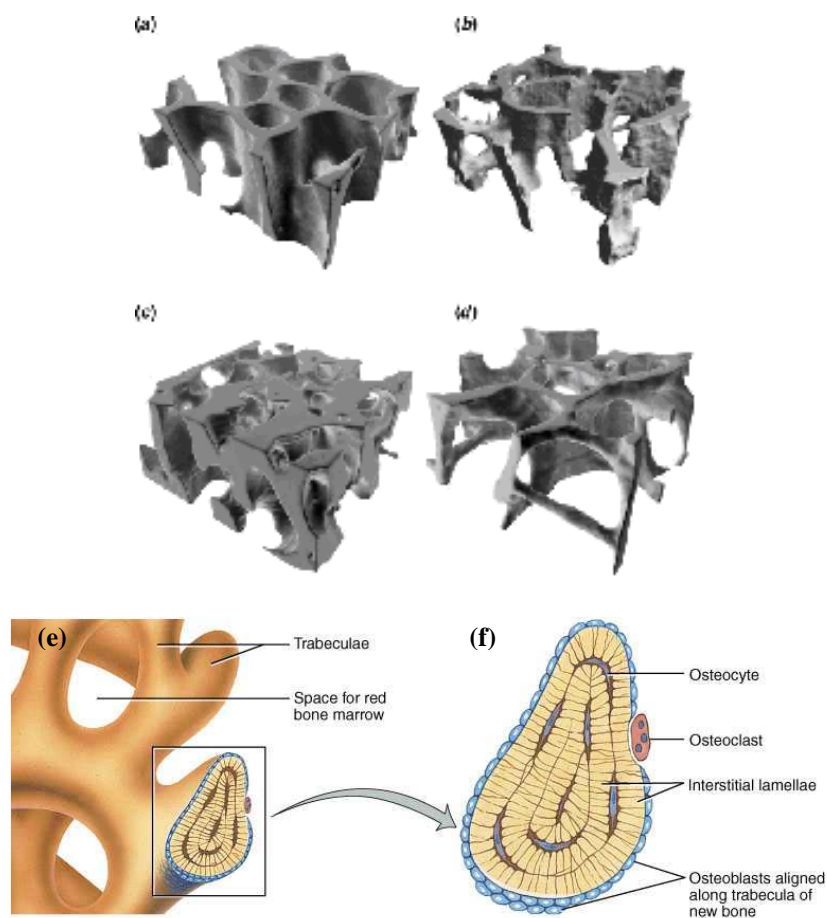


Figure 2.10. Trabecular (cancellous) bone level 1 structure (a) bovine proximal tibial, (b) human proximal tibial, (c) human femoral neck, and (d) human vertebral trabecular bone (all specimens have the same bulk dimensions of $3 \times 3 \times 1 \text{ mm}^3$), (e) schematic of spongy bone trabeculae, (f) section of a trabecula. (Source: (a), (b), (c), (d) Keaveny, et al. 2001, (e), (f) Shashidhar 2006)

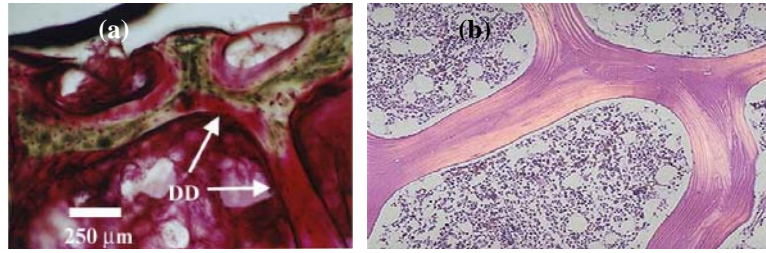


Figure 2.11. (a) and (b) Trabecular (cancellous or spongy) bone trabecular packets and level 2 structure. The bony space contains the bone marrow. (Source: (a) Vashishth 2007 (b) Shashidhar 2006)

The level 2 structural entities of trabecular bone are lamellae (~3 μm in thickness), lacunae, canaliculi, and cement lines. The differences of these entities from their counterparts in cortical bone are their size and arrangement. The lamellae are not arranged concentrically, but are rather arranged longitudinally along the trabeculae within trabecular packets (Figure 2.10, 2.11). The lacunae are higher in density and larger within metaphyseal, and epiphyseal trabecular bone than in diaphyseal and metaphyseal cortical bone. The cross sectional lacuna area in trabecular bone ranges in 50 to 54 μm², while in cortical bone it ranges in 26 to 35 μm² (Cane 1982).

The third level structure of trabecular bone consists of the same type I collagen fibers and hydroxyapatite organizations as in cortical bone. Figure 2.12 provides a summary of cortical and cancellous bone tissue organizational levels.

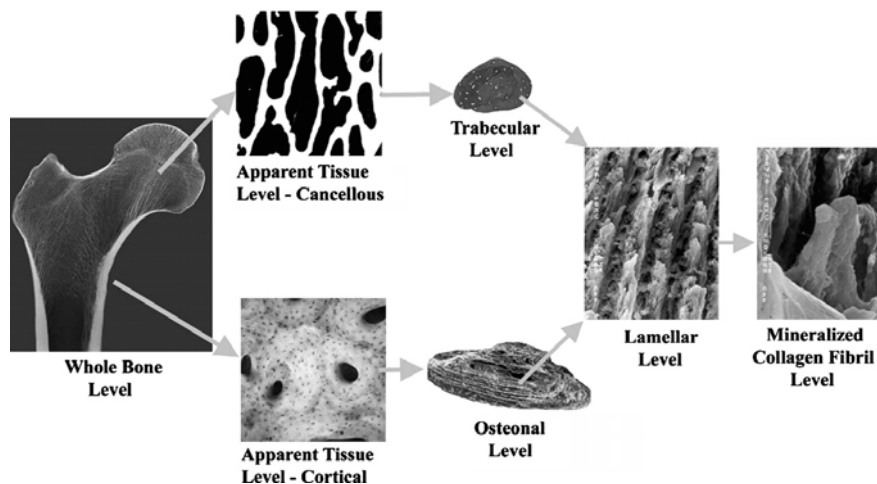


Figure 2.12. Organizational levels of cortical and trabecular bone. (Source: Vashishth 2007)

2.2. Overall Calcium and Phosphate Intake and Excretion Cycles

The extracellular fluid and plasma concentrations of calcium and phosphate ions are regulated through multiple processes involving the action and processing of vitamin D, parathyroid hormone, and calcitonin. The overall cycle of Ca^{2+} cation is given in Figure 2.13. Ca^{2+} is poorly absorbed in the intestinal tract because of the relative insolubility of many of its compounds and the relative difficulty of the absorption of bivalent cations in the intestinal epithelium in general. The normal daily intake of 1000 mg of calcium is balanced by the excretion of 900 mg through the bowels in the feces, and 100 mg through the kidneys in the urine, nevertheless, 350 mg of Ca^{2+} is absorbed in the intestinal epithelium. The concentration of calcium in the plasma varies between 9.0 and 10.0 mg/dl averaging 9.4 mg/dl (2.4 mmol/L). The calcium in plasma is present in three different forms as shown in Figure 2.14. Approximately 41% (1.0 mmol/L) of the calcium is combined with the plasma proteins and in this form is nondiffusible through the capillary membrane. 9% (0.2 mmol/L) is diffusible through the membrane but is combined mostly with citrate and phosphate which are insoluble. The remaining 50% of the calcium (1.2 mmol/L or 2.4 mEq/L) in the plasma is both diffusible through the capillary membrane and in ionic form (Ca^{2+}). The ionic form of the calcium is important for the functions of calcium in the body, including bone formation, effects on hearth and nervous system.

On the other hand almost all of the dietary phosphate is easily absorbed in the intestinal epithelium except when calcium in the diet is in excess and forms insoluble compounds with phosphate which fails to be absorbed but excreted in the feces. Later the absorbed dietary phosphate is excreted in the urine. Inorganic phosphate in the plasma is mainly in two forms HPO_4^{2-} , and H_2PO_4^- , concentrations of which are approximately 1.05 mmol/L and 0.26 mmol/L, respectively. The ratio of these anions changes with the pH of the extracellular fluid. The average total quantity of inorganic phosphorous is ~ 4 mg/dl varying in a range 3 to 4 mg/dl in adults, and 4 to 5 mg/dl in children.

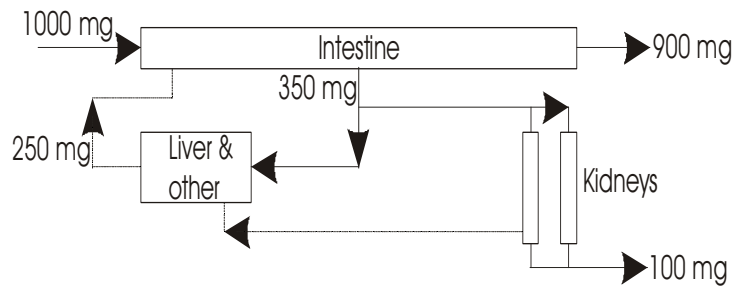


Figure 2.13. Overall calcium intake and excretion in the body.

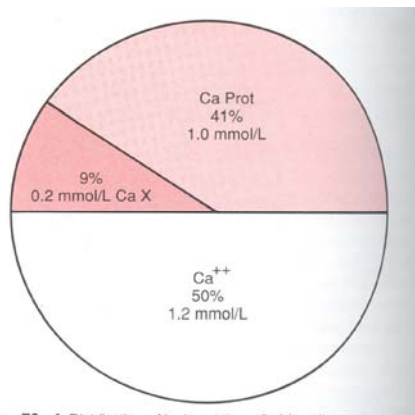


Figure 2.14. Distribution of calcium forms in blood plasma.
(Source: Guyton 1991)

Vitamin D and Its Function in Calcium and Phosphate Absorption: Vitamin D increases calcium absorption from the intestinal tract as well as its important effects on both bone deposition and reabsorption. Vitamin D itself is not an active compound, but is converted to active, regulatory forms through a succession of processes in the liver and the kidneys.

Compounds that belong to the vitamin D family are derived from sterols, and the most important vitamin D compound is cholecalciferol (vitamin D₃). Cholecalciferol is formed in the skin by the ultraviolet irradiation of 7-dehydrocholesterol. Therefore, appropriate exposure of skin to the sun prevents vitamin D deficiency. Food contains vitamin D compounds which are identical in function to cholecalciferol, and their structure differ only by a few atoms. In the liver cholecalciferol is converted to 25-hydroxycholecalciferol, which is the first step in the activation of vitamin D₃. 25-hydroxycholecalciferol has a feedback inhibitory effect on the conversion at the same time, therefore, regulating the blood plasma concentration of itself. Figure 2.15

illustrates this effect. Although the intake of vitamin D₃ can increase many times, the plasma concentration of 25-hydroxycholecalciferol remains within a few percent of its normal mean value. This strict feedback control prevents excessive action of vitamin D₃ when its intake is excessive, and also conserves vitamin D₃, since 25-hydroxycholecalciferol persists in the body for a few weeks while vitamin D₃ can be stored in the liver for many months.

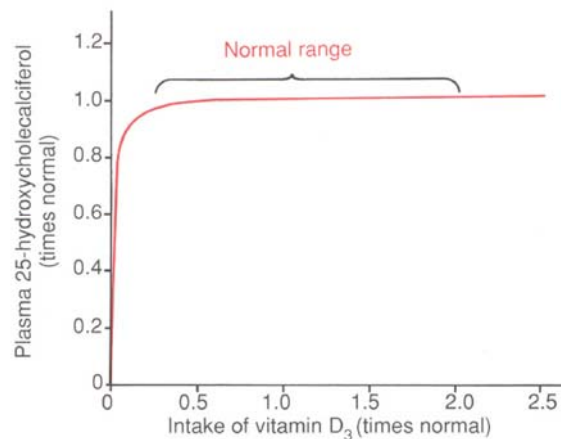


Figure 2.15. Effect of increasing vitamin D₃ intake on the plasma concentration of 25-hydroxycholecalciferol. (Source: Guyton 1991)

In the second step of the activation of vitamin D₃, 25-hydroxycholecalciferol is converted to 1,25-dihydroxycholecalciferol in the kidneys under the regulatory effect of parathyroid hormone. 1,25-dihydroxycholecalciferol is the active form of vitamin D₃ for the calcium absorption in the intestines, and in the absence of parathyroid hormone almost none of it is formed. Therefore, parathyroid hormone has a crucial potent effect on the functions of vitamin D, and hence in the calcium absorption. The plasma concentration of calcium (the normal average value is 9.4 mg/dl) inversely affects the plasma concentration of 1,25-dihydroxycholecalciferol mainly by suppressing the secretion rate of parathyroid hormone to a great extent when its plasma concentration rises above 10 mg/dl, and to a much lesser extent by direct inhibitory action on the conversion, as shown in Figure 2.16. When parathyroid hormone is suppressed 25-hydroxycholecalciferol is converted to a slightly different form, 24,25-dihydroxycholecalciferol, which has very little vitamin D effect. Therefore, when the plasma concentration of calcium is too high, the formation of 1,25-dihydroxycholecalciferol is greatly depressed, which in turn decreases the absorption of

calcium from the intestines as well as from the bones and renal tubules of kidneys causing the Ca^{2+} to fall back to its normal value. On the other hand when a very slight decrease in Ca^{2+} below normal values occurs, activated vitamin D forms excessively (by the action of parathyroid hormone), and absorption of calcium from the intestine increases greatly. The activity difference between 1,25-dihydroxycholecalciferol and other vitamin D compounds is about 1000 fold.

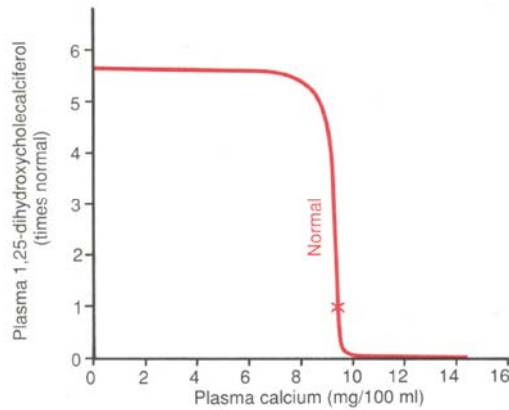


Figure 2.16. Effect of plasma calcium ion concentration on the plasma concentration of 1,25-dihydroxycholecalciferol. (Source: Guyton 1991)

The great enhancement of the calcium ion absorption through the intestinal epithelium is due to the “hormone” like effect of 1,25-dihydroxycholecalciferol. It increases the formation of a calcium-binding protein in the intestinal epithelial cells in a period of two days. The calcium-binding protein functions in the brush border of these cells to transport calcium into the cell cytoplasm, and then Ca^{2+} moves through the basolateral membrane of the cell by facilitated diffusion. The calcium absorption rate is directly proportional to the quantity of this protein. The calcium-binding protein persists in the cells for several weeks after 1,25-dihydroxycholecalciferol has been removed from the body thus causing a prolonged effect on calcium absorption. The “hormone” like effect of 1,25-dihydroxycholecalciferol also involves the formation of a calcium-stimulated ATPase in the brush border of epithelial cells, and the formation of an alkaline phosphatase in the epithelial cells, both of which promoting calcium absorption. The activation of vitamin D and its role in controlling plasma calcium concentration are summarized in Figure 2.17.

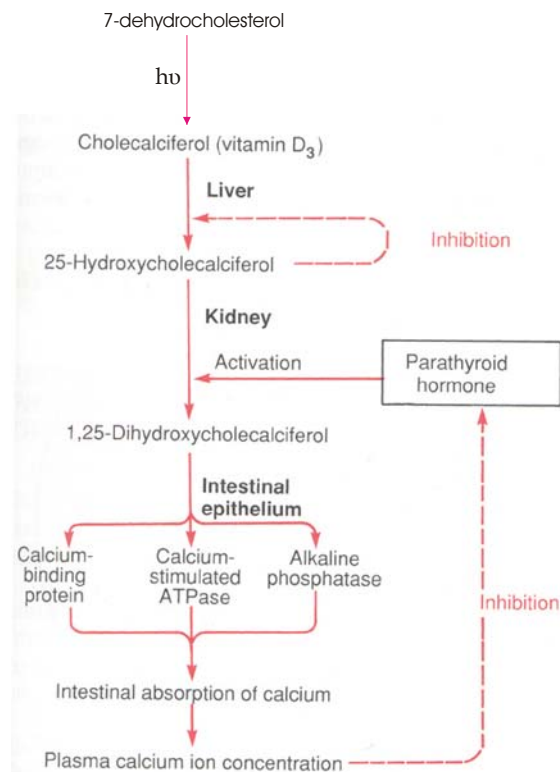


Figure 2.17. Conversion of vitamin D₃ to active forms and its role in controlling the plasma calcium concentration. (Source: Guyton 1991)

The strict control of plasma concentration of Ca²⁺ ion has crucial importance, since elevation or depletion of this ion in the extracellular fluids causes extreme immediate effects. When the extracellular concentration of Ca²⁺ falls 35% below the normal, tetany ordinarily results, because of the increased permeability of neuronal membrane to sodium ions allowing easy initiation of action potentials (the first sign of tetany that develops is carpopedal spasm). When the decrease is about 50% tetanic muscle contractions, and occasionally convulsions occur. A 60% decrease is usually lethal with common effects as dilatation of hearth, laryngeal muscle contractions obstructing respiration, changes in cellular enzyme activities, increased cell membrane permeability in cells apart from neurons, and impaired blood clotting. On the other hand when the calcium level rises above normal, nervous system and all related functions are depressed. When the level rises above 70%, calcium phosphate is likely to precipitate throughout the body, also a lethal condition.

Phosphate ion is usually absorbed relatively easily in the intestines. However, phosphate flux through the gastrointestinal epithelium is enhanced by vitamin D, both

by the direct effect of 1,25-dihydroxycholecalciferol and by the increased calcium absorption which in turn acting as a transport mediator for the phosphate.

2.3. Bone Physiology

The cortical bone comprises an organic matrix which is approximately 30%, and CaP minerals which constitute the remaining 70%. The main constituents of the organic matrix are collagen fibers which are 90-95%, and a homogeneous medium of extracellular fluid and proteoglycans (chondroitin sulfate and hyaluronic acid) termed ground substance.

The collagen fibers of bone as those of tendons, cartilage, fascia, ligaments, teeth, have great tensile strength and extend primarily along lines of tensional force on the bone. As an analogy the collagen fibers has the same kind of function of steel bars in the reinforced concrete. The mineral constituent of bone imparts the compressional strength, and mechanical stiffness. Further as the analogy, mechanical function of the mineral phase of bone compares to the “cement, sand, rock” constituent of the reinforced concrete. The combined properties together with the bondage between collagen fibers and the crystalline mineral phase provide a bony structure which has extreme tensile and compressional strength along with the necessary toughness and stiffness properties. Indeed, the compressional strength of bone is greater, and the tensile strength approaches to that of reinforced concrete.

2.3.1. Structure of Collagen

In fact collagen is the most abundant form of protein in mammals making up approximately 25% of the total protein content. The Nobel laureates James D. Watson, Francis H. C. Crick, and Linus Pauling were known to have been working on collagen structure when its essentially correct version was proposed by G. N. Ramachandran, and Gonipath Kartha in 1954 (the double helical model of DNA was constructed by Watson and Crick in 1952-1953). The sequence of part of the $\alpha 1(I)$ collagen polypeptide follows the amino acid pattern as given in Figure 2.18a. The intracellular synthesis of collagen polypeptide is followed by modifications including hydroxylation, glycosylation, disulfide-bond formation, and proteolytic cleavages that take place in the endoplasmic reticulum, Golgi complex, and the extracellular space. The polypeptide strands are of

length 300 nm, and diameter 1.5 nm. The modifications allow the formation of the “collagen molecule” which is a triple helix or super helix of three left handed helices (as different from the right handed α -helix) and is termed tropocollagen. A distinctive feature of tropocollagen is the regular arrangement of amino acids in each of the three chains (precisely 1050 amino acids in each chain) of these collagen subunits. There are 3 amino acids per turn of the helix and every third amino acid is glycine, the smallest amino acid; this is a rare feature also found in silk fibroin, a fibrous protein. The quaternary structure of tropocollagen is stabilized by multiple hydrogen bonds, and is secreted out of the cell by exocytosis. The covalent cross-linking of laterally aligned tropocollagen helices form collagen fibrils of 20-50 nm in diameter as shown in Figure 2.18c. The schematic structure of fibrous collagen, and SEM of calfskin collagen fibers stained with phosphotungstic acid are shown in Figure 2.18d. In fibrils the collagen molecules pack together side by side, while adjacent molecules are displaced by 67 nm, and a small gap separates the head of one collagen from the tail of the other. This staggered array produces a periodic pattern of striations of the packing repeated about every 64 nm, which are clearly visible. The side by side interactions are stabilized by covalent bonds, shown red, between the N-terminus of one molecule and the C-terminus of an adjacent one. There are short segments at either end of the collagen molecule that do not assume triple helix conformation. These are of particular importance because covalent cross-links between two lysine and hydroxylysine residues at C-terminus of one chain with two at the N-terminus of adjacent chain stabilize the side by side interactions, generating a strong fibril. The collagen fibrils form fiber bundles with a 0.2–1.2 μm diameter.

There are 28 types of collagen described in the literature, 12 types being more common and types I, II, III are the most abundant and forming fibrils of similar structure, while type IV forms a two dimensional reticulum (type I, II, III, IV together comprises over 90% of the collagen in body).

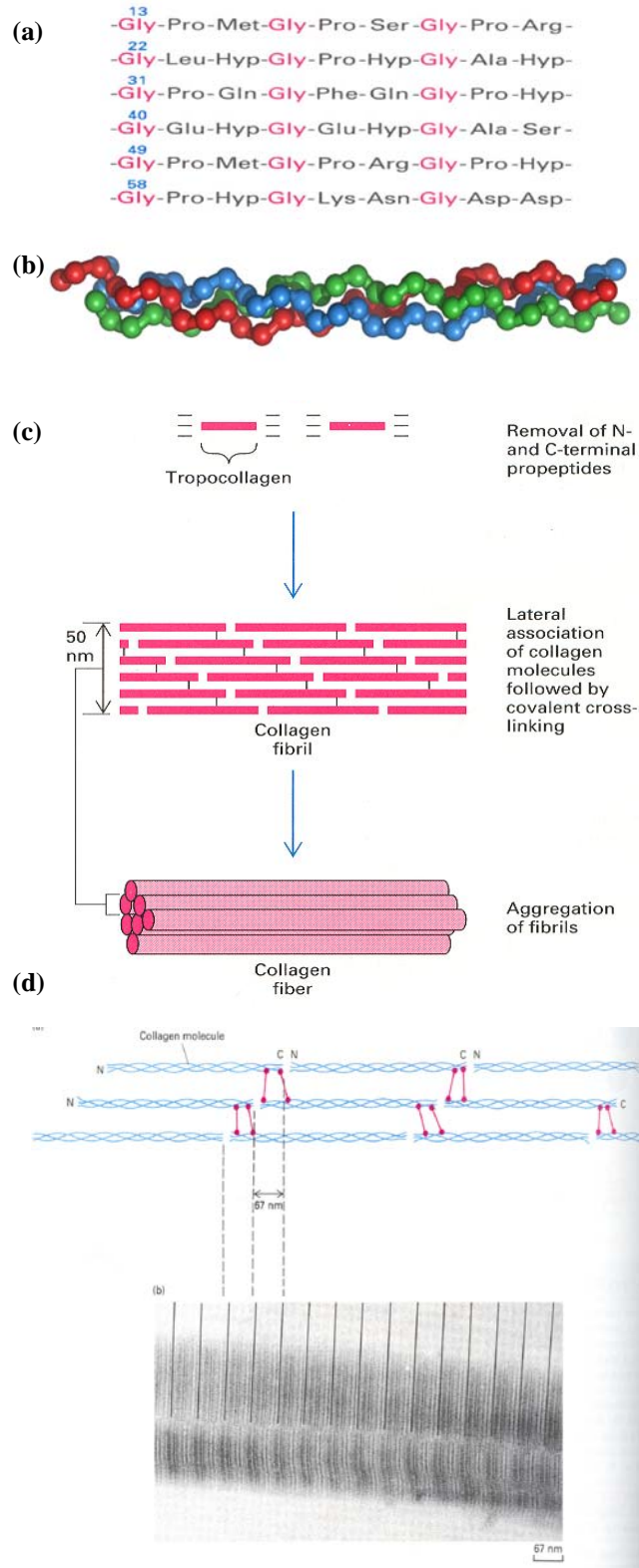


Figure 2.18. (a) Sequence of part of $\alpha 1(I)$ collagen polypeptide, (b) tropocollagen triple helix (madrax helix), (c) the lateral alignment and covalent cross linking of helices into 50 nm diameter fibrils, (d) the schematic of structure of fibrous collagen, and SEM of calfskin collagen fibers stained with phosphotungstic acid. (Source: Darnel, et al. 1990)

2.3.2. Structure of Hydroxyapatite

Calcium and phosphate are the principal components of the crystalline minerals deposited in the organic matrix of bone. The major crystal salt is hydroxyapatite (HAp) given by the chemical formula $\text{Ca}_{10}(\text{PO}_4)_6(\text{OH})_2$. HAp has a hexagonal crystal structure with the space group $\text{P6}_3/\text{m}$, and the lattice parameters $a=b=0.934$ nm, $c=0.687$ nm, $\alpha=\beta=90^\circ$, $\gamma=120^\circ$ (Peroos, et al. 2006). The crystal structure of HAp is shown in Figure 2.19. Biological apatite material has a range of lattice parameters $a=b=0.936\text{-}0.964$ nm and $c=0.678\text{-}0.690$ nm (Narasaraju, et al. 1996).

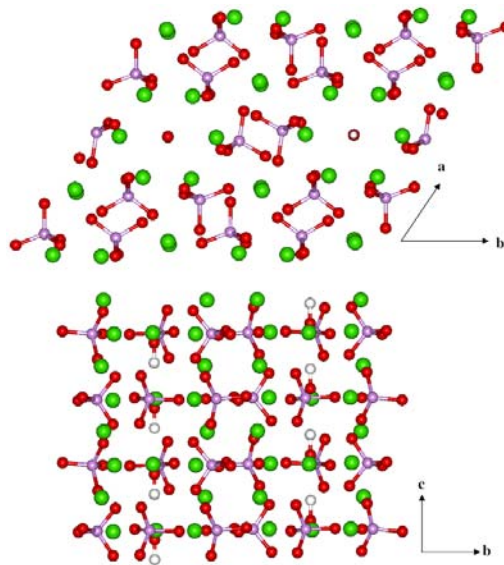


Figure 2.19. Plan and side views of the hydroxyapatite structure, showing the OH-groups in hexagonal channels surrounded by Ca ions (O: red, Ca: green, P: pink, H: white). (Source: Peroos, et al. 2006)

The relative weight ratio of calcium to phosphorous can vary from 1.3 to 2.0 (1.67 being the stoichiometric ratio) depending on the nutritional conditions. The crystal sizes are 40 nm long, 10 nm wide, and 1-3 nm thick, whereas the crystal plates formed by these crystallites are 500 nm long, 250 nm wide, and 20-30 nm thick (Guyton, 1991). Naturally the orientation of the type I collagen fibers determine the orientation of the crystal plates. The hydroxyapatite crystal plates lie adjacent to each repeating segment of the collagen fiber, intimately binding to it avoiding the slipping of fibers and crystals over each other. Additionally the segments of collagen fibers overlap each other, causing in the same time hydroxyapatite crystals keyed to each other like wall bricks.

2.3.3. Mechanism of Bone Production

Osteoblasts are the types of cells that literally produce bone. The formation of osteoid, a cartilage like tissue, is the first step in bone formation through the secretion of collagen molecules (tropocollagen) and ground substance (proteoglycans) by osteoblasts, and the collagen molecules rapidly polymerize to form collagen fibrils. As the osteoid is formed some of the osteoblasts become entrapped in the tissue, which are then termed osteocytes. The next step in bone formation is the start of the precipitation of calcium salts at the periodically repeating striations of the collagen fibers within a few days of the osteoid formation. The initial calcium salts deposited are a mixture of amorphous compounds such as $\text{CaHPO}_4 \cdot 2\text{H}_2\text{O}$, $\text{Ca}_3(\text{PO}_4)_2 \cdot 3\text{H}_2\text{O}$. The amorphous phase multiplies and grows over a period of days to weeks. Then by a process of atomic addition and substitution, brought about by repetitive reabsorption and reprecipitation, the 70 to 80% of the amorphous phase is converted to hydroxyapatite crystals over a period of weeks to months. Magnesium, sodium, potassium, and carbonate ions also precipitate along with calcium and phosphate as conjugated to hydroxyapatite crystals rather than forming distinct crystals as indicated by XRD .

The amorphous portion of the mineral phase of bone provides an exchangeable calcium stock of body, and forms a rapid buffering mechanism to keep the calcium ion concentration in the extracellular fluids from rising or falling to abnormal levels under transient conditions of excess or deficiency of calcium. The amorphous CaHPO_4 and other amorphous salt deposits of the bones are the readily exchangeable forms in equilibrium with the calcium ions in the extracellular fluid. A small quantity of exchangeable calcium is also found in other tissue cells of high permeability such as those of the liver, and the gastrointestinal tract. However, most of the exchangeable calcium was shown to be in the bone as 0.4 to 1.0% of the total bone calcium by radioactively tagged calcium studies. The buffering mechanism was shown experimentally by intravenous injection of soluble calcium salts, or removal of large quantities of calcium ions from circulating fluids which causes immediate acute rise or

¹ The ability of different types of ions to deposit as conjugated to hydroxyapatite crystals extends to the ions such as of strontium, uranium, plutonium, other transuranic elements, lead, gold, and other heavy metals, and least 9 of 14 of the major radioactive products (by nuclear explosions). If a sufficient amount of radioactive substance is deposited their effect of prolonged irradiation of the bone tissues almost invariably eventually causes osteogenic sarcoma (bone cancer).

fall to very high or low calcium levels in the body fluids; the calcium level returns to normal in about half an hour to an hour or so.

In fact, the calcium and phosphate ion concentrations in the extracellular fluid are in a supersaturated state with respect to hydroxyapatite. However, calcium salts almost never precipitate in normal tissues apart from bone, by the action of inhibitors. Pyrophosphate ($P_2O_7^{4-}$, PP_i) (Addison, et al., 2007, Christoffersen, et al. 2000) and peroxydiphosphate ($P_2O_8^{4-}$, PDP) (Moreno, et al. 1994) are believed to be such inhibitors. PP_i is formed ubiquitously by the hydrolysis of ATP to AMP in vivo. The inhibition was proposed to occur by competition between the pyrophosphate and HPO_4^{2-} anions for binding site on the apatite crystal embryo (Qui, et al. 1992). The chelation of Ca^{2+} and PP_i on the hydroxyapatite crystal surfaces inhibits growth and further precipitation. PP_i also induces increased levels of osteopontin (Opn), a single chain phosphorous rich glycoprotein, which inhibits mineralization via its negatively charged phosphate residues. During the mineralization of bone osteoblasts are supposed to secrete substances into the osteoid neutralizing pyrophosphate (or other inhibitors) that normally prevents hydroxyapatite crystallization. In the absence of an inhibiting effect the supersaturated calcium and phosphate ions precipitate, with the additional effect of the affinity of collagen fibers for calcium salts. Tissue non-specific alkaline phosphatase (Tnap) is secreted in large quantities by osteoblasts when they are actively depositing bone matrix, which in turn reverses the inhibitory effects PP_i and Opn. Tnap increases the local concentration of inorganic phosphate (P_i) by the degradation of PP_i , and hydrolysis of Opn, reducing the inhibition by decreasing the amounts of inhibitors and shifting the competitive equilibrium for the adsorption on binding sites on the crystal in favor of increased phosphate ion (P_i). Since some alkaline phosphatase diffuses into the blood, the blood level of alkaline phosphatase is usually a good indicator of the rate of bone formation.

In other parts of the body calcium salts may also precipitate under abnormal conditions, for instance, in arterial walls in the condition termed arteriosclerosis, causing the arteries to become bonelike tubes. In general calcium salts tend to deposit in degenerating tissues, and in old blood clots the case in which the inhibitor factors normally preventing precipitation have disappeared from the tissue.

2.3.4. Remodeling of Bone

Bone is continually being deposited or apposed by differentiated bone cells termed osteoblasts, and is continually being dissolved or absorbed by large phagocytic, multinucleated (up to 50 nuclei) cells termed osteoclasts, normally at equal rates keeping the total bone mass constant, except in growing bones of young organisms. Osteoblasts are found on the outer surfaces of the bones and in the bone cavities, and a constant osteoblastic activity occurs on about 4% of the total bone surface as shown in Figure 2.20. In Figure 2.20b bundles of collagen fibers both parallel and normal to the page, and the black appearing mineral phase are discernable.

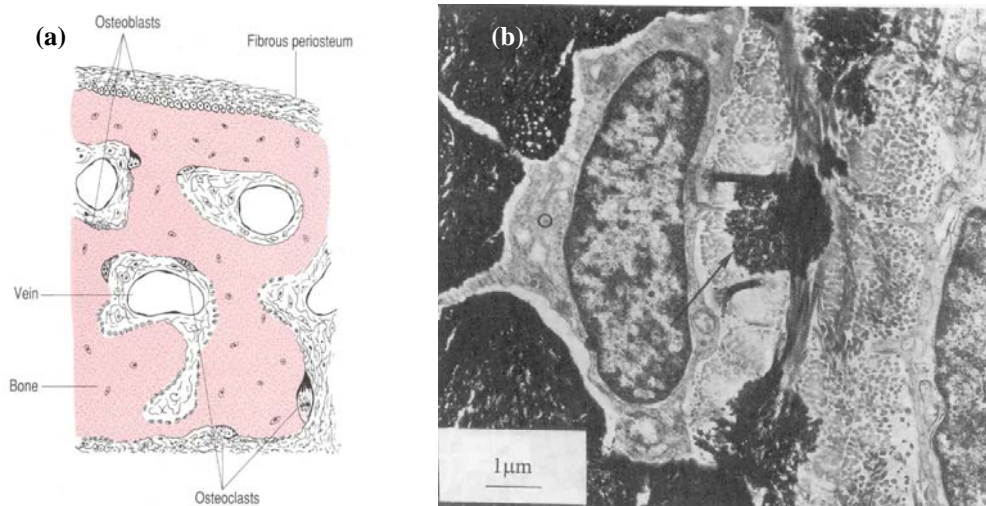


Figure 2.20. (a) Schematic of periosteal and intrasosseous osteoblasts, (b) SEM image of osteoblasts, one forming bone (the one on the right hand side, and other is being entrapped in the osteoid to become osteocyte. (Source: (a) Guyton 1991, (b) Akkus 2008)

Fracture of a bone maximally activates all the periosteal and intrasosseous existing differentiated osteoblasts. However, more importantly for proper bone healing the undifferentiated, pluripotent mesenchymal stem cells contained in bone and adjacent tissues are stimulated to develop into bone-forming lineage termed osteoprogenitor cells (or preosteoblasts) by a process known as osteoinduction. Osteoprogenitor cells develop into differentiated osteoblasts with time as shown in Figure 2.21 (Albrektsson and Johansson 2001). Osteoinduction is signaled chemically by inducive agents which are termed growth factors (also promotes cell proliferation) and cytokines, and physically by stress, and electric field, stimulating cell differentiation. Bone morphogenetic

proteins (BMPs) that belong to the transforming growth factor- β (TGF- β) superfamily, stimulate undifferentiated mesenchymal cells to be differentiated to osteoprogenitor cells by binding to specific receptors on the surface these target cells.

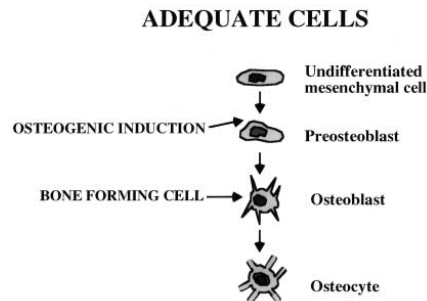


Figure 2.21. Induced stem cell differentiation into preosteoblasts which are later converted to osteoblasts. (Source: Albrektsson and Johansson 2001)

The multinucleated large osteoclasts are derivatives of monocytes or monocyte-like cells formed in the bone marrow. They are normally active on less than 1% of the bone surfaces as shown in Figure 2.20a. The osteoclasts have a ruffled-border consisting of villus like projections immediately adjacent to the bone as shown in Figure 2.22a, where the bone absorption occurs. The villi secrete proteolytic enzymes released from the lysosomes, which dissolve the organic matrix, and several acids including citric acid and lactic acid released from the mitochondria, which dissolve the mineral phase (hydroxyapatite is readily dissolvable at low pH). Usually osteoclasts exist in small but concentrated masses dissolving the bone for about 3 weeks, carving tunnels up to the sizes of 1 mm in diameter and several millimeters in length. At the end of this period osteoclasts disappear and osteoblasts invade the tunnels forming new bone in the concentric lamellae form of osteons.

The osteoclast resorbed bone surface patch of a depth of approximately one micrometer, termed Howship's lacuna (Figure 2.22b), has the histological structure of a demineralized collagen matrix with three dimensional complexity and submicron scale undercuts (Figure 2.22c). This structure is critical in the formation of the overlying cement line. The proteins, bone sialoprotein and osteopontin, secreted by the osteoblasts are adsorbed on this solid surface, and initiate the development of a mineralized (calcium phosphate crystallites), non-collagenous protein and proteoglycan matrix (the cement line) invaginating, interdigitating and interlocking with the demineralized collagenous matrix. As mentioned earlier cement line is a non-collagenous, highly

mineralized interfacial histological structure demarcating the border between the old and the new bone. The cement line matures by continuing mineralization due to crystal growth. A collagenous and mineralized matrix develops over the cement line again by interdigitating and interlocking with the minute crystallites of the cement line (Davies 2007).

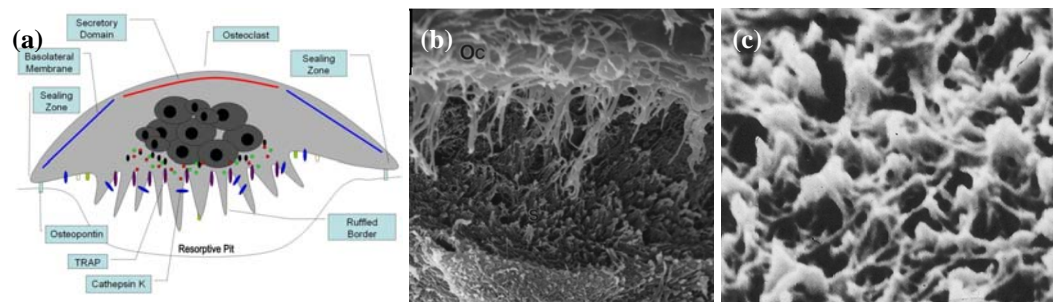


Figure 2.22. (a) Schematic of osteoclast with villus like projections on the ruffled border, (b) the resorption surface of a Howship's lacuna (rat) created by an osteoclast (Oc), (c) the demineralized collagenous matrix after osteoclast resorption. (Source: (a) Albrektsson and Johansson 2001, (b), (c) Davies 2007)

Bone remodeling provides the bone with a number of abilities, first readjusting its strength accordingly to the applied stress conditions. For instance, the bones of athletes get thicker under repetitive heavy loadings, while a leg immobilized in a cast demineralizes up to 30% in a few weeks. Second, bone remodeling can rearrange the shape of a bone for the counterbalancing of the mechanical forces by a piezoelectric effect caused by the stress patterns. Compression stresses give rise to negative electric potential in the compressed areas inducing osteoblastic activity and hence increased bone formation rate. Tensional areas are prone to positive potentials reducing osteoblastic activity and hence the rate of bone formation. Usual osteoclastic resorption of bone will be in effect anywhere, and the net change will be the reduction of bone mass in these areas. For instance a fractured long bone which was healed at an angle for some reason, would eventually become almost straight in accordance with the externally repetitive loading due to walking. Third, since the organic matrix degenerates, and micro cracks appear in the mineral phase in time, the brittleness of old bone increases. Remodeling renews bone decreasing the fracture risk. The bones of children with high absorption and deposition rates show much less brittleness in comparison to the bones of people at old age with slow remodeling.

In the surgical treatment of fractured bones the stress adaptation ability of bone by remodeling is utilized by mechanical fixation and loading of the fractured ends of the bone for the fast formation of fracture callus at the intentionally stressed area shortening the convalescence.

2.3.5. Hormonal Control of Extracellular Fluid Levels of Calcium and Phosphate, and Their Deposition to and Resorption from the Bone

The parathyroid hormone and calcitonin, together with the combined effect of vitamin D, are the two regulatory hormones for (i) the absorption of calcium and phosphate in the intestinal tract, (ii) the resorption and deposition of CaP salts by osteoclastic and osteoblastic activities, and (iii) the reabsorption of calcium and phosphate in the renal tracts or their excretion in the urine. In the case of excessive calcium intake into the body, such as after ingestion of large quantities of calcium in diet particularly in the presence of an also excess quantity of vitamin D, a person may absorb as much as 0.3 gr calcium per hour. On the other hand several grams of calcium may be lost into the feces per day in cases of diarrhea by secretion in intestinal juices, passing into the intestinal tract. When compared to the total extracellular fluid amount of calcium of about 1 gr, the addition or subtraction of such quantities would certainly cause serious hyper- or hypocalcemia, if not for the buffering function of the exchangeable calcium in the bones and the mitochondria of many other tissue cells, as a first line of defense of body, before any hormonal feedback regulation is in effect.

As mentioned earlier the amorphous portion of the deposited calcium salts in the bone amounts to about 30% of the total CaP compounds, 0.4 to 1% being in exchangeable form, and they are in reversible equilibrium with the calcium and phosphate in the extracellular fluid. Because of the high surface area of the extremely small crystallites of the amorphous phase (~an acre) exposed to extracellular fluids (or more correctly to bone fluid to be defined later) deposition and resolubility of these salts are very fast reactions, such that, all the excess calcium can be deposited in the bones, and depleted levels of calcium equilibrated by the immediate resorption, via a single passage of blood stream through the bones. About 5% of the whole blood flows through the bones in a minute, that is, 1% of all the extracellular fluid. Therefore, any excess of

calcium in the extracellular fluid is removed by half in approximately 70 minutes by this buffering action, also called exchangeable calcium mechanism. In addition to the buffering function of bones, the mitochondria of cells of the liver and intestine also provide a reasonable buffering system with a total 10 gr of exchangeable calcium.

The effect of parathyroid hormone in combination with vitamin D on the calcium and phosphate absorption from the intestinal tract was explained in some detail above. The conversion of vitamin D₃ (cholecalciferol) to the active form 1,25-dihydroxycholecalciferol is regulated by the parathyroid hormone. 1,25-dihydroxycholecalciferol signals the formation of a Ca binding protein, the chief instrument in calcium absorption through the intestinal epithelium. Plasma levels of calcium, in turn, regulate the parathyroid hormone secretion by the parathyroid gland.

Physiologic Anatomy of the Parathyroid Glands: There are four parathyroid glands in the appearance of dark brown fat tissue of sizes 6 by 3 by 2 millimeters as shown in Figure 2.23. They are located on the backside of thyroid glands; each immediately behind the two upper and the two lower poles of the thyroid. The parathyroid glands consist of mainly chief cells that secrete parathyroid hormone, oxyphil cells that are transformed or depleted chief cells (do not secrete the hormone any more).

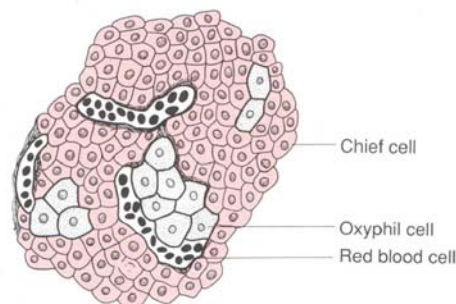


Figure 2.23. Histological structure of a parathyroid gland.
(Source: Guyton 1991)

The parathyroid hormone is first synthesized in the ribosomes in the form of a preprohormone (a polypeptide chain of 110 amino acids), then first cleaved to a prohormone, and finally to the hormone by the endoplasmic reticulum and Golgi apparatus and packed in the secretory granules in the cytoplasm, usually composed of 84 amino acids with a molecular weight of ~9500. Smaller compounds of a chain length of 34 amino acids adjacent to the N terminus of the compound found in the parathyroid

glands, was also shown to exhibit full parathyroid hormone activity. Removal of most of this tissue, apart from of a transient hypoparathyroidism, usually causes little physiological abnormality. The remaining parathyroid tissue is capable of hypertrophying satisfactorily fulfilling the function of glands.

Effect of Parathyroid Hormone on Calcium and Phosphate Concentrations in the Extracellular Fluid: Figure 2.24 shows the effect of intravenous administration of the parathyroid hormone on the calcium and phosphate concentrations in the extracellular fluid. At the onset of infusion the calcium ion concentration begins to rise and reaches a plateau level in about 4 hours. The phosphate ion falls more steeply and reaches a depressed constant level within two hours. The trends depend on the absorption of calcium and phosphate from the bones, and control of renal excretion of calcium and phosphate.

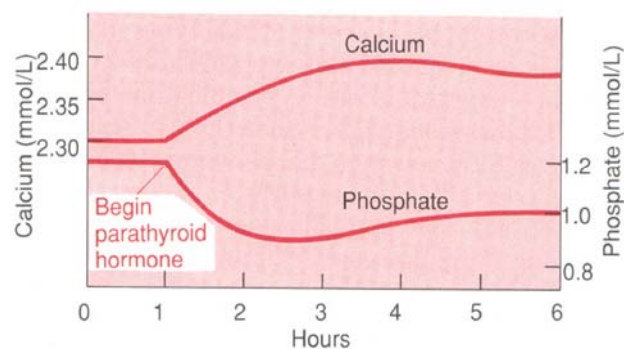


Figure 2.24. Approximate changes in calcium and phosphate concentrations during the 5 hours of parathyroid hormone infusion. (Source: Guyton 1991)

Renal excretion of calcium in the urine is in two steps. Two thirds of calcium in the glomerular filtrate is reabsorbed in the proximal tubules. Increasing levels of parathyroid hormone then increases tubular reabsorption of calcium in the ascending limbs of the loops of Henle, distal tubules, and collecting ducts of kidney. On the other hand increasing plasma concentration of parathyroid hormone causes immediate and rapid loss of phosphate in the urine due to diminished proximal tubular reabsorption of phosphate ion. In the same time increasing parathyroid hormone increases reabsorption of magnesium and hydrogen ions, while it decreases reabsorption of sodium, potassium and amino acid ions in the same way as phosphate ion. Since increasing levels of parathyroid hormone increase the reabsorption of exchangeable CaP compounds from

the bones, and decrease the renal excretion of calcium, the extracellular fluid concentration rises in the beginning until the other mechanisms balance the calcium increase to a plateau level. Although phosphate concentration also increases by bone reabsorption, the increased renal excretion of phosphate overrides this effect causing the observed trend of steep decrease until reaching a plateau level.

Calcium and Phosphate Absorption from the Bone by Parathyroid Hormone: There are two separate mechanisms that parathyroid hormone acts for the calcium and phosphate absorption from the bone. The rapid phase of calcium and phosphate resorption is termed osteolysis, and takes effect within minutes. Interestingly enough osteoblasts and osteocytes, the cells associated with bone deposition and calcification, are involved in the bone resorption. Osteoblasts and osteocytes form a system of interconnected cells that spreads all over the bone surfaces (except in the vicinity of osteoclasts). The long filmy processes extending from one osteocyte to another throughout the bone structure together with the connections to the surface osteoblasts, form the osteocytic membrane system. It separates the bone from extracellular fluid, isolating a small amount of fluid in between, termed the bone fluid. The membranes of osteoblasts and osteocytes have receptor proteins for binding parathyroid hormone, and the parathyroid hormone strongly activates the calcium pump in the presence of the active form of vitamin D (1,25-dihydroxycholecalciferol) by increasing the calcium permeability of the bone fluid side of the osteocytic membrane. The stimulation of the osteocytic membrane thus causes the diffusion of calcium from the bone fluid into cell and the calcium pump activated on the other membrane side of the cell transfers calcium ions into the extracellular fluid. It is known by indirect experiments that the calcium pumping action of the osteocytic membrane system yields a calcium ion concentration in the bone fluid that is one third in the extracellular fluid. When the osteocytic pump is excessively activated the calcium concentration in the bone fluid falls even to lower values, causing the exchangeable calcium phosphate salts to dissolve and thus to be absorbed from the bone without degrading the organic matrix, a phenomenon termed osteolysis. When the osteocytic pump is inactivated (by decreasing levels of parathyroid hormone, and by the action of calcitonin to be described later) concentration of calcium in the bone fluid again rises and the calcium phosphate salts are redeposited in the organic matrix.

The slow phase of bone absorption and calcium phosphate release involves the activation of osteoclasts. Strangely enough osteoclasts do not have receptor sites for the

parathyroid hormone, however, the activated osteoblasts and osteocytes send a secondary signal to the osteoclasts activating them for their usual task of bone resorption. The exact mechanism and details of this phenomenon are unknown. The osteoclastic resorption of bone has two stages; one starts with the immediate activation of existing osteoclasts, the second involves the formation of new osteoclasts. A few days of parathyroid hormone stimulation causes an activation of the osteoclastic system that will continue for even months. After a few weeks to a few months of osteoclastic bone resorption, bones become weakened, in turn, secondarily stimulating the osteoblastic activity for bone formation. Altogether there is an increased osteoclastic and osteoblastic activity. Still in the late stages there is more bone absorption than deposition.

Nevertheless, bone contains so much calcium that amounts to about 1000 times of the quantity in the extracellular fluids, even with the great rise of calcium concentration in the body fluids, any immediate effect to bones is hardly discernable. Only in the case of prolonged administration or secretion of parathyroid hormone, such as many months to years, evident absorption of bone results with the development of large cavities filled with osteoclasts.

Additional Effects via Vitamin D and Cyclic Adenosine Monophosphate (cAMP) for Bone Absorption in Relation to Parathyroid Hormone: Again interestingly enough vitamin D plays important roles on bone absorption as well as bone deposition. Above vitamin D was examined for its indispensable effect on calcium and phosphate absorption through the intestinal epithelium, and hence, enhancing bone mineralization indirectly. Also it is known that in small quantities it mineralizes bone directly by the ability of 1,25-dihydroxycholecalciferol to cause transport of calcium ions through cell membranes, but in the opposite direction of the osteocytic membrane system calcium pump. However, administration of extreme quantities of vitamin D causes absorption of bone in much the same way as parathyroid hormone. Moreover, in the absence of vitamin D, the bone absorption effect of parathyroid hormone is excessively reduced or even prevented. The exact mechanisms of these intertwined phenomena are not known.

Parathyroid hormone administration causes the concentration of cAMP to increase in osteoclasts and other target cells within a few minutes by a secondary messenger mechanism (indirect mechanism). The cAMP is responsible for the release of proteolytic enzymes, and acids by osteoclasts for bone reabsorption, also formation of

1,25-dihydroxycholecalciferol in the kidneys. But these are secondary to the direct parathyroid hormone effects.

Calcitonin: The thyroid glands in human secrete a hormone termed calcitonin that has the effect of reducing plasma concentration of calcium ion (in fish, amphibians, reptiles, and birds calcitonin is secreted by ultimobranchial glands). The 0.1% of the thyroid gland tissue is composed of parafollicular cells or C cells responsible for the secretion of calcitonin. Calcitonin is a polypeptide chain of 32 amino acids with a molecular weight of ~3400.

In especially young animals, but also very little in humans calcitonin has the effect of decreasing calcium ion concentration within minutes after its injection. The effect of calcitonin on blood calcium ion concentration, when compared to parathyroid hormone, hence, is exactly opposite, and several times faster.

The calcitonin acts via two separate mechanisms. The immediate effect is to inactivate osteoclasts, and osteocytic membrane calcium pump, therefore, shifting the balance in the bone fluid in favor of exchangeable CaP salt deposition. This effect is more significant in young organisms in which the interchange of deposition and absorption of calcium is fast. The second, prolonged effect of calcitonin is to decrease the formation of new osteoclasts. Since osteoclastic activity secondarily stimulates osteoblastic activity the overall effect is to reduce the osteoclasts and osteoblasts in number, and hence osteoclastic and osteoblastic activity. Therefore, in the long run there is not a significant effect on the plasma calcium ion concentration. The effect of calcitonin is a transient one that lasts only a few hours, or a few days at most.

Calcitonin also has the effect on the kidney tubules, and intestinal tract that is the exact opposite of parathyroid hormone, but the effect is a minor one persisting very short in comparison to the parathyroid hormone.

Control of Parathyroid Hormone and Calcitonin Secretion by the Calcium Ion Concentration: Figure 2.25 summarizes the plasma concentration effect of calcium ion on the parathyroid hormone, and calcitonin plasma concentrations. The solid red curve shows the acute (a few hours) relationship between the plasma calcium concentration and plasma parathyroid hormone concentration. A decrease in calcium concentration from its normal value of 9.4 mg/dl to 8.4 mg/dl almost triples the plasma parathyroid hormone concentration, increasing the rate of its secretion within minutes. The approximate chronic (a period of many weeks) relation is shown as the dashed red line. A decrease in plasma calcium concentration of as little as a fraction of mg/dl

doubles the parathyroid hormone plasma concentration. This illustrates the extremely potent feedback control system, calcium ion concentration being the input variable. For instance, parathyroid glands become greatly enlarged in the case of rickets, during pregnancy, and lactation, even calcium is only slightly depressed and the change in its extracellular concentration is hardly measurable. On the other hand, increases of calcium concentrations in the plasma, such as excess quantities of calcium in the diet, increased vitamin D in the diet, and bone absorption caused by factors other than parathyroid hormone (e.g. bone absorption caused by disuse of bone), causes decreased activity, and reduced size of the parathyroid glands.

An increase in plasma calcium concentration of about 10% causes an immediate three- to six-fold increase in the rate of secretion of calcitonin as illustrated in Figure 2.25 by the dot-dash line. This proves to be the second hormonal feedback mechanism for controlling the plasma calcium ion concentration, but by the difference of acting more rapidly reaching its peak activity in less than hour in contrast to 3 to 4 hours required for the peak activity of parathyroid hormone. A second difference is the short lasting regulating effect of calcitonin because of the much powerful overriding effect of parathyroid control mechanism. The initial reduction of the calcium ion concentration caused by calcitonin was antagonized by the strong stimulation of parathyroid hormone secretion within an hour. Besides, in the adults the daily absorption and deposition of calcium are very small and the deposition increased by calcitonin has only a slight effect on the plasma calcium concentration. However, in children the effect is more pronounced since the absorption and deposition rates can be as high as 5 gr/day (5 to 10 times the total calcium quantity in the extracellular fluid). Also, in certain bone diseases, such as Paget's disease during which osteoclastic activity is accelerated, calcitonin then has the potent effect of reducing calcium absorption. In general, over a prolonged period parathyroid hormone almost entirely sets the calcium ion concentration in the extracellular fluid. When the thyroid glands are totally removed the long term blood concentration of calcium is not measurably altered again indicating the overriding controlling effect of parathyroid hormonal system.

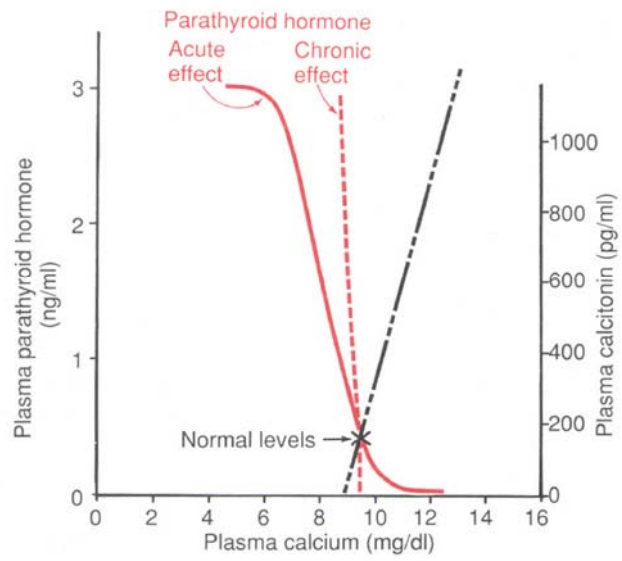


Figure 2.25. The approximate relation of plasma concentrations of parathyroid hormone and calcitonin with plasma calcium concentration. (Source: Guyton 1991)

CHAPTER 3

BIOMEDICAL IMPLANTS

3.1. Overview of Biomedical Implants

The Clemson University Advisory Board for Biomaterials has formally defined a biomaterial to be “a systemically and pharmacologically inert substance designed for implantation within or incorporation with living systems” (Park and Lakes 2007). More specifically, a biomaterial is a natural or synthetic, nonviable material that comprises whole or part of a living structure or biomedical device which performs, augments, or replaces a natural function in interaction with a biological system, and intended to be used and adapted for medical applications. A biomedical implant is a biomedical device inserted in a living tissue site for tissue growth, controlled release, or formation of an organic union. Prostheses are artificial devices that are externally incorporated to body through a barrier of skin such as wearable limbs, and hearing aids, and are not classified as biomaterials or implants. The successful, that is, safe, reliable, economic, and physiologically acceptable application of an implant depends on:

- ability to fixate to the host tissue surface,
- pharmacological acceptability (nontoxic, nonantigenic, nonallergenic, nonimmunogenic, nonmutagenic, noncarcinogenic, etc.),
- chemical inertness and stability (no time-dependent degradation),
- adequate weight and density,
- proper mechanical strength, fracture toughness,
- adequate fatigue life,
- sound engineering design,
- being relatively inexpensive, reproducible, easy to fabricate, and process for mass-scale production.

These conditions can only be satisfied by an understanding of the structure, property, function of the biological material (structured tissues that are the products of and at the same time comprising biological systems, such as, bone, skin, or artery), living tissue and living systems (organs, and organisms), and on the other hand the properties (toughness, flexibility, texture, etc.), and biocompatibility of the implant materials.

Condition of recipient, and surgical competency are the other factors determining the success of implant application.

Bioactivity is defined as the specific biological response at the implant-host tissue interface resulting in a bond after implantation (Hench, et al., 1971). There are, in general, four types of host tissue response to implanted material as given in Table 3.1.

Table 3.1. The possible host tissue responses to implant material
(Source: Hench L. L. 1998)

If the material is toxic, the surrounding tissue dies.
If the material is nontoxic and biologically inactive (almost inert), a fibrous tissue of variable thickness forms.
If the material is nontoxic and biologically active (bioactive), an interfacial bond forms.
If the material is nontoxic and dissolves, the surrounding tissue replaces it.

The main types of host tissue-implant anchorage, for hard tissue repair, are given as a list below (Hench, 1998, Albrektsson and Johansson 2001):

- Morphological fixation of dense, nonporous, biologically inactive device by *press-fitting* (into a defect), or by *cementing*, and the attachment is reinforced by subsequent bone growth into surface irregularities. However, in the case of a relative movement between the device and the surrounding tissue, progressive development of a nonadherent fibrous capsule in both the soft and hard tissues accompanies, which is a prelude to functional deterioration.
- Osseointegration is the clinically asymptotic rigid fixation of alloplastic material or device (an implant of origin other than autogeneic-own body source) by direct bone to implant rigid contact without the formation of fibrous capsule at the bone-implant interface. Osseointegration was reported to be the preferred anchorage method in oral and craniofacial implantology with very high success rates, and excellent functional results (Albrektsson and Johansson 2001).
- Biological fixation of porous, biologically active or inactive device by tissue ingrowth starting on the surface, and down into the pores, channels or pipes, resulting in mechanical attachment (osteoconduction).

- Bioactive fixation of surface-reactive ceramics, glasses, and glass-ceramics attached directly to the bone by chemical bonding.
- Replacement of resorbable device or material implantation by healing tissue at matching rates of resorption and tissue formation.

Another aspect of bone bonding at natural and biomaterial surfaces alike, depends on bone formation by contact osteogenesis, which requires a sufficiently stable implant surface providing a surface topography in the micrometer range with undercuts in the sub-micron scale. The sufficiently stable implant surface has to be insoluble in vivo; with a surface soluble (eg. β -TCP) in the physiological environment distance osteogenesis takes place (as opposed to contact osteogenesis). This results in the development of bony spicules in the surrounding soft tissues advancing toward the target surface which in turn will not result in bone-implant integration. The first tissue that forms on implanted materials is the highly mineralized and non-collagenous cement line as in the bone remodeling. It is necessary that the implant surface has to bear a three dimensionally complex topography with undercuts in the sub-micron scale so that the developing cement line can interdigitate and interlock. This phenomenon is the key to a successful bone-implant bonding, corroborating that the mechanism of bone bonding is the result of the micro- and nano-mechanical interdigitation of the bone tissue with the implant surface (Davies 2007).

In contrast, biocompatibility refers to the “required” and “undesirable” localized and general chemical, mechanical, pharmacological, and surface interactions between implant materials and the living tissue. Properties related to biocompatibility are illustrated in Figure 3.1. The required biocompatibility tests are, in general, acute systemic toxicity, cytotoxicity, hemolysis, intravenous toxicity, mutagenicity, oral toxicity, pyrogenicity, and sensitization.

The general classes of implant materials are given in Table 3.2., and the surgical uses of implant materials are given in Table 3.3.

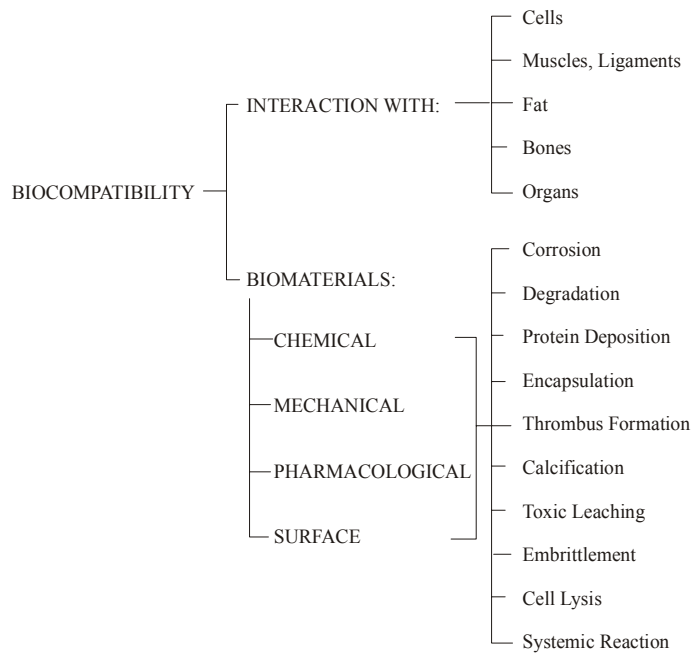


Figure 3.1. Schematic illustration of biocompatibility.
(Source: Park and Lakes 2007)

Table 3.2. Classification of implant materials
(Source: Park and Lakes 2007)

Materials	Advantages	Disadvantages	Examples
Polymers (nylons, silicone polytetrafluoroethylene, rubber, polyester, etc.)	Resilient Easy to fabricate	Not strong Deforms with time May degrade	Sutures, blood vessels, other soft tissues, hip socket, ear, nose
Metals (Ti and its alloys, Co-Cr alloys, Au, Ag, stainless steel, etc.)	Strong, tough, ductile	May corrode Dense Difficult to manufacture	Joint replacements, dental route implants, pacemaker and suture wires, bone plates and screws
Ceramics (alumina, zirconia, calcium phosphates including hydroxyapatite, carbon)	Very biocompatible	Brittle Not resilient Weak in tension	Dental and orthopedic implants
Composites (carbon-carbon, wire- or fiber- reinforced bone cement)	Strong, tailor-made	Difficult to manufacture	Bone cement, dental resin

Table 3.3. Surgical use of implant materials
(Source: Park and Lakes 2007)

Permanent Implants
Muscular skeletal system – joints in upper (shoulder, elbow, wrist, finger) and lower (hip, knee, toe) extremities, permanently attached artificial limb
Cardiovascular system – heart (valve, wall, pacemaker, entire heart), arteries, veins
Respiratory system – larynx, trachea and bronchus, chest wall, diaphragm, lung, thoracic plombage
Digestive system – tooth filling, esophagus, bile, ducts, liver
Genitourinary system – kidney, ureter, urethra, bladder
Nervous system – dura, hydrocephalus shunt
Special senses – corneal and lens prosthesis, ear cochlear implant, carotid pacemaker
Other soft tissues – hernia repair sutures and mesh, tendons, visceral adhesion
Cosmetic implants – maxillofacial (nose, ear, maxilla, mandible, teeth), breast, eye, testes, penis, etc.
Transient Implants
Extracorporeal assumption of organ function – heart, lung, kidney, liver, decompressive-drainage of hollow visceraspaces, gastrointestinal (biliary), genitourinary, thoracic, peritoneal lavage, cardiac catheterization
External dressings and partial implants – temporary artificial skin, immersion fluids
Aids to diagnosis – catheters, probes
Orthopedic fixation devices – general (screws, hip pins, traction), bone plates (long bone, spinal, osteotomy), intertrochanteric (hip nail, nail-plate combination, threaded or unthreaded wires and pins), intramedullary (rods and pins), staples, sutures, surgical adhesives

Despite the very high success rates with a strict quality assurance system, the main concern of device implantation is the probability of failure, and in some cases catastrophically, and much effort has been devoted for the perfection of design, material, and function of implants (Hech 1998, Rahaman and Yao 2007). In Figure 3.2 time dependent failure probability of implants for specific reasons, for hip joint replacement is shown schematically.

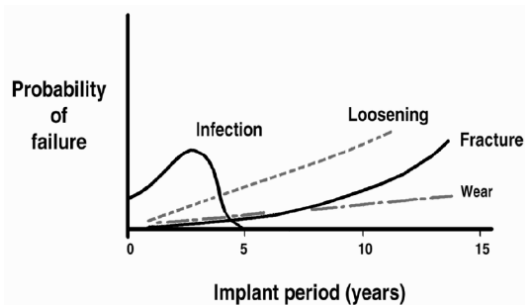


Figure 3.2. A schematic illustration of probability of failure versus implant period for hip joint replacements. (Source: Park and Lakes 2007)

Organ transplantation is widely applied due to the imperfect properties and functioning of the implant devices, and restore functions that cannot be performed by artificial devices or materials. The adverse immunological response is the major drawback of such allogeneic (involving or derived from the individuals of the same

species that carry sufficient genetic differences to interact antigenically) procedures. Nevertheless, tissue engineering directed to the growth of living tissue on designed and manufactured substrates – *scaffolds* – provides an alternative to both implanted devices and organ transplantations. The biodegradable scaffolds guide cell proliferation forming tissues in the desired shape and size, and ideally are resorbed at the end of the process leaving a very thin layer of interface. Scaffolds are made from natural or synthetic polymers, or in the hard tissue cases from calcium phosphate compounds. Some clinical success has been achieved with scaffolds in the repair of large skin area injuries, and cartilage defects.

3.2. Polymeric Implant Materials

The polymeric implant materials have the advantage of being processed into fibers, textiles, films, rods, viscous liquids. The synthetic polymeric materials are used, in general, to mimic the functions of natural polymeric materials, and some has the ability to bond to natural polymeric tissue.

Natural polymers or bioderived macromolecules include *collagen* (for soft tissue injectables, coatings, wound dressings), *chitosan* (for wound dressing, controlled release), *elastin* (coatings), *gelatin*, *cross-linked* (for artificial heart bladder coating), *hyaluronic acid* and *chondroitin sulfate* (for coatings, wound dressing, surgical non-adhesion, joint lubrication) (Helmus, 1991; Park and Lakes 2007).

Polyamides or nylons derive their axial strength by the interchain hydrogen bonding (due to –CONH– groups), and high degree of crystallinity that impart its fiber-forming characteristic. Nylon 6, 66, 11, 610 are convenient materials for suture. Kevlar (p-phenylene terephthalate), an aromatic polyamide has the tensile strength per unit weight 5 fold that of steel. Nylons due to their hygroscopic character and proteolytic enzyme interaction, are plasticized in vivo, and lose their strength.

Polyethylene (together with polypropylene and their copolymers termed polyolefins) are commercially available in three grades: low density (LDPE), high density (HDPE), and ultra high molecular weight (UHMWPE; $MW > 2 \times 10^6$ g/mol). HDPE are used for suture, and hernia repair mesh manufacturing. UHMWPE is an extensively used material for hip and knee joint load bearing surfaces. Its modified form, DePuy, has a higher crystallinity of longer chain folds, imparting higher hardness, modulus of elasticity, tensile yield strength, and creep and wear resistance. The cross-

linked form of UHMWPE, with its low wear rate, is used for articulating joint material; the acetabular cup of hip joint prosthesis is a common example. Polypropylene with its exceptionally high flexural fatigue life is used for integrally molded hinges of finger joint prostheses.

Polyacrylates: Polymethyl acrylate (PMA), and polymethyl methacrylate (PMMA) are extensively used for biomedical applications. These usually amorphous polymers are light transparent (92% transmission), have high refraction index, and good weathering properties, hence are used for hard contact lens, and implantable ocular lenses. They have high chemical resistance, and are highly biocompatible, but are hard and brittle. They are easy to fabricate by casting, molding, and machining with conventional tools. Polyhydroxyethyl methacrylate (poly-HEMA) due to its ability of water absorption of over 30% of its weight, is the first hydrogel suitable for soft contact lens applications. Ethylene glycol dimethylacrylate, and polyacrylamide are the other hydrogels. However, because of their lower O₂ permeability in contrast to silicon rubber, they are used to coat the hydrophobic silicon rubber for soft lens applications.

PMMA is a major component for bone cements that are used to firmly fix hip and knee joint prostheses. The typical bone cement comprises the liquid components methyl methacrylate (monomeric form), N,N,-dimethyl-p-toluidine (for the promotion and acceleration of cold curing), hydroquinone (for prevention of premature polymerization), and the solid components PMMA, methyl methacrylate-styrene-copolymer, barium sulfate (BaSO₄)-USP, dibenzoyl peroxide (Park and Lakes 2007).

Acrylates are also used for dentures and maxillofacial prostheses due to their physical, and coloring properties and ease of fabrication.

Fluorocarbon polymers: Polytetrafluoroethylene (PTFE) or Teflon, polytrifluorochloro ethylene (PTFCE), polyvinylfluoride (PVF), fluorinated ethylenepropylene (FEP) are the most widely used fluorocarbon polymers. PTFE can be injection molded, and melt extruded. PTFE in fibrous expanded form is used to knit vascular grafts avoiding blood leakage.

Rubbers and elastomers: Rubbers or elastomers are prominent with their remarkable ability of extreme stretchability and retractability. Silicone rubbers (the repeating unit dimethyl siloxane with cross links) are developed for soft tissue reconstruction, and tubing. Polyurethane rubbers are used to coat implant materials and for soft contact lens.

High strength thermoplastics are used to replace light metals for implant applications with their matching strength. Polyacetalys, polysulfones can be used as implant materials. Polycarbonates can be used in heart/lung assist devices.

Some of the in vivo changes associated with the implanted polymeric materials are given in Table 3.4.

Table 3.4. Effects of implantation on polymers
(Source: Bloch and Hastings 1972)

Polymers	Effects of Implantation
Polyethylene	Low-density PE absorb some lipids and lose tensile strength. High-density PE are inert and no deterioration occurs.
Polypropylene	Generally no deterioration
Polyvinylchloride (rigid)	Tissue reaction, plasticizers may leach out and materials become brittle.
Polyethyleneterephthalate	Susceptible to hydrolysis and loss of tensile strength (in polyester).
Polyamides (nylon)	Absorb water and irritate tissue, lose tensile strength rapidly.
Silicon rubber	No tissue reaction, very little deterioration.
Polytetrafluoroethylene	Solid specimens are inert. If is fragmented into pieces irritation will occur.
Polymethylmethacrylate	Rigid form: crazing, abrasion, loss of strength by heat sterilization. Cement form: high heat generation, unreacted monomers during and after polymerization may damage tissues.

3.3. Metallic Implant Materials

Metals and metal alloys are employed as implants mainly due to their strength, fracture toughness, and fatigue resistance. Usually there is a tradeoff complementary relationship between strength and toughness. The major applications are joint, long bone, and teeth hard tissue replacements, orthopedic wires, screws and plates, vascular stents, heart valve stents, artificial hearth housing. The metallic material used for implant manufacturing are subject to corrosion in a hostile body environment, and the corrosion products can easily be released in quantities well over the toleration limits of the body, rendering the biocompatibility a major concern. The material loss due to corrosion also may cause the implant to loosen in time. These disadvantages are overcome by biocompatible coatings on metallic material. The major metal and metal alloys used for impant devices are given below.

Stainless Steel: The first stainless steel used for implants was type 302 (18-8 by original classification), later to be replaced by type 316 (18-8sMo) improving corrosion resistance. The corrosion resistance was further enhanced by reducing the carbon content from 0.08% to 0.03 % with the designation 316L. Its composition is given in Table 3.5. The 316 and 316L austenitic stainless steels are still in use for implant manufacturing. A wide range of properties can be imparted depending on the heat treatment (for softer material), and cold working (for higher strength, and hardness) as indicated in Table 3.6.

Table 3.5. Composition of 316L stainless steel surgical implants (ASTM 2000)
(Source: Park and Lakes 2007)

Element	Composition (w/o)
Carbon	0.030 max
Manganese	2.00 max
Phosphorous	0.025 max
Sulfur	0.010 max
Silicon	0.75 max
Chromium	17.00-19.00
Nickel	13.00-15.00
Molybdenum	2.25-3.00
Nitrogen	0.10 max
Copper	0.50 max
Fe	Balance

Table 3.6. Mechanical properties of stainless steel surgical implants (ASTM 2000)
(Source: Park and Lakes 2007)

Condition	Ultimate tensile strength, min ksi (MPa)	Yield strength (0.2% offset), min ksi (MPa)	Elongation 2 in. (50.8 mm) min %	Rockwell hardness max
Bar and wire (F138)				
Annealed	71 (490)	27.5 (190)	40	-
Cold worked	125 (860)	100 (690)	12	-
Extra hard	196 (1350)	-	-	-
Cold drawn	125 (860)	-	-	-
	150 (1035)	-	5	-
Sheet and strip (F139)				
Annealed	71 (490)	27.5 (190)	40	95 HRB
Cold worked	125 (860)	100 (690)	10	-

Co-Based Alloys: There are four types of Co alloys. The CoCrMo (F75) is used for cast products, such as, artificial joints, and dental materials. The CoNiCrMo (F562), CoCrW Ni (F90), CoNiCrMoWFe (F563) are wrought by hot forging, and are used for making the stems of hip and knee joint prostheses that bear heavy loading. The chemical composition, and mechanical properties of Co-based alloys are given in Table 3.7, and Table 3.8, respectively.

Table 3.7. Chemical compositions of Co-based alloys (ASTM 2000)
(Source: Park and Lakes 2007)

Element	Co28Cr6Mo (F75) Castable		Co20Cr15W10Ni F(90) Wrought		Co28Cr6Mo F(1537) Wrought		Co35Ni20Cr10Mo F(562)	
	Min.	Max.	Min.	Max.	Min.	Max.	Min.	Max.
Cr	27.0	30.00	19.00	21.00	26.0	30.0	19.0	21.0
Mo	5.0	7.00	-	-	5.0	7.0	9.0	10.5
Ni	-	2.5	9.00	11.00	-	1.0	33.0	37.0
Fe	-	0.75	-	3.00	-	0.75	9.0	10.5
C	-	0.35	0.05	0.15	-	0.35	-	0.025
Si	-	1.00	-	1.00	-	1.0	-	0.15
Mn	-	1.00	-	2.00	-	1.0	-	0.15
W	-	0.20	14.00	16.00	-	-	-	-
P	-	0.020	-	0.040	-	-	-	0.015
S	-	0.010	-	0.030	-	-	-	0.010
N	-	0.25	-	-	-	0.25	-	-
Al	-	0.30	-	-	-	-	-	-
Bo	-	0.01	-	-	-	-	-	0.015
Ti	-	-	-	-	-	-	-	1.0
Co	Balance							

Table 3.8. Mechanical properties of Co-based alloys (ASTM 2000)
(Source: Park and Lakes 2007)

Condition	Ultimate tensile strength min ksi (MPa)	Yield strength (0.2% offset) min ksi (MPa)	Fatigue strength ksi (MPa)	Elongation min (%)	Reduction of area min (%)
Co28Cr6Mo (F75) As cast	95 (655)	65 (450)	45 (310)	8	8
Co20Cr15W10Ni (F90) Annealed	125 (860)	45 (310)	-	30	-
Co28Cr6Mo (F1537) Annealed	130 (897)	75 (517)	-	20	20
Hot worked	145 (1000)	101 (700)	-	12	12
Warm worked	170 (1172)	120 (827)	-	12	12
Co35Ni20Cr10Mo (F562) Annealed	115 (793)	35 (241)	49.3 (340)	50.0	65.0
Cold worked, aged	145 (1000)	65 (448)	-	8.0	35.0
	260 (1793) min	230 (1586) min			

Ti and Ti-based alloys: The use of titanium as implant material dates back to late 1930s. The strength of titanium and its alloys is around the values for 316 stainless steel, and Co alloys, however, its density of 4.5 g/cm^3 as compared to 7.9 g/cm^3 for 316 stainless steel, 8.3 g/cm^3 for cast CoCrMo, and 9.2 g/cm^3 for wrought CoNiCrMo alloys provides a specific strength that is unsurpassed by any other implant material. Figure 3.3 compares the specific strengths of some metallic implant materials.

The modulus of elasticity of $\sim 110 \text{ GPa}$ which is half the value for Co-based alloys, minimizes the stress-strain mismatch at the interface between the implant and the surrounding tissue, avoiding stress shielding, and hence the improper loading of the bone. The corrosion resistance of titanium alloys is also superior to other metallic implants due to the in vivo formation of a passivating thin film of TiO_2 . Nevertheless, titanium has a poor shear strength, a disadvantage for bone screws, and it tends to seize with other metal parts when in sliding contact. The most widely used titanium alloy for implant applications is Ti6Al4V. The chemical composition of titanium and its alloys are given in Tables 3.9, 3.10, and 3.11. Titanium is an allotropic material assuming hexagonal close packed structure of α -Ti below $862 \text{ }^\circ\text{C}$, and body centered cubic structure of β -Ti above that. Aluminum tend to increase α - β transformation temperature, while vanadium tend to decrease it as seen in the phase diagram shown in Figure 3.4. The optical micrographs showing the granular microstructure of α - β Ti6Al4V alloy are given in Figure 3.5.

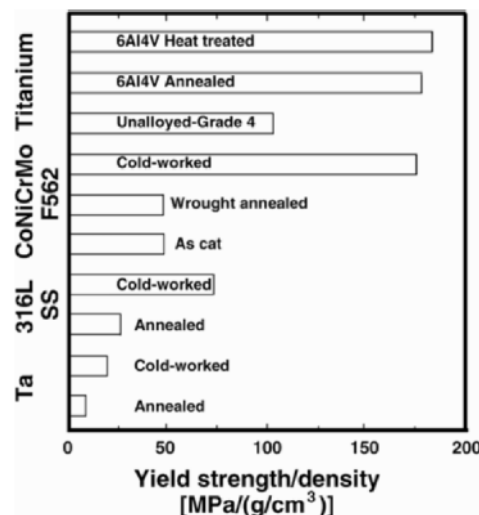


Figure 3.3. Yield strength to density ratio of some metallic implant materials. (Source: Hille 1966)

Table 3.9. Chemical composition of pure titanium (F67, ASTM 2000) all values are in maximum allowable w% (Source: Park and Lakes 2007).

Element	Grade 1	Grade 2	Grade 3	Grade 4
N	0.03	0.03	0.05	0.05
C	0.10	0.10	0.10	0.10
H	0.015	0.015	0.015	0.015
Fe	0.20	0.30	0.30	0.50
O	0.18	0.25	0.35	0.40
Ti	Balance			

Table 3.10. Chemical composition of wrought Ti alloys (ASTM 2000) All values are in maximum allowable w% (Source: Park and Lakes 2007)

Element	Wrought Ti8Al7Nb (F1295)	Wrought Ti3Nb13Zr (F1713)	Wrought Ti121Mo6Zr2Fe (F1813)
N	0.05	0.05	0.05
C	0.08	0.08	0.05
H	0.009	0.012	0.020
Fe	0.25	0.25	1.5-2.5
O	0.20	0.15	0.08-0.28
Ta	0.50	-	-
Al	5.5-6.5	-	5.50-6.75
Zr	-	12.5-14.0	5.0-7.0
Nb	6.5-7.5	12.5-14.0	-
Mo	-	-	10.0-13.0
Ti	Balance		

Table 3.11. Chemical composition of Ti6Al4V alloys (ASTM 2000) All values are in maximum allowable w%. (Source: Park and Lakes 2007)

Element	Wrought, forging (F136, F620)	Casting (F1108)	Coating (F1580)
N	0.05	0.05	0.05
C	0.08	0.10	0.08
H	0.012	0.015	0.015
Fe	0.25	0.30	0.30
O	0.13	0.20	0.20
Cu	-	-	0.10
Sn	-	-	0.10
Al	5.5-6.50	5.5-6.75	5.50-6.75
V	3.5-4.5	3.5-4.5	3.50-4.50
Ti	Balance		

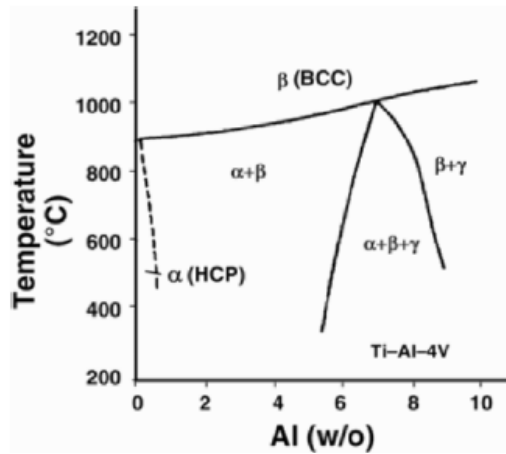


Figure 3.4. Part of phase diagram of Ti-Al-V (at 4 w% V).
(Source: Park and Lakes 2007)

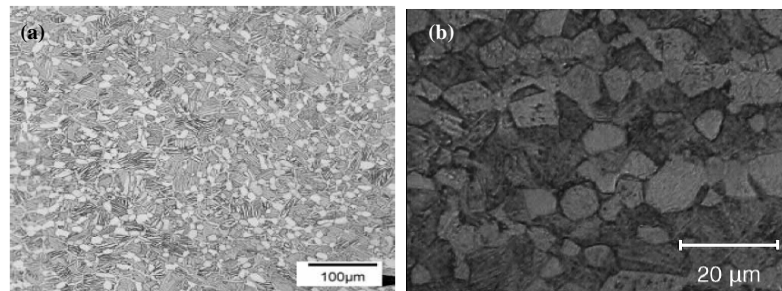


Figure 3.5. (a) optical micrograph of a chemically etched α - β Ti6Al4V alloy, (b) optical micrograph of Ti6Al4V alloy showing typical grain structure. (Source: (a) Miller 2006, (b) Cheschini, et al. 2008)

The inclusion of Al as α phase stabilizer promotes good weldability by oxidation resistance upto 600 °C. The inclusion of V as β phase stabilizer imparts higher strength as that phase persists in the solid solution below transformation temperature. The mechanical properties of Ti and its alloys are given in Table 3.12, 3.13 and 3.14

Table 3.12. Mechanical properties of pure titanium (F67, ASTM 2000)
(Source: Park and Lakes 2007)

Properties	Grade 1	Grade 2	Grade 3	Grade 4
Tensile strength ksi (MPa)	35 (240)	50 (345)	65 (450)	80 (550)
Yield strength (0.2% offset) ksi (MPa)	25 (170)	40 (275)	55 (380)	70 (485)
Elongation (%)	24	20	18	15
Reduction of area (%)	30	30	25	25

Table 3.13. Mechanical properties of wrought Ti alloys (ASTM 2000)
(Source: Park and Lakes 2007)

Alloys	Tensile strength ksi (MPa)	Yield strength ksi (MPa)	Elongation (%)	Reduction of area (%)
Wrought Ti8Al7Nb (F1295)	130.5 (900)	116 (800)	10	25
Wrought Ti3Nb13Zr (F1713)				
Aged	125 (860)	105 (725)	8	15
Annealed	80 (550)	50 (345)	15	30
Unannealed	80 (550)	50 (345)	8	15
Wrought Ti121Mo6Zr2Fe (F1813)	135 (931.5)	130 (897)	12	30

Table 3.14. Mechanical properties of Ti6Al4V (ASTM 2000)
(Source: Park and Lakes 2007)

Properties	Wrought (F316)	Casting (F1108)
Tensile strength ksi (MPa)	125 (860)	125 (860)
Yield strength (0.2% offset) ksi (MPa)	115 (795)	110 (758)
Elongation (%)	10 min	8 min
Reductiojn of area (%)	20 min	14 min

Dental Metals: Dental amalgam is composed of a minimum of 65% silver, and a maximum of 29% tin, 6% copper, 2% zinc, and 3% mercury. Solid powder alloy is mixed with liquid Hg in a mechanical triturator resulting in a paste, then, used to fill tooth cavity, and hardens with time. Gold and gold alloys are used in dentistry due to their durability, stability and high corrosion resistance. Gold restorations are made by casting or malleting. In the alloys copper and platinum improves strength while silver compensates for copper color. Nickel-titanium alloys are used in orthodontic dental arch wires, as well as arterial blood vessel stents, vena cava filters, intracranial aneurism clips, and orthopedic implants, due to their remarkable property of thermoelastic martensitic transformation providing shape memory effect.

Other Metals: Tantalum owing to its high corrosion resistance is used as wire sutures. Single woven filaments are used as arterial stents. Radioactive tantalum (Ta182) is used to treat head and neck tumors. Porous tantalum (72-81% porosity) has the potential use of bone graft substitute for femoral head. NiCu and CoPd alloys are

used in hyperthermia cancer treatment due to their magnetic properties. Pt, Pd, Rh, Ir are used as electrodes due to their extremely high corrosion resistance (poor mechanical strength).

3.4. Ceramic Implant Materials

The term bioceramics refers to the class of ceramic materials that are used as medical implantation for the repair and reconstruction of the diseased or damaged tissues of the musculo-skeletal system, in the bulk form, as coatings on and composites with other implant materials. The bioceramics are classified according to the type of bonding reaction they induce in the tissue as listed below. These reactions depend on the composition, crystallinity, thickness of coating, and size of particulates of the bioceramic (Hench 1998).

- Dense, nonporous, almost inert, crystalline bioceramics; they bond to the tissue by morphological fixation.
- Porous bioceramics; they bond to the bone by biological fixation or osteoconduction, in bulk form or porous coatings on metals and polymers.
- Bioactive glasses and glass ceramics; the bonding is achieved by the direct chemical bond of the surface active implant to hard and/or soft tissues (bioactive fixation).
- Resorbable ceramics and glasses to be replaced by tissue at a designed pace, in bulk or powder form.

3.4.1. Almost Inert Crystalline Bioceramics

The major biomedical uses of dense, bioinert ceramics are in the hip joint articulations as femoral head balls, and acetabular cup linings, in the knee articulations as bearing couple, bone screws, jaw bone (alveolar ridge), and maxillofacial reconstruction, ossicular (middle ear) bone substitutes, keratoprotheses (corneal replacements), segmental bone replacements, and blade and screw and post-type dental implants. The main materials are discussed below.

Alumina ceramics: High density, high purity (>99.5%) α -Al₂O₃ has been used for artificial joint prostheses (total hip arthroplasty (THA), and total knee arthroplasty

(TKA)) since 1970s (Rahaman and Yao 2007). The microstructure is composed of grains of size less than a few micrometers with the incorporation of ~0.25% MgO for to restrict the grain growth during sintering, and to achieve near theoretical density. Dense, fine grained alumina has the remarkable properties of excellent biocompatibility, very low friction coefficient and wear rates, good flexural strength, excellent compressive strength, high resistance to dynamic and impact fatigue and high resistance to subcritical crack growth. In the THA procedure, the use of alumina femoral heads, and acetabular liners, together with the improved device design, and implantation techniques, the risk of catastrophic failure reported from the years 2000 to 2004 to be as low as 0.02%.

Zirconia ceramics: Zirconia based ceramics were introduced in the 1980s to replace alumina for femoral head manufacturing. Yttria (Y_2O_3) stabilized tetragonal phase of zirconia (ZrO_2) (Y-TZP) has flexural strength and fracture toughness of two to three times of Al_2O_3 , and the femoral head fracture risk was anticipated to reduce while retaining excellent wear performance of smaller heads against UHMWPE acetabular liners. The microstructure of Y-TZP consists of fine grained (0.1-1 μm) metastable tetragonal phase of ZrO_2 with the fracture toughness maximized at 2 mol% Y_2O_3 , and 0.3 μm grains. However, Y-TZP was withdrawn from the femoral head manufacturing due to its serious limitation of degradation in moist atmosphere at temperatures as low as 150°C by the slow tetragonal to monoclinic transformation starting at the implant surface.

Composites of alumina and zirconia: ZTA, with the microstructure of fine ZrO_2 particles dispersed in a dense fine grained Al_2O_3 matrix, combines the high hardness of Al_2O_3 , and the flexural strength and fracture toughness of ZrO_2 . The degradation in moist environment does not pose the risks of Y-TZP when ZrO_2 is less than 16 vol% (percolation threshold). ZTA also optimizes the t-m transformation toughening during manufacturing suppressing crack propagation. Alumina matrix composite (AMC) based on the main structure of ZTA includes SrO and Cr_2O_3 as additives. It provides improvements in hardness, flexural strength, fracture toughness, wear resistance, as well as better tailoring of microstructure.

Non-oxide ceramics: The strength and hardness of dense Si_3N_4 ceramics, manufactured by hot pressing, are higher than that of alumina. By the control of sintering characteristics it can be tailored to acquire high fracture strength and fracture toughness. Ultra-low wear rates of Si_3N_4 ceramic bearings were reported. Wear debris in THA and TKA applications was totally eliminated. It passed all the required

biocompatibility tests (Rahaman and Yao 2007). The strength and hardness of hot pressing manufactured SiC are higher than, and the fracture toughness is similar to Al_2O_3 , and is used in articulating joint bearings.

Hard Coatings on Metals: Nitrogen ion implantation, thermal diffusion, and vapor deposition of nitride methods are used to increase the surface hardness and wettability of metals for total articulating joint replacements, which in turn improves the wear and corrosion resistance. Nitrogen ion implantation forms a surface layer of less than a micrometer thick but it is prone to wearing. Thermal diffusion method can form thicker surface layers but it is also prone to scratching and oxidative wear. Vapor deposition of TiN coatings yields surface hardening, but wear debris can cause stress amplification which may cause third body wearing. DLC (diamond like carbon) coatings have low friction, high wear and corrosion resistance, and good surface to bone bonding verified experimentally. Diamond coatings also have very high surface abrasion resistance, but clinical outcomes has not been sufficiently monitored. Because of its mechanical reliability and thromboresistance carbon coated mechanical hearth valves have been extensively used.

Surface modification of metals is most easily achieved by thermal diffusive oxidation, creating a thick oxide layer (5 μm) on the metal surface for improved hardness, corrosion resistance, superior cohesion, adhesion, and lubrication properties.

Nanoceramics and ceramic nanocomposites: The ultrafine nanoscale grain sizes (<50-100 nm) of ceramic materials proved effective for third body wearing in the articulating joints. The improvement of the mechanical properties (hardness, strength toughness, etc.) with the decreasing grain size, especially, to nanoscale dimensions is a known phenomenon. Al_2O_3 , $\text{Al}_2\text{O}_3/\text{SiC}$, $\text{Al}_2\text{O}_3/\text{ZrO}_2$, $\text{Al}_2\text{O}_3/\text{TiO}_2$, $\text{ZrO}_2/\text{Al}_2\text{O}_3$, $\text{Si}_3\text{N}_4/\text{SiC}$ nanocomposites are under development for enhanced mechanical properties.

The mechanical properties of some dense ceramics in comparison to CoCr alloy and cortical bone is given in Table 3.15.

Table 3.15. Mechanical properties of dense Al₂O₃ and ZrO₂ based ceramics in comparison to CoCr ally and cortical bone. (Source: Rahaman and Yao 2007)

Property	Al ₂ O ₃	Mg-PSZ	Y-TZP	ZTA	CoCr	Bone (cortical)
Composition	99.9% Al ₂ O ₃	ZrO ₂ -8 mol% MgO	ZrO ₂ -3 mol% Y ₂ O ₃	Al ₂ O ₃ -20 vol% ZrO ₂		
Density (g/cm ³)	>3.97	5.75	6.05	4.40	~8.5	1.7-2.0
Grain size (µm)	1-5	50		1-2		
Strength (MPa)			0.1-1.0			
Tensile	250-300	300-400		-	600-1800	-
Compressive	2000-3000	2000-3000	-	-		130-180
Flexural	300-500	600-700	3000-4000	700-1000		60-160
Fracture toughness, K _{IC} (MPa.m ^{1/2})	4-5	6-10	1000-1500	6-10	50-100	2-12
Fracture threshold, K _{I0} (MPa.m ^{1/2})	2.0-2.5		6-12	4		
Elastic modulus, (GPa)	400-450	200-250	3.0-3.5	300-350	210-250	3-30
Hardness (Vickers) (HV)	1800-2000	1200	200-250	1600-1800	300-400	
Thermal expansion coefficient, (10 ⁻⁶ K ⁻¹)	8	7-10	1200	8.5	~14	
Thermal conductivity (Wm ⁻¹ K ⁻¹)	30	2	11	17	~100	
			2			

3.4.2. Porous Ceramics

Porous ceramics in the form of bioactive coatings, powders, and substrates offer molecular control over the incorporation of proteins, and biological behavior of cells, leading to accelerated biological fixation of implant by a sequence of osteoinductive and osteoconductive events. The implant serves as a structural bridge, model, or scaffold for bone formation. The bone ingrowth down into the pores of the coating provides the required rigid fixation. Vascular bone tissue growth takes place on the materials with interconnected pores of sizes over 100 µm (Hench 1998, Hench and Wilson 1991). However, the low strength of porous ceramics limits their use to low load, or no load bearing applications. The major clinical applications are the porous hydroxyapatite coatings on load bearing implants, porous calcium phosphates as fillers for the bone defects, (Hench 1998), and calcium phosphate bone grafts (Best, et al. 2008).

The porous hydroxyapatite coating provides an intricate surface for bioactive fixation of the stem and cup of hip joint, and the bearing stems of knee joint prostheses, as an alternative to cement fixation. The porous metal surfaces prepared by the sintering of balls, wires, meshes on its surface are then coated by plasma spraying of

hydroxyapatite. It was clinically observed that the rate of bone ingrowth into porous titanium was accelerated by plasma sprayed hydroxyapatite coating, and the interfacial adhesion strength as a function of implantation time increased more than three folds followed up to 36 weeks (Hench, 1998). The elastic modulus mismatch of the bone and the metallic implant leads to improper load transfer to the host bone tissue by stress shielding, and eventual loosening and failure of the implant by the direct bone to metal contact, which is avoided by hydroxyapatite coating of the metallic implant (Hench 1998).

The uses of calcium phosphates for bone grafting and bone tissue engineering are under development as an alternative to biological materials (Best, et al. 2008). A high degree of porosity (70-80%) with fully interconnected pores of sizes over 100 μm is required for cell mobility and vascularization. The bioceramic bone graft or scaffold is either seeded with cells before implantation, or is designed to be invaded and populated by cells after implantation.

3.4.3. Bioactive Glasses and Glass Ceramics

Bioactive glasses and glass ceramics form a strong adhesion bond to bone and in some cases to soft tissues (tendons, ligaments, etc.) as well. Bioactive materials were classified into Class A and Class B according to the tissue reaction they induce. Class A materials induce osteoinduction, followed by osteoconduction, that is, mesenchymal stem cells migrate on and differentiate into osteogenic cell lineages generating bone tissue on the implant material surface. Hench originally termed the recruitment and differentiation of stem cells as osteoproduction, however, osteoinduction is the correct term in the contemporary terminology. Class B materials are not osteoinductive but still have the ability to induce osteoconduction. However, for the Class A bioactive materials the osteoconduction, that is bone growth along the bone-implant interface is much faster, and the durability is much longer. The interfacial adhesion between bone and the implant was reported to be stronger than the cohesion strength of either the bone or implant material (Hench 1998). The surface reaction stages induced by a Class A bioactive material is shown in Figure 3.6.

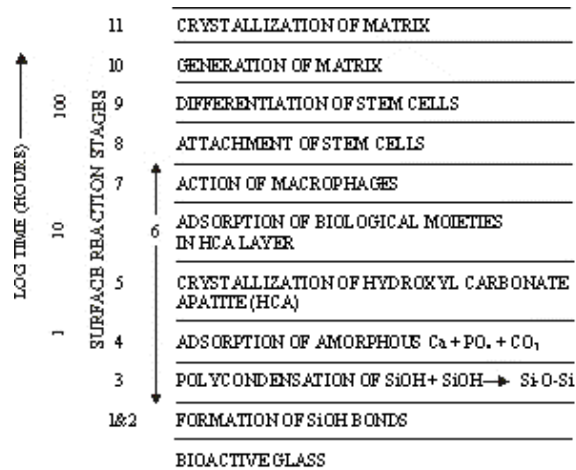


Figure 3.6. Sequence of interfacial reactions involved in forming tissue-bioactive implant bond. (Source: Hench 1998)

Bioglass[®] was introduced in the early 1970s as the particular compositions of $Na_2O-CaO-P_2O_5-SiO_2$ system as a bioactive implant material capable of directly bonding to bone, and at a certain composition to soft tissue as well. The main features of this material distinguishing it from traditional soda-lime-silica glasses are less than 60 mol% SiO_2 , content, high Na_2O and CaO contents, and high CaO/P_2O_5 ratio. The composition denoted by 45S5 is 45w% SiO_2 , S stands for the matrix former, and 5 is the CaO/P_2O_5 ratio. Substitution of 5–15 wt% B_2O_3 for SiO_2 , or 12.5 wt% CaF_2 for CaO , or crystallizing the glass compositions do not have influence on the bone bonding ability of the material. However, addition of more than 3w% of Al_2O_3 impairs bonding. Hench defined an in vivo bioactivity index $I_B = 100/t_{50bb}$, (t_{50bb} is the time for 50% of the interface to be bonded) useful in determining the limiting contours of bioactivity in the phase diagrams of bioactive material systems. The thickness of the bonding zone between a bioactive implant and bone is proportional to the I_B value of the implant material at elongated times (e.g. 1 year). The bioglass compositions with 6 w% P_2O_5 , and with a SiO_2 content of 42-53 mol% provides a very rapid bonding to bone and also to collagenous parts of soft tissues ($I_B=8-10$). The bonding requires 2-4 weeks for a SiO_2 content of 54-60 mol% ($I_B=0-8$). Above 60 mol% SiO_2 there is no bonding. Window, bottle, microscope glasses fall in this range, and are almost bioinert, eliciting fibrous capsule at the implant-tissue interface. The elastic modulus transition thickness of the naturally occurring interfaces from the low values of the soft tissues such as ligaments and tendons to the higher values of the bone and teeth, is mimicked on the

bioglass by the 30-60 μm thick hydroxy carbonate apatite (HCAp)/collagen region of the 100-200 μm total thickness (Hench 1998).

In 1982 Kokubo and Yamamuro introduced apatite-wollastonite (A-W) glass-ceramics used as bone substitute. The formula consists of 38w% oxyfluoroapatite ($\text{Ca}_{10}(\text{PO}_4)_6(\text{OH}_x\text{F}_{2-x})$), and 34w% wollastonite ($\text{CaO}\cdot\text{SiO}_2$) crystals of 50-100 nm dispersed in a 28w% glassy matrix (17w% MgO, 24w% CaO, 59w% SiO_2) (Best, et al., 2008). The highest values of the bending strength, fracture toughness, Young's modulus of the A-W glass ceramics within the bioactive glasses and glass ceramics, enable its use as load bearing implants in such applications as vertebral prostheses, and iliac crest (pelvic bone) substitutions (Best, et al. 2008).

Another bioactive silica-phosphate containing phlogopite mica ($(\text{Na},\text{K})\text{Mg}_3(\text{AlSi}_3\text{O}_{10})\text{F}_2$) and apatite crystals, has the advantage of easy machinability (Hench 1998).

3.4.4. Calcium Phosphate Ceramics

The use of calcium phosphate compounds for medical and dental applications is prominent since 1970's as porous coatings on porous or nonporous metals, bulk, granule, or powder forms as scaffolds, grafts and fillers, in formulations of bioactive bone cements and as bioactive layers in the bone-PMMA cement interfaces. These include orthopedic and dental implants, total hip and knee arthroplasties, alveolar ridge augmentation, maxillofacial surgery, and otolaryngology (Hench 1998), spinal fusion (Best, et al. 2008).

The phase diagram for calcium phosphate compounds is given in Figure 3.7. The formation of stable phases depends on temperature and water partial pressure. At 37°C, and in body fluids, dicalcium phosphate (brushite), $\text{CaHPO}_4\cdot 2\text{H}_2\text{O}$, is stable for $\text{pH}<4.2$, hydroxyapatite, $\text{Ca}_{10}(\text{PO}_4)_6(\text{OH})_2$ (HAp), is the stable phase for $\text{pH}>4.2$. At elevated temperatures α,β -tricalcium phosphate (TCP), $\text{Ca}_3(\text{PO}_4)_2$, and tetracalcium phosphate (TetrCP), $\text{Ca}_4\text{P}_2\text{O}_9$, are the stable phases. TCP is soluble in physiological fluids, and is employed as a biodegradable bioceramic. Among the four polymorphs, α and β TCP are the most common.

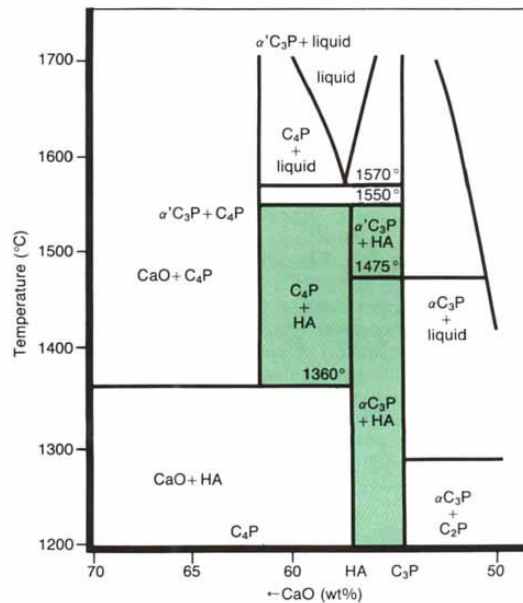


Figure 3.7. The phase diagram for CaO and P₂O₅ under 500 mm Hg water partial pressure. Shaded area is the region that hydroxyapatite containing implants can be obtained. (Source: Hench 1998)

The sintering of calcium phosphate ceramics takes place in the temperature range of 1000-1500°C in the bulk form. When water partial pressure is sufficiently high HAp phase can be stable up to 1360°C as shown in Figure 3.7. In the absence of water TCP, and TetrCP are the high temperature stable phases. The temperature range of stability of HAp widens with the increasing water partial pressure. The stoichiometric ratio of Ca/P is important in determining the synthesized phases. When Ca/P > 1.67, CaO forms along with HAp, and α - and β -TCP are among the products for Ca/P < 1.67. The ratio of the high temperature stable phases that form during sintering and their relative stability upon cooling down are often difficult to predict. The biphasic calcium phosphates (BCP), mixtures of HAp and TCP, have solubilities increasing with the TCP ratio. Adjusting of the solubility of BCPs, resorbable implant devices can be engineered with the matching resorption, and tissue regeneration rates.

HAp powders can be prepared by mixing, aqueous solutions of CaNO₃, and (NH₄)₃PO₄ in the appropriate molar ratio that yields a precipitate of stoichiometric HAp. During synthesis or in the physiological environment cationic substitutions for Ca²⁺ including sodium, potassium, magnesium, strontium, and manganese, and anionic substitutions of F⁻ and Cl⁻ for OH⁻, and the carbonate, CO₃²⁻, substitutions for OH⁻ (termed as type A), and for PO₄³⁻ (termed as type B) affect crystal morphology, crystallinity, solubility, and thermal stability by the changing lattice parameters. The

fluorapatite ($\text{Ca}_{10}(\text{PO}_4)_6(\text{OH})_{2-x}\text{F}_x$, with $0 < x < 2$), is found in dental enamel. The carbonate apatite ($\text{Ca}_{10}(\text{PO}_4)_6(\text{OH})_{2-2x}(\text{CO}_3)_x$ or $\text{Ca}_{10-x+y}(\text{PO}_4)_{6-x}(\text{OH})_{2-x-2y}(\text{CO}_3)_x$, where $0 < x < 2$ and $0 < y < x$) exists in bone. The carbonate apatite formed around HAp increases the bone apposition rate. Silicon substituted HAp, $\text{Ca}_{10}(\text{PO}_4)_{6-x}(\text{SiO}_4)_x(\text{OH})_{2-x}$, was reported to significantly increase the bone apposition rate, and tissue organization around the implant (Best, et al. 2008).

Incorporation of biological agents such as growth factors, cytokines, and cells into the HAp implants improves the rates of implant integration to bone.

Tensile and compressive strength and fatigue resistance depend on the total volume of porosity. Porosity can be in the form of micropores (<1 mm diameter, due to incomplete sintering) or macropores (>100 mm diameter, created to permit bone growth).

Calcium phosphate bone cements first appeared in 1980s, provided injectability and in situ molding. The formulations include a variety of calcium phosphate compounds such as TCP and dicalcium phosphate, and the end product is based on a calcium deficient HAp (Best, et al. 2008).

3.5. Composite Implant Materials

Composite implants attract much attention in attempts to enhance the material properties (bioactivity, biodurability, resorbability, mechanical properties, etc.) and to engineer structures and materials for biomedical applications. Incorporation of Bioglass, and A-W glass ceramics within polyethylene for enhanced bioactivity and biodurability, carbon nanotube incorporation in HAp ceramics for enhanced mechanical performance, homogeneously distributed micron scale HAp particles extruded in a HDPE matrix used for the middle ear implants (HAPEX) are examples of successful applications of composites in medicine (Best, et al. 2008).

CHAPTER 4

PREPARATION OF HYDROXYAPATITE THIN FILMS

4.1. Plasma Spray Hydroxyapatite Coating

Ceramic oxides has been coated on metallic substrates by atmospheric plasma spraying since the mid 1950s. The general operating principle of a DC plasma gun is the formation of a continuous plasma by the continuous feed of an inert gas, most commonly Argon, being ionized by the plasma current between the anode and the cathode. The ionization is started by the cathode-anode arc. The Ar ions recombine with the electrons at the exit of the gun orifice, as shown in Figure 4.1, which evolves thermal energy (plasma enthalpy) increasing the temperature of the neutralized gas. Ceramic powder is fed into the gun at this hot neutralization zone. Higher temperatures can be achieved through the use of a bimolecular gas, such as H₂ and N₂, as the secondary plasma gas. The powder melts within the hot plasma flame while being discharged from the gun in a spray form, accelerated to the work substrate, and solidifies upon impact forming the required coating. The cathode and anode are water cooled internally. The drawing of a spray gun is depicted in Figure 4.2.

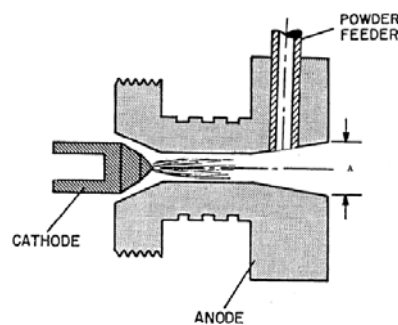


Figure 4.1. Schematic cross-section of non-transferred DC arc plasma spray gun with internal particle feed injector. The electrodes are water-cooled. The exit opening has a diameter A which is a design parameter. (Source: Herman, et al. 2000)

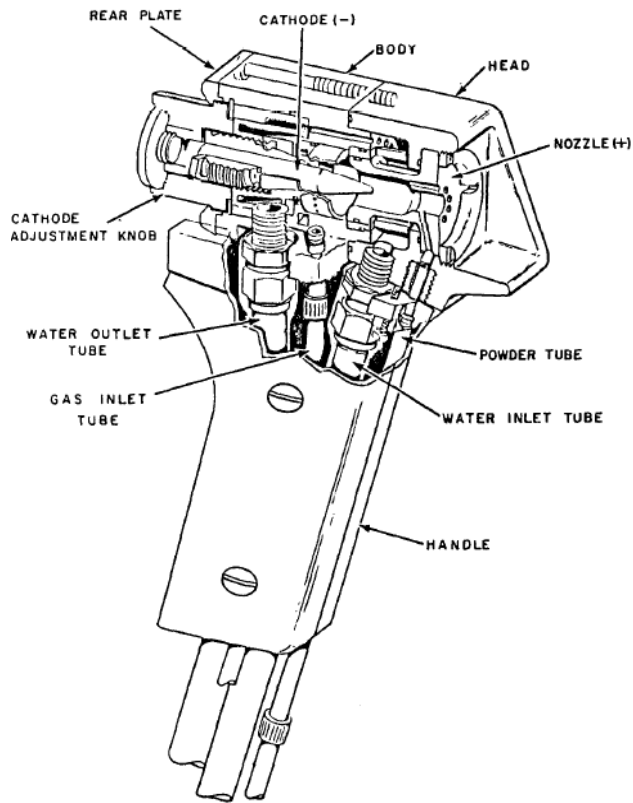


Figure 4.2. A view of the internal workings of a DC arc plasma gun.
(Source: Herman, et al. 2000)

Normally the plasma spray guns are power rated between 35 to 80 kW, and the powder capacity (Al_2O_3) ranges within 2-5 kg/hr or more. The energy content versus the temperature of various plasma gases is illustrated in Figure 4.3.

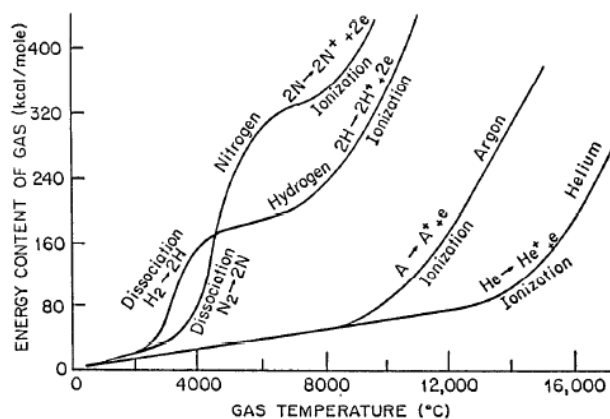


Figure 4.3. Energy content vs. gas temperature for a DC thermal plasma operating with different plasma gases. (Source: Herman, et al. 2000)

There are a number of interrelated parameters determining the characteristics of the ceramic coating. The gas type, pressure and flow rate, spray distance, gun design (especially exit orifice design), the particle shape, size, size distribution, and chemical homogeneity of mixed oxides. For example powder of flake-shaped particles do not flow into the plasma chamber continuously, and a pulsed irregular spray results causing inferior coatings (Herman, et al. 2000).

The plasma spray coatings of hydroxyapatite are applied most commonly to hip and knee prostheses, dental root implants and bone replacement plates. The mechanical, chemical, and biological performances of the coating are crucially dependent on the phase composition, crystallinity and microstructure as well as the adhesion to the implant surface. There are a number of serious drawbacks associated with the plasma spray coated HAp. The inhomogeneous chemical composition and crystallinity by the formation of phases such as amorphous calcium phosphates (ACP), α - and β -TCP, tetracalcium phosphate (Tetr CP), oxyhydroxyapatite (OHAp), oxyapatite (OAp), and CaO affect the biodegradation rate. Thermal and amorphous to crystalline phase transformation stress crackings, and delamination or even detachment of the coating layer of the already weak adhesion of the coating carry the potential of catastrophic in vivo failures. It is difficult or even not possible to coat porous and intricately shaped substrates. The in-flight evolution of the CaP phases based on a specific decomposition model is shown in Figure 4.4. The core is at 1570°C, and HAp is transformed into TCP and TetrCP phases between 1360-1570°C. OHAp, OAp, HAp are the stable phases in the partially molten particles (Herman, et al. 2000).

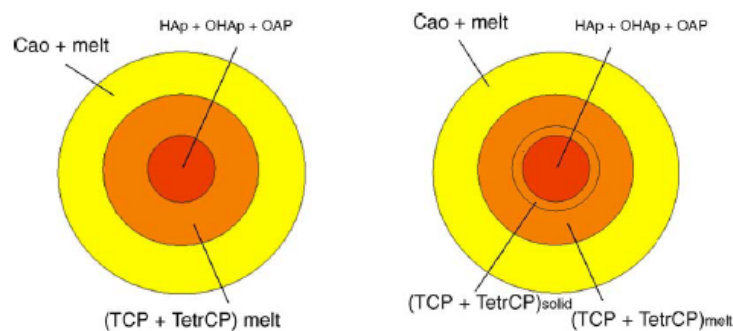


Figure 4.4. Schematic model of the thermal decomposition of a spherical hydroxyapatite particle subjected to high temperature in a plasma jet at a water partial pressure of 65.5 kPa (left) and at a water partial pressure of 1.3 kPa (right). (Source: Heimann 2006)

When the HAp particle impinges at the metal surface the clear and entirely neat phase separation shown in Figure 4.4 will be lost. The result is an extremely inhomogeneous calcium phosphate layer in which HAp, OHAp, TCP (α -TCP; β -TCP, whitlockite), TetrCP (hilgardite), CaO (oldhamite), and ACP of various compositions are interspersed on a nano- to microcrystalline scale. At the immediate interface to the metallic substrate a thin layer of ACP exists formed by rapid quenching of the outermost shell with heat transfer rates beyond 106 K/s. This thin layer has a specific significance as its high solubility in vivo and pronounced cracking by shrinking on transformation to HAp by rehydroxylation are considered one of the leading causes of coating delamination observed in clinical application. Hence, much research is directed towards deposition of well crystallized hydroxyapatite layers with a minimum content of ACP. However, there is a trade-off: too high a crystalline content may compromise coating performance in hip and dental prostheses owing to reduced adhesion strength and enhanced dissolution through a crack network. In Figure 4.5 the hypothetical sequence of events upon the impact of a semi-molten CaP particle accelerated supersonically on the substrate surface are shown.

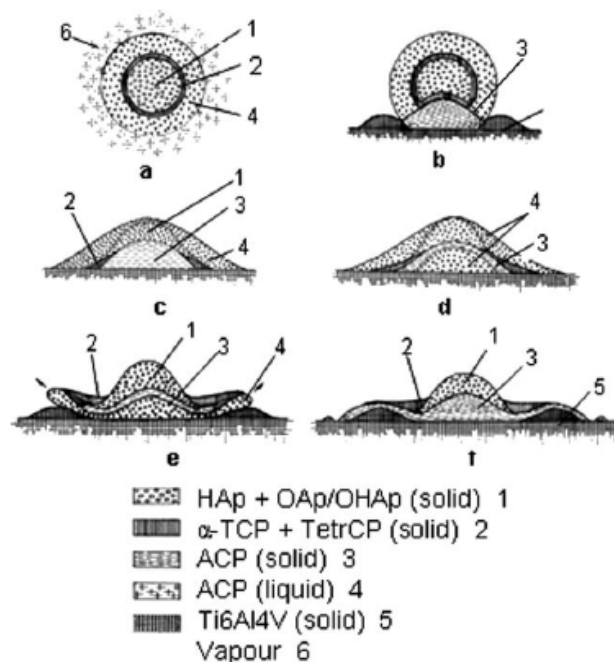


Figure 4.5. Sequence of events a to f occurring during deposition of a supersonically accelerated semi-molten hydroxyapatite particle impinging on a roughened Ti6Al4V substrate. (Source: Heimann 2006)

4.2. Sol-Gel Routes for Thin Film Preparation

A sol is a colloidal suspension of solid particles in a liquid (an aerosol is a colloidal suspension of particles in a gas). A colloid is a suspension in which the dispersed particles size range is 1-1000 nm. In this size range gravitational forces on particles are negligible and interactions are dominated by short range forces such as van der Waals attraction and surface charge electrostatic repulsion. A sol is distinguished from a solution by the existence of a separate dispersed phase of colloidal size range solid particles in a dispersing liquid medium, whereas a solution is a single phase of homogeneous mixture of solute atoms, molecules, or ions with the solvent atoms or molecules. The underlying property of a sol is its stability, that is, the suspended solid particles remain in the colloidal size range without aggregating to form precipitate or gel (Brinker and Scherer 1990).

Sols are prepared either by the oligomerization of monomeric precursors (starting compounds) which consists of a metal or metalloid element surrounded by various ligands (organic appendages not including another metal or metalloid atom, e.g. alkoxides) in non-aqueous medium, or by the solvation of metal cations (introduced as inorganic salts) in aqueous medium. The non-aqueous medium contains solvents other than or in addition to water, whereas aqueous medium consists of only water as the solvent. Sols are classified as polymeric sols for suspensions of branched macromolecules, and as particulate sols which contains suspensions of dense oxide particles.

A gel is a substance that contains a continuous solid phase (or skeleton) enclosing a continuous liquid phase both of which are of colloidal dimension in at least one direction. Continuity means that it is possible to travel through the solid phase from one side of the sample to the other without having to enter the liquid; conversely the same trip can be made entirely within the liquid phase. The wet gel which incorporates solvent is elastic.

The polymeric gel structure is in general fractal, conveniently to be described as tumbleweeds including void space, in the sense that it is not a dense structure. During gelation the fractal clusters grow until they begin to impinge on one another and eventually are linked together which is termed random bond percolation. As a result a single cluster (spanning cluster) forms extending throughout the sol at the gel point which is also called the percolation threshold.

Aging of the gel is the process of change in structure and properties after gelation. Aging involves the formation of the new links within the spanning cluster, and further condensation, dissolution, reprecipitation of monomers, oligomers and particles (since the gel is still within the sol), or phase transformations within the solid or liquid phases. Some gels exhibit spontaneous shrinkage called syneresis as new bond formations or attractions between certain molecular groups (on the same cluster), contract the network accompanied by liquid expulsion.

Drying is the process of evaporation of the sol liquid. If drying is performed under normal conditions liquid-vapor interphases are formed within the pores of the gel, which give rise to capillary pressures up to 200 MPa. This capillary pressure causes the shrinkage of the gel network by the internal stresses and strains. The resulting dried gel is called xerogel. If the wet gel is dried under supercritical conditions (inside an autoclave) no interphase exists within the gel pores and there is no capillary pressure, and the drying is accompanied by little or no shrinkage. This process is called supercritical (or hypercritical) drying, and the resulting gel is called an aerogel. Most gels are amorphous after drying, and crystallization or further densification of the gel is achieved by heat treatment.

The resulting gel microstructure can be tailored by the selection of precursor ligands, dispersing medium, drying surfactants, by adjusting the parameters for stabilizing the sol or for gelation such as temperature, pH of the sol (serves as the acidic or basic catalysis), ion types and concentrations, chemical modification agents, by selecting drying conditions, and by heat treatment parameters such as temperature, duration and the method of heating.

Thin film (normally less than 1 μm in thickness) preparation is one of the technologically important aspects of sol-gel processing, in which the sol, prior to gelation, is deposited on a substrate by one of the spinning, dipping, spraying processes, or by electrophoretic, thermophoretic, settling (sedimentation), or hybrid techniques. The rest of the process is quite similar to bulk sol-gel processes.

Thin film microstructure depends on the selection of precursor ligands, dispersing medium (solvent), agents modifying the solvent properties, and on the adjustment of the parameters for stabilizing the sol or for gelation such as temperature, pH of the sol (serves as the acidic or basic catalysis), ion types and concentrations, chemical modification agents, on the selection of drying conditions, and on the heat treatment parameters such as temperature, duration and the method of heating. These, in

turn, determine the size and extent of branching (or aggregation) of the sol species prior to deposition, and the relative rates of condensation and evaporation during film deposition which are related to the microstructural properties. For example, the pore volume may be varied from 0 to 65%, the pore size from less than 0.4 nm to more than 5.0 nm, and the surface area from less than 1 to more than 250 m²/gr.

Dip and Spin coatings are being extensively used for research purpose preparation and industrial manufacturing of thin films. Compared to the conventional thin film forming processes such as CVD, evaporation, or sputtering, sol-gel dip or spin coating requires considerably less equipment, and is potentially less expensive. Their major advantage, however, is the ability to precisely control the microstructure of the deposited film in terms of pore volume, pore size, and surface area.

The process involves the stages of immersion, start up, deposition, drainage, and evaporation as illustrated schematically in Figure 4.6, and 4.7.

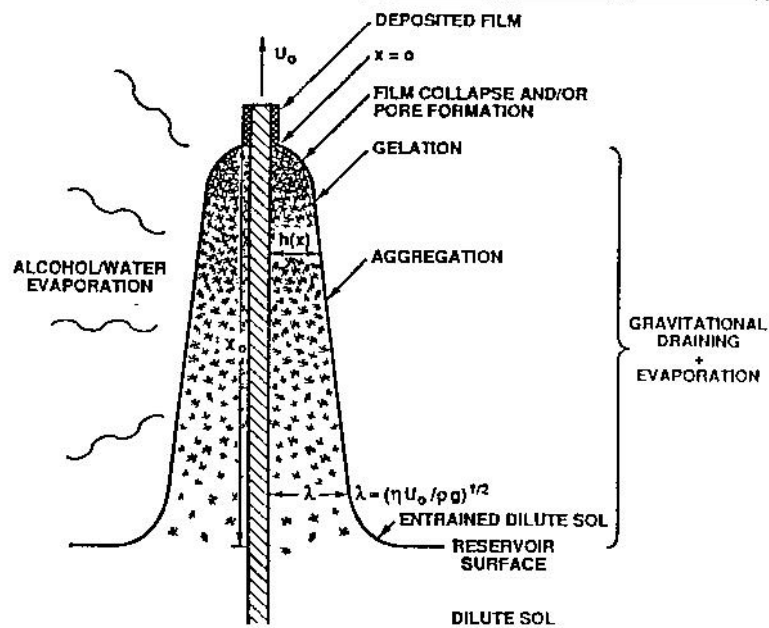


Figure 4.6. Schematic of the steady state sol-gel dip coating process depicting structural development of a gel film. (Source: Brinker and Scherer 1990)

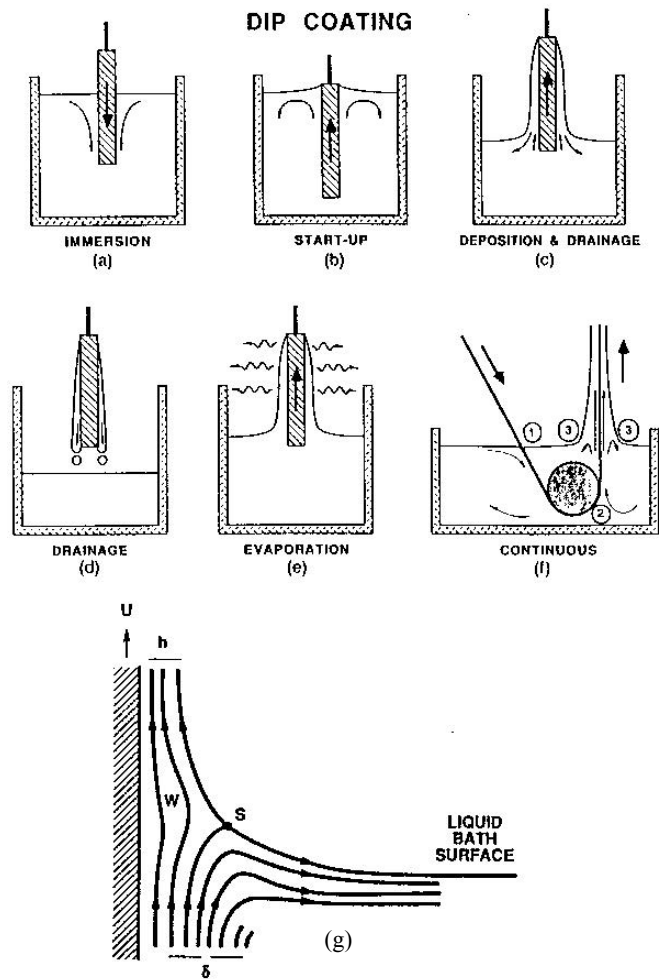


Figure 4.7. Schematic of the stages of the dip coating: (a-e) batch process, (f) continuous process, (g) liquid flow streamline pattern at area 3 of the continuous process, U is withdrawal speed, S is stagnation point, h is the thickness of the fluid film, δ is the boundary layer. (Source: Brinker and Scherer 1990)

The substrate moving upward entrains liquid, and the film thickness is governed by the streamline split position S (Figure 4.7g). The position of S is determined by the balance of the forces (1) viscous drag upward on the liquid by the moving substrate, (2) gravitational force, (3) resultant surface tension force in the concave meniscus, (4) inertial resistance force of the accelerated liquid, (5) surface tension gradient, disjoining or conjoining pressure force (important for films with thickness $<1 \mu\text{m}$). The film thickness decreases with the decreasing substrate retraction rate, and increasing extent of overlap of the deposition and the evaporation stages. The condensation continues during the film formation, and during the deposition and drainage stages, the relative condensation and evaporation rates determine the extent of further cross linking for the polymeric sols, and the particle packing density for particulate sols.

Spinnability is achieved, in general, under conditions in which the condensation rate and the extent of branching are low enough to allow the precursor monomers and clusters to highly concentrate (causing the viscosity to increase) without premature gelation. Thus the criteria for spinnability are also those expected to promote dense packing during film deposition.

Spin coater is an equipment that fixes the substrate or the wafer in place by application of vacuum from the bottom of the wafer through an adapter (vacuum chuck) conveniently designed for the shape and weight of the substrate. The substrate is rotated at desired acceleration, dwell, and deceleration rates and durations, which must be vibration free for successful coatings.

Spin coating process is examined in four stages: deposition, spin-up, spin-off, and evaporation as schematically illustrated in Figure 4.8.

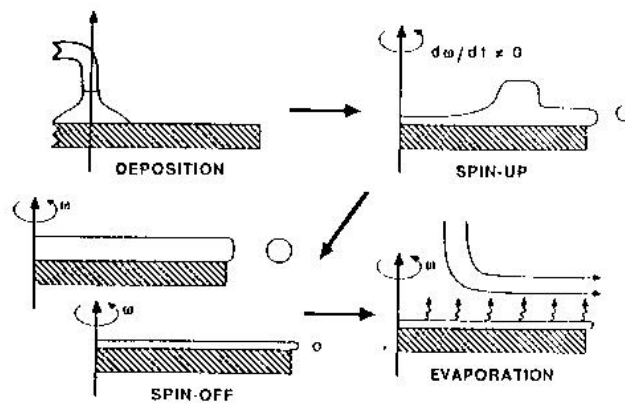


Figure 4.8. Stages of the batch spin-coating process.
(Source: Brinker and Scherer 1990)

During the deposition stage an excess of the coating liquid is dispensed onto the substrate or wafer. This can be done using a nozzle that pours out the coating sol, or it can be sprayed on to the surface. For many sols it is often beneficial to dispense through a submicron sized filter to eliminate particles that could lead to flaws. Another potentially important issue is whether the solution wets the surface completely during the dispense stage. If this is not the case incomplete coverage can result.

Spin-up stage is the acceleration of the substrate up to its final desired rotational speed. This stage is usually characterized by the outward radial flow, and expulsion of the fluid from the wafer surface by the centrifugal effect of the rotational motion. Because of the initial depth of fluid on the wafer, spiral vortices may be present briefly.

These would form as a result of the rotational velocity gradients in the fluid. Eventually the fluid becomes thin enough to be completely corotating with the wafer (velocity gradients in the fluid disappear), and the thickness of the film becomes uniform.

During the spin-off stage the rotational speed of the wafer is constant, and the viscous forces dominate the fluid thinning behavior. It is characterized by gradual uniform liquid thinning as the excess liquid flows to the perimeter and leaves as droplets. As the film thins, the rate of removal of excess liquid by spin-off slows down, since the thinner the film the greater is the resistance to flow, and since the concentration of the nonvolatile components increases raising the viscosity. When the fluid is thin enough the viscous shear drag exactly balances the rotational acceleration.

In the fourth stage evaporation takes place as the primary mechanism of thinning. The gelation of the film effectively starts since the sol species are forced into close proximity.

During the overall spin coating process dilute, noninteracting polymeric species that make up the coating bath are concentrated on the substrate surface by centrifugal flow accompanied by vigorous evaporation, and further condensation reactions. The solution concentration increases by a factor of 20 to 30, forcing the initially dilute precursors into close proximity. Correspondingly, the viscosity progressively increases due to the increasing concentration and further condensation reactions promoted by the increasing concentration. Polymer growth during the deposition stage occurs by monomer-cluster, cluster-cluster aggregation with trajectories ranging from Brownian diffusion (random walk motion) to ballistic (motion in linear path) in the later parts of this stage where strong convective motions exist due to evaporation. Gelation is referred as the moment when the condensing network is sufficiently “stiff” to withstand flow due to centrifugal force, yet is still filled with solvent. After that point further evaporation may cause the film to collapse due to capillary forces, reducing porosity. The overlap of stages from deposition to evaporation establishes a competition between evaporation (which compacts the structure), and the continuing condensation reactions (which stiffens the structure), thereby increasing the resistance to compaction.

Compared to bulk systems, in thin film formation aggregation, gelation, and drying occur in seconds to minutes during spinning rather than days or weeks. Nevertheless, precursor transport by Brownian diffusion remains dominant in the film up to about the last 10% of the drying time, as opposed to evaporation driven convection, while gelation occurs by random bond percolation (described in

Introduction) at a critical solid volume fraction of about 16%. The short duration of the deposition and drying stages causes films to subject considerably less aging (cross linkings within the gel) than bulk gels.

Tailoring the microstructure of thin films in terms of pore volume, pore size, and surface area, depends on the size and extent of branching of the sol particles or clusters, and the relative rates of condensation reactions and evaporation of the dispersing medium.

During deposition and drying (evaporation) stages the various species contained in the sol are rapidly concentrated on the substrate surface. Porosity (pore volume fraction) increases with the increasing extent of branching or aggregation prior to deposition, and with the increasing precursor or aggregate size. This low packing density is due to the steric constraints posed by the extensive branching and increasing size of the clusters, and the resulting structure resembles tumbleweed like assemblages. Conversely if the branching is weak, densely packed, low porosity films are formed, since particles or polymeric chains are able to interpenetrate as they are forced into close proximity by the increasing concentration due to evaporation, and an entangled worm structure is formed. For dense, monodisperse (a single, sharp particle size distribution) particles, the porosity increases with the decreasing particle size. Polydispersity of particles tend to lower the porosity. However, the pore size decreases with the decreasing particle or cluster size. Therefore, care must be taken while adjusting porosity and pore size together, since the former may decrease while the latter increases.

The possible structures of the sol precursors range from highly branched polymeric species (low density fractal particles) to dense (nonfractal) oxide particles that may or may not be aggregated. The branching, cluster size, and the size distribution depends on (and can be controlled by) the type of precursor ligands, dispersing medium, the adjustment of the parameters for stabilizing the sol or for gelation such as temperature, pH of the sol, counterion types, and concentrations, and chemical modification agents. For example, low temperatures, very low and very high pH values, low counter ion concentrations, substitution with massive, positively inductive molecules the branching and size of the sol species are low.

Condensation rate, relative to evaporation rate, is an important parameter on the film structure. Even highly branched structures interpenetrate if their condensation rate is low enough. However, the higher the cluster size and branching, the lower is the rate

of interpenetration. Low relative condensation rate combined with weak branching allows the sol species to highly interpenetrate in response to the decreasing solvent concentration (evaporation process) promoting dense packing and low porosity.

One important aspect of the film formation is the development of capillary pressure inside the pores, which may cause the film to shrink by the collapse of the pores, resulting in a denser structure. This phenomenon is related to the solvent surface tension (γ_{lv}), solid-liquid contact angle (θ), and the pore radius (pore size). These properties of the solvent can be modified by the introduction of agents such as surfactants prior to deposition. At the final stages of drying, the liquid-vapor menisci recede into the film interior, that is, into the pores, causing capillary pressures as high as 200 MPa. There is a synergistic (mutually reinforcing) mechanism for dense film formation, since dense packing (high interpenetration) reduces the pore radii, increasing the magnitude of the capillary pressure, consequently increasing the extent of the film collapse, resulting in more densification.

Surface area of thin films which may be important for sensor, and catalyst support applications can be controlled by the same parameters which are described above, since surface area increases with increasing porosity and decreasing pore size.

Further densification and crystal structure development can be achieved by heat treatment of the film. When the gel is heated to a sufficiently high temperature sintering takes place which reduces the porosity by the minute melting combinations of the solid phase. In amorphous materials, during sintering, atoms are transported by viscous flow, wherein crystal materials sintering involves diffusion which is a much slower process. For instance if densification is required sintering has to be completed before any crystal phase appears. For thin films formed on substrates, annealing at relatively lower temperatures is the preferred heat treatment method to minimize the internal stresses developed during drying and to achieve densification.

Temperature, duration, and method of heat treatment are important parameters. In general, initial heat treatment for annealing purposes in between multilayer coatings, is performed at 150-400°C, on a hot plate or with a pulsed heating system. After the multilayer deposition has been completed the final heat treatment is done at temperatures exceeding 500°C, for up to one hour duration in various types of furnaces.

4.3. Particulate Sols

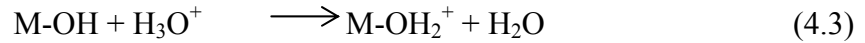
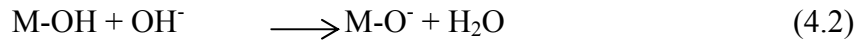
Particulate sols are defined as the systems that comprise dense (nonfractal) identifiable primary particles >1 nm. The stability of particulate sols depends on the balance of the attractive and the repulsive and/or steric hindering forces between the particles. The attractive van der Waals forces (dispersion energy) arise from the polarizabilities of the atoms by permanent dipole-permanent dipole (Keesom forces), permanent dipole-induced dipole (Debye forces), transitory dipole-transitory dipole (London forces) interactions. The fluctuating dipoles, namely London forces are mainly responsible for the long range attraction between colloidal particles. Since the dipoles in atoms fluctuate with a period of 10^{-16} s, for separations over 30 nm there is no net attraction, due to the fact that electromagnetic waves cannot traverse any farther within the fluctuation period. The van der Waals force between atoms is proportional to the polarizability of the atom and declines with the 6th power of the distance separating them. The attractive forces are also approximately additive and, hence, for infinite slabs separated by a distance h , the attractive potential is

$$V_A = \frac{-A}{12\pi h^2} \quad (4.1)$$

where A is the Hamaker constant which is a material property, and in general, of the order of 10^{-19} - 10^{-20} J. The DLVO (Derjaguin, Landau, Verwey, Overbeek) theory describes how electrostatic repulsion barrier brought about by ionic double layer (charge determining ions charging the surface of the particles, and counterions that are packed around the particle in the solution screening the full potential of the surface) avoids the particle aggregation due to attractive forces. An adsorbed thick layer of organic molecules also forms a steric barriers avoiding particles to come close enough for aggregation. In stable colloidal suspensions (sols) the electrostatic barrier of double layer repulsion is greater than $\sim 10kT$, where k is the Boltzmann constant, so that, the kinetic energy of the particles in Brownian motion cannot overcome the barrier (this corresponds to a repulsive zeta potential, $\zeta \geq 30$ -50 mV to be defined later).

The pH at which suspended particles are neutrally charged is called the point of zero charge (PZC). For hydrous oxides at $\text{pH} > \text{PZC}$ Equation 4.2 predominates and the

particles are negatively charged, whereas at $\text{pH} < \text{PZC}$ Equation 4.3 predominates giving the particles positive charges.



In an electric field charged colloidal particles move toward the oppositely charged electrode carrying the adsorbed counterions with a delimiting border termed slip plane or plane of shear (it separates the region of the fluid moving with the particle from the free flowing region). The potential at the slip plane is termed zeta potential, ζ , which is, in general, smaller than the surface charge potential due to the screening effect of counterions within the slip plane. The pH at which $\zeta=0$, is termed the isoelectric point (IEP). In general, PZC and IEP have different values, though for practical purposes they are used interchangeably (Brinker and Scherer 1990).

4.4. Sol-Gel Methods for Hydroxyapatite Coating

In the literature there exists numerous applications of hydroxyapatite thin film coatings on various substrates. In general two routes are used to prepare coating suspensions or sols. The inorganic route that corresponds to particulate sol method is shown schematically in Figure 4.9. It involves the preparation of a CaP precipitate by the mixing of precursor solutions of calcium nitrate tetrahydrate and ammonium hydrogen phosphate solutions in the molar ratio $\text{Ca/P}=1.67$. The pH is adjusted to the vicinity of 12 with concentrated ammonium hydroxide. The precipitate is dispersed in water of ethanol, and additives such as polyethylene glycol, and glycerol are blended with the suspensions and ultrasonicated to obtain suspensions for dip coating or spin coating (Mavis and Tas 2000, Babu 2004). The inorganic route can also be utilized without CaP precipitation, and dip coating is achieved in the solution (Gan and Pilliar 2004, Gan, et al. 2005, Cavalli, et al. 2001).

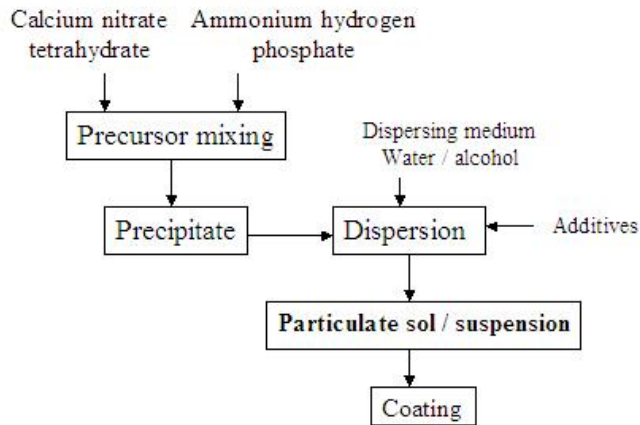


Figure 4.9. An inorganic route for the preparation of particulate sol hydroxyapatite coatings.

The organic route corresponds to polymeric route lacking the presence of any dense particles >1 nm as summarized in Figure 4.10. Calcium nitrate tetrahydrate, triethyl phosphite are used as Ca and P precursors. Triethyl phosphite is first hydrolyzed for 24 hrs, and the calcium nitrate tetrahydrate dissolved in absolute ethanol dropwise added to the hydrolyzed triethyl phosphite solution. The sealed solution was aged at 40°C for 4 days. The aged sol was diluted with absolute ethanol (2 parts sol and 1 part ethanol) and further aged for two days to be ready for dip coating (Gan and Pilliar 2004, Gan, et al. 2005, Liu, et al. 2002) Slight modifications in the general route and used materials were applied by several researchers (Wang and Chen 2008, Weng 1999, Weng and Baptista 1998).

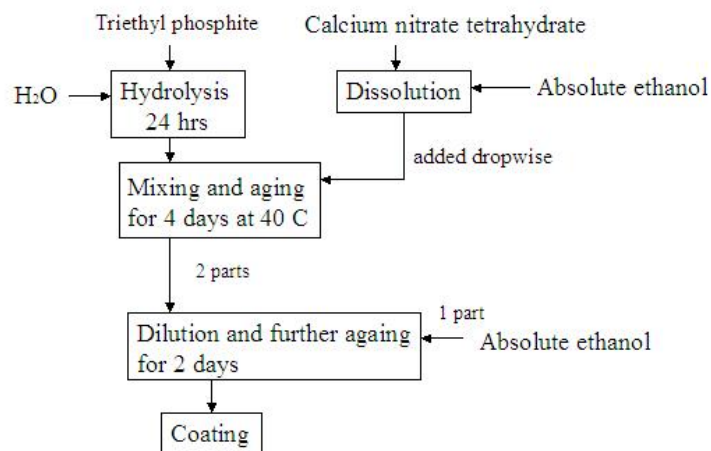


Figure 4.10. An organic route without the presence of any dense particles $>1\text{nm}$ for the preparation of hydroxyapatite particles.

The surfaces of the Ti6Al4V alloy (Mavis and Tas 2000), stainless steel, 316L (Babu 2004) substrates are ground to various grits with SiC paper, or polished (Gan and Pilliar 2004), or sand blasted for strong adhesion.

In general the characterization techniques for microstructure are TFXRD (thin film x-ray diffraction), DRIFT (diffuse reflectance infrared Fourier transform), XPS (x-ray photoelectron spectroscopy), SEM/EDX (scanning electron microscopy/energy dispersive x-ray analysis), TEM (transmission electron microscopy), AFM (atomic force microscopy). Some of the mechanical tests are shear lag strain method for interfacial shear strength, tensile testing for adhesion strength, nanoindentation for adhesion strength, microindentation for residual shear stress, surface hardness, surface roughness, circular ellipsometry for film thickness.

CHAPTER 5

HYDROXYAPATITE-PROTEIN INTERACTIONS

5.1. Hydroxyapatite-Silk Protein Interactions

Silk from silkworm (*bombyx mori*) is a protein polymer that consists of fibrous fibroin (70%) bound in a sericin matrix. Silk fibroin and silk sericin are easily separable by the degumming process. Silk fibroin is highly biocompatible, and combines unique mechanical and biochemical properties. In its fiber, mesh, foam, and film forms, silk fibroin is utilized in controlled release, as biomaterial (e.g. sutures, artificial skin and tendon), and in designing scaffolds for tissue engineering to be employed in vitro and in vivo bone and ligament formation (Altman, et al 2003).

Silk fibroin is characterized by the repetitive primary sequence of amino acids of a long chain of 350 kDa, connected to a shorter chain by disulfide linkage. The long chain consists of 12 crystallizable domains of Gly-Ala-Gly-Ala-Gly-Ser, $[\text{Gly-Ala}]_n$ -Gly-Tyr, $[\text{Gly-Val}]_n$ -Gly-Ala ($n=1-8$), followed by 11 amorphous domains of mainly Gly-Ala-Gly-Ser, Gly-Ala-Gly-Ala-Gly-Ser. These amino acid sequences are hydrophobic, only Ser and Tyr with hydroxyl groups provide a water affinity, and the negatively charged R groups of Glu and Asp at the chain ends impart the polyelectrolyte nature. The short chain of 25 kDa consists of a nonrepetitive amino acid sequence, and hydrophilic in nature. The highly repetitive long chain leads to an orderly secondary structure of water insoluble β -sheets (Hossain, et al. 2003, Yamada, et al. 2001). The mechanical properties of strength and toughness of the fibroin fibers reside in the numerous, nanoscale, oriented β -sheet crystals, their fuzzy interfaces with the less crystalline domains, and the shear alignment of the chains (Altman, et al 2003).

Fibroin in aqueous solution at neutral pH assumes the random coil structure, and transforms to metastable α -helix structure (silk I) which, in turn, is easily convertible to β -sheet structure (silk II), under adjustable process conditions of solution concentration and temperature, quenching temperature, drying temperature and time, electric field intensity, pH, presence of certain enzymes (Putthanarat, et al. 2002), methanol treatment (Nam and Park 2001). The IEP of fibroin was reported to be 3.8-3.9, and water soluble α -helix structure is favored for $\text{pH}>6$, since the negative charges cause a strong

repulsion between peptide chains. The peptide chains assume a stable β -sheet structure through hydrophobic interactions at $\text{pH} < 4.5$ with the decreasing negative repulsive charges, together with an increase in gelation tendency (Hossein, et al., 2003). In practice, the transformation to β -sheet structure is affected by drying at over 40°C (Magoshi, et al. 2000), and methanol treatment (Nam and Park 2001).

Fibroin is regarded as biodegradable due to losing its tensile strength *in vivo* in one to two years. Silk fibroin is known to offer versatility in matrix scaffold designs in which mechanical performance, and rate of degradation matches the rates of tissue ingrowth including bone, ligaments, tendons, blood vessels, and cartilage. Silk fibroin is known to be highly thrombic when in contact with blood because of its binding capacity of the blood clotting cascade proteins of fibrin and fibrinogen (Altman, et al. 2003).

Sericin, a glue like protein exhibits high hydrophilicity due to its high content of hydrophilic amino acids with the uncharged but polar R groups, including Serine (35%) and Threonine (10%) (Teramoto, et al. 2007). Its secondary random coil structure is water soluble, while transition to the β -sheet structure by dehydration (drying at 40°C , or by treating with methanol) renders it water insoluble (Nam and Park 2001; Lee, et al. 2003). The abundant hydroxyl groups in sericin play a crucial role in its structural formation. The hydroxyl side chains of Ser and Thr residues in the β -sheet structure which remain rigid after hydration were assumed to clump adjacent β -sheets by hydrogen bonding at their OH groups. Hence, Ser and Thr linkage sequences in the crystal domain are responsible for forming β -sheet aggregates and generating the structural stability of sericin as depicted in Figure 5.1 (Teramoto, et al. 2007).

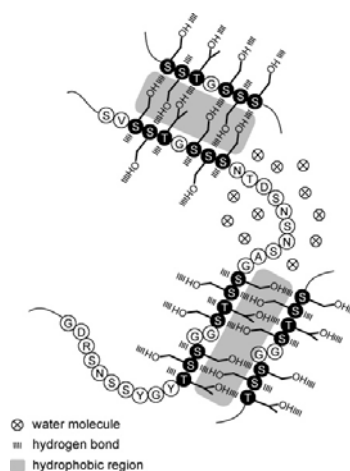


Figure 5.1. In the sericin structure Serine and Threonine linkage sequences in the crystal domain forming β -sheet aggregates. (Source: Teramoto, et al. 2007)

Mimicking the natural bone the HAp-collagen nanocomposites were prepared by the precipitation of HAp nanocrystals on collagen type I utilizing the ability of collagen to induce mineralization. The cost, difficulty to control cross-infection, poor definition of commercial sources are the drawbacks of the practical uses of collagen for the purpose (Chang, et al., 2003). Silk fibroin was reported to regulate the mineralization of hydroxyapatite nanocrystals as a template, in efforts to develop alternative materials to collagen (Kong, et al., 2004) (the other reported alternatives are gelatin (Chang, et al., 2003), chitosan (Zhao, et al., 2007), poly(D,L-lactide) (Deng, et al., 2001), chondroitin sulfate (Rhee, et al., 2001), hyaluronic acid (Nemoto et al., 2004)). It was shown that (Kong, et al., 2004) the calcium phosphate crystals precipitated in the aqueous solution of silk fibroin at pH=8, and at room temperature. The XRD analysis of the deposits collected at different incubation times indicated that fibroin significantly promoted HAp crystal growth. The FTIR analysis revealed that HAp crystals were carbonate substituted. The strong chemical interaction between the fibroin and HAp was evidenced by the blue shift of amide II peak, corresponding to N-H in plane bend and C-H stretch, of fibroin protein, from 1517 to 1539 cm^{-1} . The interaction was most probably between the calcium ions of HAp and amide groups of fibroin. TEM images showed that fibroin and HAp crystals are compounded in the form of mineralized nanofibrils of rod shapes 2-3 nm in diameter. The electron diffraction patterns indicated polycrystalline HAp phase with 002 orientations. The precipitated HAp crystals in the absence of fibroin were much larger (Kong, et al. 2004).

The hydroxyl, carboxyl, and carbonyl groups of fibroin have the potential to induce the mineralization of HAp crystals. The aspartate, arginine, glutamate residues are not uniformly distributed along the peptide chains but are arranged in polar clusters inducing a surface charge distribution that have an affinity for calcium ions, which in turn provide, a local concentration of Ca^{2+} leading to nucleation. The reason for the deposition of HAp in the form of tiny crystals on fibroin is, therefore, the regular surface arrangement of nucleation sites distributed on a molecular scale (Kong, et al. 2004).

It was shown that (Kong, et al., 2006) the concentration of fibroin strongly affected the kinetics of biomineralization of CaP. The extinction (of reactants) versus time monitored by a UV/vis spectroscopy method, the plateau level in the extinction and the start of calcium phosphate deposition decreased with the increasing fibroin concentration, indicating an increase in the deposition rate of CaP compounds. The

width of the calcium phosphate compounds was 100 nm in the presence of fibroin while it is 200 nm in the absence of it. It was demonstrated that fibroin could provide active sites for the nucleation and growth of crystals within nanoscaled spaces during the mineralization. The fibroin fibrils assembled in a supramolecular nanoscaled framework construct reminiscent of collagen fibrils. The increasing concentration of fibroin, in a dense three dimensional network, delimited the crystal growth to larger sizes to some extent. However, the relation between the deposition kinetics and the morphogenesis of calcium phosphate was not conclusive. It was also monitored by XRD studies that sudden increases and decreases in the extinction curve pointed out to the formation of amorphous CaP compound phases which were transformed to HAp and brushite crystalline forms accelerated by the increasing concentration of fibroin leading to phase separation (Kong, et al. 2006).

The relation between the structure of sericin and hydroxyapatite deposition under biomimetic conditions (metastable calcium and phosphate solution; 1.5 SBF) was reported (Takeuchi, et al. 2005). It was observed that sericin effectively induced heterogeneous nucleation of HAp in the high molecular weight, β -sheet secondary structure. Sericin films were prepared with the sericin extracted from raw silk by autoclave degumming at 105°C (MW=159 kDa) and 120°C (MW=43 kDa). When the extracted sericin was aged at 4°C for 2 weeks the proportion of the β -sheet structure increased for both, the highest proportion being in the 105°C extract. The sericin film with the highest β -sheet structure and higher molecular weight induced heterogeneous HAp nucleation. Previously carboxyl groups in the sericin structure were reported to be effective in HAp nucleation in self assembled monolayers (Tanahashi and Matsuda 1997). The number of carboxyl groups in sericin was higher than in fibroin (Komatsu 2000), and the β -sheet structure of sericin molecules consisted of a perpendicular arrangement of 10% of the carboxyl groups to the plane of the sheet providing nucleation sites for HAp (Takeuchi, et al., 2005). The periodic arrangement of repeating functional groups provides a periodic charge distribution on the surface that induces electrostatic affinity, especially, for the Ca^{2+} ions. The characteristics of the surface charge periodicity for effective HAp nucleation have yet to be studied.

5.2. The Effect and Delivery of Growth Factor and Cytokine for Bone Fracture and Peri-Implant Healing

Bone has the ability to repair and regenerate itself if the extent of damage is below a critical size. If the damage is extensive autografts, or allografts will be required to repair the damaged bone area. However, bone implants are required due to the difficulty of harvesting sufficient material, increased surgical time and cost, and donor site morbidity in the case of autografts, and the risk of pathogenic transmission, and immune response in the case of allografts. The failure rates are unacceptably high which are 13-30% for the former, and 20-35% for the latter (Winn, et al. 1998). Fracture repair, peri-implant healing, and bone remodeling in endosseous sites are very similar histodynamic phenomena, with the difference of the presence of extravasated blood between the healing and remodeling bone. Bone fracture and surgical implant plantation are marked by a loss of continuity in the bone tissue. The histodynamics of healing involves the interactions between the critical physical, molecular, and cellular elements inducing the sequence of events such as cell recruitment, attachment, expansion, differentiation, interactions of cellular elements with extracellular matrix proteins and endogeneous molecules, leading to the reconstitution of continuity in the bone tissue.

Secondary bone union of a fractured bone tissue, and endosseous implant integration (the bone bonding to the implanted material surface within a continuous bone tissue) comprise three phenomenologically distinct mechanisms which are osteoinduction, de novo bone formation or contact osteogenesis, and bone remodeling (Davies and Hosseini 2000). **Osteoinduction** is the event that involves the recruitment of potentially osteogenic cell populations including vascular pericytes, stromal cells, undifferentiated mesenchymal stem cells (MSC) from the bone marrow and adjacent tissues to the wound site. Cytokines from the disrupted matrix, and chemoattractive active proteins from degranulation of platelets in the hemorrhage zone signals and guides MSCs to migrate through the resolving blood clot to the surface of bone fragments or implant within the damaged site. MSCs are converted to preosteogenic cells on the site, which in turn transformed into osteoblastic, chondroblastic, or fibroblastic differentiated cell lineages depending on the local fracture environment, under correct and orchestrated cellular, humoral (endocrinal and immunological), and

mechanical stimulus (Kraus and Kirker-Head 2006). The participation of the already existing osteoblasts and osteocytes in the healing process is minor as compared to the total osteoinductive activity. In the case of endosseous peri-implant healing, fibrin in a hyaluronan matrix forms a degradable, three dimensional meshwork of fibrin clot that adheres on the implant surface and provides a scaffold for the cascade of cell migration and differentiation. The traction of the migrating cells result in contractile forces transduced to the implant surface. This causes the gradual detachment of the anchored fibrin clot, a phenomenon that overlaps with bone tissue formation. ***De novo bone formation or contact osteogenesis*** is the early endosseous healing that involves of the formation of woven bone (as opposed to lamellar bone) as a fast response to wound. The formation of non-collagenous cement line is a key step in the bone bonding to implant surface. The cement line is the histological interface that provides the necessary interdigitation and interlocking of the old and new bone tissues, and the new bone tissue and implant surface. ***Remodeling*** is a relatively slow process by which the lamellar structure of osteonal bone tissue is reconstructed from the random structure of the earlier fast apposed woven bone.

The osteoinductive class of materials is known as bone morphogenetic proteins (BMP) and BMPs 2-15 are classified within the transforming growth factor, TGF- β superfamily of growth factors (Winn, et al. 1998). BMP-2, -4, -6, -7, -9 have been shown to have a clear role in bone-inducing. BMP-3 and -3b function as negative regulator (inhibitor) of osteogenesis (Bessa, et al. 2008). During bone formation, fracture or peri-implant healing the concentrations of BMPs are regulated according to specific temporal sequences, as well as are expressed in site-specific patterns. After injury BMP-2 appears in day 1, BMP-14 (effective in chondrogenesis and angiogenesis) peaks around day 7, and BMP-3, -4, -7, -8 are expressed after 2 weeks (Bessa, et al. 2008). The extracellular retention and modulation of BMP, intracellular BMP signaling and gene transcription for cell proliferation or differentiation, is shown in Figure 5.2 schematically. The enhanced heparin binding sites on BMP-2 was reported to give way to enhanced bone formation by retaining the BMP-2 in the extracellular matrix for longer times. Noggin, chordin, and gremlin are antagonists that function extracellularly by binding to BMP and modulating and mediating its eventual bone-inducing activity. Intracellular pathways for gene transcription starts with the binding of BMP to serine-threonine kinase receptors on the cell surface which phosphorylate the signal transducing protein molecules (R-Smads). Two R-Smads and one Co-Smad molecules

form a heterotrimeric complex which is translocated into the nucleus and modulates gene transcription in cooperative interaction with other gene transcription factors. Smurfs are other protein molecules that induce ubiquitination or degradation of Smads providing control mechanisms for BMP signaling. Mitogen-activated protein kinase (MAPK) provides alternative pathways for signal transduction of BMPs. The characterized intracellular MAPK pathways in mammalian cells are the c-Jun-NH₂-terminal kinase (JNKs) and the p38. The X-linked apoptosis inhibitor (XIAP) links the BMP receptor signaling to TGFβ₁-activated tyrosine kinase 1 (TAK1) and activates JNK and p38 which in turn cooperatively interact with Smads, thus interfering with osteogenic differentiation. When translocated in the nucleus Smads bind to specific DNA binding proteins (Runt-related transcriptional factors, Runx) and interact with specific DNA sequences leading to cell differentiation or proliferation. Runx2-induced transcription lead to the differentiation of mesenchymal progenitor cells into osteoblasts, whereas Id proteins lead to cell proliferation (Bessa, et al 2008).

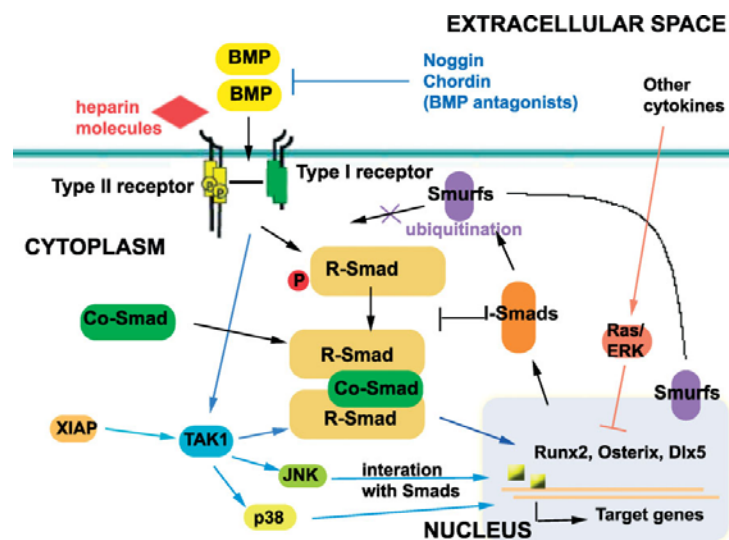


Figure 5.2. Schematic of the extracellular and intracellular BMP signaling pathways. (Source: Bessa, et al. 2008)

Bovine collagen (Miller and Rhodes 1982), demineralized bone matrix (Damien, et al. 1994), calcium phosphate ceramics (Ohgushi, et al. 1993), bioglasses (Ducheyne, et al. 1994), organoapatites (Stupp and Ciegler 1992), polylactic homopolymers (Hollinger and Leong, 1996), poly(lactic-co-glycolide) polymers (Mikos, et al. 1993), polyanhydrides (Lucas, et al. 1990), organophosphates (Reiner and Kohn 1997), and polyphosphazenes (Laurencin 1993) are used as BMP carrier osteoconductive scaffold

materials and are engineered to induce osteoinduction for the accelerated bone tissue formation, and healing, as practical and functional alternatives to conventional therapies. The yield of BMPs from natural sources is so low that (1-2 $\mu\text{g}/\text{kg}$ cortical bone) DNA recombinant technology is used to produce and purify viable amounts (Clokie 2000, Bessa 2008). In 2002 Food and Drug Administration (FDA) approved the use of rhBMP-2 and rhBMP-7 loaded in absorbable collagen sponge carriers for spinal vertebrae fusion and long bone non-union treatment (Bessa 2008).

Hydroxyapatite, and other CaP ceramic coatings are used to impart excellent biocompatibility to metallic implant devices (Delecrin, et al. 1994; Lind, et al. 1999), with good clinical results (Daculsi, et al. 2002). The technology to use CaP compound coatings as BMPs carrier is under development by imparting enhanced affinity between hydroxyapatite and proteins. Another aspect of enhanced affinity of implant surfaces to the growth factors, and cytokines is the ability to increase their concentration locally in the wound site, which in turn may result in faster and augmented localized osteoinduction for an accelerated healing process. The initial interaction of the biological environment with the implant surface is the adsorption of proteins and other macromolecules. The interaction of the cells with the adsorbed proteins follows, forming an interdigitated and interlocked bone tissue on the recipient implant surface (Davies and Hosseini 2000). In most of the studies bovine serum albumin (BSA) is used as a model protein to mimic the behavior of BMPs (Bansal, et al. 2005).

5.3. BSA Adsorption onto Hydroxyapatite

HAp, with its multiple binding sites (or zones), may induce cooperative adsorption of adsorbates such as proteins, especially of flexible structure and that have multiple interaction groups. The cooperativity in adsorption is the result of multiple matching interactions between the adsorbent and the adsorbate, and the extent that adsorbate protein molecules can deform to augment the fortifying interactions. The deformation can be induced by the particular adsorbent surface charge distribution and the lateral interactions between the adsorbate protein molecules; the degree of cooperativity can be influenced positively or negatively as a result. The Langmuir equation normally represents the adsorption phenomena of gaseous adsorbates onto adsorbents, and previously used for protein adsorption on HAp (Wassel, et al. 1995), however, it does not include the cooperative adsorption effect as in the case of protein

adsorption. Therefore, Hill equation is used to represent the protein adsorption phenomenon and to demonstrate the degree of cooperativity for protein adsorption:

$$\frac{\theta}{(1-\theta)} = K[P]^n \quad \text{or} \quad \log \frac{\theta}{(1-\theta)} = \log K + n \log [P] \quad (5.1)$$

where θ is the fractional saturation of the adsorbate surface, $[P]$ is protein concentration in the solution, K is the Hill constant, and n is the Hill coefficient which in fact is a measure of the degree of cooperativity. In general the degree of cooperativity is defined in the ranges $n > 1.5$ as positive, $1.5 > n > 1$ as partially positive, $1 > n > 0.5$ as partially negative, and $n < 0.5$ as negative. The corresponding matching (or non-matching) interactions that determine the degree of cooperativity, and the effect of protein flexibility on adsorption are depicted schematically in Figure 5.3.

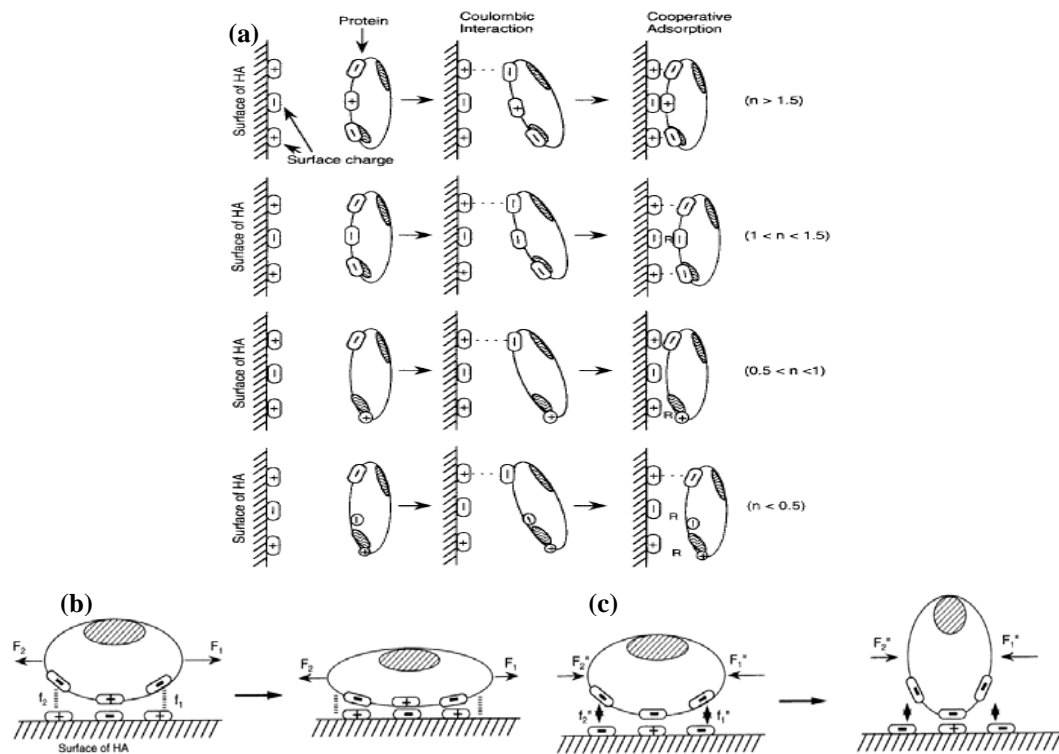


Figure 5.3. The schematic representation of HAp-protein surface interactions, (a) the charge distributions on the adsorbent surface and adsorbate interaction groups that determine the degree of cooperativity, (b) and (c) the increasing degree of cooperativity by the deformation of a flexible protein molecule brought about by the matching, or non-matching adsorbent surface charge distribution, respectively. The deformations may be also due to the lateral interactions between adsorbate protein molecules. (Source: Luo and Andrade 1998)

The Hill plots of protein adsorption onto HAp, in general, have 3 zones with distinct n values, depending on rigidity or flexibility of protein molecules. The adsorbate lateral or adsorbent surface driven deformations become more effective with increasing protein concentration in determining the degree of cooperativity. The IEP, pH, and ionic strength are also the determining factors, since they affect charge distribution and Θ_c of the adsorbent and the protein molecules.

The cooperative adsorptions of bovine serum albumin (BSA), hen-egg lysozyme (LSZ), human holo-transferrin (HHT), and bovine milk lactoferrin (BML) onto hydroxyapatite were examined by Hill plots (Luo and Andrade 1998). BSA has an IEP of 4.6, a flexible structure, and a medium size (94x94x40 Å) with three domains (Luo and Andrade 1998). The BSA adsorption on HAp was examined in three different suspension media with pH and ionic strength as parameters. In all of the media the Hill plots showed three regions of cooperativity. The degree of cooperativity decreased with increasing pH since the negative charges on both the adsorbent and the adsorbate increased; while it increased with increasing ionic strength at higher pH values since the surface charges are screened more effectively by the increasing concentration of counter ions. More importantly with the increasing concentration of BSA the degree of cooperativity increased drastically from negative or partially negative to positive values showing the effect of flexible molecule as in the case of Figure 5.3b especially by lateral interactions between the protein molecules.

Competitive adsorption of BSA and collagen, on hydrophobic and hydrophilic silicon surfaces, were studied by atomic force microscopy (AFM) and imaging ellipsometry methods (Ying, et al. 2003). The hydrophobic surface adsorption of BSA and collagen, separately as single components, was approximately double of the adsorption on hydrophilic surface. In the competitive case BSA was preferentially adsorbed on the hydrophobic surface (100%), while collagen was adsorbed on the hydrophilic surface (96%).

The competitive adsorption of BSA and bovine fibrinogen (Fg) was utilized to assess the surface hemocompatibility of implants (Ombelli, et al. 2005). A quantitative HPLC method was developed to determine the surface coverage of multiple adsorbed proteins. Relative to untreated silicon, dextranized silicon surface inhibited both of the BSA and Fg adsorption to the extent of reducing the surface coverage by 76 and 60%, respectively.

The adsorption affinities of BSA and lysozyme (LSZ) to HAp were evaluated by a desorption and two step adsorption method (Kandori, et al. 1998). The adsorption of BSA was found to be irreversible, while the pre-adsorbed LSZ was slightly desorbed. This was most probably due to the weak electrostatic attraction of LSZ on the phosphate ions at the ac and bc faces of HAp. On the other hand BSA was adsorbed strongly on the positive calcium ions on the same crystalline faces. The LSZ amount adsorbed was significantly increased on the pre-BSA adsorbed surfaces. The adsorption amount of BSA did not change on the pre-LSZ adsorbed surface. The LSZ adsorbed on the pre-BSA adsorbed surface was not desorbed indicating a strong electrostatic interaction between the proteins, and since the surface coverage of BSA was extensive, LSZ adsorption was enhanced. However the BSA adsorption on the LSZ pre-adsorbed surface was not enhanced due to the low surface coverage of LSZ.

The separate chemical, and topographical effects, on the serum protein adsorption and human osteoblast adhesion on calcium phosphates were studied (Santos, et al. 2008). The effectiveness of surface energy of calcium phosphates on protein adsorption and cell adhesion was evaluated. The dense phosphate ceramics, HAp and β -TCP provided surfaces with different chemistry, and nano-roughness. Some substrates were sputter gold coated to mask the surface chemical effects without changing the surface topography. The results indicated that the surface topography was the more important variable than the chemical structure for protein adsorption. The seeding efficacy of osteoblasts did not change with the surface chemistry or topography, however, the cell spreading was inferior on the β -TCP, due to its chemical structure. It was observed that albumin and fibronectin adsorption decreased with the decreasing polar component of the surface energy of gold coated samples, however, the cell adhesion enhanced.

5.4. Hydroxyapatite-Protein Interactions by Molecular Modeling

Theoretical chemistry uses mathematical tools and the laws of physics to explain or predict chemical phenomena, especially chemical reactivities, and involves the studies of electronic structure of atoms and molecules by quantum chemistry, molecular dynamics by classical mechanics and electromagnetism, and statistical mechanics. The main branches of theoretical chemistry can be classified as, quantum chemistry (the application of quantum mechanics to chemistry), molecular mechanics (the modeling of

intra- and inter-molecular interactions by potential energy surfaces, and sum of interaction forces by classical physics), molecular dynamics (the modeling of the motion and interactions of assemblies of atoms and molecules by classical physics), computational chemistry or molecular modeling (synonyms; the application of computer codes to chemical problems in general, and especially simulating atomic and molecular structures and their interactions and motions in clusters by quantum chemical and molecular dynamics techniques), theoretical chemical kinetics (the explanation and prediction of the behavior of dynamic molecular systems, especially the chemical reactivities by mathematical tools, and the laws of physics), mathematical chemistry, and cheminformatics.

The computational chemistry (or molecular modeling) techniques are, in general, capable of predicting:

- molecular energies and structures,
- transition state energies and structures,
- bond and reaction energies,
- molecular orbitals,
- multipole moments,
- atomic charges,
- electron density surfaces and electrostatic potentials,
- vibrational frequencies,
- IR and Raman spectra,
- NMR properties,
- polarizabilities and hyperpolarizabilities,
- thermochemical properties,
- reaction pathways,

in the gas phase and in solution, in the ground or excited state (Foresman and Frisch 1996). Computational chemistry is rather an adjunct than a replacement for experimental observations. It can provide information about reaction pathways through predictions on transition states which are impossible to observe, and can provide explanations of observed phenomena.

In computational chemistry, the molecular structure and reactivity are dealt with two main approaches: molecular mechanics and dynamics (classical mechanics and electromagnetism), and electronic structure methods (quantum chemistry). In both approaches, energy (E) associated with a given structure of nuclei and electrons (spatial

arrangement of atoms), geometry optimizations as the lowest energy associated with respect to atomic position vectors, \mathbf{r}_i , or molecular structure ($\sum_i \partial E / \partial \mathbf{r}_i = 0$), vibrational frequencies resulting from interatomic motion within the molecule ($\sum_i \partial^2 E / \partial \mathbf{r}_i^2 = 0$).

The molecular mechanics methods use the laws of classical physics and do not explicitly involve electrons. Electronic effects are implicit in a particular force field with parameter sets defining force constants (the values used in the equations relate atomic characteristics to energy components and bond length and angle structural data). The force field between a group of atoms consists of bonding interactions which are bond stretching, angle bending, torsion angle, cross terms correlating the first three terms (a decreasing bond angle causes an increase in bond length), and nonbonding interactions which are van der Waals, electrostatic and hydrogen bonding interactions. The atoms and bonds are modeled as balls connected with springs that obey Hook's law. Therefore molecular mechanics allows inexpensive computations (CPU requirement and computation time), can even be used for systems as large as containing many thousand atoms. The force fields SYBYL (simple), MMFF (more complex) are among the most common force fields. This approach cannot be used to describe molecular properties that require subtle electronic details, and for systems involving bond breakage and formation (Hehre 2003).

The electronic structure methods use the laws of quantum mechanics which actually relate the energies and properties of molecules by the solution of Schrodinger equation. The exact solution of the Schrodinger wave equation is only possible for hydrogen atom. Beyond that approximations are necessary for the solution, and the two main approaches are ab initio methods and semi-empirical methods.

The ab initio methods, as the name implies, are based on the first principles and are purely theoretical, without the use of any experimental parameters. The first approximation for the solution of Schrodinger equation for complex chemical systems is the Born-Oppenheimer approximation that simplifies the Schrodinger equation by assuming atomic nuclei as stationary with respect to electron motion. This approximation is reasonable since the nuclear mass is at least thousands of times greater than the electron mass, and hence the nuclei move very slowly with respect to electrons, and electrons respond virtually instantaneously to nuclear position change. This approximation allows the solution of Schrodinger equation for electron motion in the field of fixed nuclei, as well as predicting the vibrational spectra of molecules when separately solved for nuclear motion (neglecting electron motion). The Hartree-Fock

approximation assumes one electron orbitals in interaction with the average field created by all the other electrons and the nucleus. The self consistent field method (SCF) in solving the simplified Schrodinger equation uses an iterative approach by guessing an input function for the orbital and obtaining a solution function until these functions are sufficiently close or self consistent. The orbitals so derived are termed Hartree-Fock orbitals. Usually the trial orbital function is a Slater orbital, a specific parameterized orbital function. The method of using linear combinations of Slater functions in Hartree-Fock calculations is termed the Hartree-Fock-Roothaan procedure (McQuarrie 1983). The further LCAO-MO approximation assumes molecular orbitals as linear combinations of atomic orbitals, and transforms the coupled differential equations of the Hartree-Fock approximation into a set of algebraic equations, termed Roothaan-Hall equations. The set of atomic orbitals in an LCAO-MO is called a basis set. The accuracy or reliability of a molecular orbital function depends on the size of basis set used. The calculations involving large basis sets are termed near Hartree-Fock calculations.

In general, the Hartree-Fock models overestimate the electron-electron repulsion energy. The correlated models account for the electron motion coupling (with opposite spins) or correlation. Density functional theory (DFT) models introduce an approximate correlation term explicitly. The DFT developed by Hohenberg, Kohn and Sham depends on the calculation of the exchange and correlation energies of a uniform electron gas from its density. The ground state electronic energy is the sum of electron kinetic energies, electron-nuclear interaction energy, coulomb energy, exchange/correlation energy, all of the components being functions of the total electron density. BP, BLYP and EDF1 models are examples that require only the Hartree-Fock coulomb terms. The B3LYP model utilizes the Hartree-Fock exchange terms. The Configuration Interaction models CIS, CID, CIDS and QCISD(T) account for the inner-shell single, double, triple electron promotions. The second order Moller-Plesset model, MP2, utilizes perturbation theory. The higher order Moller-Plesset model MP4 includes single, double, triple and quadruple electron promotions of the inner shells. DFT calculations yield more accurate results than Hartree-Fock theory, and require about the same computational resources as Hartree-Fock models, the computationally least expensive ab initio methods.

The semi-empirical methods use experimentally derived parameters for the approximations to the Schrodinger equation. However, they are limited by the availability of the experimentally obtained appropriate parameter sets for the chemical system being investigated. Some examples are AM1, MINDO/3, PM3. Their

parameterization depend on the experimental data including equilibrium geometries, heats of formation, dipole moments and ionization potentials.

The minimal basis sets use fixed size atomic orbitals. The minimal basis set Slater-type orbitals that uses three Gaussian primitives (functions), STO-3G, is a minimal basis set needed for each atom with a spherical atomic environment bias. In order to increase the accuracy of the results the basis sets can be made larger by increasing the number of basis functions for each atom. The 3-21G, 6-31G split valence basis sets represent core and valence atomic orbitals by one and two sets of functions, respectively. 6-311G basis sets split the valence functions into three parts. Split valence basis sets allow the orbitals to change size but not the shape. Polarized basis sets allow orbitals with angular momentum per atom. For example they add d functions to carbon atoms, f functions to transition metals, and p functions to hydrogen atoms, hence allowing hybrid orbitals. 6-31G*, 6-31G**, 6-311G* and 6-311G** are polarization basis sets (** indicates additional p-type polarization for hydrogen atom). The diffuse function basis sets are used to model the systems with electrons that are relatively far from the nucleus, especially molecules with lone pairs, anions and systems with high negative charge, excited states, low ionization potential systems, descriptions of absolute acidities. 6-311+G**, 6-311++G** are diffuse basis sets (++ indicates diffuse function addition to hydrogen atoms).

In literature there exists a number of computer modeling and simulation studies related to protein-hydroxyapatite interactions. Molecular simulation of protein adsorption and desorption on hydroxyapatite surfaces (Shen, et al. 2008), computer modeling of the uptake, structure and distribution of carbonate defects in hydroxyapatite (Peroos, et al. 2006), molecular orbital study of hydroxyapatite nucleation at silica bioceramic surfaces (Sahai and Tossell 2000), molecular modeling of inhibition of hydroxyapatite by phosphocitrate (Wierzbicki and Cheung 2000) constitute examples of the computer modeling and simulation work.

The energy minimization molecular dynamics (MD) and steered molecular dynamics (SMD) simulations were carried out revealing that the interaction between the (001) surface of hydroxyapatite and different orientations of the model protein, 10th type III module of fibronectin (FN-III₁₀), was dominated by the electrostatic energy (Shen, et al. 2008). The SMD simulation comprised an attachment of harmonic restraint (with variable stiffness) to one or more atoms in the system. The simulations were carried out assuming water medium. The charged and polar side groups of residues of the protein

module neighboring the charged HAp moved closer to its (001) surface, while the hydrophobic groups moved away. The charged -COO^- and -NH_3^+ groups on the protein residues exhibited the strongest interaction with the HAp surface. Guanido group, neutral amino group and hydroxyl group also have affinities for the (001) surface of the HAp, but numerically about one half of the -COO^- and -NH_3^+ groups. It was noted that, though, the major force giving rise to protein adsorption was electrostatic attraction, the water-bridged hydrogen bond might have also had a minor role in the adsorption affinity between HAp and proteins. In the calculations the distance between the HAp surface and protein molecule was varied between 118 to 164 Å (Shen, et al. 2008).

The uptake and distribution of substitutional carbonate groups in the hydroxyapatite lattice were investigated by computer modeling techniques (Peroos, et al. 2006). The energy minimization calculations were carried out by MD simulations employing METADISE code. The calculations showed that in the A-type defect, two hydroxy groups were replaced with one carbonate group in the hydroxy channel located in the midway between the hydroxy vacancies, in a total of 4 unit cells, and it was the most stable defect. In the first B-type defect, one phosphate was replaced by one carbonate and one hydroxy, in a total of two unit cells, and it was also energetically favorable. Energetically there was no preference for replacement of a particular phosphate group. Both the carbonate and the hydroxy groups moved away from the vacant phosphate position. In the second B-type defect, one calcium ion and a phosphate group were replaced by one monovalent cation (Na^+ or K^+) and one carbonate group, in a total of two unit cells. In the most stable substitutions the substitutional monovalent cation and carbonate were located closely together. It was also observed that the formation of a B-type defect was promoted by the presence of A-type defects in the lattice (Peroos, et al. 2006).

Molecular orbital calculations were used to predict the reaction sequence for apatite nucleation by the interactions of Ca^{2+} , H_2PO_4^- , HPO_4^{2-} and H_2O with bioceramic surface sites represented by $\text{Si}_7\text{O}_{12}\text{H}_{10}$, $\text{Si}_4\text{O}_8\text{H}_8$, $\text{Si}_3\text{O}_6\text{H}_6$ (Sahai and Tossell 2000). Energies and vibrational frequencies were calculated by the core and double valence basis sets, 3-21G* and 6-32G* (for the clusters). It was concluded that the partially deprotonated $[\text{Si}_3\text{O}_6\text{H}_6]$ was the active surface site for the promotion of calcium ion dehydration as calcium was adsorbed; the formation of $[\text{SiO-Ca-OPO}_3\text{H}]$ bonds were energetically preferred over direct Si-O-P bonds; an acidic precursor with bidentate, $\text{Ca} > \text{OPO}_3\text{H}$ nucleated within minutes to an hour on the bioceramic surface. The complex

$[\text{Si}_3\text{O}_6\text{H}_5\text{CaHPO}_4(\text{H}_2\text{O})_3]^-$ and young bone, and bioceramic reacting with SBF shared unique infrared/Raman bands at 631, 1125-1145 cm^{-1} which are distinct from the bands of crystalline hydroxyapatite and mature bone.

The molecular modeling methods was used to show the inhibition of hydroxyapatite crystals, that is, diminished crystal growth or its total cessation by the binding of phosphocitrate on the (100) surface (Wierzbicki and Cheung 2000). The interaction of phosphocitrate with the neutral and charged slab of hydroxyapatite (100) surface was studied by the geometry optimization of the system. The binding of phosphocitrate to (100) surface of hydroxyapatite resulted in significant enlargement of these faces while the other faces shrank. The lattice disruption together with the steric hindrance of the adsorbed phosphocitrate in its vicinity, brought about the hydroxyapatite crystal growth inhibition.

CHAPTER 6

EXPERIMENTAL

6.1. Materials

The materials used in this study for the thin film preparation are:

- Hydroxyapatite powder, $\text{Ca}_{10}(\text{PO}_4)_6(\text{OH})_2$, SIGMA, C 567-500G, FW=1004.6, mp=1670 °C, d=3.14 g/cm³
- Hydropalate 64 (sodium di-isooctylsulfosuccinate), $\text{C}_{20}\text{H}_{38}\text{O}_7\text{S}$, MW=422.58, Henkel
- D-Fructose, SIGMA, F 0127-100G
- Calgon (sodium hexametaphosphate)
- Silk sericin, Silk Biochemical Co. Ltd., ref: 46-3-108
- Raw silk, Silk Biochemical Co. Ltd., ref no: biosilk 04056
- Titania powder, TiO_2 , Degussa, aeroxide, P25S, CAS-13463-67-7

The materials used for protein adsorption:

- Bovine serum albumin, BSA, SIGMA CAS 9048-46-8, A2153-100G, Albumin from bovine serum, min. 96%, electrophoresis
- Collagen type I, SIGMA C-9879 1 g, Type I, Insoluble, from Bovine Achilles Tendon, 9007-34-5
- sodium phosphate monobasic monohydrate, $\text{NaH}_2\text{PO}_4 \cdot \text{H}_2\text{O}$, SIGMA S-9638 500G ACS reagent 10049-21-5, FW=138, 99.3%
- di-sodium hydrogen phosphate 12 hydrate dibasic, $\text{Na}_2\text{HPO}_4 \cdot 12\text{H}_2\text{O}$, Pancreac 131678.1211, FW=358.14, 99-102%

The materials used for electrochemical anodization of Ti6Al4V:

- Ti6Al4V alloy sheet, thickness: 1 mm; ASTM grade 5
- ortho-Phosphoric acid, MERCK, 99%, 1.00565.0500, 98 g/mol, H_3PO_4
- Glycerol, Fluka, $\geq 98\%$, M=92, d=1.26, $\text{C}_3\text{H}_5(\text{OH})_3$

6.2. Methods

6.2.1. Powder Dispersion, and Characterization

The hydroxyapatite powder size reduction: The commercially available hydroxyapatite powder (c-HAp) was used for thin film preparations, as received, and after dry ball milling in a 250 ml tungsten-carbide jar revolved in a gyrator. The grinding medium comprised 30 pieces tungsten-carbide balls of 1 cm in diameter. Each load for milling consisted of 15 gr of c-HAp. The milling was carried out for a maximum of 120 min at 400 rpm with intermittent 15 min grinding and cooling periods (from this point on the 120 min dry milled powder will be denoted as m-HAp powder; m for dry milled). The tapped powder densities were determined as a function of dry milling time. A tapped volume of 10 cm³ of each powders, measured in a graduated cylinder, was weighed to calculate the tapped density.

The particle size distribution measurements were carried out with the X-ray sedigraph (Micromeritics Sedigraph 5100), and the measurement concentration of the suspensions were 0.02 gr/ml (1.0 gr of solids was diluted to 50 ml with deionized water). c-HAp powder was dispersed in deionized water by various methods (and also combinations of methods), by various dispersant additions, and at various solids loadings. The dispersion methods were ultrasound bath, wet ball milling, fast mixing in baffled blender, suspension quenching in liquid nitrogen, thermal shock by water quenching of heated powder. The dispersants used were hydropalate (2%), calgon (1%), and D-fructose (3%)².

For particle size distribution measurements, deionized water was added to 4.0 gr of HAp powder completing the volume to 50 ml (7.6%) and the appropriate amount of dispersant was added dropwise, and the suspension was mixed for around 60 sec. The dispersion in the ultrasound bath (Elmasonic S80, 160W, 30 kHz) was applied to the suspensions in beakers at various durations. The wet ball millings (in 100 cm³ mill, with zirconia balls; 30gr of Ø5mm, and 15 gr of Ø3mm) were carried out for 2 hrs at 200 rpm. The suspensions were dispersed in the fast baffled mixer for a total of continual 15, and 30 min periods (with 1-2 min of waiting periods in between 5 min mixing). The nitrogen quenching was applied by pouring liquid nitrogen into the suspension in a glass

² All concentrations are given in weight percent (w/w%) unless otherwise stated throughout the document.

beaker, and the totally frozen suspension was melted by natural convection at ambient conditions. For the double nitrogen quenching the suspension freezing-melting cycle was repeated twice. The thermal shock method involved the heating of the powder to 450 °C, keeping at that temperature for 20 min and then quenching in ambient temperature water. After the dispersion operation(s) the mixture was divided to four aliquots, each being diluted to a 50 ml final volume, the convenient concentration for the X-ray sedimentation measurements.

For measurements with high solids loading, 30% hydroxyapatite powder was dispersed in water by hydroxylate (2%), calgon (1%), and fructose (3%). The dispersion operations were carried out in the same conditions described above with the only difference of a higher solid content in the suspensions. The dispersed suspensions were diluted to the required concentration for the X-ray sedimentation measurements. The measurements were repeated after 5 days considering that, especially, the adsorption of fructose on HAp particles might be slow.

The hydroxyapatite powder PZC measurement: The point of zero charge (PZC) of the commercial (c-HAp) and dry milled (m-HAp) hydroxyapatite powders were measured by the automatic titration method. 0.25 gr of each c-HAp and m-HAp powders, were suspended in 25 ml of deionized water in an ultrasound bath while continuously stirring for 65 min (without the addition of any organic dispersant). The pH of both suspensions were measured to be 7.4, after which it was adjusted to approximately 11.5 by the addition of 1.0 N of NH_4OH solution, and the final suspension volumes were 50 ml. The automatic titrations were carried out by automatic dispense of 1.0 N HNO_3 solution into the suspensions, and the pH was continuously recorded. The initial dispense rate was approximately 0.05 ml/s, and near the inflection point it was reduced to 0.005 ml/s. During acid dispensing the suspensions were stirred with a magnetic stirrer. The inflection points in the pH versus volume of acid added were determined, and taken as the threshold points at which the surface charges of the HAp particles were reversed (from negative to positive), hence determining the PZCs.

Zeta Potential Measurements were carried out with the zeta sizer (Malvern Instruments Ltd. 3000 HSA). 0.25 gr of each c-HAp and m-HAp powders, were suspended in 25 ml of deionized water in the ultrasound bath while continuously stirring for 65 min (without the addition of any organic dispersant). The c-HAp and m-HAp powder suspensions were finally diluted to approximately 0.17 gr/L (the convenient concentration for zeta sizer measurements) and the pH of a sequence of suspensions

were adjusted between 3.5 and 10.5. The zeta potentials were measured for each suspension. The pH range was so chosen to yield both positive and negative zeta potentials determining the isoelectric points (IEP) of the HAp powder suspensions.

The pH, and organic dispersant ratio for the optimum dispersion of c-HAp, and dry milled powder suspensions were determined by the zeta sizer. Stock suspensions of c-HAp and dry milled HAp powders were prepared by adding 10 gr of powder into 47 gr of deionized water. The organic dispersant, hydropalate 64, was added at various amounts (0-0.36 gr or 6 drops). The deagglomeration was carried out by wet ball milling in glass jars with a grinding medium of zirconia balls (30gr of Ø5mm, and 15 gr of Ø3mm) for 2 hours at 200 rpm. The stock suspension was then diluted to a solid content convenient for measurement in the zetasizer. 0.2 ml of the stock solution was first diluted to 10 ml. The diluted suspension was ultrasonicated for 30 minutes, and 1.0 ml of it was diluted to 20 ml in a beaker that corresponds to an overall 1000 fold dilution. The final solid content was approximately 0.17 gr/L. Before the measurements the pH of the suspension in the beaker was adjusted in the range from 7 to 11 by 0.1 N NH₄OH addition, and ultrasonicated for an additional 15 minutes while stirring. The number mean particle size distributions were determined by the zeta sizer.

The thermal expansion and sintering behavior: The linear thermal expansion and sintering behavior of c-HAp, m-HAp and c-TiO₂ powders was evaluated by dilatometric measurements. The instrument used was Linseis L75/1550B-1600°C AE-5502/02 dilatometer. The powders were shaped cylindrically in a die of 5 mm inner diameter using a manual hydraulic press (Carver 10 ton max.). Single c-HAp, c-TiO₂ pellets, mixtures of powders (50% c-HAp and 50% c-TiO₂), and layered c-HAp/c-TiO₂ pellets were formed. The dilatometric measurements were carried out up to 1200°C.

6.2.2. Preparation of Hydroxyapatite/Silk Protein Thin Films by Dip Coating

Thin film coatings of hydroxyapatite were achieved by dip coating of bioinert glass slide substrates in dispersed suspensions. The glass slides were cleaned by detergent solution, ethyl alcohol, and acetone subsequently. 1.0%, 15%, and 25% aqueous suspensions of c-HAp, and m-HAp powders were prepared in deionized water. The steric dispersant hydropalate 64 was added in the ratio 2.4%. The pH of the c-HAp,

and m-HAp suspensions were adjusted to 9.8-10.0, and 9.4-9.6 (with 1.0 N NH₄OH), respectively. The 50 ml suspensions were ultrasonicated (30 kHz) while stirring for 30 min, followed by wet ball milling in 100 ml jars with a grinding medium of zirconia balls (30gr of Ø5mm, and 15 gr of Ø3mm) for 2 hours at 200 rpm. Finally the suspensions were ultrasonicated for 2 hr. before dip coating.

The bioinert glass substrates were dip coated in the c-HAp and m-HAp suspensions at 25°C with a retraction rate of 100 mm/min. The substrates were coated up to 5 layers with 30 min of ambient drying in between. Some of the thin films on glass substrates were heat treated at 560°C, for 30 minutes with a heating ramp rate of 15°C/min.

The sericin and fibroin film coatings on glass substrates were prepared by dip coating in the sericin and fibroin solutions with a retraction rate of 100 mm/min at ambient temperature (25°C). The preparations of sericin and fibroin solutions are described below. The substrates were coated with three layers of sericin and fibroin, with 30 minutes of ambient drying between coatings. The sericin and fibroin coated glass slides were then coated with c-HAp and m-HAp in the same way described above.

The sericin solution was prepared by dissolution of 4.2 gr of commercial sericin in 48 ml of deionized water.

Silk fibroin solutions were prepared by the subsequent processes of degumming and dissolution of the raw silk. The degumming was carried out by boiling in 0.05% aqueous Na₂CO₃ solution (2.0 gr of silk in 100 mL solution) for 30 min. The degummed silk was washed with deionized water and left over for drying at ambient conditions. 1.2 gr of the degummed silk was further treated with 20 times of Ajisawa's reagent (24 mL of CaCl₂/ethanol/water: 111/92/144 by weight) in a 250 mL Schott bottle by stirring at 78 °C for 2 hrs to obtain a clear solution. Higher concentrations were avoided due to the gelation tendency during the following dialysis step. The fibroin solution was dialyzed in cellulose dialysis tubings against deionized water at 4 °C by frequent change of dialysis water for the removal of CaCl₂ and other neutral salts until tested negative for AgCl precipitation by AgNO₃ (approximately 3 days). The treated cellulose tubings were rated to retain protein molecules of over 12,000 gr/mol. The silk fibroin solution (1-2% w/v) in the dialysis tubings was filtered (Filtrak 389 filter paper) and concentrated to approximately 10% w/v by a rotary vacuum evaporator at 30 °C, 30 rpm.

The cellulose dialysis tubings were prepared by cutting 30 cm long pieces from the roll. The protective glycerine layer was washed in running water for 3-4 hours. The sulfur components were removed by treating the tubes with 0.3% (w/v) sodium sulfide solution at 80°C for one minute followed by washing with water at 60°C for two minutes. The tubes were then acidified with 0.2% (v/v) sulfuric acid and rinsed with warm water.

6.2.3. Bovine Serum Albumin and Collagen Adsorption on Thin Films

The adsorption behavior of bovine serum albumin (BSA, the adsorbate) on the hydroxyapatite thin films (c-HAp, and m-HAp) was investigated. The quantity of BSA adsorbed on the HAp surfaces was determined as a function of contact time. The adsorbent substrates were glass/c-HAp, glass/m-HAp, glass/sericin/c-HAp, and glass/sericin/m-HAp.

The bovine serum albumin (BSA) solution was prepared in 100 mM PBS (phosphate buffer saline). 50 mg/L solution was prepared and diluted in two steps to 0.050 mg/mL (50µg/mL). All dilutions were carried out by 100 mM PBS solution.

The PBS solution was prepared by dissolving 5.42 gr $\text{NaH}_2\text{PO}_4 \cdot \text{H}_2\text{O}$ (sodium phosphate monobasic monohydrate), and 22.07 gr $\text{Na}_2\text{HPO}_4 \cdot 12\text{H}_2\text{O}$ (di-sodium hydrogen phosphate 12 hydrate dibasic) in 1.000 L deionized water, for a pH equal to 7.4.

The adsorption was carried out in 100 mL beakers in the incubator kept at 37°C, and 60 rpm. 5 substrates were placed in each beaker to form 59.8 cm² adsorption area. The BSA concentration was measured as a function of contact time.

The BSA concentration was measured by an HPLC size exclusion method. The column used was ZORBAX bio series GF-250 (LX14004 PN 884973.901 max pressure 350 bar). The mobile phase used was 100 mM PBS solution. The UV-vis detector module set at 210 nm wavelength. The 50 µL of the BSA solution sample was manually injected. Two peaks were obtained for BSA; the small peak belonged to the dimer of BSA, and a major peak with the retention times of 4.55 min and 4.96 min, respectively. The results were reported as the corresponding total area of the two peaks. The calibration curve was formed for a range of concentrations from 0.01-0.10 mg/L.

BSA solution, and collagen type I aqueous suspension were prepared in 10 mM PBS (phosphate buffer saline) for AFM imaging of their adsorption behavior. The

concentration of BSA was adjusted to 1.0 mg/mL (total volume 25 ml). Collagen type I was water insoluble and it was dispersed as a homogeneous suspension in ultrasound bath. The concentration was 0.1 mg/mL (total volume 25 ml).

The glass, glass/sericin, glass/fibroin, glass/c-HAp, glass/m-HAp, glass/sericin/c-HAp, glass/sericin/m-HAp, glass/fibroin/c-HAp, glass/fibroin/m-HAp substrates were prepared by dip coating as described previously, and the samples were cut into maximum 1x1 cm size suitable for AFM measurements. Two samples of each type of coating were placed separately in the BSA solution and the collagen type I suspensions perpendicularly to avoid any gravitational settling on the films. The samples were kept in the suspensions for 4 hr. The samples were rinsed with deionized water to sweep away the loosely bound BSA particles and collagen fibers, and left over for ambient drying.

6.2.4. Electrochemical Anodization of Ti6Al4V

The electrochemical anodization of Ti6Al4V alloys were achieved in an electrolyte solution of 0.33 M H₃PO₄ in deionized water mixed with variable amounts of glycerol as the applied potential difference was changed. The required amounts of glycerol for delimiting the ionic mobility by the increasing viscosity of the electrolyte solution were determined for a constant anodization current of ~15 mA, at potential differences of 20 V, 60V, 120 V, 240 V, and 400 V. The anodization was carried out in an electrolyte solution of 30 ml for 50 min. The titanium alloy to be anodized were employed as the anode while the same type of titanium alloy was used as cathode. The distance between the electrodes was 25 mm. The DC power source employed was LABCONCO, 5000V Power Supply, Labconco Corporation.

6.2.5. Preparation of Titania/Hydroxyapatite Thin Films by Spin Coating

Aqueous and ethanol suspensions of 30% c-HAp and 30% c-TiO₂ powders were prepared. The c-HAp powder was dispersed in deionized H₂O at pH=10, 2% hydropalate was added as dispersant. The suspension was ultrasonicated for 2 hrs, followed by double quenching with liquid N₂, wet ball milling in 100 cm³ mill with zirconia balls (30gr of Ø5mm, and 15 gr of Ø3mm), and ultrasonication for another 2

hrs. The resulting suspension was centrifuged at 3000 rpm for 3 min (SIGMA laboratory centrifuges 6-15) to separate the agglomerated particles. Approximately 15% of the initial powder sedimented, and the separated stable suspension contained 15% solid. The aqueous suspension of the c-TiO₂ powder was prepared in exactly the same manner. The ethanol suspensions were prepared without NH₄OH, and any dispersant addition. The initial ultrasound treatment of 2 hrs, followed by wet ball milling for 2 hrs, and ultrasound treatment for another 2 hrs. The agglomerated particles were separated by the same method.

The Ti6Al4V substrates were grinded to 1200, and 180 grids (either 1 cm diameter disks, or 1x1 cm square plates), and were spin coated by aqueous c-HAp, and c-TiO₂ suspensions at 4000 rpm, 20 seconds dwell time. The ethanol suspensions were coated at 3000 rpm, 20 seconds dwell time. The c-HAp was coated in 1 and 3 layers, while c-TiO₂ was coated in 1, 2 and 3 layers, with heat treatment at 360°C, for 20 min between coatings. The spin coater used was SCS (Specialty Coating Systems) G3P-8 Spincoat, Cookson Electronics Equipment. Some films were heat treated at 700°C, or 850°C, for 60 min.

6.2.6. Characterization of Thin Films

6.2.6.1. Microstructural Characterization

The microstructure of the HAp, silk sericin, and silk fibroin thin films were characterized with SEM/EDX, AFM, XRD, and FTIR. The SEM images of the thin films were obtained by Philips XL-30S FEG. EDX analysis were carried out for some of the films. The AFM, Digital Instruments MMSPM Nanoscope IV, was used in the tapping mode to obtain the 3-dimensional surface topology, and phase information of the film surfaces, before, and after the BSA and collagen type I adsorption. The XRD measurements were carried out by Philips X-Pert Pro x-ray diffractometer (CuK α) for crystalline phase identification. The grazing incidence method with an incidence angle of 1° was employed between 5-90° of 2 θ values. The FTIR spectra of the thin films were obtained by FTIR spectroscope Digilab-Merlin with the 80° V-gold mirror grazing apparatus accessory.

6.2.6.2. Mechanical Characterization

The film thicknesses were measured with Mitutoyo SJ-301 surface roughness tester in the primary profile mode, generating a length-depth profile of the film scratched with a 85 shore A hard rubber.

The surface roughness of the thin films were determined with Mitutoyo SJ-301 surface roughness tester in the roughness profile mode, curve corrected by Gaussian filter in accord with JIS B0601-2001. Arithmetic mean deviation (Ra), root mean square deviation (Rq), maximum height (Ry), Ten-point height of irregularities (Rz) roughness parameters were recorded.

The Vickers hardness of the films and metallic substrates were determined with TIME Testing Instruments – Digital Microvickers Hardness Tester, HVS-1000. The indentation was applied for 10 seconds.

The adhesion strength of the films was measured by tensile adhesion pull-out test. The tensile test system was Testometric AX M500-100 kN (Rochdale, England). The samples (substrate and thin film coating) were glued on both sides to stainless steel screw tops with epoxy resin, and cured for 16 hr at 70°C. Blank samples, to test the adhesion of screw to screw, and screw to Ti6Al4V (without film) to screw, were prepared. The adhesion/cohesion strength of the epoxy resin itself was determined by the blank tests. The tensile tests were carried out at a strain rate of 0.5 mm/min according to ASTM C633 (Yang, et al. 2009). The maximum tensile force (T_b) at the film breakage was recorded and the adhesion strength was reported as $\sigma_b = T_b / \text{area of the film surface}$.

The adhesion strength of the coatings was also evaluated by scanning scratch test. Shimadzu Scanning Scratch Tester SST-W101 equipped with a standard off-line Zeis metallographic microscope was used for the measurements. The stylus tip was Rockwell C diamond of radius 15 μm . The applied load was increased linearly from 0 to 98 mN with a loading speed of 1 $\mu\text{m/s}$, and the scratch speed of 2 $\mu\text{m/s}$. The critical force at which the coating was peeled-off was determined as the steep increase in the resisting force on the tip during scratching of the surface. The average of three measurements were taken. The adhesion strength of the coatings (σ) was calculated by Equation 6.1.

$$\sigma = \frac{H}{\left[(\pi R^2 H - W_c) / W_c \right]^{1/2}} \quad (6.1)$$

where H is the Brinell hardness of the metal substrate in kg/mm², R is the stylus radius, and W_c is the critical force for peeling-off.

6.2.7. Molecular Modeling Methods

The molecular modeling calculations were performed by the softwares GaussView and Gaussian 3 by Gaussian Inc. Pittsburgh, Pennsylvania. The geometry optimization of the ion Ca²⁺, and ionic groups PO₄³⁻ and OH⁻ in hydroxyapatite crystal were carried out by B3LYP DFT method, with the basis set 6-31Gd. The hydroxyapatite unit cell and crystal structure were constructed by the crystal editor function of GaussView using hexagonal system, P6₃/m space group, and data from “American Mineralogist Crystal Structure Database” hydroxylapatite by Wilson, et al. 1999, sample: H6G, synthetic.

The electrostatic potential distributions (ESP) were mapped on the electron isodensity surface with the isovalues in the range 0.0004-0.1 e/Bohr³ (see section 7.5) of the Ca²⁺, PO₄³⁻ and OH⁻ fragments, and hydroxyapatite crystal composed of one and two unit cells by the 3-21G basis set. These type of calculations were limited to maximum two unit cells of hydroxyapatite, since the method was limited to calculations with maximum 100 atom systems (the hydroxyapatite unit cell contained 44 atoms).

CHAPTER 7

RESULTS AND DISCUSSION

7.1. Hydroxyapatite Powder Dispersion, and Characterization

As a result of the dry ball milling of the c-HAp powder an abrupt increase in the tapped bulk density was observed (Figure 7.1.). The change was from 0.44 gr/cm³ of the c-HAp powder to 0.96 gr/cm³ of the m-HAp powder. The increase is due to the closer packing of the crushed particles, within a threshold milling time of less than 30 minutes. The corresponding SEM images are given in Figure 7.2. The commercial powder consisted of rod like particles of 150-250 nm in length and 50-80 nm in diameter, while the dry milled powder consisted of particles of 40-100 nm in diameter.

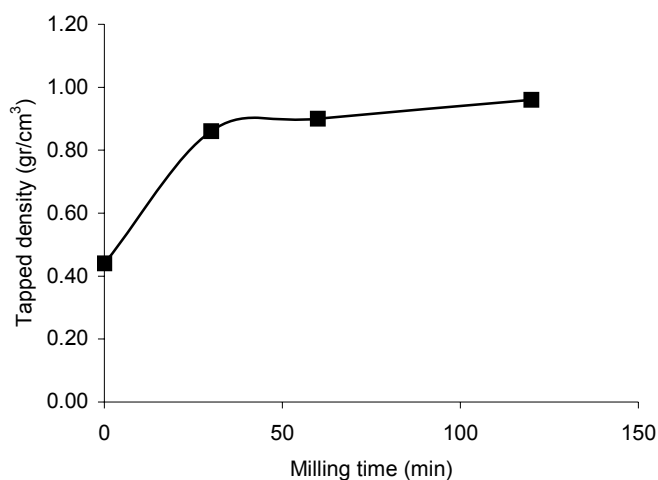


Figure 7.1. Change in the tapped apparent density of the c-HAp powder as a function of dry milling time in tungsten carbide mill.

The dispersion characteristics of the c-HAp powder in aqueous suspensions were evaluated by the dispersion methods of ultrasound bath, wet ball milling, fast mixing in baffled blender, suspension quenching in liquid nitrogen, thermal shock by quenching of heated powder (450°C) in ambient temperature water. The dispersants used were hydropalate (2%), calgon (1%), and fructose (3%). The c-HAp powder content of the suspensions was 1.0%, 7.6%, 11%, 15%, 25% and 30%.

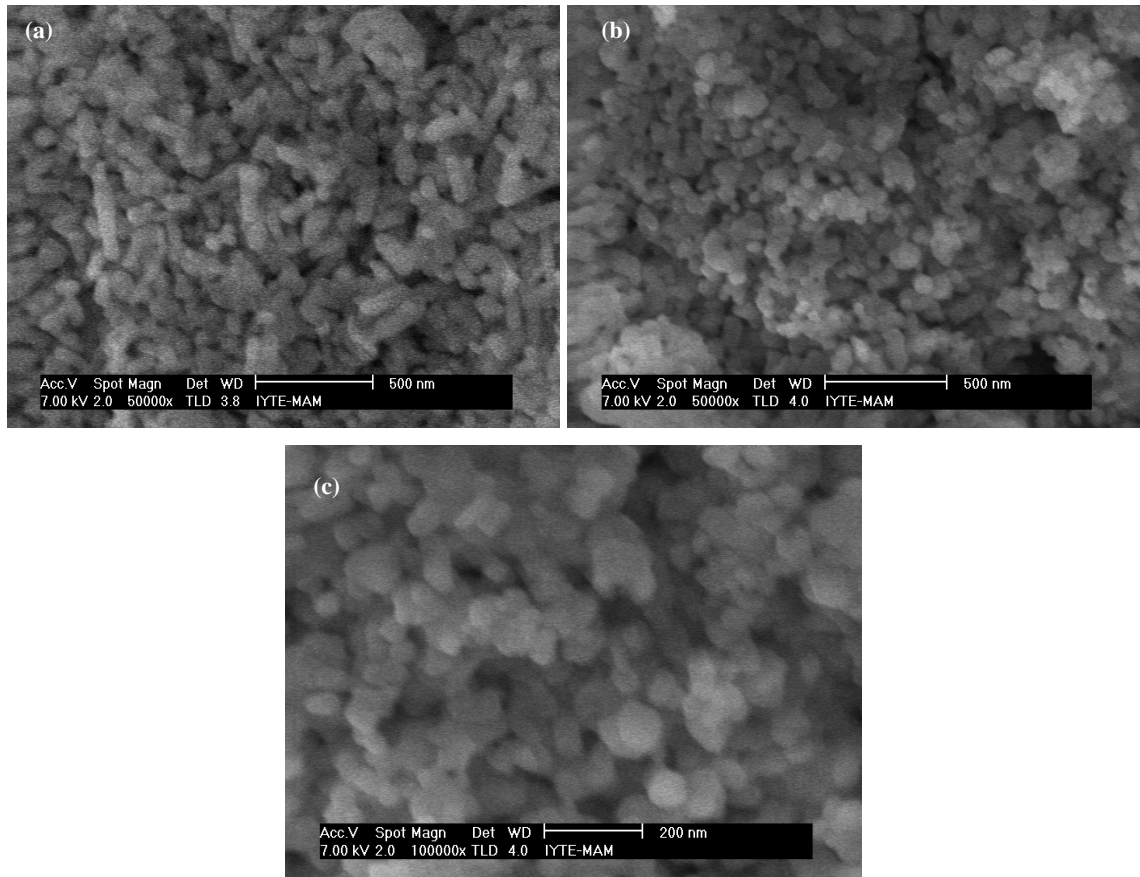


Figure 7.2. Hydroxyapatite powder SEM images (a) c-HAp (commercial powder), (b), (c) m-HAp (120 min. dry milled)

The particle deagglomerations of the suspensions with 7.6% c-HAp powder content are illustrated in Figure 7.3. to Figure 7.7. The dispersions with ultrasound in the presence of 2% organic dispersant hydroxypalate is shown in Figure 7.3. After ultrasound for 5, 20 and 65 min, 20.5%, 25.0% and 38.6% of the particles were below 1 μm , respectively. However, as seen in Figure 7.4, with calgon for 5 min ultrasound there were no particles below 4.6 μm , and 20 and 65 min ultrasound yielded 21.5% and 32% below 1 μm . These results showed that particle deagglomeration was better with hydroxypalate in comparison to calgon at all ultrasound durations. It can also be seen that ultrasound was an effective means in the deagglomeration of the c-HAp particles.

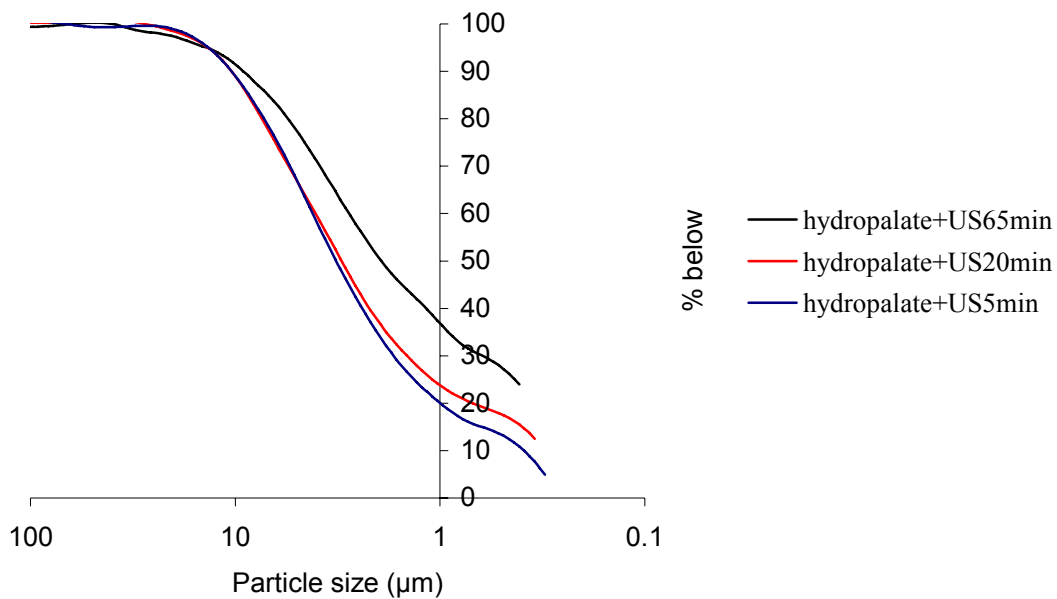


Figure 7.3. Particle size distribution of c-HAp powder (7.6%) dispersed with ultrasound and the dispersant hydropalate (2%).

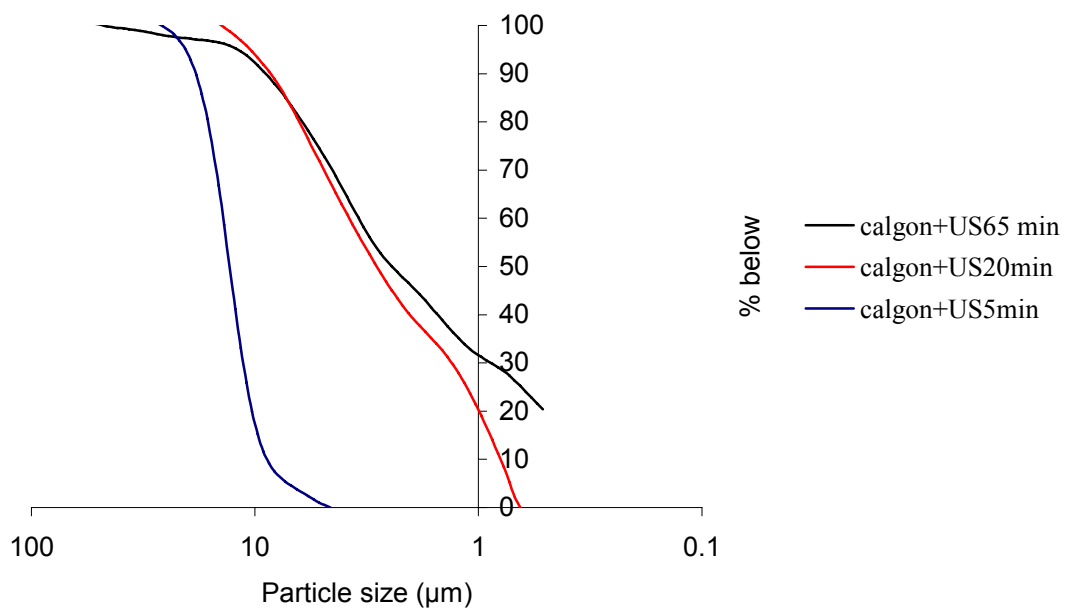


Figure 7.4. Particle size distribution of c-HAp powder (7.6%) dispersed with ultrasound and the dispersant calgon (1%).

As seen in Figure 7.5 liquid nitrogen quenching alone yielded a deagglomeration with 15.6% of particles below 1 μm . However, the single liquid nitrogen quenching followed by 5 and 65 min. of ultrasonic treatment yielded deagglomerations of 26.3% and 55.6% of the particles being under 1 μm . When compared to dispersion by ultrasonic treatment alone these results indicated that by nitrogen quenching followed by the same ultrasound duration the ratio of particles under 1 μm increased from 20.5% to 26.3% for 5 min, and from 38.6% to 55.6% for 65 min ultrasonic treatment, corresponding to a decisive increase. Moreover, the double nitrogen quenching followed by 65 min of ultrasonic treatment yielded 76.8% of the particles below 1 μm . Therefore, the nitrogen quenching proved to be an effective deagglomeration means, especially when followed by ultrasound treatment, and better deagglomerations were achieved with increasing ultrasonic treatment durations.

The deagglomeration effect of the nitrogen quenching can be due to twofold phenomena. One is the thermal shock effect from -195.8°C (the boiling temperature of liquid N_2) to ambient temperature of 20°C , a temperature difference of $\sim 216^{\circ}\text{C}$ which will cause thermal stresses to strain the particles at the grain boundaries which later make them prone to separation at lower mechanical microblast forces of ultrasonic treatment. The other is the strain created by the phase transformation of the suspending medium, water to ice and back to water, accompanied by the corresponding volume changes. The thermal shock effect is illustrated in Figure 7.6. The thermal shock effect with a ΔT of 430°C , was also found to be effective for deagglomeration. However, the particle size ratios below 1 μm of 37.6% and 49.0% for 5 and 65 min following ultrasound times were lower in comparison to the single and double nitrogen quenching followed by the same ultrasonic treatment times. It can be deduced that volume change due to phase transformation of the dispersing medium is also a major mechanism for deagglomeration in conjunction to thermal shock effect.

In Figure 7.5 it can be seen that the effectiveness of wet ball milling for two hr followed by 65 min of ultrasonic treatment for particle deagglomeration fell between the single and double N_2 quenchings with 65.8% of the particles being below 1 μm .

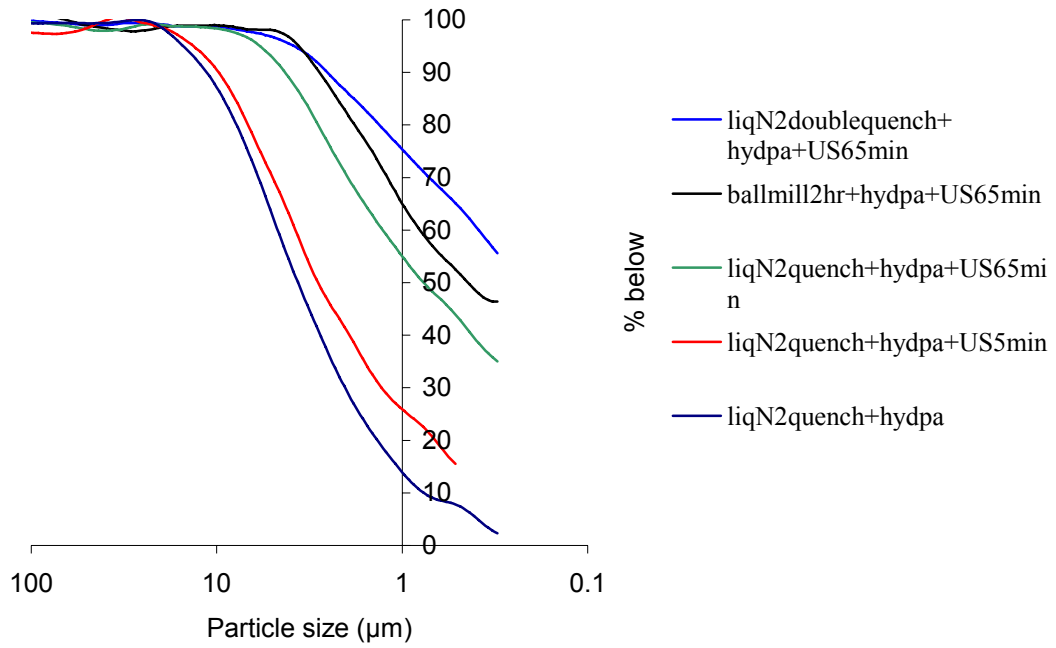


Figure 7.5. Particle size distribution of c-HAp powder (7.6%) dispersed with liquid nitrogen quenching (single and double), wet ball milling with zirconia balls, followed by ultrasound, and with 2% hydropalate as dispersant.

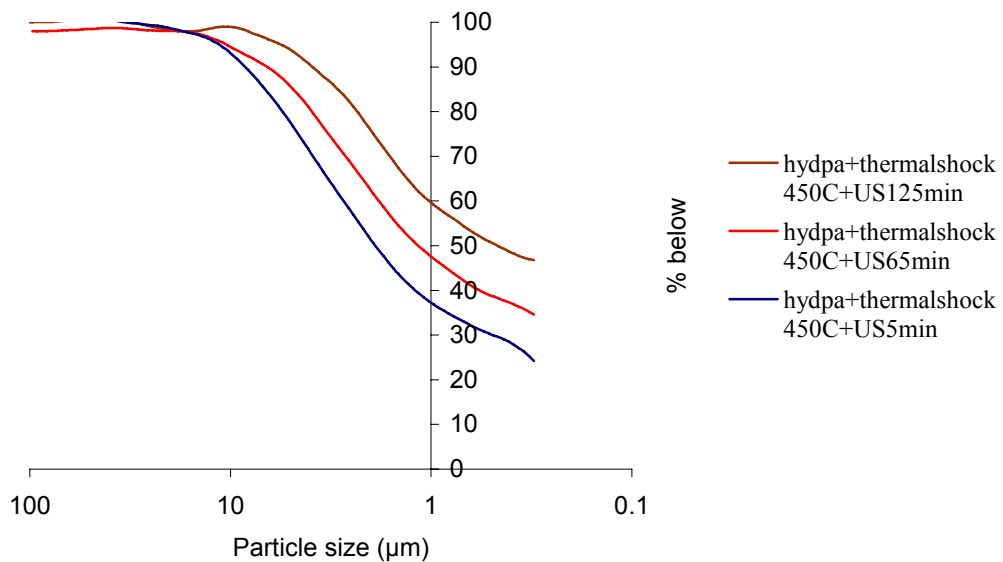


Figure 7.6. Particle size distribution of c-HAp powder (7.6%) dispersed with thermal shock (from 450 C powder quenched in ambient T water), followed by ultrasound, and with 2% hydropalate as dispersant.

In Figure 7.7 the results for the deagglomeration of hydroxyapatite with calgon as dispersant, and with N₂ quenching, fast propeller mixing followed by ultrasound treatment are given. The ratios of particles below 1 μm were 35.7% for the single N₂ quench plus 20 min ultrasound treatment, 52.6% for the 15 min. propeller mixing, 56.6% for the 30 min propeller mixing, 56.6% for the N₂ quench plus 65 min ultrasound treatment, 73.1% for the double N₂ quenching plus 65 min. ultrasound treatment, 79.1% for the double N₂ quenching plus 125 min ultrasound treatment. When the N₂ quenches were compared to their counterparts with hydroxylapatite as dispersant, for the single N₂ quenching the deagglomeration was nearly the same, while for double quenching with the same ultrasonic treatment duration hydroxylapatite seems to be the slightly better dispersant.

For the fast propeller deagglomeration the ratio of particles under 1 μm. increased with increasing mixing time; from 52.6% to 56.6% for 15 and 30 min. mixing times, respectively, which was considered to be a slight increase with time.

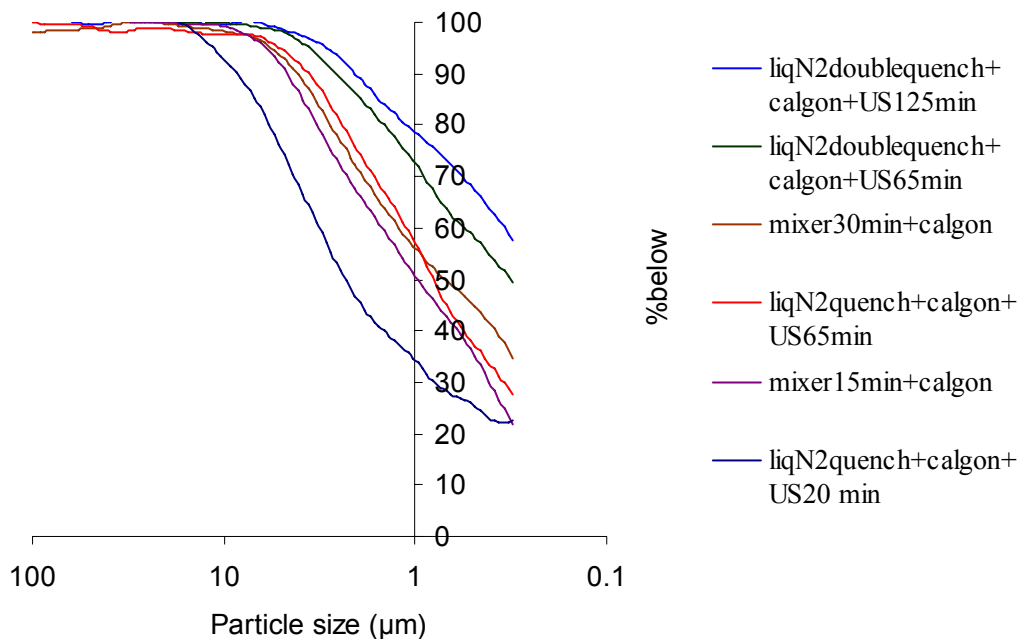


Figure 7.7. Particle size distribution of c-HAp powder (7.6%) dispersed with liquid nitrogen quenching (single and double), fast propeller mixing, followed by ultrasound, and with 1% calgon as dispersant.

Dispersion characteristics of the suspensions with 30% solid loading are illustrated in Figure 7.8 to Figure 7.10. It was observed that with 30% solid loading calgon and fructose were not effective dispersants at all, and even for the measurements after 5 days to observe the effect of time dependent adsorption, especially for fructose, no dispersion effect was observed. Actually the systems were probably flocculated.

However, with hydropalate as dispersant with extensive ultrasonic treatment time (245 min.) deagglomeration was achieved with particles ratio of 42.8% below 1 μm . Again with double nitrogen quenching followed by ultrasonic treatment for 125 min, the ratio of particles below 1 μm was 56.6%, and remained constant after 5 days. These ratios were lower than the corresponding 7.6% solid loading suspensions.

Interestingly enough wet ball milling for two hr followed by 125 min ultrasound yielded the best deagglomeration of particles, the ratio under 1 μm being 78.7% a value comparable to the best achieved for the lower solid loading.

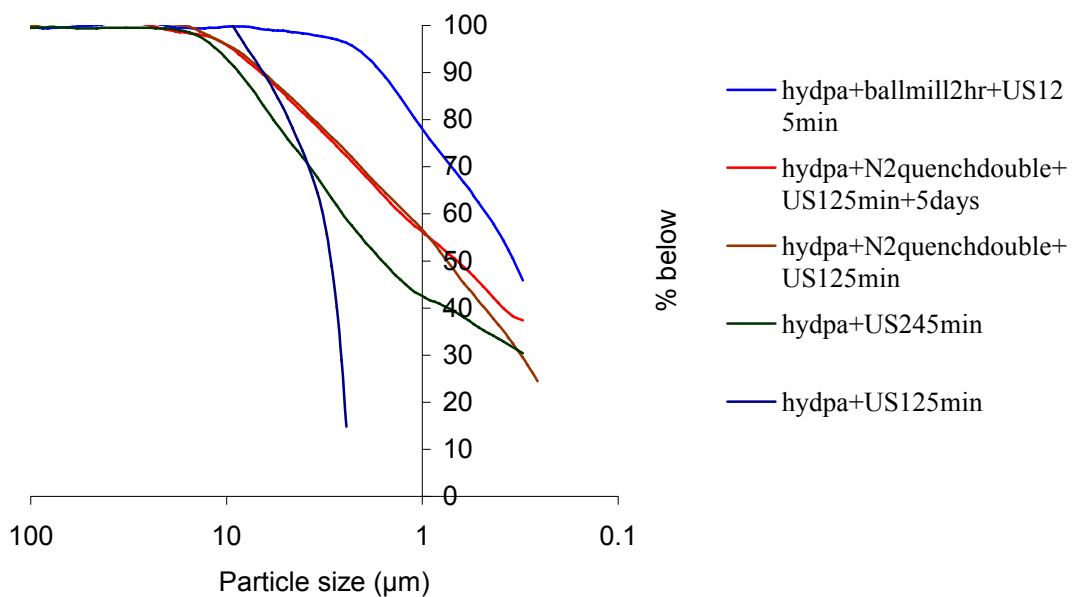


Figure 7.8. Particle size distribution of c-HAp powder (30%) dispersed with liquid nitrogen quenching (double), wet ball milling with zirconia balls, followed by ultrasound, and with 2% hydropalate as dispersant.

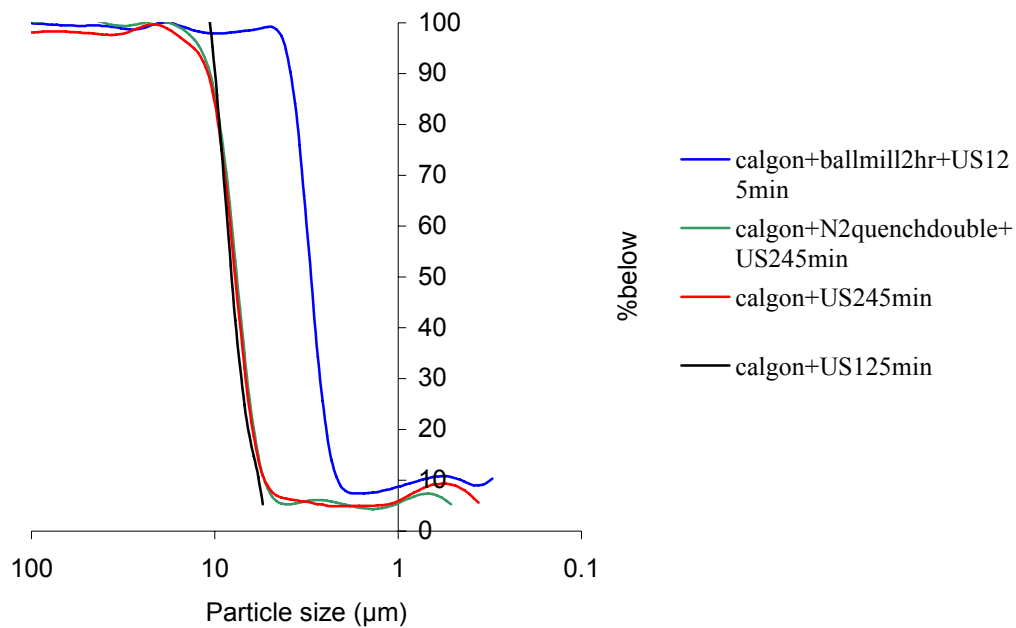


Figure 7.9. Particle size distribution of c-HAp powder (30%) dispersed with liquid nitrogen quenching (double), wet ball milling with zirconia balls, followed by ultrasound, and with 1% calgon as dispersant.

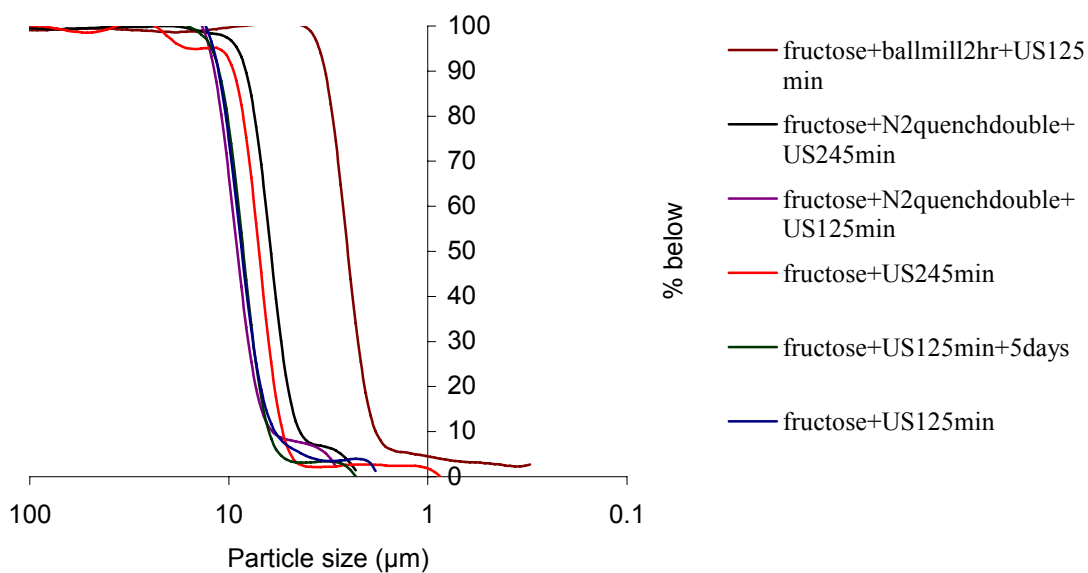


Figure 7.10. Particle size distribution of c-HAp powder (30%) dispersed with liquid nitrogen quenching (double), wet ball milling with zirconia balls, followed by ultrasound, and with 3% fructose as dispersant.

Hydroxyapatite powder PZC, and IEP measurements: The aqueous suspensions of hydroxyapatite powders prepared by wet ball milling, were used for the PZC and IEP measurements. The pH versus the added acid volume for the c-HAp powder, and the m-HAp powder suspensions are given in Figure 7.11a, and Figure 7.11b, respectively. In Figure 7.11a the inflection point was determined to occur at pH=5.71 for the c-HAp powder, and in Figure 7.11b it was at pH=5.47 for the m-HAp powder. These results showed that the surface charges of the c-HAp and m-HAp powders were neutralized at pH 5.71 and 5.47, respectively. These values theoretically correspond to the point of zero charge values of the HA powders. When acid solution was dispensed into the suspension at a determined pace, first the OH⁻ ions were neutralized. Since an equilibrium existed between the charged surfaces of the particles and the OH⁻ ions in the solution, when the OH⁻ ions became scarce in the solution the particle surfaces started to lose their charge. Since the total charge determining ions on the surface were only a small fraction of the total OH⁻ ions initially present in the solution, the rate of change of pH was fastest in the vicinity of the inflection point. When the inflection point was crossed over, the particle surfaces started adsorbing H₃O⁺ ions and became positively charged. The surfaces were saturated with the H₃O⁺ ions which was very fast due to the limited total charge adsorption capacity of the HA surfaces, and after the pH started to decrease due to acidic solution addition. Therefore, the inflection point in the pH versus volume of acid solution added was a good indicator of the PZC.

The zeta potential measurements of the HAp suspensions at various pH values are shown in Figure 7.12a for the c-HAp powder suspension, and Figure 7.12b for the m-HAp powder suspension. The zeta potential, $\zeta=0$ corresponds to the IEP. The IEPs for the c-HAp powder and the m-HAp powder suspensions were determined to be 5.86 and 5.69, respectively. These values indicated that the counterions surrounding the particles screen the surface charge, and the potential at the slip plane was lower than the surface potential. The potential at the slip plane reduced to zero before the surface charge diminished to zero by decreasing pH.

It is possible to calculate the charge carried in the slip plane at the IEP by the difference of the PZC and the IEP. For the commercial powder and the dry milled powder suspensions the calculations are given below.

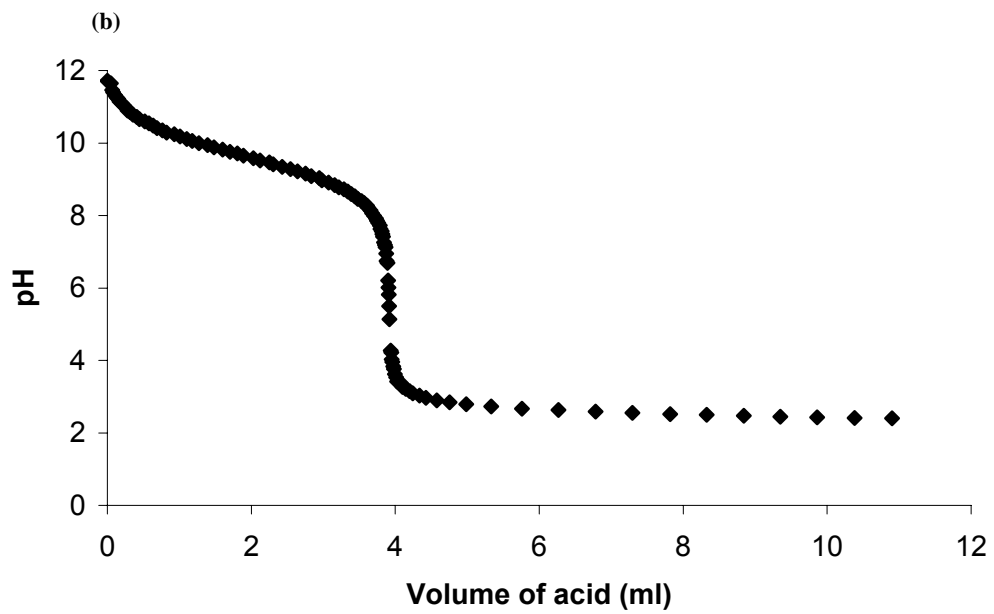
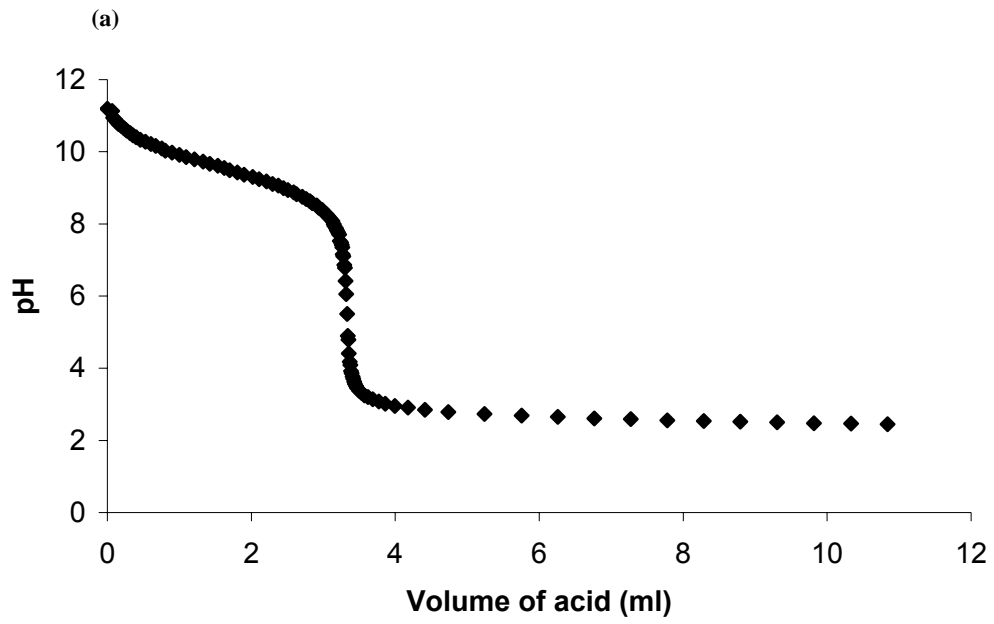


Figure 7.11. pH versus 1.0 N HNO₃ solution volume added obtained by autotitrator for (a) c-HAp powder suspension, (b) m-HAp powder suspension.

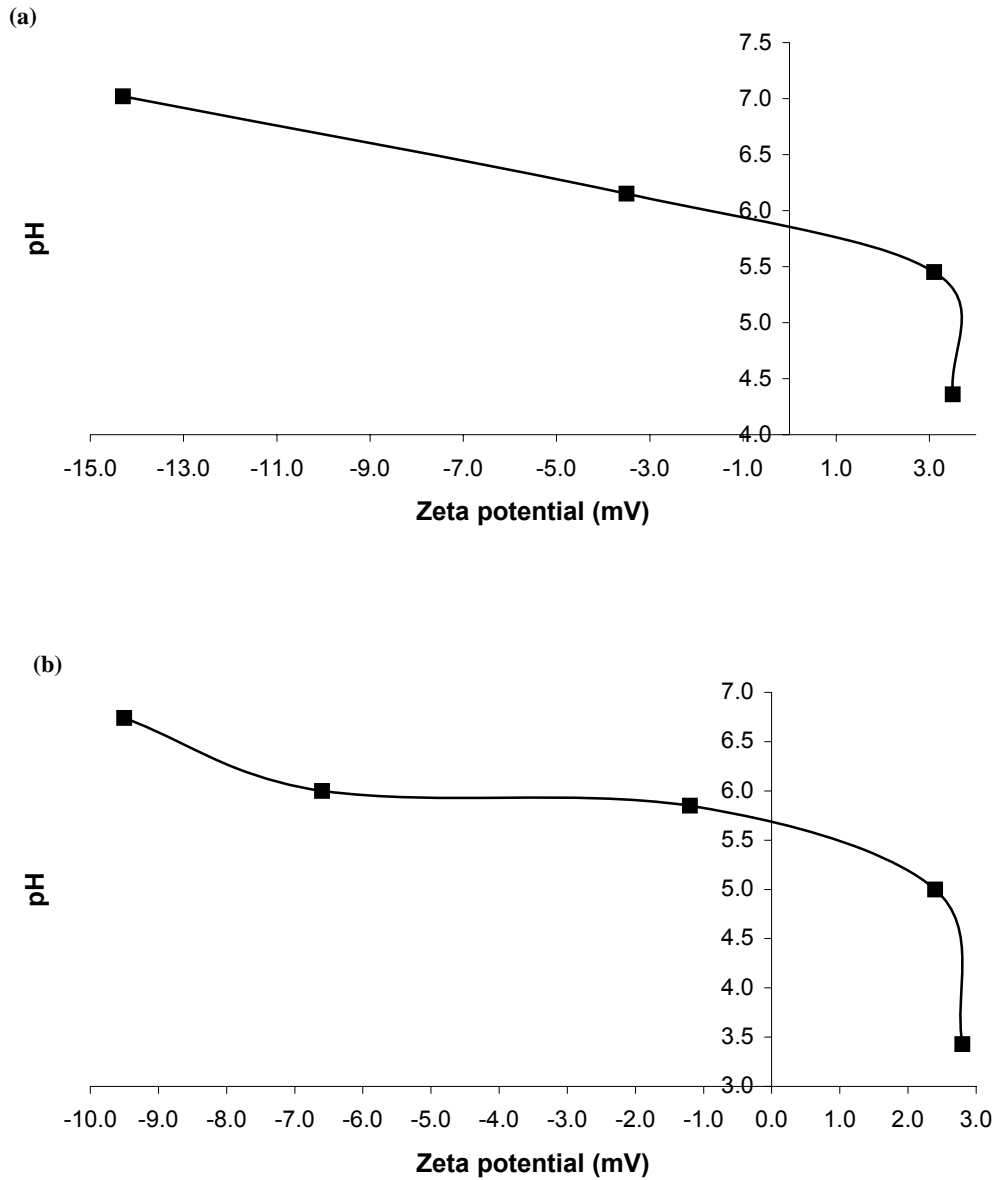


Figure 7.12. pH versus zeta potential for (a) c-HAp powder suspensions, (b) m-HAp powder suspensions.

c-HAp: PZC = 5.71, $[H_3O^+]_{PZC} = 1.95 \times 10^{-6} M$
 IEP = 5.86, $[H_3O^+]_{IEP} = 1.38 \times 10^{-6} M$
 $\Delta[H_3O^+]_{(PZC-IEP)} = 5.70 \times 10^{-7} M$

Charge carried in the slip layer =

$$\left(\frac{1.0L}{0.17grHA} \right) \left(\frac{5.70 \times 10^{-7} molH_3O^+}{L} \right) \left(\frac{6.023 \times 10^{23} protons}{molH_3O^+} \right) \left(\frac{1.602 \times 10^{-19} coul}{proton} \right) = 0.32coul / grHAp$$

$$\begin{aligned}
\text{m-HAp: PZC} &= 5.47, [\text{H}_3\text{O}^+]_{\text{PZC}} = 3.39 \times 10^{-6} \text{M} \\
\text{IEP} &= 5.69, [\text{H}_3\text{O}^+]_{\text{IEP}} = 2.04 \times 10^{-6} \text{M} \\
\Delta[\text{H}_3\text{O}^+]_{(\text{PZC-IEP})} &= 1.35 \times 10^{-6} \text{M}
\end{aligned}$$

Charge carried in the slip layer =

$$\left(\frac{1.0L}{0.17 \text{ grHA}} \right) \left(\frac{1.35 \times 10^{-6} \text{ molH}_3\text{O}^+}{L} \right) \left(\frac{6.023 \times 10^{23} \text{ protons}}{\text{molH}_3\text{O}^+} \right) \left(\frac{1.602 \times 10^{-19} \text{ coul}}{\text{proton}} \right) = 0.77 \text{ coul / grHA}$$

The optimum pH values for the dispersion of c-HAp and dry milled powder suspensions were determined by the laser scattering (zeta sizer) measurements, and the results are shown in Figure 7.13. The pH values for the minimum size agglomerates were in between 10.2 for the c-HAp powder, and 9.4 for the m-HAp powder (120 min. dry milled). The pH for the minimum number mean agglomerate size decreased with the increasing dry milling time and for that matter with the increasing particle surface area.

According to the DLVO theory the colloidal suspensions can be electrostatically stabilized by the double ionic layer repulsion (Brinker and Scherer 1990). The increasing surface negative charge with the increasing pH was counteracted with a concentration of positive counter ions within the double layer. For the suspension systems of HAp examined, there existed threshold values of the negative surface charge (or of pH), beyond which further increase caused an increase in the double layer counter ion charge at a rate higher than the adsorption rate of surface ion charge (most probably beyond the mono layer surface coverage). This, in turn, gradually lowered the absolute value of the zeta potential (ζ) at the slip plane, beyond the threshold pH, resulting in the observed minimums in Figure 7.13.

On the other hand, the increasing surface negative charge with the increasing surface area was counteracted with a concentration of positive counter ions within the double layer, nevertheless, increasing at a rate higher than the increasing surface area. This phenomenon rendered a lower magnitude of negative ζ with the increasing surface area (or decreasing particle size), and the maximums of ζ occurred at lower pH values, corresponding to the minimums in Figure 7.13. Direct measurements confirmed this argument, since $\zeta(\text{c-HAp, pH}=10.2)=-26.3 \text{ mV}$, while $\zeta(\text{m-HAp, pH}=9.4)=-19.9 \text{ mV}$.

The PZCs of the suspensions were determined as the threshold points at which the surface charges of the HAp particles were reversed (from negative to positive) during the continuous automatic titration indicated by the inflection points in the pH versus added acid volume diagrams. The results showed that the surface charges of the c-HAp and m-HAp powders were neutralized at pH 5.71 and 5.47, respectively, which are, in fact, the PZC values. The IEPs for the c-HAp and the m-HAp powder suspensions were determined to be 5.86 and 5.69, respectively, as the pH values corresponding to $\zeta=0$. Since the surface is still negatively charged at the IEP, H_3O^+ ion concentration is to be lower compared to the zero surface charge case, and $\zeta=0$ occurs at a higher pH, hence, $IEP > PZC$ for both of the suspensions. The PZC and IEP of the m-HAp powder were lower as compared to the c-HAp powder indicating a higher surface charge due to the higher surface area of the dry milled powder. The charge carried within the slip plane at the IEP was calculated from the difference of the PZC and the IEP, as +0.32 coul/gr HAp for the c-HAp powder, and +0.77 coul/gr HAp for the m-HAp powder as shown above. An increase in particle surface area of 23% (from 22 m²/gr of the c-HAp powder to 27 m²/gr of the m-HAp powder; estimated geometrically from the SEM images in Figure 7.2) brought about a 2.4 times increase in the slip layer charge. The decreasing particle size (or the increasing particle surface area) reduced the double layer repulsive barrier potential, because of the increased screening of the counter-ions within the double layer, hence deteriorated the suspension stability. It also indicated a higher agglomeration tendency of the dry milled powders as compared to c-HAp during thin film formation when particles were forced to compact together by suspension medium evaporation.

In Figure 7.14 the steric dispersion effect of hydropalate 64, is shown. The agglomerate sizes for all of the powders rapidly decreased until about 1.2% dispersant (hydropalate 64) was added and higher quantities did not significantly affect the deflocculation.

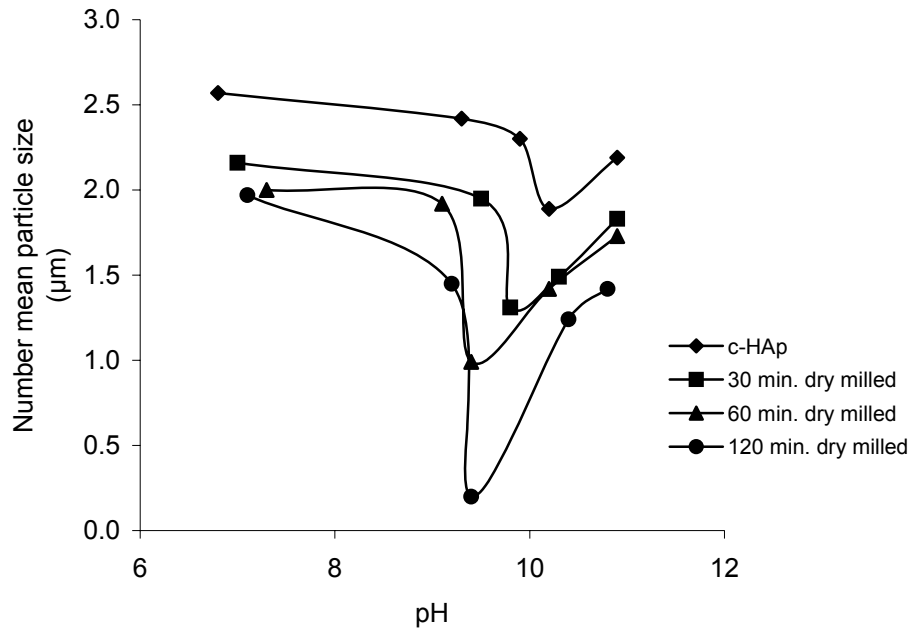


Figure 7.13. Number mean particle size distributions of HAp suspensions as a function of pH, measured by zeta sizer (without any dispersant).

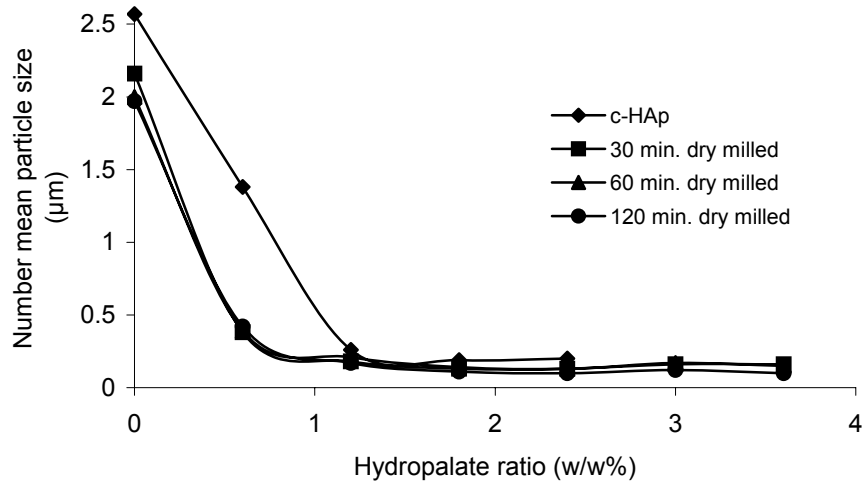


Figure 7.14. Number mean particle size distributions HAp suspensions as a function of hydropalate 64 ratio (organic dispersant), measured by zeta sizer.

7.2. Particulate Sol Route Hydroxyapatite/Silk Protein Thin Film Surface Interactions

The coatings of HAp were prepared on bioinert glass substrates by dip coating. The aqueous suspensions of HAp contained 2.4% hydroxylapatite 64 as the dispersant. The SEM images of the coatings with 1.0% solid content suspensions of c-HAp and m-HAp powders are shown in Figure 7.15, and 7.16, respectively. Both types of the coatings consisted of sporadic lumps of HAp particles, and the substrate surfaces were over 90% empty.

The effect of multi layer coatings with the same powder ratio is shown in Figure 7.17, and 7.18. The 5 layers of coatings, only slightly increased the covered percentage of the substrate area mostly by the thickening and enlargement of the existing aggregates.

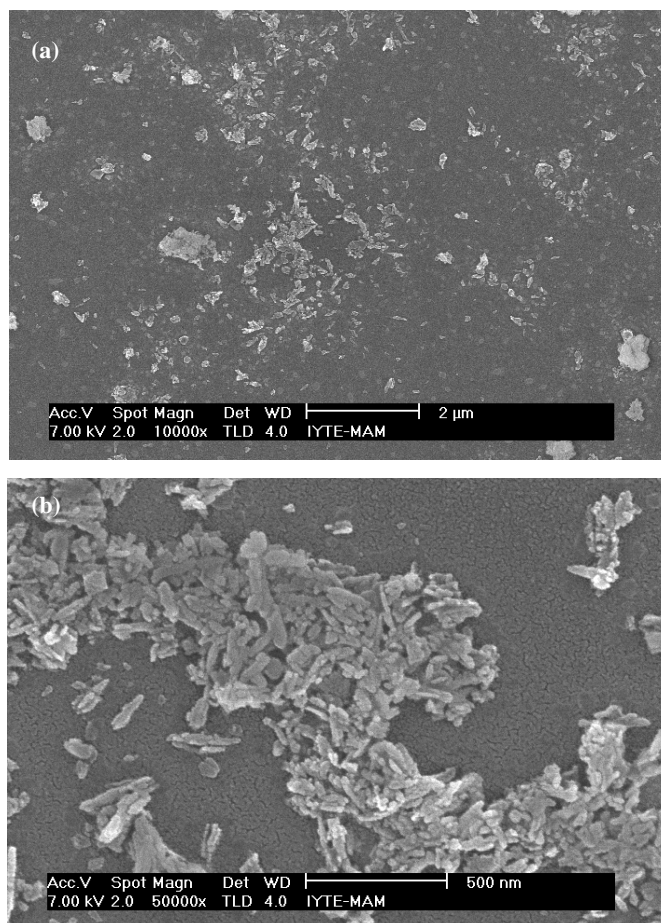


Figure 7.15. The SEM images of c-HAp coating on glass substrates by dip coating in 1.0% solid content suspension at various magnifications.

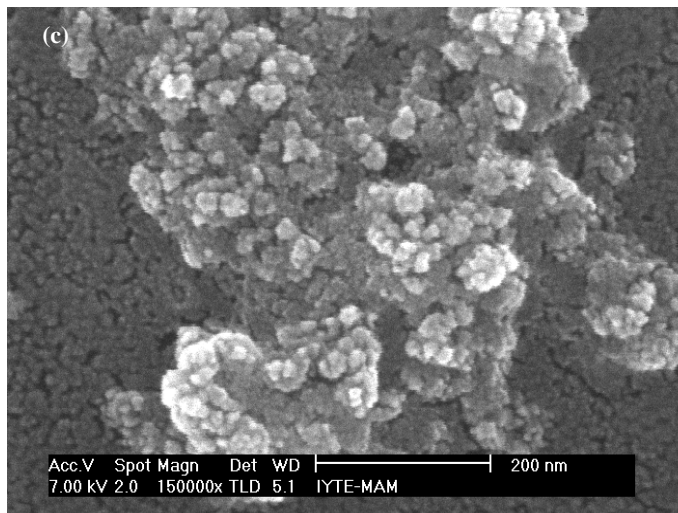
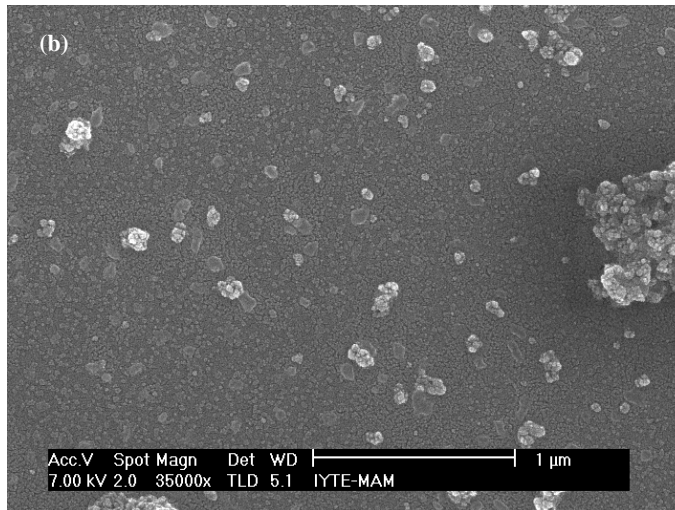
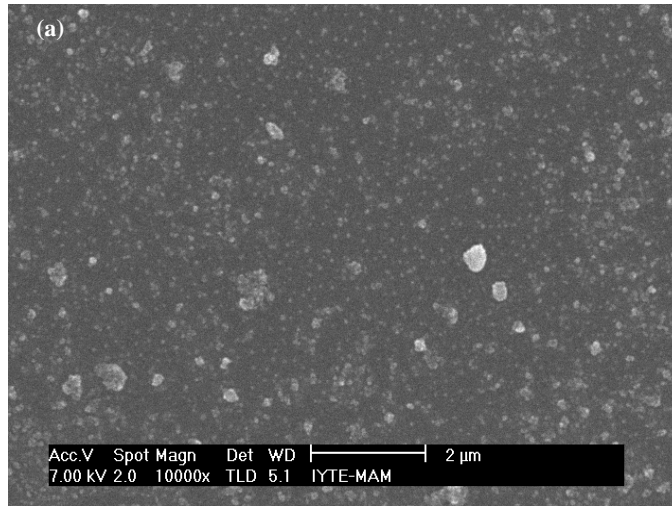


Figure 7.16. The SEM images of m-HAp coating on glass substrates by dip coating in 1.0% solid content suspension at various magnifications.

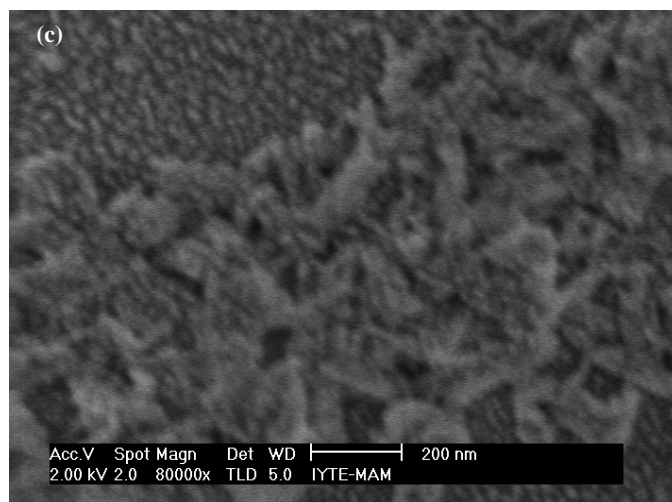
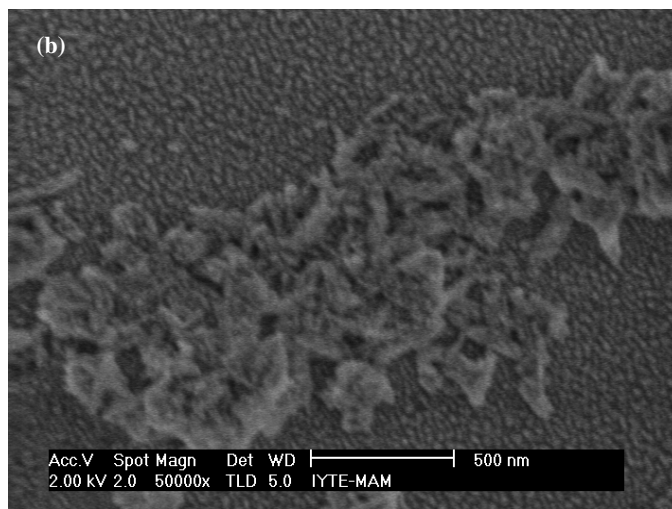
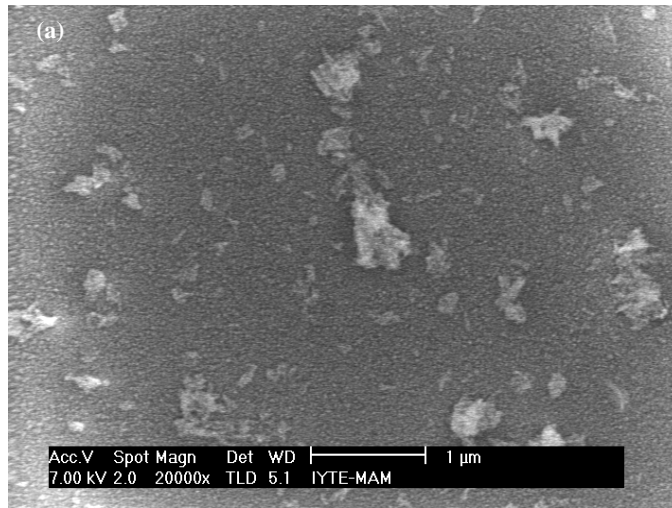


Figure 7.17. The SEM images of the coatings on glass substrates prepared by 5 times dip coating in the 1% c-HAP powder sol at various magnifications.

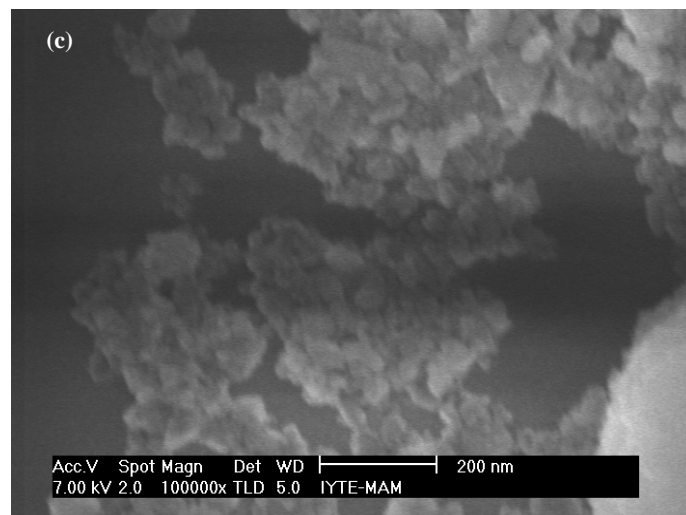
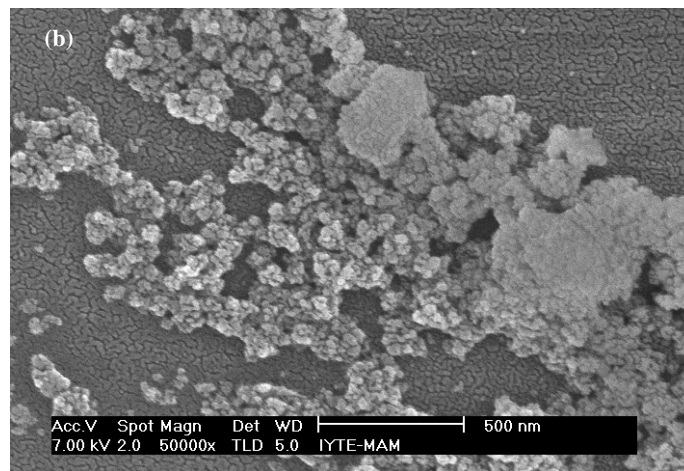
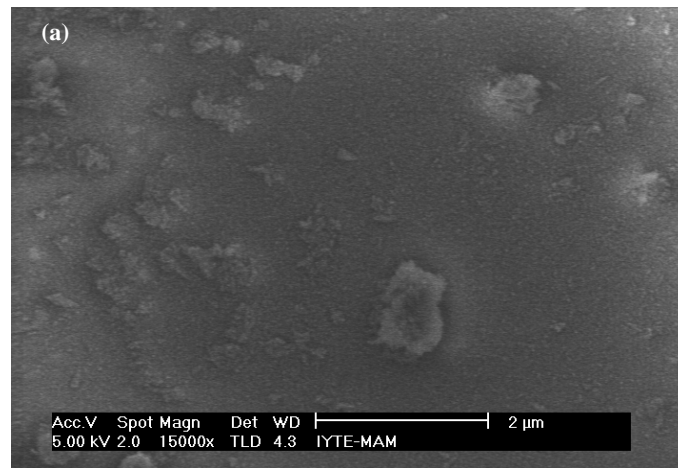


Figure 7.18. The SEM images of the coatings on glass substrates prepared by 5 times dip coating in the 1% m-HAp powder sol at various magnifications.

The minimum solid content of the suspensions was determined to be 15% for complete surface coverage of the substrates coated with c-HAp powder suspension; with the same solid ratio approximately 90% of the substrate surfaces were coated with the m-HAp powder suspension. The SEM images of the thin film coatings prepared with 15% c-HAp and m-HAp powders are given in Figure 7.19 and Figure 7.21, respectively. The maximum agglomerate sizes were determined to be 2 μm for the coatings of c-HAp, and 5 μm for the coatings of the m-HAp. The agglomerates of the sizes from 450 nm to 1 μm were most abundant for both type of coatings. Although the solid content of the m-HAp suspension was the same as the c-HAp suspension, the reason that the substrates coated with the former being slightly short of full surface coverage, was most likely because of the agglomerates larger in size and number, consuming more HAp particles, and depriving the rest of the film of the coating material. The agglomerates larger in number and size in the m-HAp coatings, proved to be an indication of the higher agglomeration tendency, during the drying/particle compaction step of the thin film formation, with increasing surface area, and hence, lower zeta potential of the crushed particles in the suspensions. The AFM images of the similarly prepared c-HAp and m-HAp thin films are given in Figure 7.20 and 7.22, respectively. The topographical and phase images alike showed the same features as SEM images, regarding the primary particle and agglomerate sizes.

The thicknesses of the thin films prepared with the c-HAp powder were determined to be in the range 450 nm to 650 nm, while the ones with the m-HAp were in the range 500 nm to 750 nm.

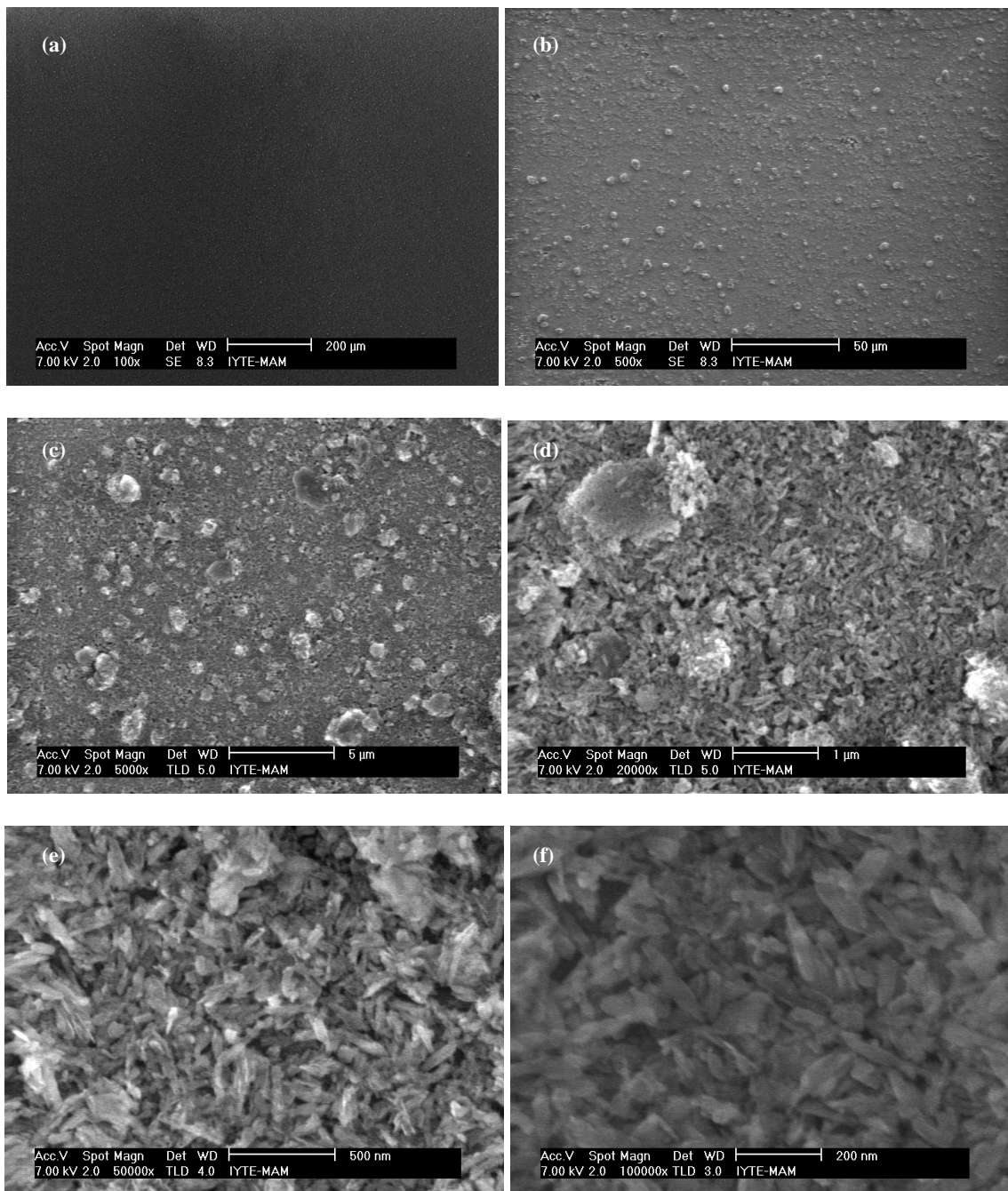


Figure 7.19. The SEM images of the c-HAp coatings on the glass substrates prepared by 15% solid content sol by dip coating, at various magnifications (a) 100x, (b) 500x, (c) 5,000x, (d) 20,000x, (e) the region without agglomerate, 50,000x, (f) the region without agglomerate, 100,000x.

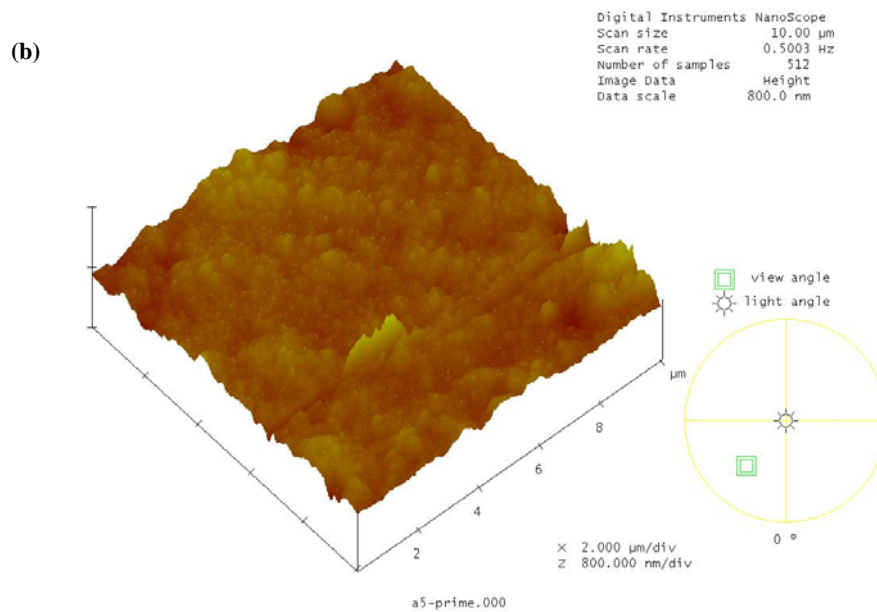
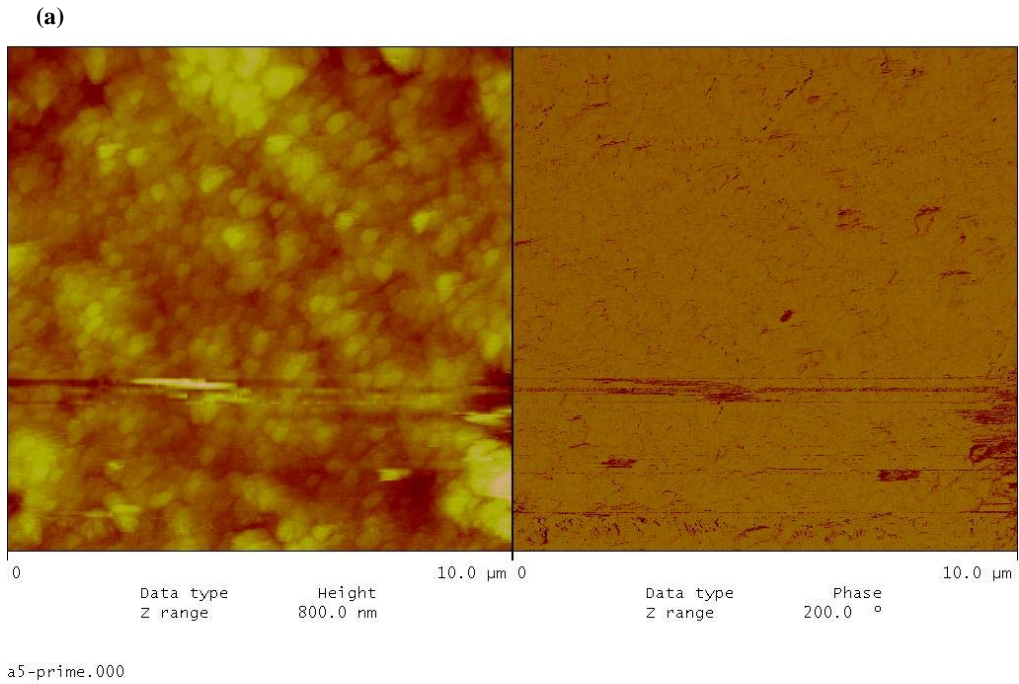


Figure 7.20. The AFM images of the c-HAp coated on the glass substrates prepared by 15% solid content sol by dip coating (a) 2-dim. topographical and phase images 10x10 μm, (b) 3-dim. topographical image 10x10 μm, (c) 2-dim. topographical and phase images 1.96x1.96 μm, (d) 3-dim. topographical image 1.96x1.96 μm.

(cont. on next page)

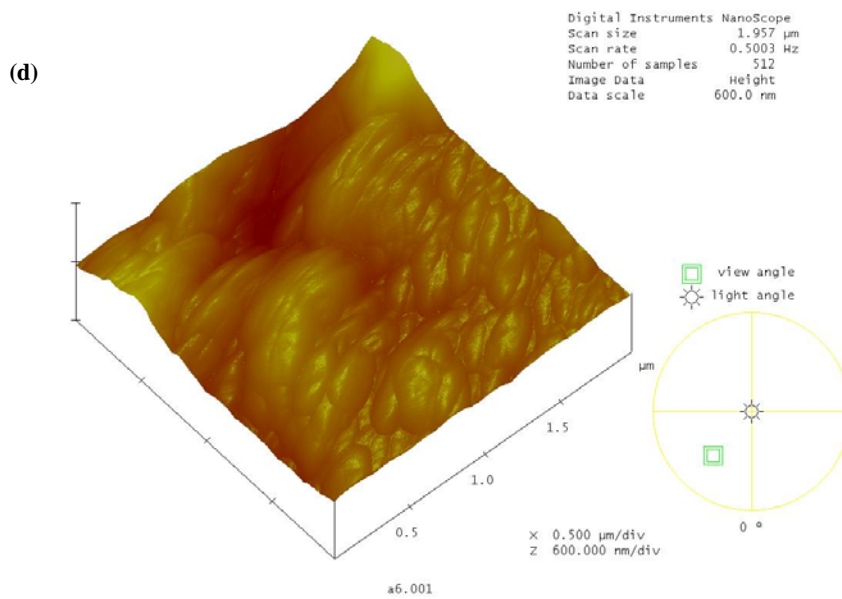
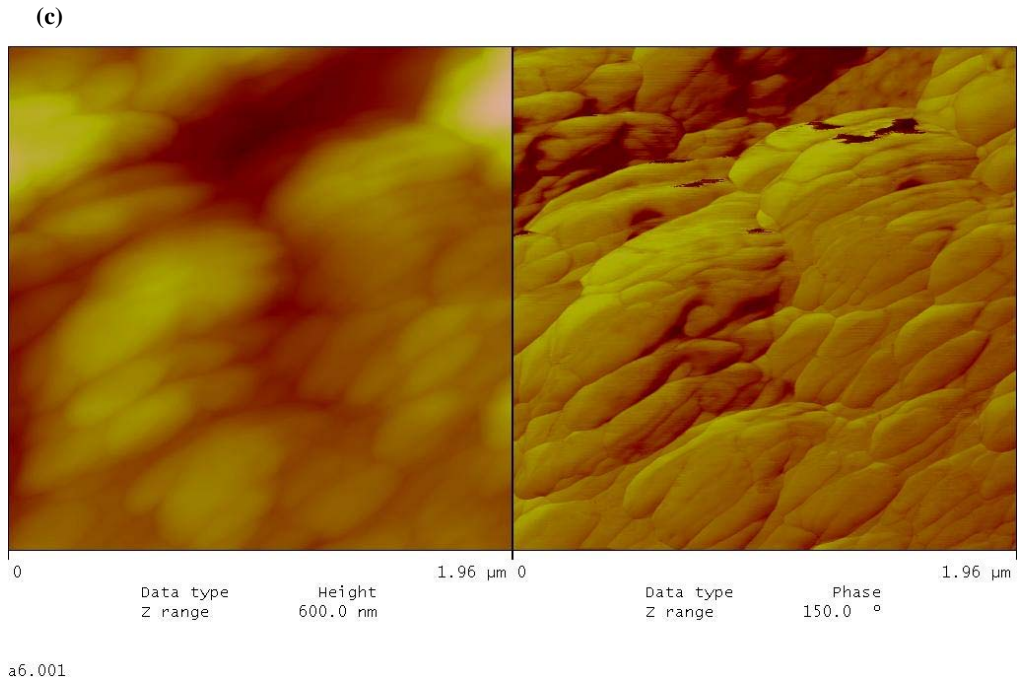


Figure 7.20. (cont.) The AFM images of the c-HAp coated on the glass substrates prepared by 15% solid content sol by dip coating (a) 2-dim. topographical and phase images $10 \times 10 \mu\text{m}$, (b) 3-dim. topographical image $10 \times 10 \mu\text{m}$, (c) 2-dim. topographical and phase images $1.96 \times 1.96 \mu\text{m}$, (d) 3-dim. topographical image $1.96 \times 1.96 \mu\text{m}$.

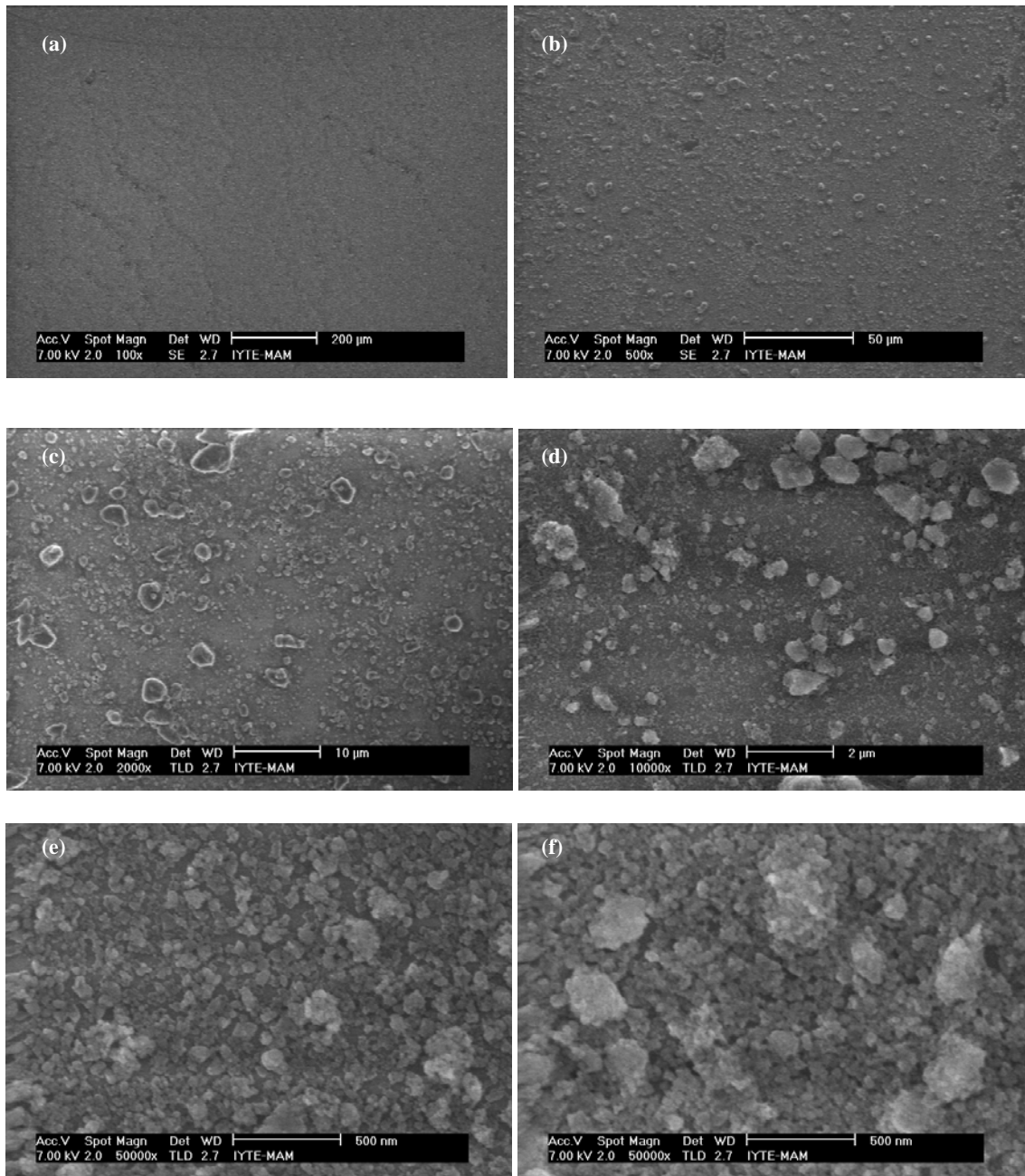


Figure 7.21. The SEM images of the m-HAp coatings on the glass substrates prepared by 15% solid content sol, by dip coating at various magnifications (a) 100x, (b) 500x, (c) 2,000x, (d) 10,000x, (e) 50,000x, depicts region short of full surface coverage, (f) 50,000x, (g) the region with homogeneously distributed voids, (g) the region without agglomerate, 150,000x, (h) the agglomerate, 100,000x. (i) m-HAp particles.

(cont. on next page)

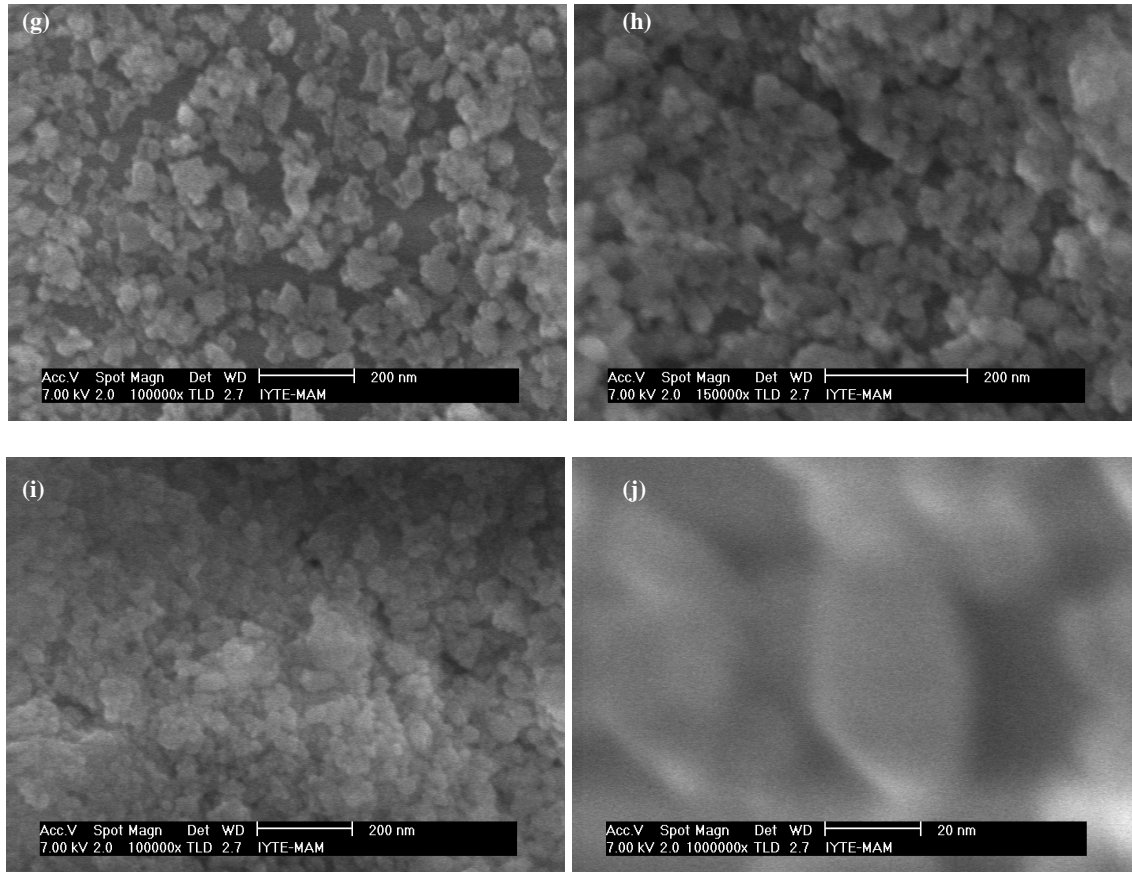


Figure 7.21. (cont.) The SEM images of the m-HAp coatings on the glass substrates prepared by 15% solid content sol, by dip coating at various magnifications (a) 100x, (b) 500x, (c) 2,000x, (d) 10,000x, (e) 50,000x, depicts region short of full surface coverage, (f) 50,000x, (g) the region with homogeneously distributed voids, (g) the region without agglomerate, 150,000x, (h) the agglomerate, 100,000x. (i) m-HAp particles.

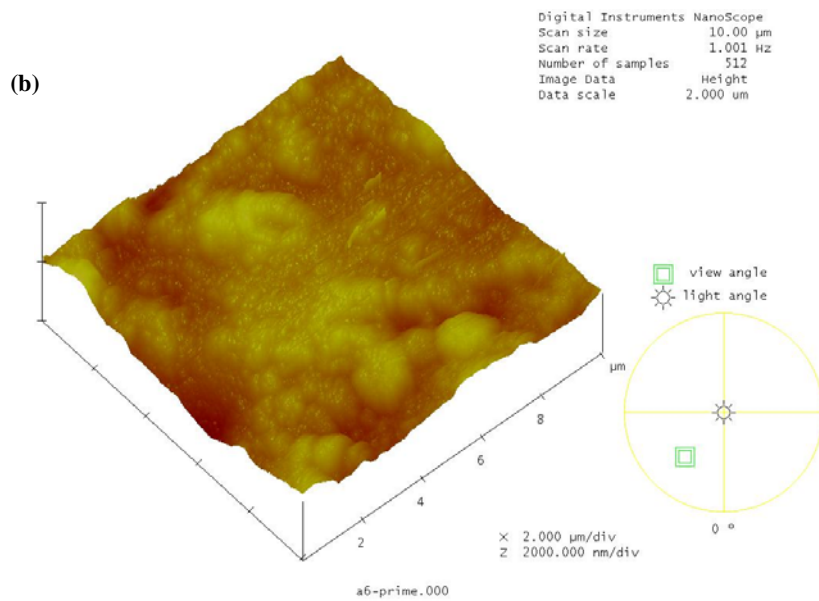
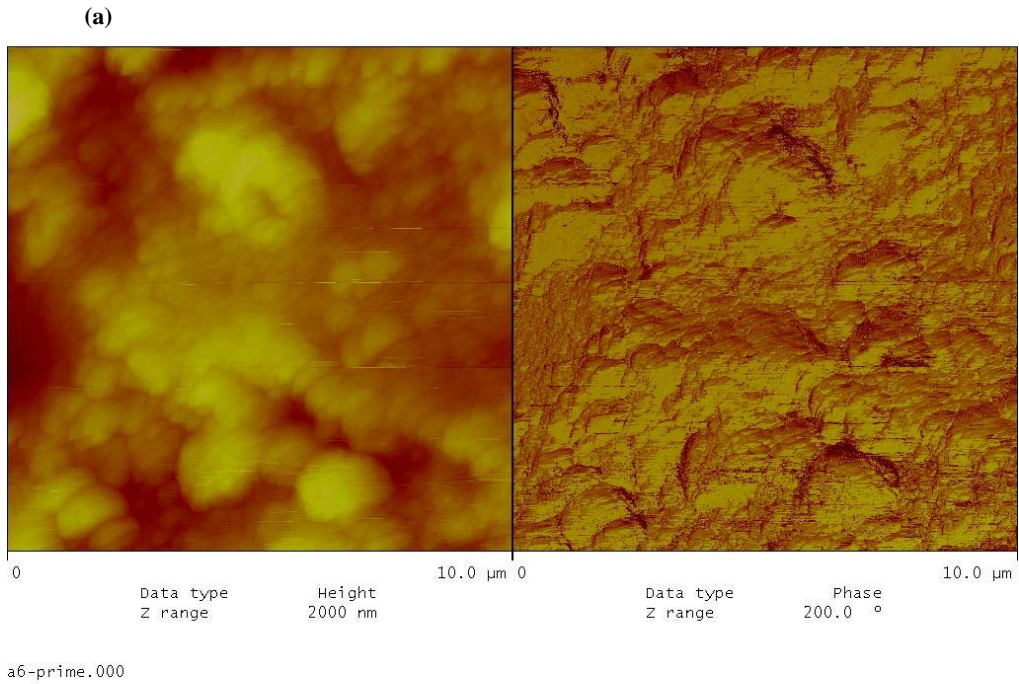
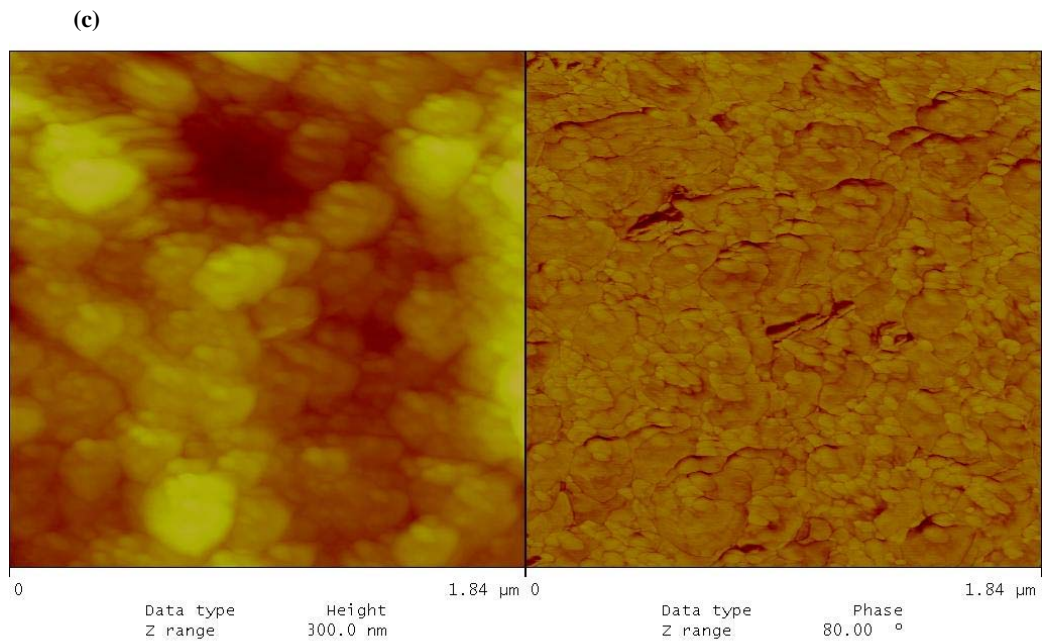


Figure 7.22. The AFM images of the m-HAp coatings on the glass substrates prepared by 15% solid content sol by dip coating (a) 2-dim. topographical and phase images 10x10 μm, (b) 3-dim. topographical image 10x10 μm, (c) 2-dim. topographical and phase images 1.84x1.84 μm, (d) 3-dim. topographical image 1.84x1.84 μm.

(cont. on next page)



a5-prime.001

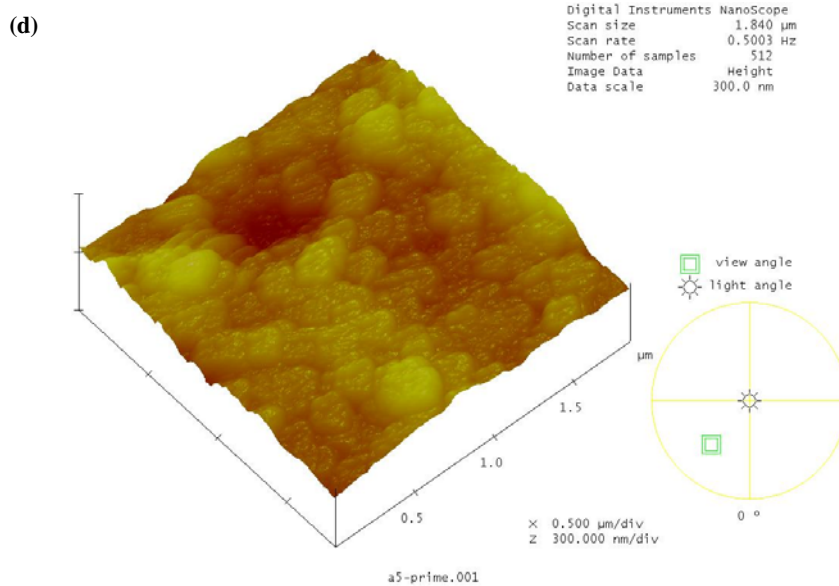


Figure 7.22. (cont.) The AFM images of the m-HAp coatings on the glass substrates prepared by 15% solid content sol by dip coating (a) 2-dim. topographical and phase images $10 \times 10 \mu\text{m}$, (b) 3-dim. topographical image $10 \times 10 \mu\text{m}$, (c) 2-dim. topographical and phase images $1.84 \times 1.84 \mu\text{m}$, (d) 3-dim. topographical image $1.84 \times 1.84 \mu\text{m}$.

When the solid content of the m-HAp suspension was increased to 25%, the film coatings of about 2.4 μm thick were obtained as shown in Figure 7.23. At this solid content of the suspension the tendency for the particles to coat the surface in agglomerated forms was more pronounced. The surfaces of these dip coated thick films were riddled with cracks of length well over micrometer.

Figure 7.24, and 7.25 shows the effect of heat treatment, at 560°C, for 30 minutes with a heating ramp rate of 15°C/min, on the thin films prepared with 15% solid ratio suspensions of c-HAp and m-HAp powders, respectively. There were no cracks forming de novo, or propagating. Nevertheless, the onset of sintering, particles fusing together, could be seen in Figure 7.24f and 7.25g, for c-HAp and m-HAp coatings, respectively.

The effects of heat treatment on the film prepared with the 25% of the m-HAp suspension can be seen in Figure 7.26. The width and the length of the cracks increased along with the partial fusion of the particles during sintering as seen in Figure 7.26c and 7.26d.

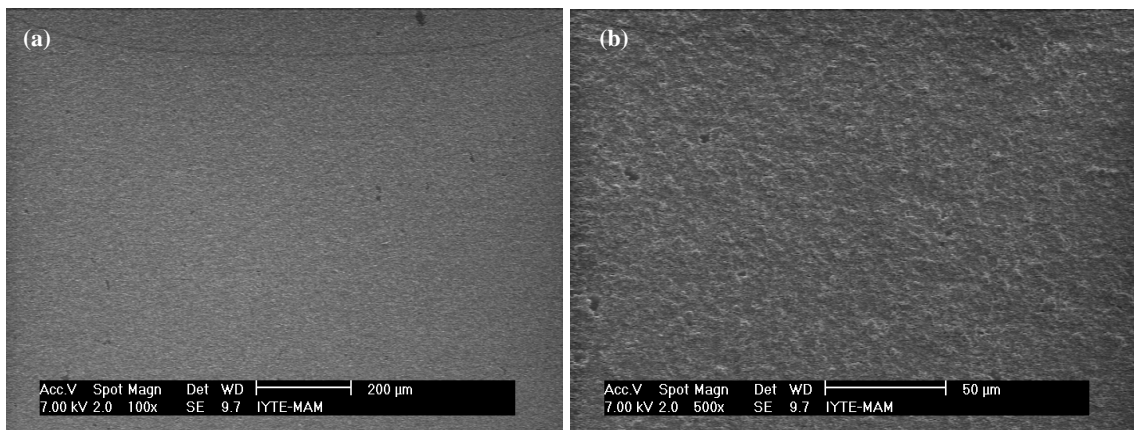


Figure 7.23. The SEM images of the m-HAp coated on the glass substrates prepared by 25% solid content sol by dip coating at various magnifications (a) 100x, (b) 500x, (c) 2,000x, (d) 5,000x, (e) 10,000x, (f) 20,000x, (g) 50,000x, (h) 100,000x.

(cont. on next page)

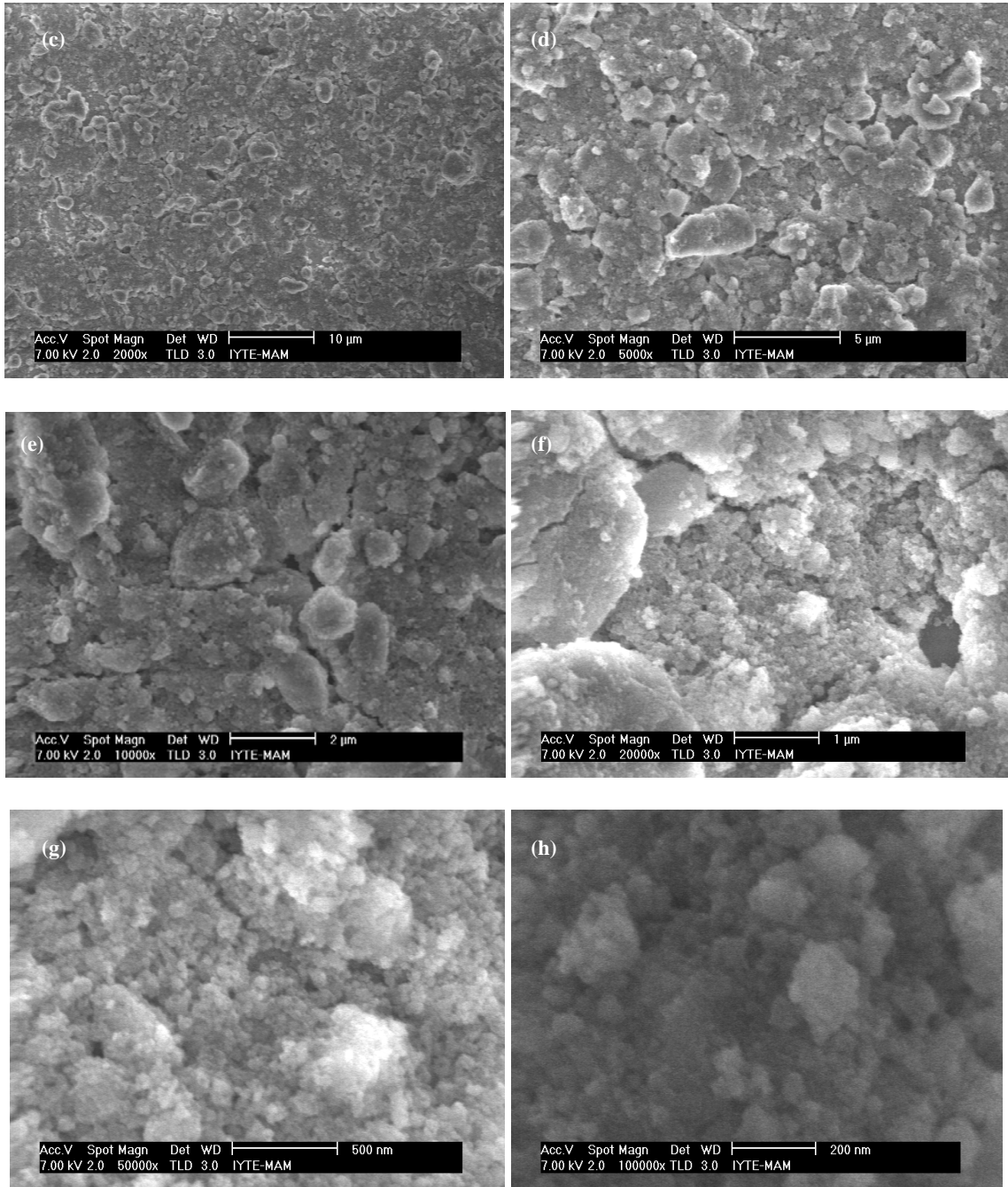


Figure 7.23. (cont.) The SEM images of the m-Hap coated on the glass substrates prepared by 25% solid content sol by dip coating at various magnifications (a) 100x, (b) 500x, (c) 2,000x, (d) 5,000x, (e) 10,000x, (f) 20,000x, (g) 50,000x, (h) 100,000x.

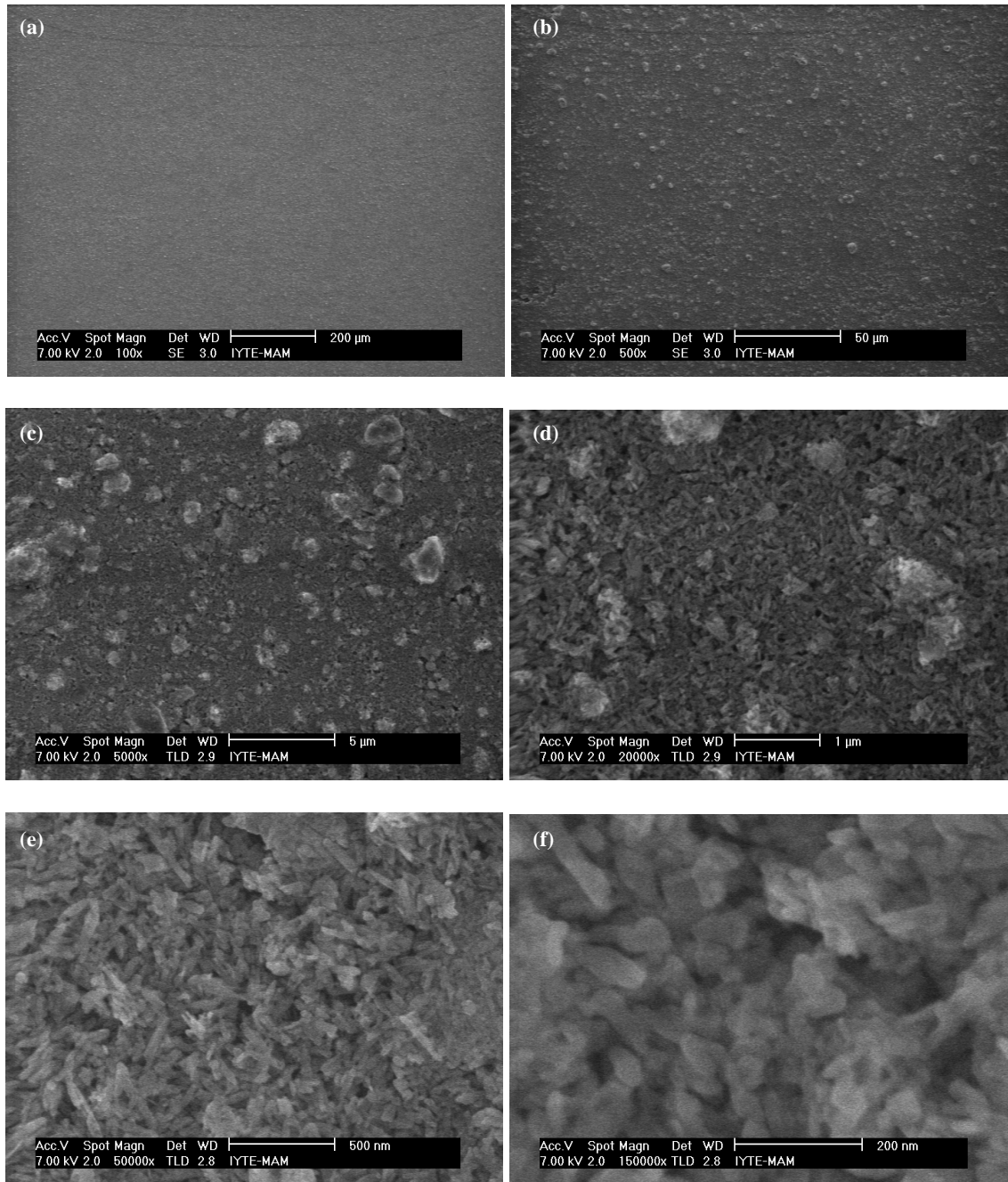


Figure 7.24. The SEM images of the thin films prepared with 15% c-HAp suspension after the heat treatment at 560°C, for 30 min. with a heating rate of 15°C/min at various magnifications (a) 100x, (b) 500x, (c) 5,000x, (d) 20,000x, (e)50,000x, (f) 150,000x.

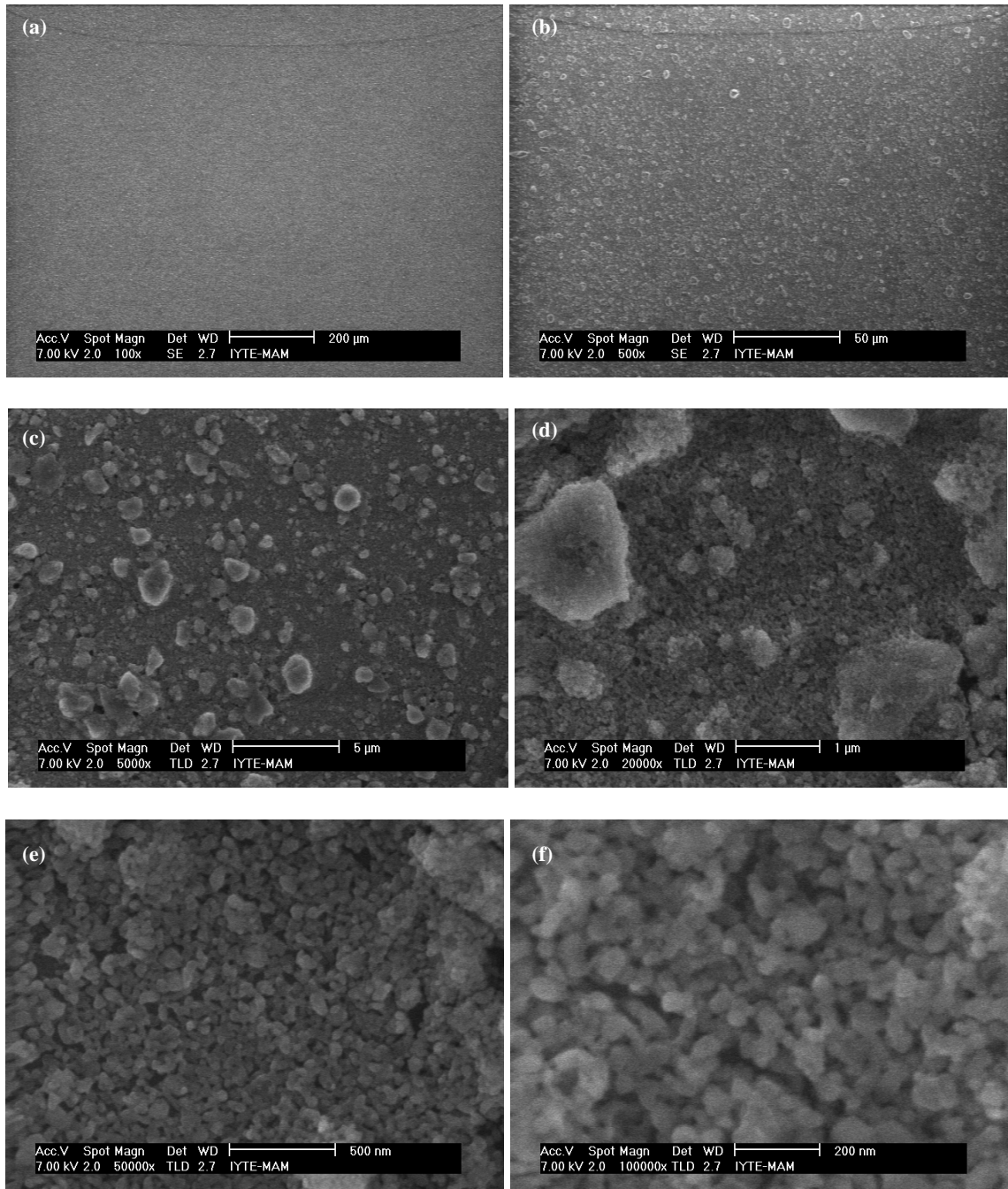


Figure 7.25. The SEM images of the thin films prepared with 15% m-HAp suspension after the heat treatment at 560°C, for 30 min. with a heating rate of 15°C/min at various magnifications (a) 100x, (b) 500x, (c) 5,000x, (d)20,000x, (e)50,000x, (f)100,000x, (g)150,000x, (h) agglomerate, 120,000x.

(cont. on next page)

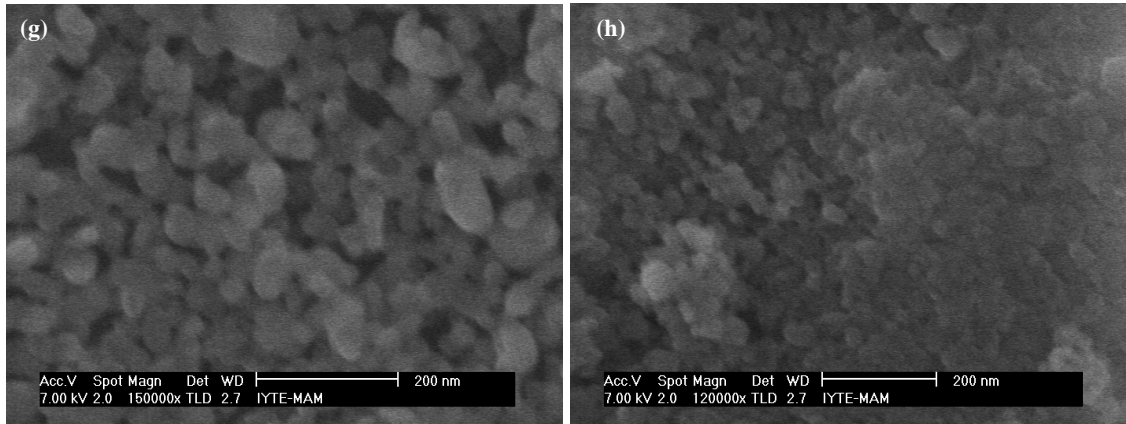


Figure 7.25. (cont.) The SEM images of the thin films prepared with 15% m-HAp suspension after the heat treatment at 560°C, for 30 min. with a heating rate of 15°C/min at various magnifications (a) 100x, (b) 500x, (c) 5,000x, (d)20,000x, (e)50,000x, (f)100,000x, (g)150,000x, (h) agglomerate, 120,000x.

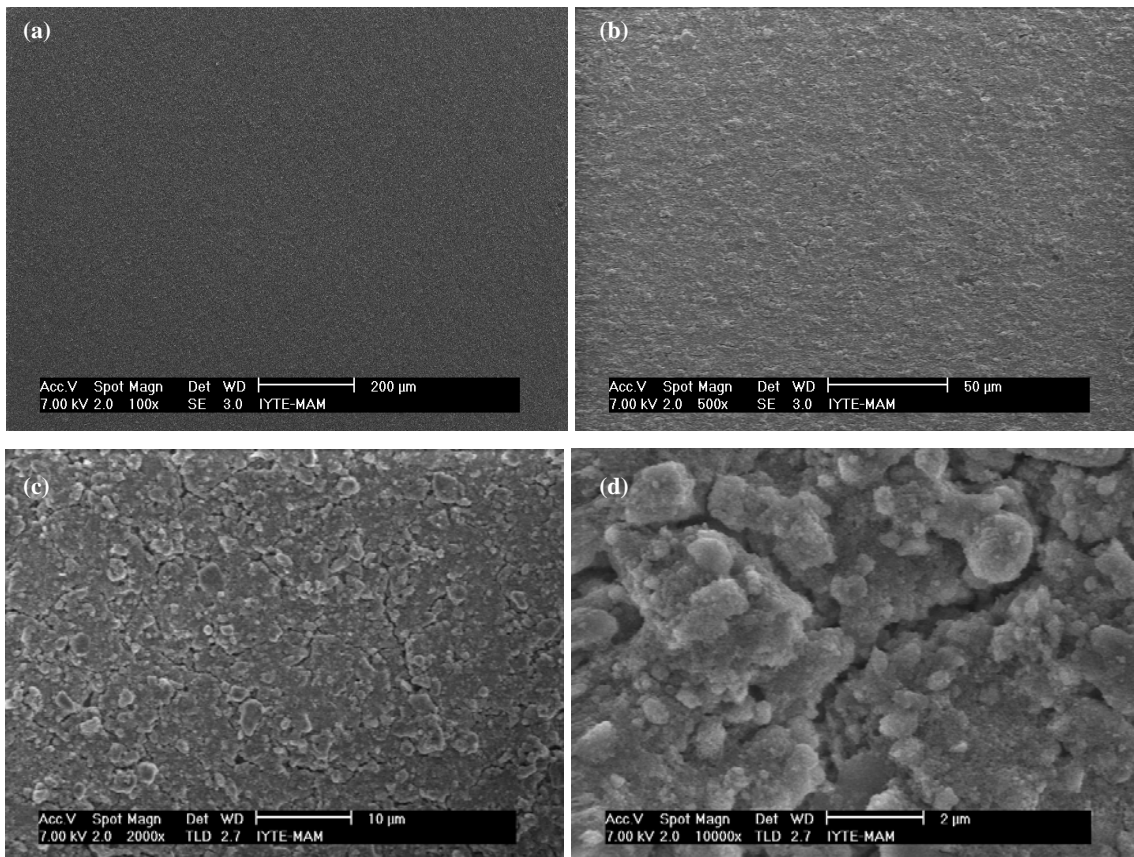


Figure 7.26. The SEM images of the thick film prepared with 25% m-HAp suspension, after the heat treatment at 560°C, for 30 min. with a heating rate of 15°C/min, at various magnifications (a) 100x, (b) 500x, (c) 2,000x, (d) 10,000x.

Thin Film Characterization by XRD and FTIR: XRD and FTIR were employed for the characterization of the thin films. The thin film grazing incidence XRD patterns of the c-HAp and m-HAp coatings before, and after the heat treatment at 560°C for 30 min are given in Figure 7.27 and Figure 7.28, respectively. All of the patterns were identified as hydroxyapatite, the peaks of which superimposed on the broad peak that belonged to the amorphous glass substrate. The major peaks in all of the patterns were at 2θ values of 32.9, 32.2, 31.8, 28.9, 25.9 degrees. The relative intensities of the peaks of c-HAp films at $2\theta=32.9, 32.2, 31.8$ degrees were lower, in comparison to m-HAp films. The peaks at $2\theta=28.9$ and 25.9 coincided with the broad peak of the glass substrate, and their relative intensities were inconclusive. The relative peak intensities of the heat treated (560°C, 30 min) films were slightly higher as compared to their counterparts, which might have been due to crystal size increase. However, heat treatment had no detectable effects on the crystallinity of the hydroxyapatite films, and there were not any phase changes, as can be expected. The chemistry of the c-HAp and the m-HAp surfaces were thus taken as identical (Santos, et al. 2008).

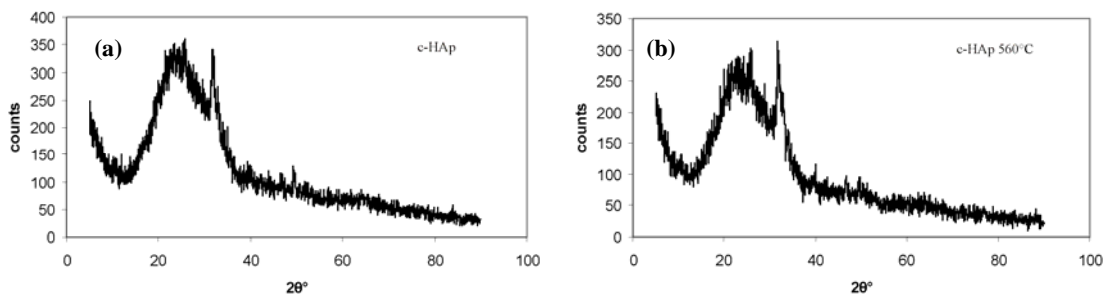


Figure 7.27. (a) Grazing incidence XRD pattern of the glass/c-HAp thin film, (b) the same film heat treated at 560°C for 30 min.

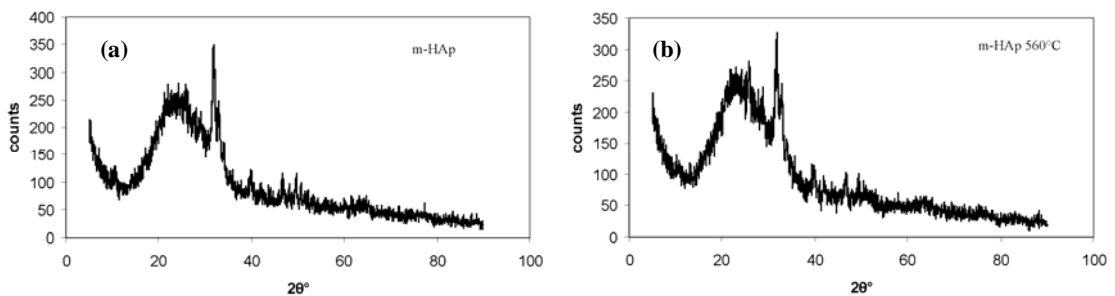


Figure 7.28. (a) Grazing incidence XRD pattern of the glass/m-HAp thin film, (b) the same film heat treated at 560°C for 30 min.

The FTIR spectrum of the bulk commercial powder is given in Figure 7.29. The FTIR spectra (obtained in the grazing mode) of the thin films are given in Figure 7.30 and 7.31. All the major peaks matched to the bulk hydroxyapatite (PO_4^{3-} and OH^- peaks between $650\text{-}530\text{ cm}^{-1}$, PO_4^{3-} peaks between $1050\text{-}970\text{ cm}^{-1}$).

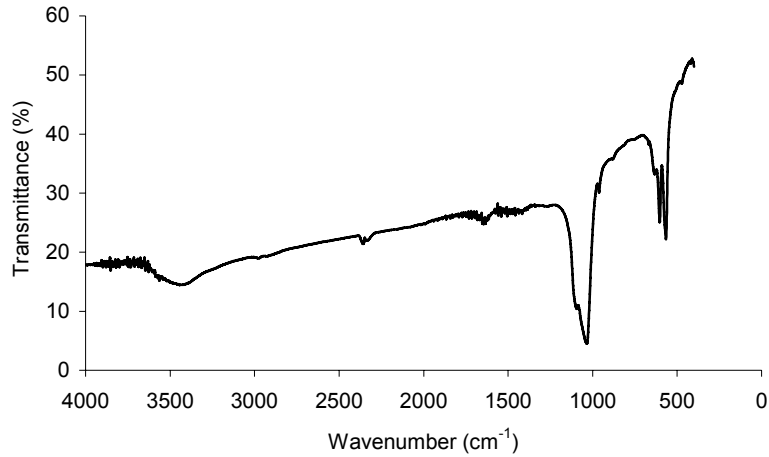


Figure 7.29. FTIR spectrum of bulk commercial hydroxyapatite (c-HAp) powder.

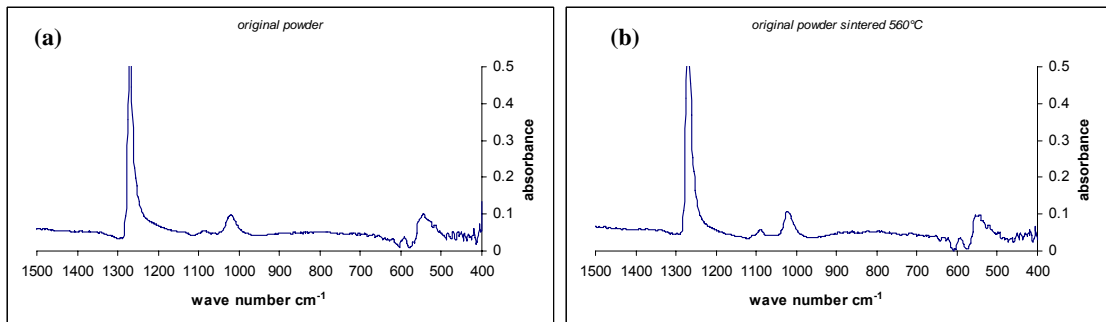


Figure 7.30. (a) The FTIR spectrum of the glass/c-HAp thin film, (b) the same film heat treated at 560°C for 30 min.

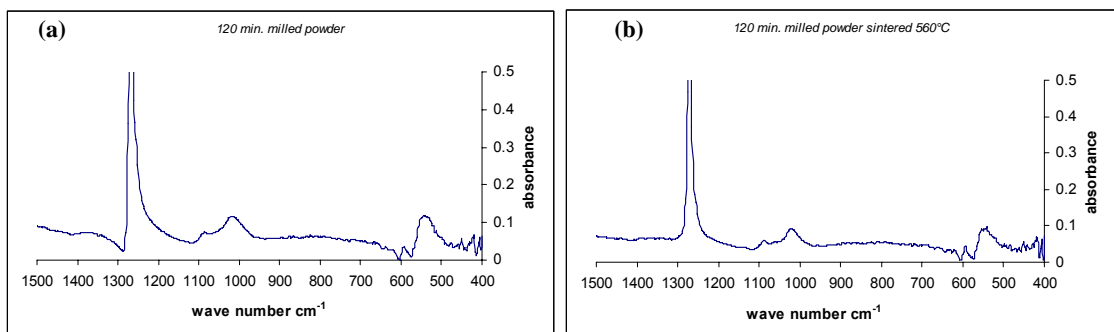


Figure 7.31. (a) The FTIR spectrum of the glass/m-HAp thin film, (b) the same film heat treated at 560°C for 30 min.

The FTIR spectra of the sericin and fibroin films on glass substrates (Figure 7.32) showed amide I (C=O stretching), and amide II (N-H in-plane bending) vibrations. The amide III peaks coincided with the signal from the glass. The amide I ν C=O peaks at 1645 cm^{-1} for the fibroin film and at 1640 cm^{-1} for the sericin film and shoulders at 1626 cm^{-1} for both films, and the amide II δ N-H peaks at 1535 cm^{-1} and shoulders at 1525 cm^{-1} and 1517 cm^{-1} for both films were attributed to the β -sheet structures of the proteins rather than random coil structures (Takeuchi, et al. 2005, Hofmann, et al. 2006).

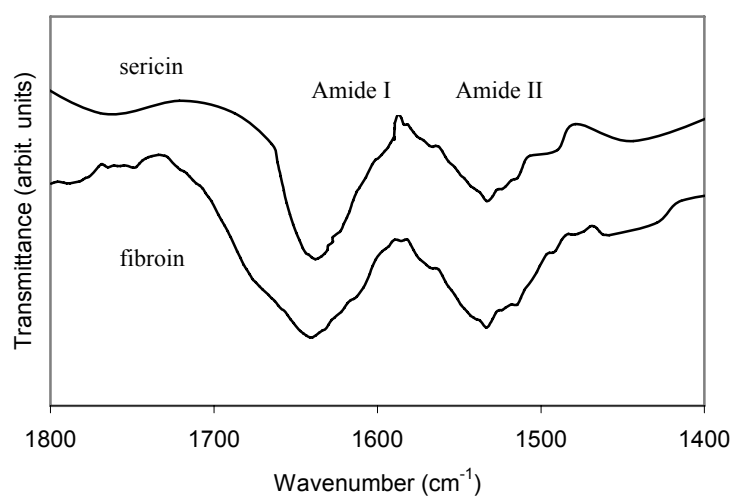


Figure 7.32. The FTIR spectra of sericin and fibroin films on glass substrates.

The SEM images of the sericin, and fibroin films on the glass are shown in Figure 7.33, and 7.35, respectively. Both of the films were transparent, and featureless, hence the specs and scratches were included in the images on purpose (the electron beam burn darkened square patch is also visible in Figure 7.33c). The thicknesses of the sericin films were determined to be $2\text{ }\mu\text{m}$ and that of the fibroin films were $1.5\text{ }\mu\text{m}$ on the average.

The topographical AFM image for the sericin film on the glass substrate (Figure 7.34) showed a granular total surface coverage with the average granular size being in the range of $150\text{-}250\text{ nm}$, and sporadic agglomerates in the range of $400\text{-}600\text{ nm}$. The phase images (Figure 7.34) indicated a homogeneous surface with insignificant

agglomeration. This phenomenon is most likely due to an isotropic structure exhibiting abrupt thickness differences in a short traversed distance.

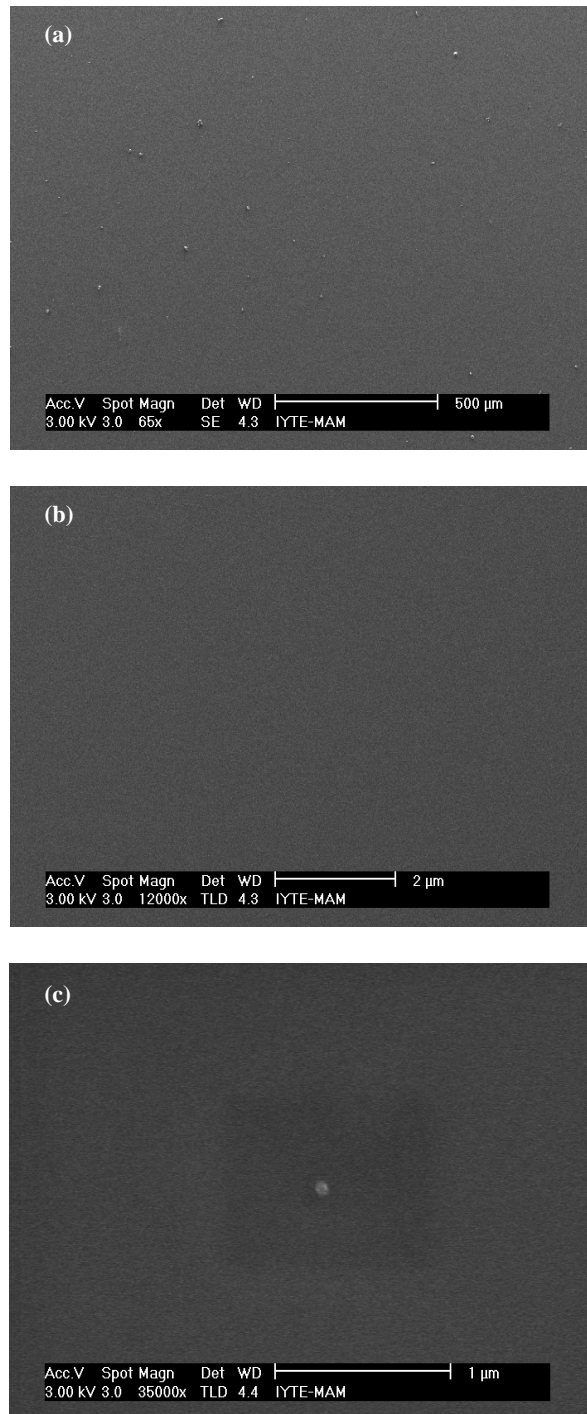


Figure 7.33. The SEM images of the sericin film on glass substrate at various magnifications (a) 65x, (b) 12000x, (c) 35,000x, the organic film burned out in a rectangle shape by the electron beam.

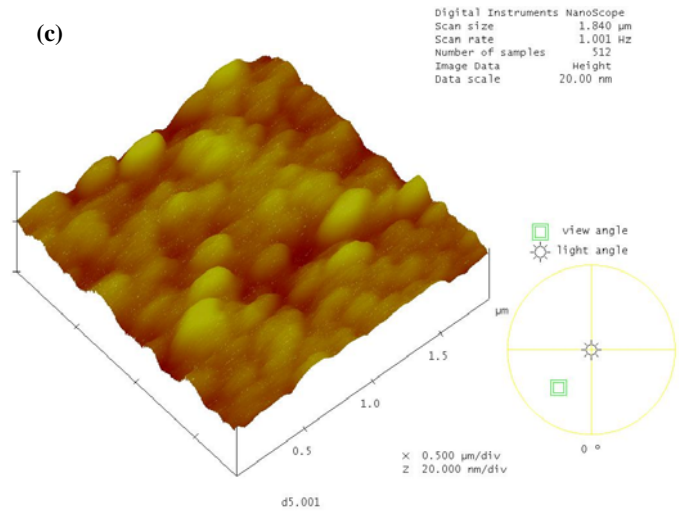
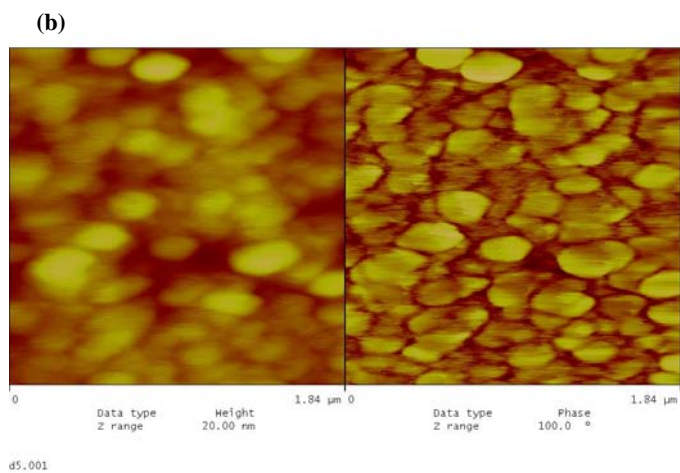
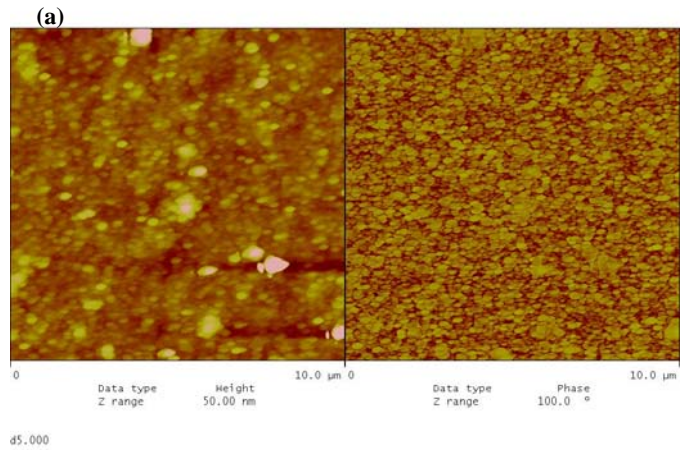


Figure 7.34. The AFM images of the sericin film on glass, (a) 2-dim. topographical and phase images 10x10 μm , (b) 2-dim. topographical and phase images 1.84x1.84 μm , (c) 3-dim. topographical image 1.84x1.84 μm .

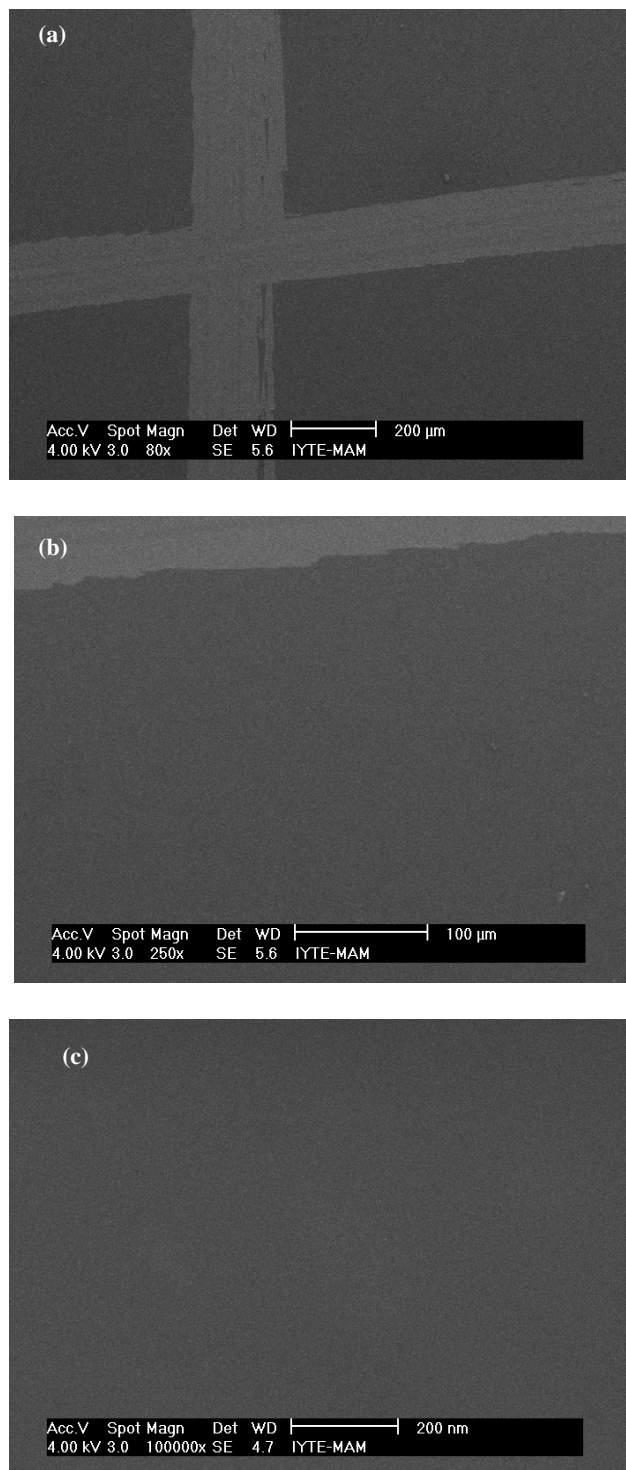


Figure 7.35. The SEM images of the fibroin film on glass at various magnifications (a) 80x, (b) 250x, (c) 100,000x

The AFM image for the fibroin film on glass substrate (Figure 7.36) showed that the surface was totally covered with fibroin and with discernable grains of sizes 100-200 nm. The grains tend to align in straight lines reminiscent of fibrous structures. The topographical image showed sporadic lumps of fibroin agglomerates in the range of

400-600 nm while the phase image did not indicate such agglomeration. This again most probably points out to a fluctuating thickness of an isotropic film.

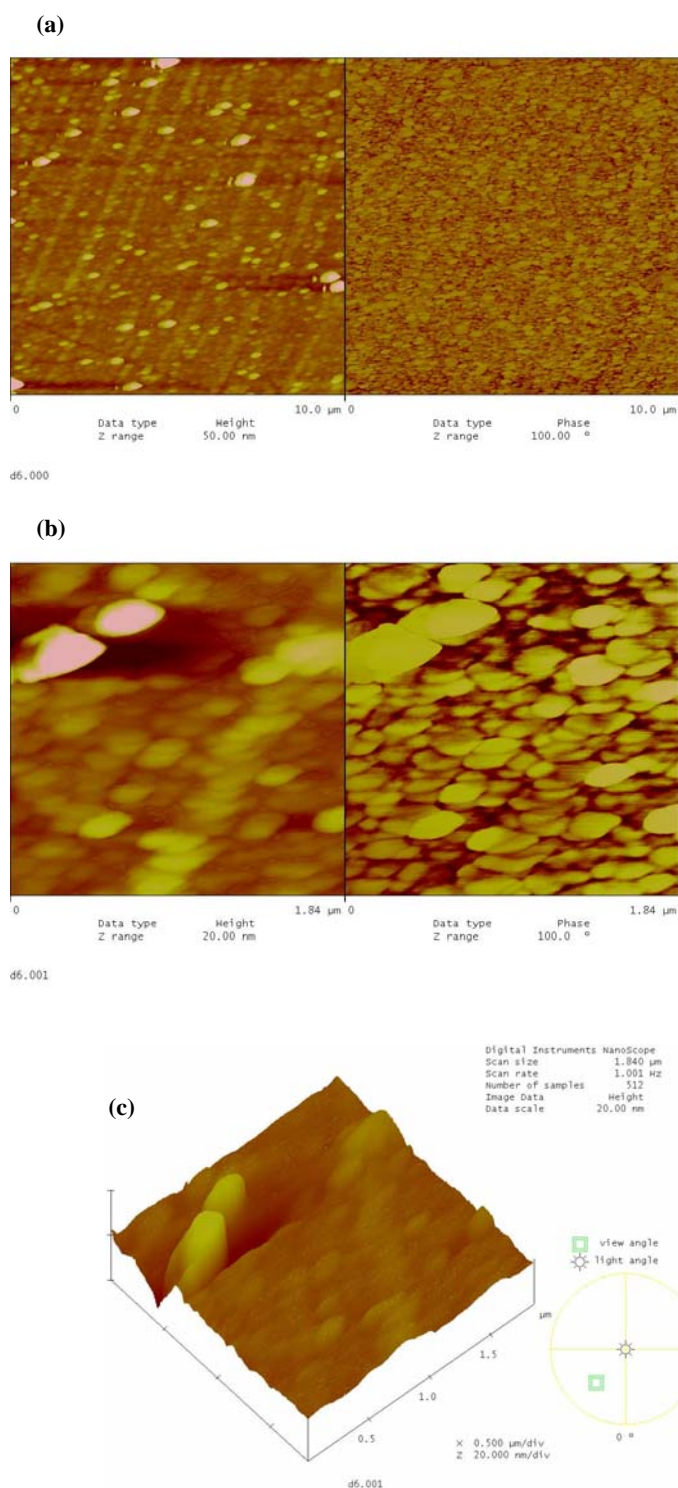


Figure 7.36. The AFM images of the fibroin film on glass substrate, (a) 2-dim. topographical and phase images 10x10 μm, (b) 2-dim. topographical and phase images 1.84x1.84 μm, (c) 3-dim. topographical image 1.84x1.84 μm.

These sericin and fibroin coated glasses were used as substrates for the dip coating of 15% solid content suspensions of c-HAp, and m-HAp particulate sols. The films coated on the glass/sericin substrates were totally transparent, while the films coated on the glass/fibroin substrates were slightly opacified.

The SEM images of the c-HAp films on glass/sericin substrates are shown in Figure 7.37. The films were decisively more homogeneous as compared to their counterparts coated on the glass substrates. The agglomerate sizes were also less than 300 nm explaining the visible light transparency of the films. The surfaces were predominantly covered by primary particles, and the thickness of the HAp layer on top of the sericin layer was measured to be 150-200 nm, indicating a film of 3-4 layers of primary particles compaction.

The AFM images of the c-HAp films are given in Figure 7.38. The phase image showed the same homogeneous feature of the films. The agglomerate like structures in the topographical images were most probably due to the fluctuating thickness differences of the intermediate sericin film.

The SEM images of the m-HAp films on glass/sericin substrates are shown in Figure 7.39. Again the films were decisively more homogeneous as compared to their counterparts coated on glass substrates. However, the surfaces were covered predominantly by agglomerates, evidencing the increased agglomeration tendency of the higher surface area particles. The films were still visible light transparent since the agglomerate sizes were less than 300 nm. The agglomerates consisted of primary particles with sizes less than 50 nm (Figure 7.39e, and 7.39f). The thickness of the HAp layer on top of the sericin layer was measured as 150-200 nm.

The AFM images of the m-HAp films are given in Figure 7.40. The phase image also showed agglomerates as in the SEM images. The highly fluctuating thickness of the sericin film beneath was responsible of the lumps in the topographical image.

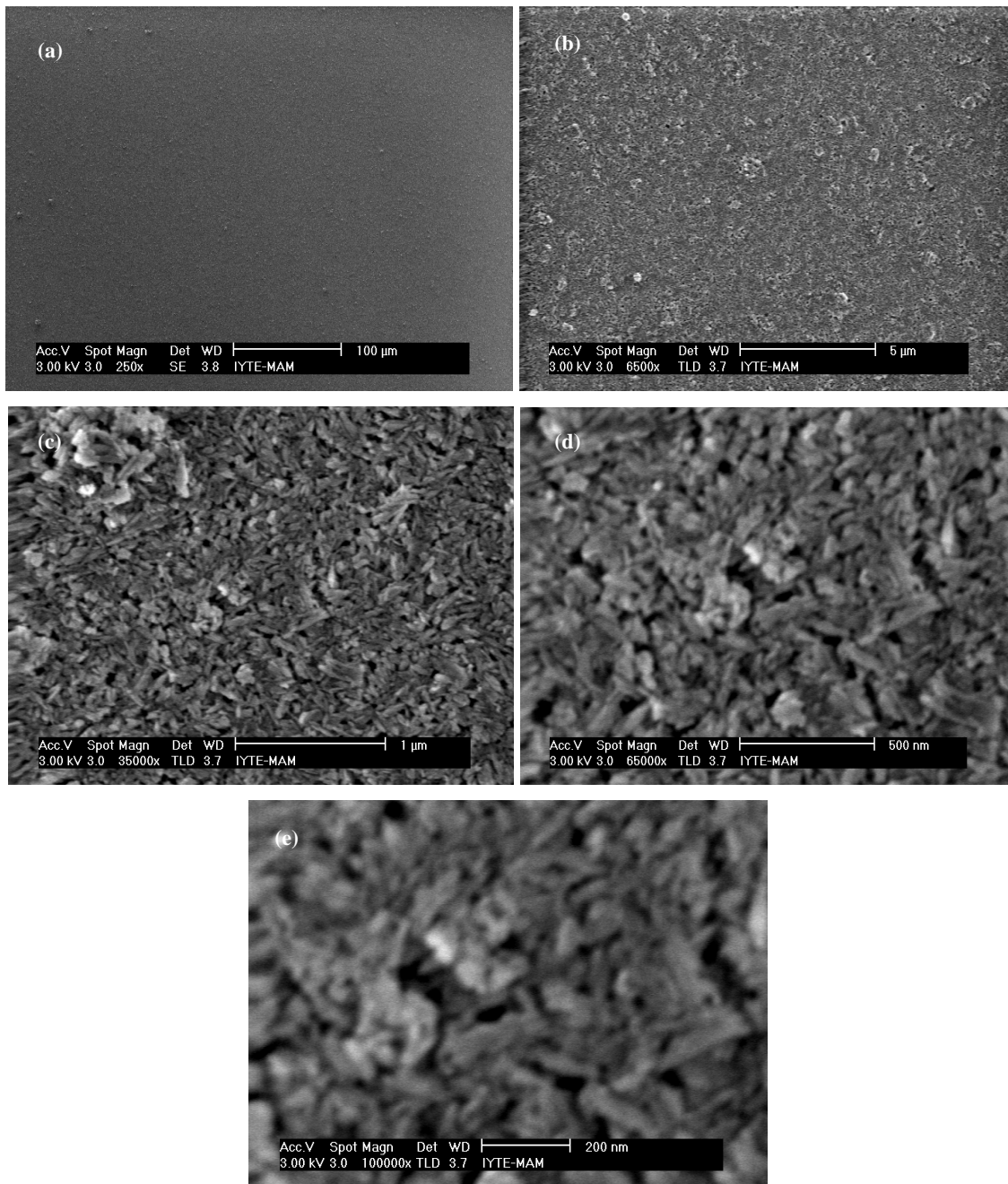


Figure 7.37. The SEM images of the c-HAp films (with 15% solid content suspension) on the glass/sericin substrate at various magnifications (a) 250x, (b) 6,500x, (c) 35,000x, (d) 65,000x, (e) 100,000x

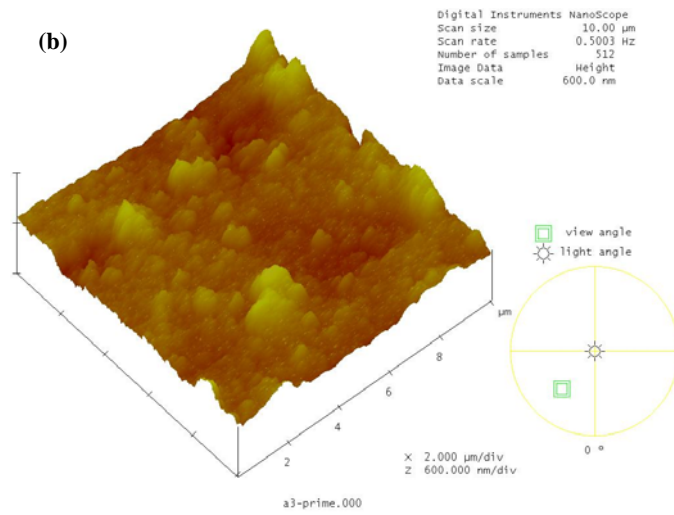
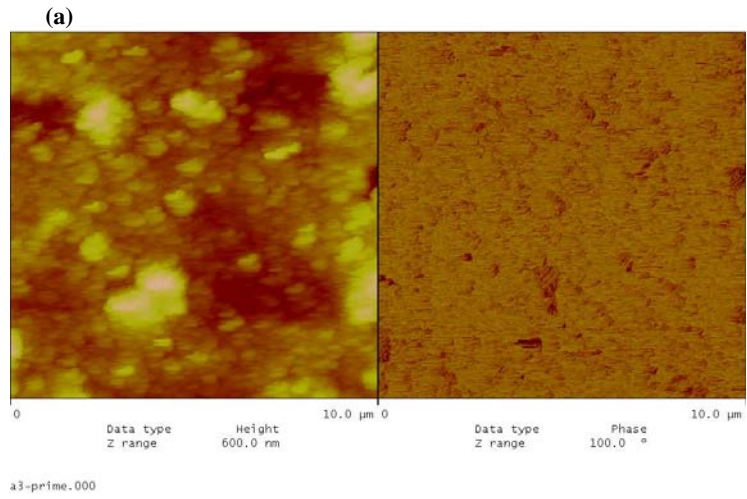


Figure 7.38. The AFM images of the c-HAp films (with 15% solid content suspension) on the glass/sericin substrate, (a) 2-dim. topographical and phase images 10x10 μm , (b) 3-dim. topographical image 10x10 μm .

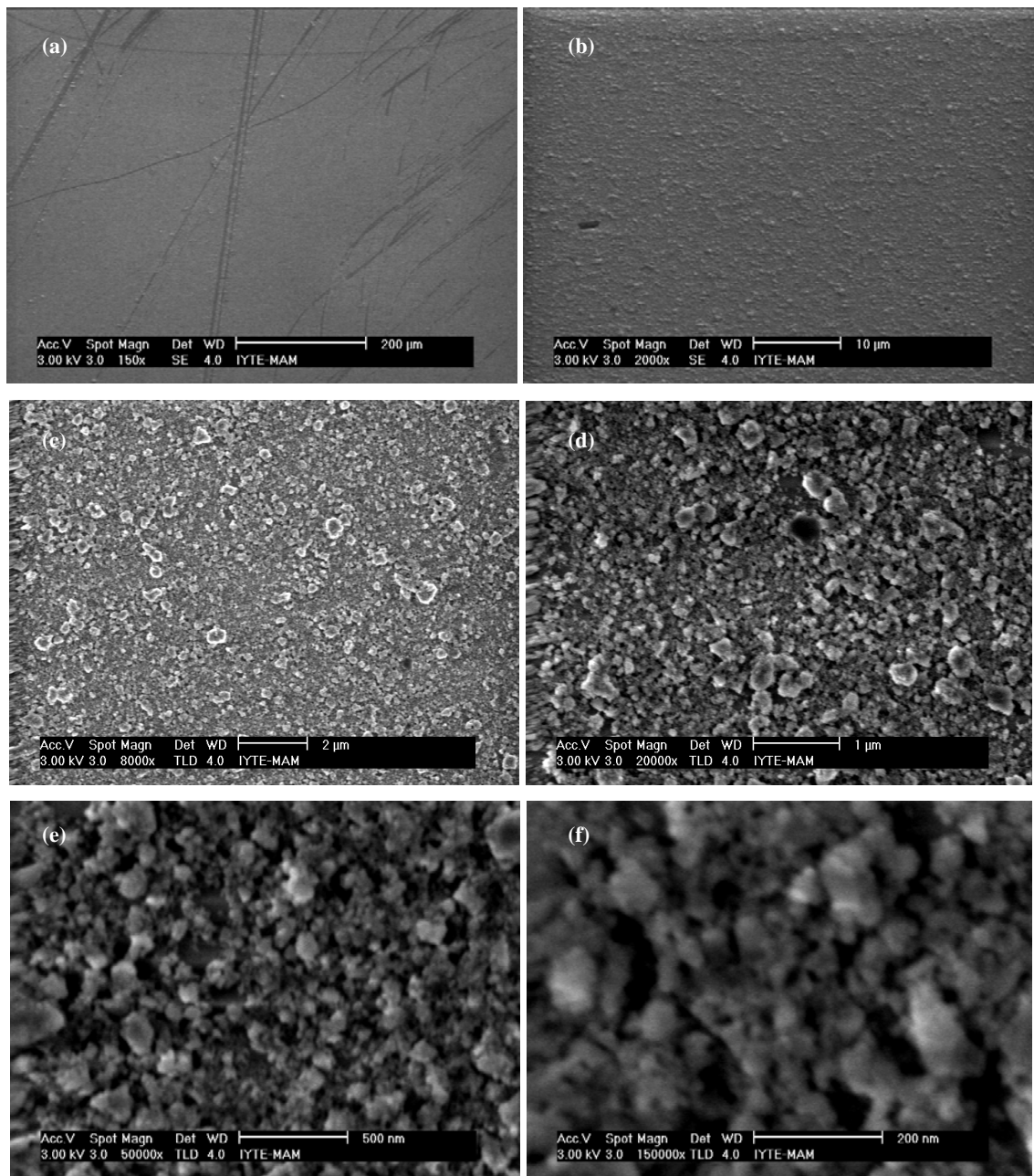


Figure 7.39. The SEM images of the m-HAp films (with 15% solid content suspension) on the glass/sericin substrate at various magnifications (a) 150x, (b) 2,000x, (c) 8,000x, (d) 20,000x, (e) 50,000x, (f) 150,000x

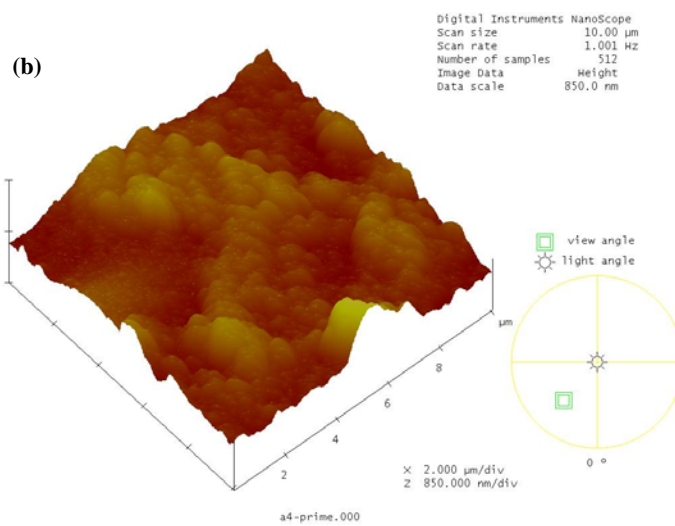
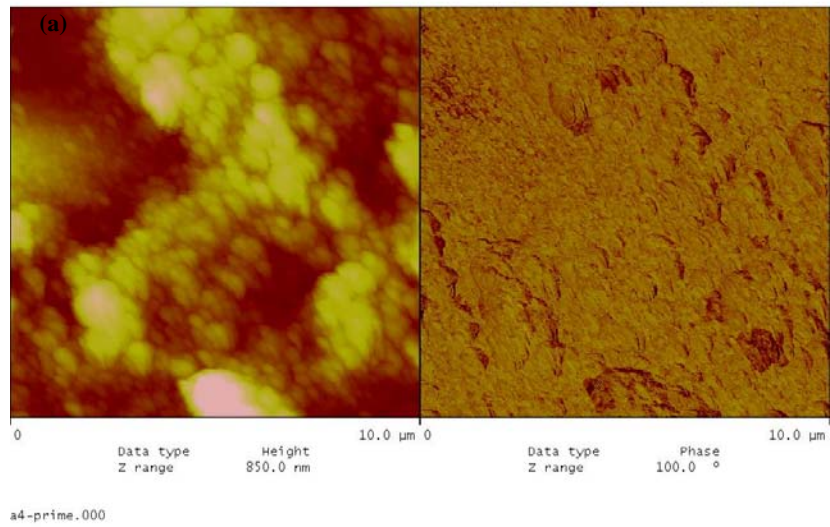


Figure 7.40. The AFM images of the m-HAp films (with 15% solid content suspension) on the glass/sericin substrate, (a) 2-dim. topographical and phase images 10x10 μm , (b) 3-dim. topographical image 10x10 μm .

The SEM images of the c-HAp films on glass/fibroin substrates are shown in Figure 7.41. The films were more homogeneous as compared to their counterparts coated on glass substrates. However, the agglomerate sizes were in the range 400 nm - 1 μ m, and covered approximately 35% of the surface, partially reflecting light as well as scattering, which explains the slightly opacified appearance of the films. The thickness of the c-HAp layer on top of the fibroin layer was measured to be 150-200 nm (determined by profile measurements). This again corresponds to a film of 3-4 layers of packed primary particles.

The corresponding AFM images of the c-HAp films are given in Figure 7.42. The phase image showed the same particle and agglomerate features of the films. The thickness fluctuation of the fibroin films (1 μ m to 2 μ m) were not so extensive as in the case of sericin films, however, the effect was still visible with the agglomerate like structures in the topographical images.

The SEM images of the m-HAp films on glass/fibroin substrates are shown in Figure 7.43. Again the films were more homogeneous as compared to their counterparts coated on glass substrates. The maximum agglomerate size was close to 2 μ m, and predominantly the agglomerate sizes were less than 500 nm. The films were again slightly opacified. The thickness of the m-HAp layer on top of the fibroin layer was measured to be 250-600 nm.

The AFM images of the m-HAp films are given in Figure 7.44. The phase images also showed agglomeration with agglomerates dominant in the range 100-500 nm, as in the SEM images. The effect of the variable thickness of the intermediate fibroin film was seen in the topographical images.

The SEM images of glass/sericin/m-HAp (Figure 7.39), and glass/fibroin/m-HAp (Figure 7.43) surfaces showed that m-HAp powder coatings fell just below the full surface coverage due to more extensive agglomerates in contrast to corresponding c-HAp coatings (Figure 7.37 and Figure 7.41). Again the minimum threshold solid content of suspensions in order to obtain full surface coverage on the sericin and fibroin layers, was 15%. When the solid content ratio of the c-HAp and m-HAp powder suspensions were reduced to 11%, patchy surface coverages on the glass/fibroin substrate surfaces were observed for both of the suspensions as shown in Figure 7.45 and 7.46, respectively.

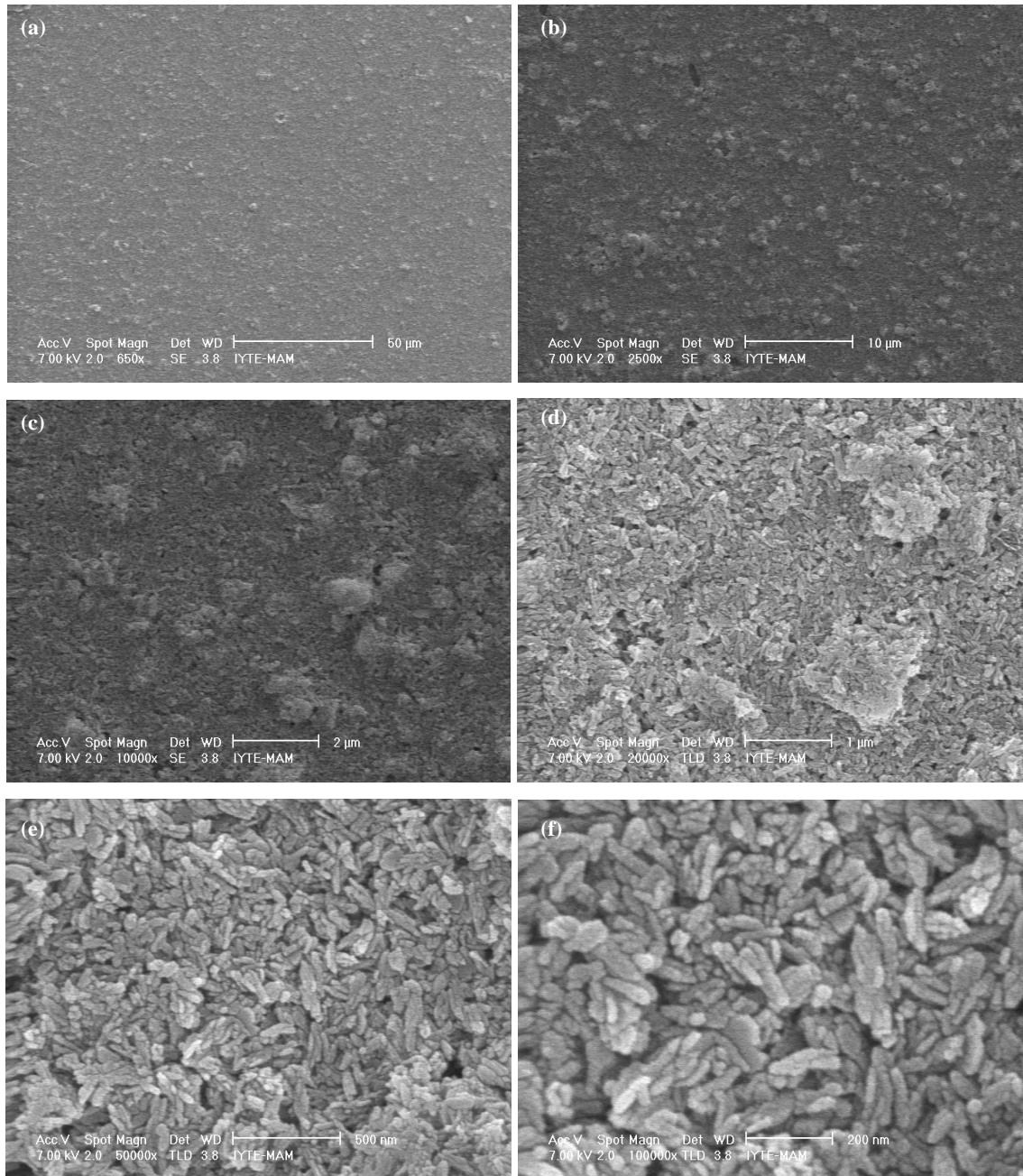


Figure 7.41. The SEM images of the c-HAp films (with 15% solid content suspension) on glass/fibroin substrate at various magnifications (a) 650x, (b) 2,500x, (c) 10,000x, (d) 20,000x, (e) 50,000x, (f) 100,000x

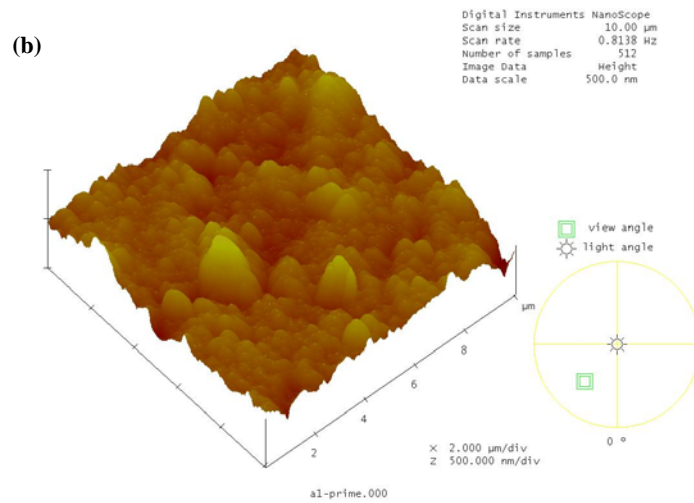
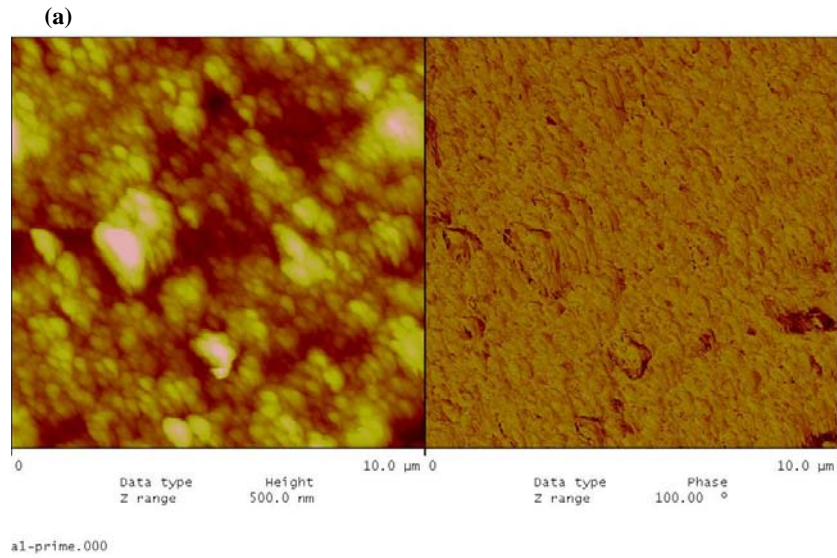


Figure 7.42. The AFM images of the c-HAp films (with 15% solid content suspension) on glass/fibroin substrate, (a) 2-dim. topographical and phase images 10x10 μm, (b) 3-dim. topographical image 10x10 μm, (c) 2-dim. Topographical and phase images 1.84x184 μm, (d) 3-dim. topographical image 1.84x1.84 μm.

(cont. on next page)

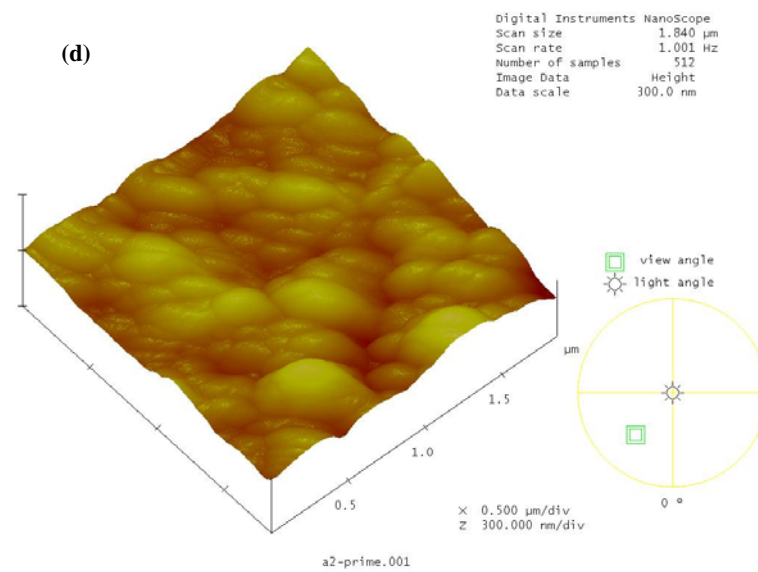
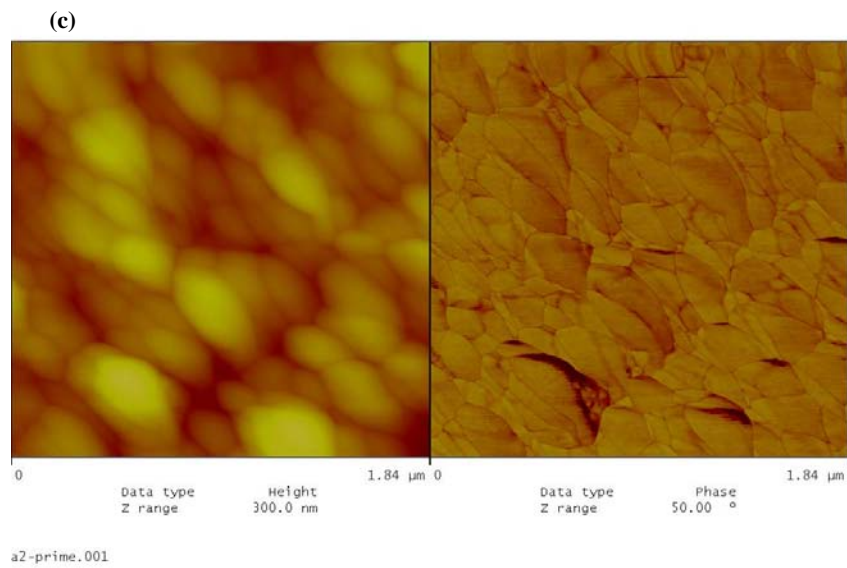


Figure 7.42. (cont.) The AFM images of the c-HAp films (with 15% solid content suspension) on glass/fibroin substrate, (a) 2-dim. topographical and phase images $10 \times 10 \mu\text{m}$, (b) 3-dim. topographical image $10 \times 10 \mu\text{m}$, (c) 2-dim. Topographical and phase images $1.84 \times 1.84 \mu\text{m}$, (d) 3-dim. topographical image $1.84 \times 1.84 \mu\text{m}$.

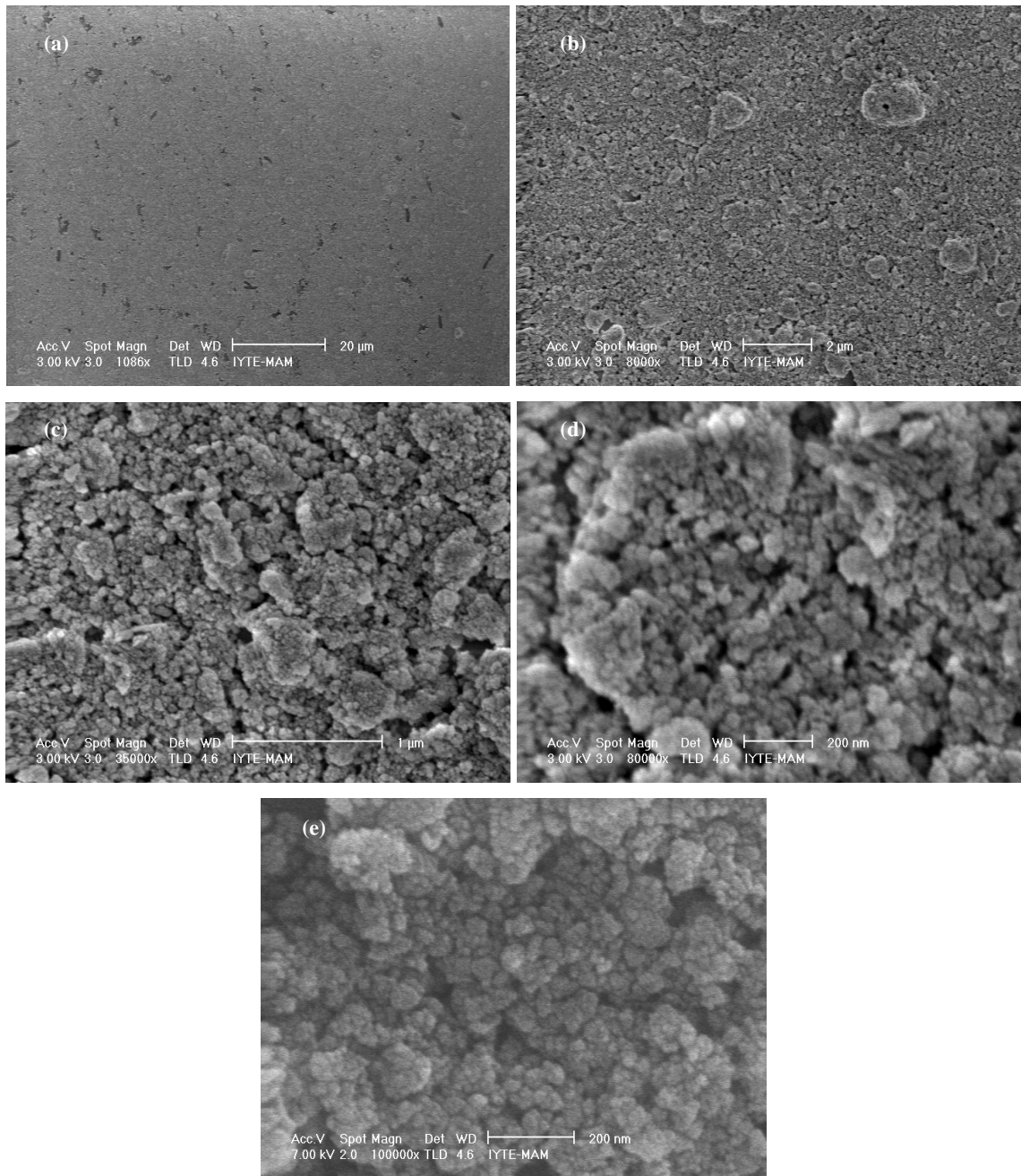


Figure 7.43. The SEM images of the m-HAp films (with 15% solid content suspension) on the glass/fibroin substrate at various magnifications (a) 1,086x, (b) 8,000x, (c) 35,000x, (d) 80,000x, (f) 100,000x

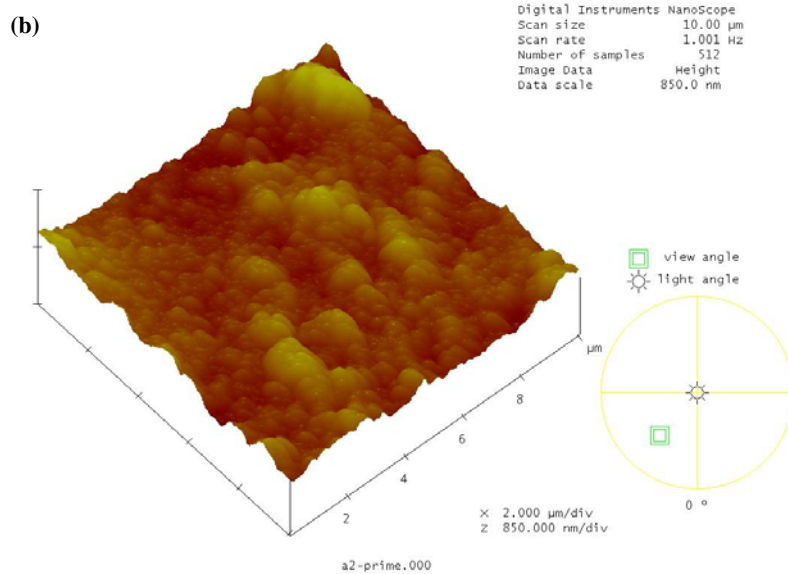
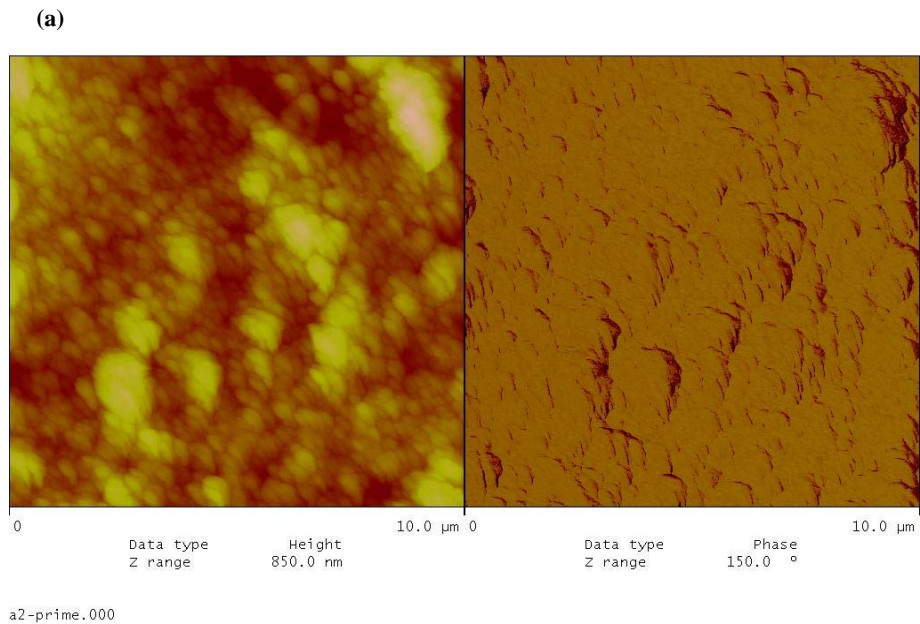


Figure 7.44. The AFM images of the m-HAp films (with 15% solid content suspension) on the glass/fibroin substrate, (a) 2-dim. topographical and phase images 10x10 μm, (b) 3-dim. topographical image 10x10 μm, (c) 2-dim. topographical and phase images 1.84x1.84 μm, (d) 3-dim. topographical image 1.84x1.84 μm.

(cont. on next page)

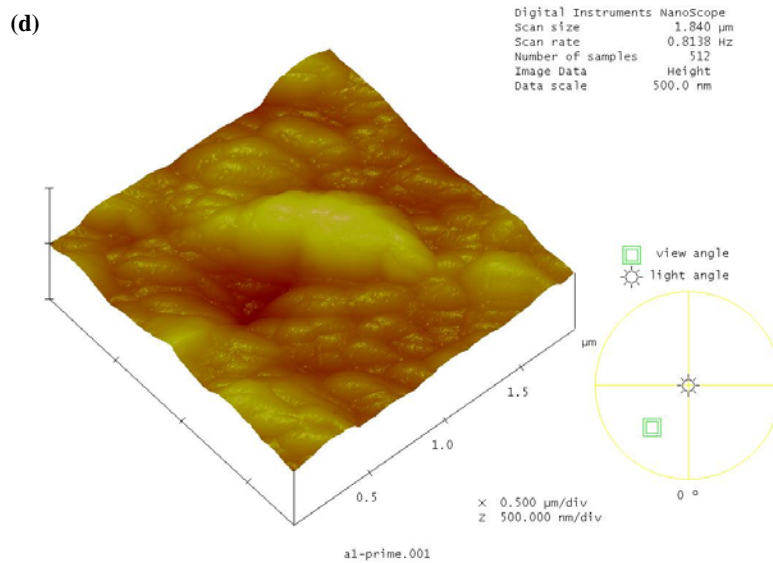
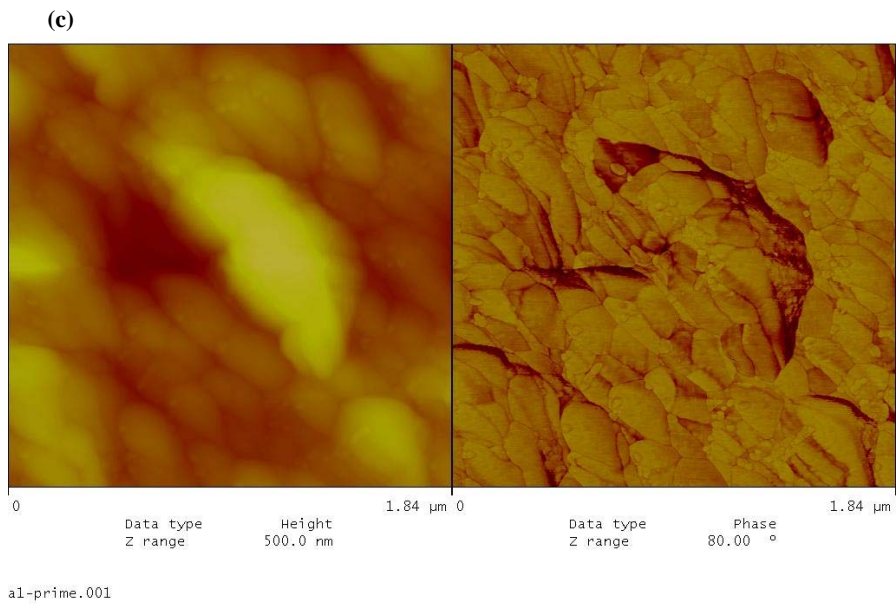


Figure 7.44. (cont.) The AFM images of the m-HAp films (with 15% solid content suspension) on the glass/fibroin substrate, (a) 2-dim. topographical and phase images $10 \times 10 \mu\text{m}$, (b) 3-dim. topographical image $10 \times 10 \mu\text{m}$, (c) 2-dim. topographical and phase images $1.84 \times 1.84 \mu\text{m}$, (d) 3-dim. topographical image $1.84 \times 1.84 \mu\text{m}$.

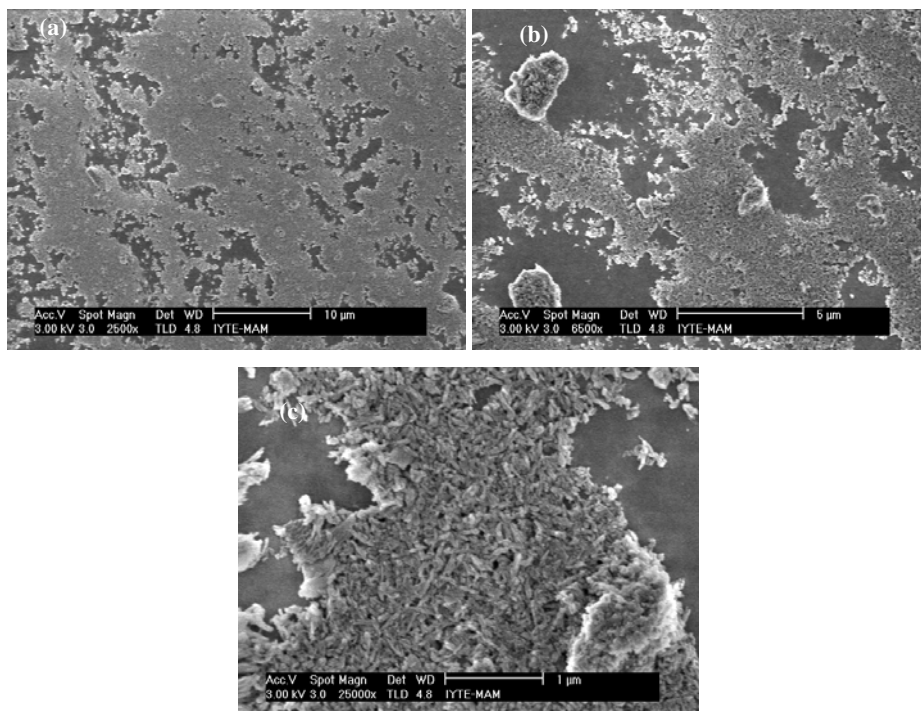


Figure 7.45. (a), (b), (c) The SEM images of the c-HAp films (with 11% solid content suspension) on glass/fibroin substrate at various magnifications.

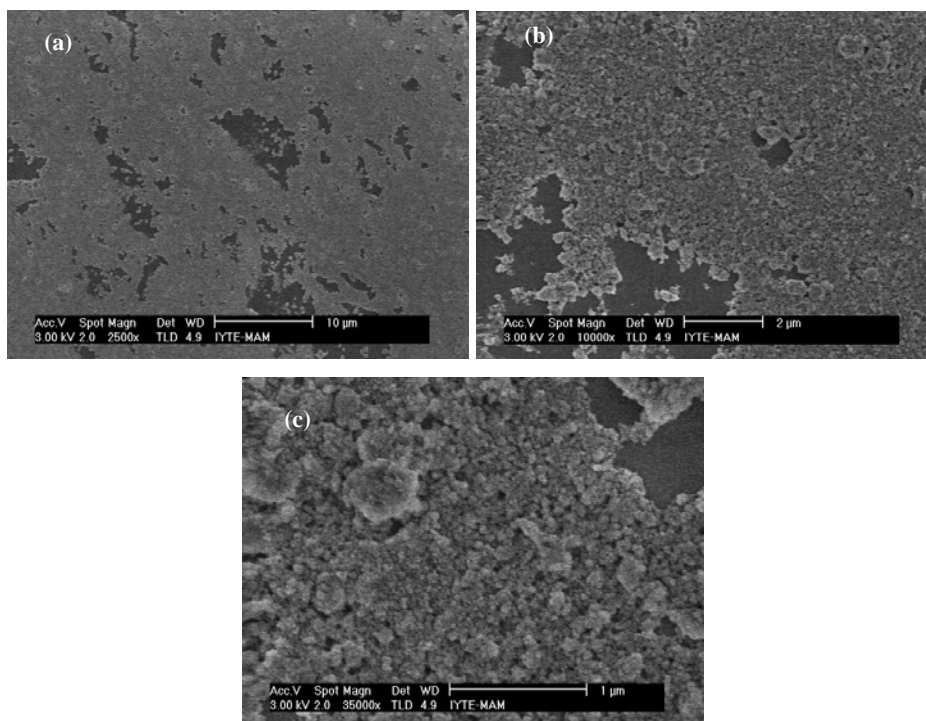


Figure 7.46. (a), (b), (c) The SEM images of the m-HAp films (with 11% solid content suspension) on glass/fibroin substrate at various magnifications.

The glass/sericin/c-HAp, glass/sericin/m-HAp, glass/fibroin/c-HAp and glass/fibroin/m-HAp structures were heat treated at 560°C, for 30 minutes with a heating ramp rate of 15°C/min, and the effect is shown in Figure 7.47. The hydroxyapatite coatings remained intact, and the onset of sintering was apparent especially for the coatings on the sericin layer. The hole-like gaps (some of which are indicated by the arrows) were formed most probably because of the gaseous products evolution during the burning of sericin and fibroin layers.

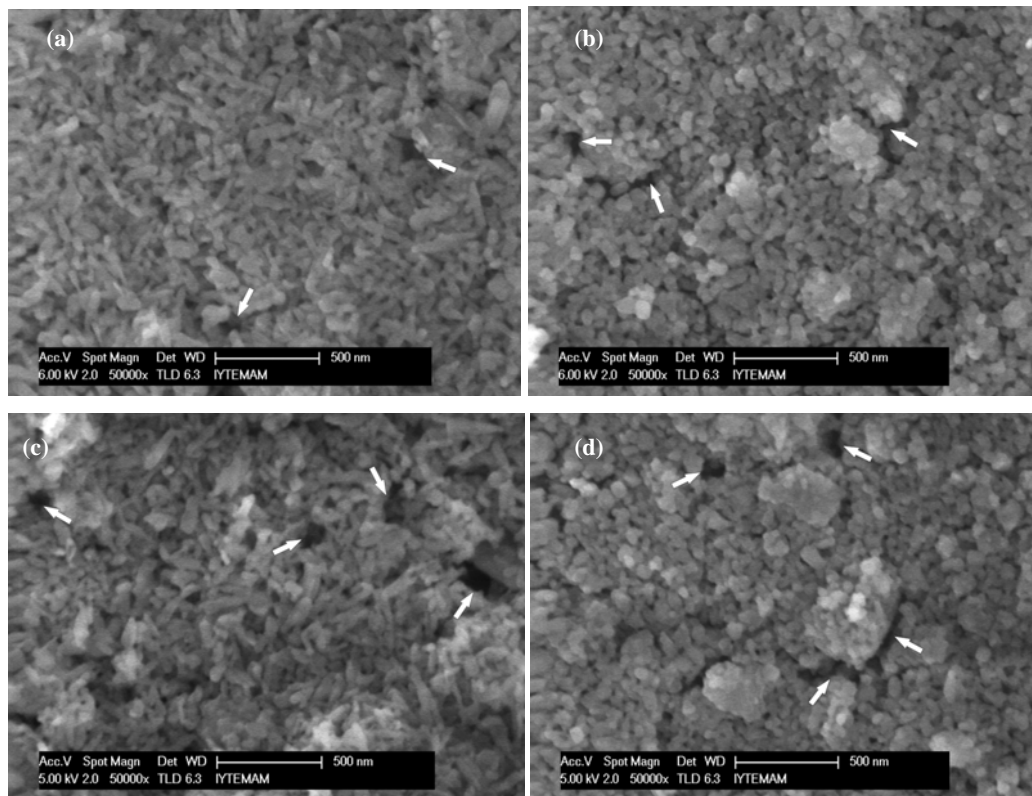


Figure 7.47. (a) glass/sericin/c-HAp, (b) glass/sericin/m-HAp, (c) glass/fibroin/c-HAp, (d) glass/fibroin/m-HAp thin film structures after heat treatment at 560°C; the arrows indicate some of the hole-like gaps through which sericin and fibroin burnt out.

Apparently the effect of intermediate sericin and fibroin films was the selective deposition of particles of minimal available sizes, predominantly of the primary particles. The affinity of the spatially recurring carboxyl groups ($-\text{COO}^-$) in the β -sheet structure of silk proteins, for Ca^{2+} of the hydroxyapatite crystal was reported in the literature; the other possibility that amino groups, $-\text{NH}_3^+$ or $=\text{NH}_2^+$, to have an affinity for PO_4^{3-} in the hydroxyapatite crystal was considered as a minor effect in comparison to the former because of the polar concentrated arrangement (rather than regular spatial

arrangement) of these groups in the β -sheet protein structure (Takeuchi, et al. 2005, Altman, et al. 2003, Kong, et al. 2006, Kong, et al. 2004).

The forces in effect for the hydroxyapatite particle deposition on the silk sericin and fibroin films were the same as adsorption phenomenon. By that token the HAp particle deposition during the thin film formation process was most likely due to the coulombic interaction between the regular arrangement of surface negative charge distribution of sericin and fibroin in the β -sheet structure provided by the $-\text{COO}^-$ groups, and the recurring positive surface charge site strips rich in Ca^{2+} on the (100) and (010) faces of hexagonal HAp crystals. On the (001) face of the HAp crystal lattice, 6 oxygen ions that belong to three crystal phosphates create negative charge sites, which may have a coulombic attraction for the polar $-\text{NH}_3^+$ groups in the β -sheet structure. The former coulombic interaction probably provided a partially positive degree of cooperativity for the HAp particle deposition on the sericin and fibroin surfaces; together with the latter coulombic interaction the degree of cooperativity might change from partially positive to positive (Luo and Andrade 1998). However, the agglomeration tendency between the HAp particles was a factor that reduced the degree of cooperativity.

The thin coatings of essentially primary particles of HAp, with drastically reduced number and size of agglomerates, and homogeneity on the sericin, and the fibroin films were thus resulted from the surface energy minimization of the deposition process driven by coulombic attraction, and probably pointed out to a high degree of positive cooperativity. The agglomeration tendency of the smaller size HAp particles deteriorated the degree of cooperativity, and hence, the surface homogeneity which was visible in the glass/sericin/m-HAp, and especially glass/fibroin/m-HAp coatings shown in Figure 7.39 and 7.43, respectively. The coatings with the larger particle size HAp, namely, glass/sericin/c-HAp and glass/fibroin/c-HAp in Figure 7.37 and 7.41, respectively, indicated a lower tendency for agglomeration and a more homogeneous film structure, which was most probably the result of a higher degree of positive cooperativity in the deposition.

On the other hand the HAp coatings on sericin were more homogeneous with less agglomerates of smaller sizes in comparison to coatings on fibroin. This might be due to a more pronounced random coil structure with respect to β -sheet structure in the fibroin films, and due to an inherent surface charge distribution even in the β -sheet structure of fibroin reducing the degree of positive cooperativity for HAp deposition.

The surface charge distribution regularities are expected to be delimited by the surface topography, and crystal size and shape which were also factors in determining the HAp particle deposition on the sericin and fibroin surfaces.

7.3. Enhanced Model Protein Adsorption of Silk Protein/Hydroxyapatite Thin Films

In this study the affinities of BSA, a globular protein, and collagen, a fibrillar protein for the silk protein surfaces were investigated by AFM imaging. BSA was used to model the adsorption behavior of bone growth factors or cytokines on the hydroxyapatite coated surfaces. The effect of an intermediate silk sericin thin layer beneath the hydroxyapatite coatings, on the BSA adsorption, was quantified.

The AFM image of the BSA adsorbed on glass is given in Figure 7.48. The glass surface was virtually featureless, and the BSA particles were discernable in both the topological and the phase images as equiaxed particles in accord with the fact that BSA particles are globular (Ying, et al., 2003). BSA particles occupied less than ~8% of the glass surface.

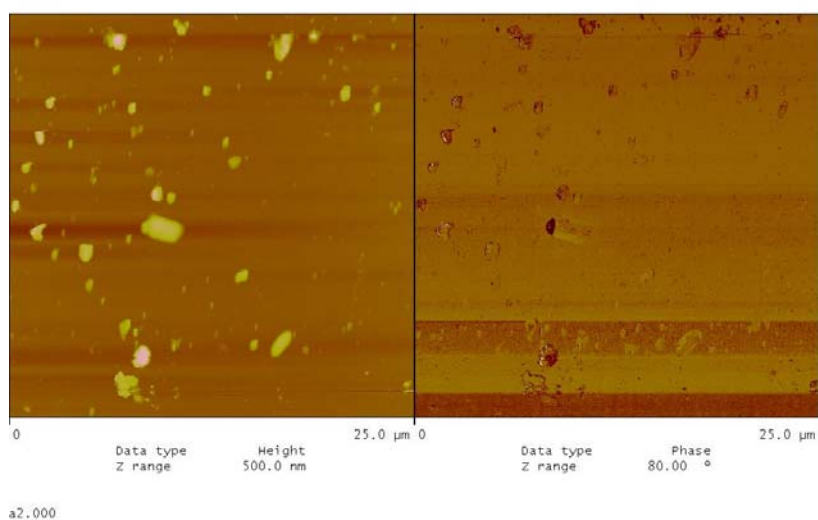


Figure 7.48. BSA particles adsorbed on glass surface.

The AFM images of the BSA adsorbed on the fibroin film are given in Figure 7.49. BSA particles were clearly discernable especially on the phase image with approximate size range of 50-150 nm. Interestingly enough BSA particles showed a

tendency to be adsorbed on the fiber like bumpy elongations of the striations formed by the fibroin particles. However, sporadic BSA adsorption was also noticeable on large flat regions of the fibroin film. BSA roughly covered 65-70% of the fibroin surface which was a drastic increase over glass adsorption.

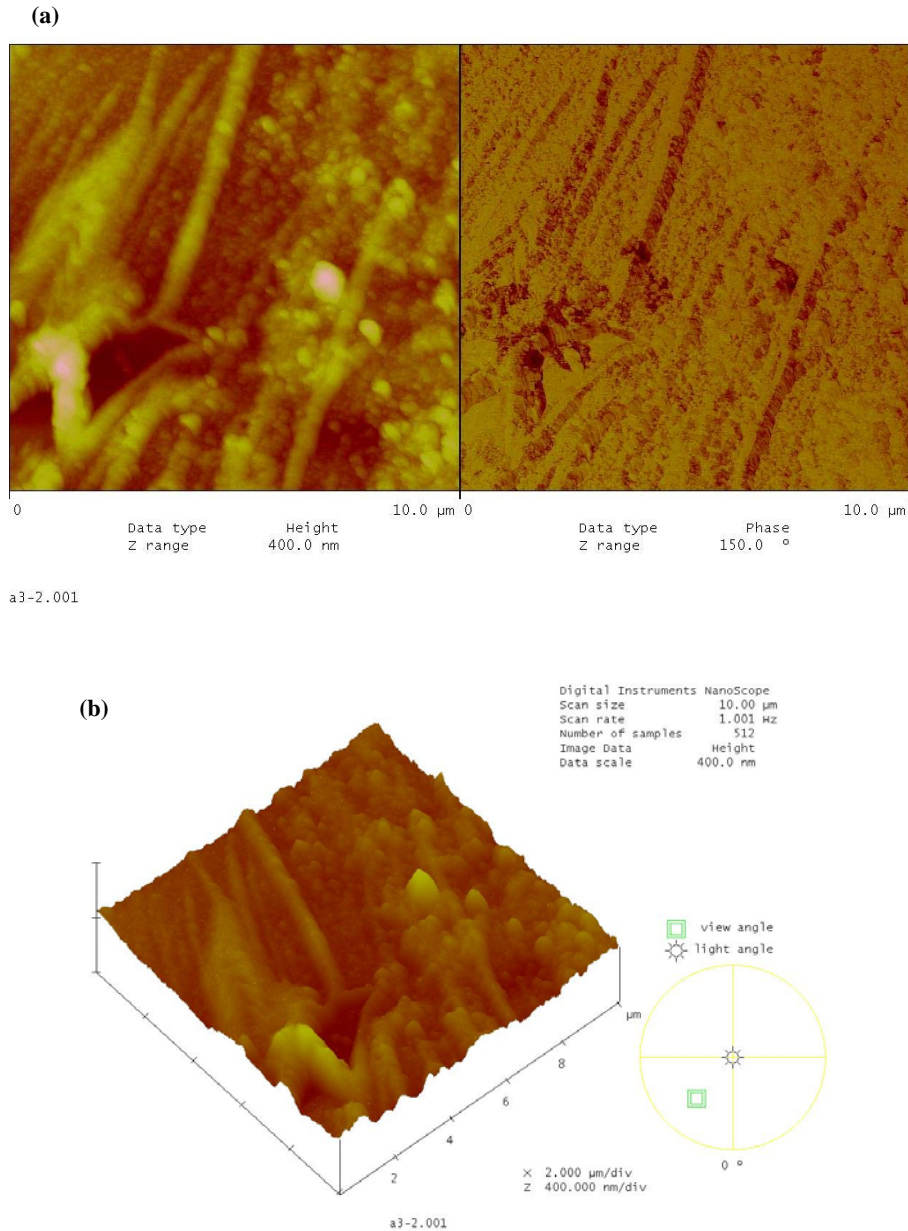


Figure 7.49. The AFM image of the BSA adsorption on fibroin film, (a) 2-dim. topographical and phase images 10x10 μm, (b) 3-dim. topographical image 10x10 μm, (c) 2-dim. topographical and phase images 1.84x1.84 μm, (d) 3-dim. topographical image 1.84x1.84 μm.

(cont. on next page)

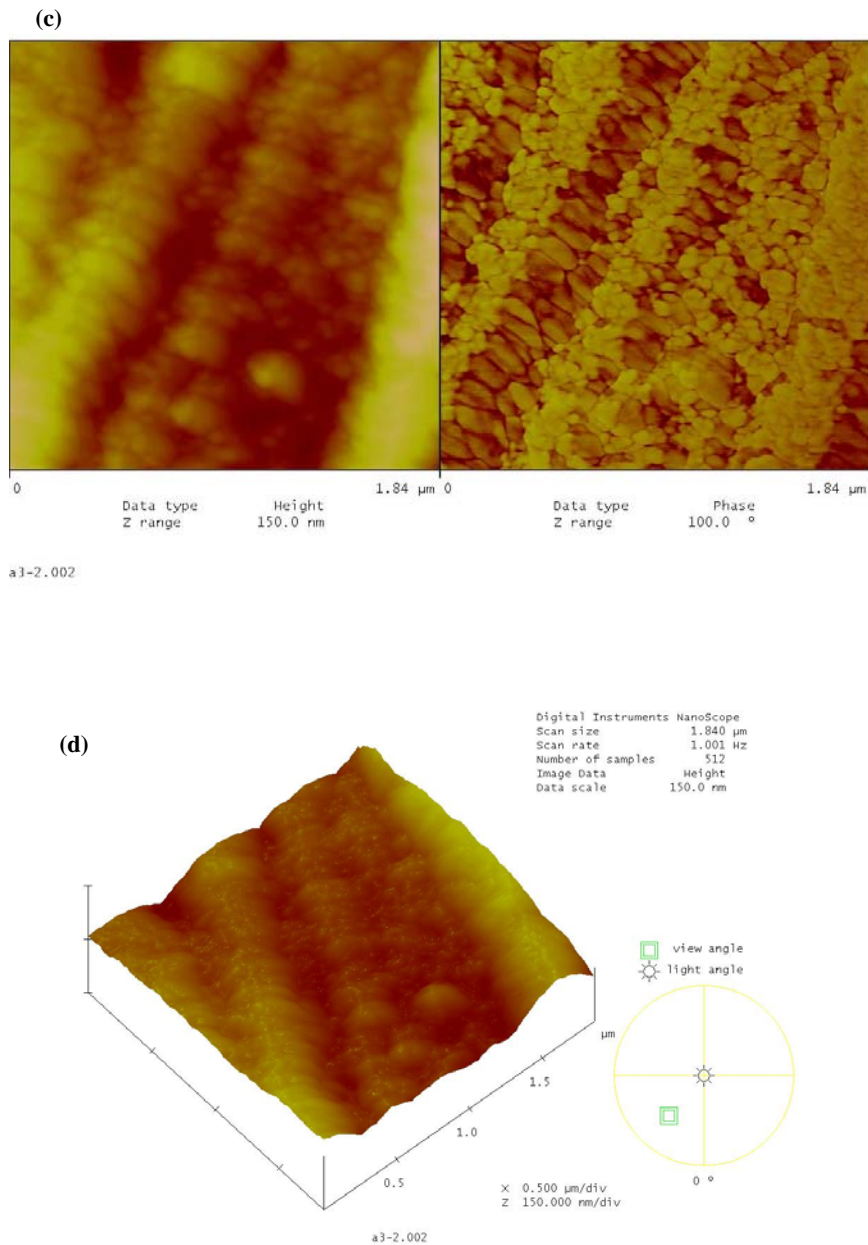


Figure 7.49. (cont.) The AFM image of the BSA adsorption on fibroin film, (a) 2-dim. topographical and phase images $10 \times 10 \mu\text{m}$, (b) 3-dim. topographical image $10 \times 10 \mu\text{m}$, (c) 2-dim. topographical and phase images $1.84 \times 1.84 \mu\text{m}$, (d) 3-dim. topographical image $1.84 \times 1.84 \mu\text{m}$.

The AFM images of the BSA adsorbed on the sericin film are given in Figure 7.50. Randomly adsorbed agglomerates of BSA were seen on the sericin surface with the agglomerate sizes ranging in 50-350 nm. The surface coverage was approximately 60-65%. This again indicated a drastic jump in adsorption compared to glass. The BSA adsorption of the sericin film seemed to be slightly lower than the fibroin film.

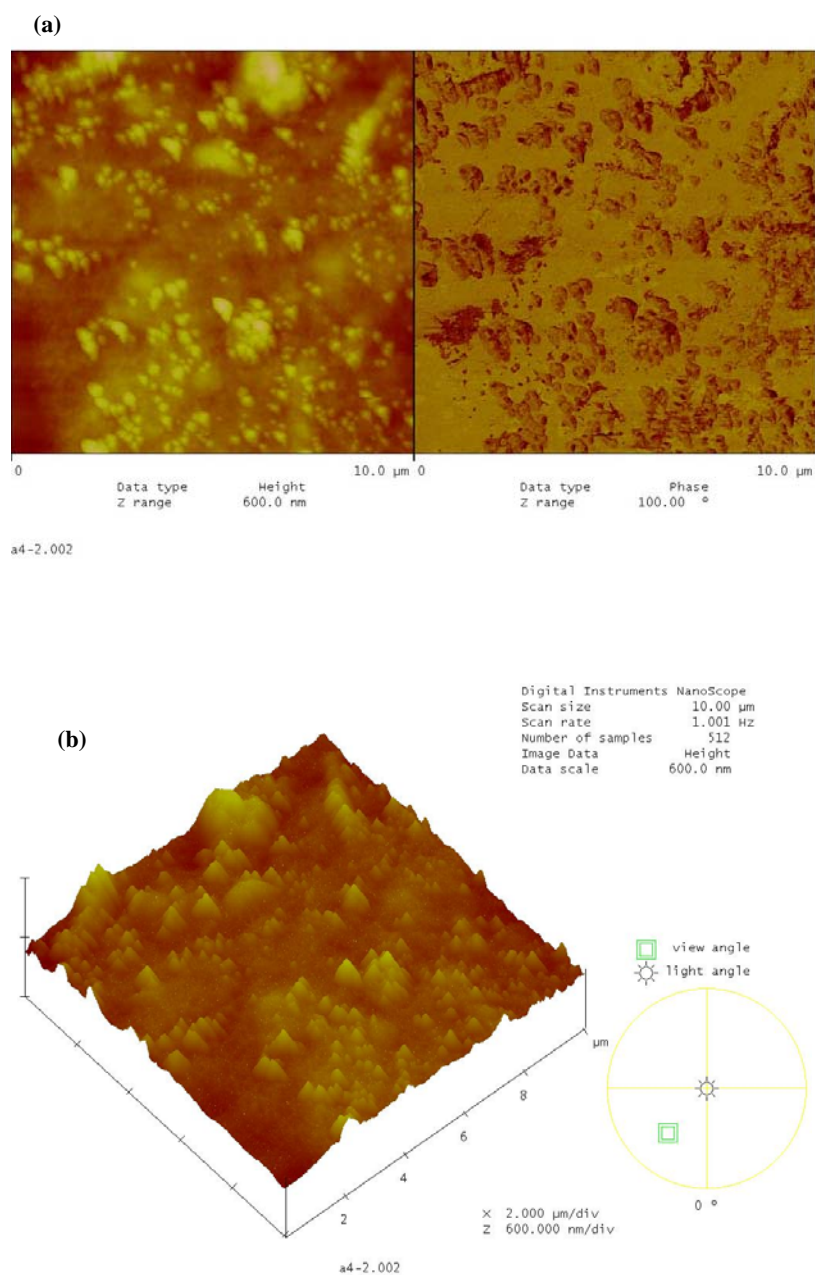


Figure 7.50. The AFM image of the BSA adsorption on sericin film, (a) 2-dim. topographical and phase images 10x10 μm, (b) 3-dim. topographical image 10x10 μm, (c) 2-dim. topographical and phase images 1.84x1.84 μm, (d) 3-dim. topographical image 1.84x1.84 μm.

(cont. on next page)

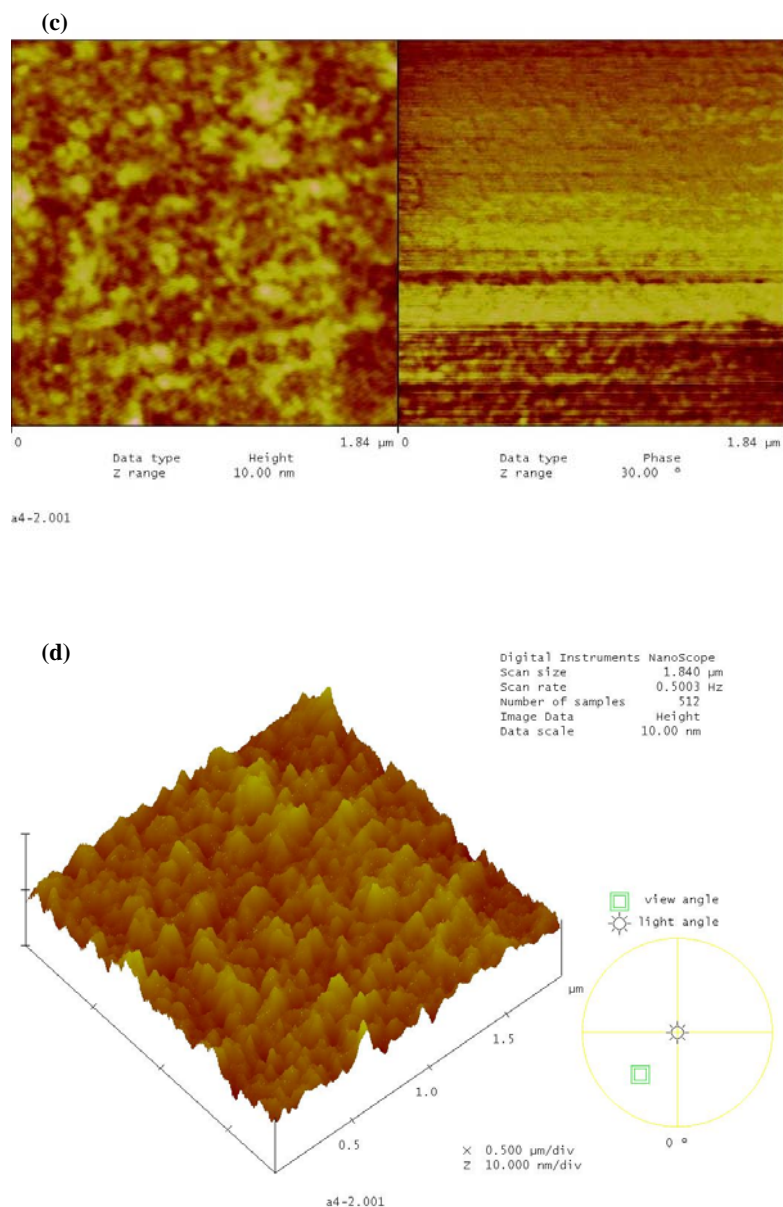


Figure 7.50. (cont.) The AFM image of the BSA adsorption on sericin film, (a) 2-dim. topographical and phase images $10 \times 10 \mu\text{m}$, (b) 3-dim. topographical image $10 \times 10 \mu\text{m}$, (c) 2-dim. topographical and phase images $1.84 \times 1.84 \mu\text{m}$, (d) 3-dim. topographical image $1.84 \times 1.84 \mu\text{m}$.

The AFM images of BSA adsorbed on c-HAp and m-HAp films on glass substrates are shown in Figure 7.51 and 7.52, respectively. Although BSA particles were not discernable in the $10 \times 10 \mu\text{m}$ images, the $1.84 \times 1.84 \mu\text{m}$ images illustrated the adsorption of BSA particles of the approximate size range of 20-50 nm. The adsorbed BSA quantity on the c-HAp film (approximately 40% surface coverage) was higher than on the m-HAp film (approximately 5-10% surface coverage).

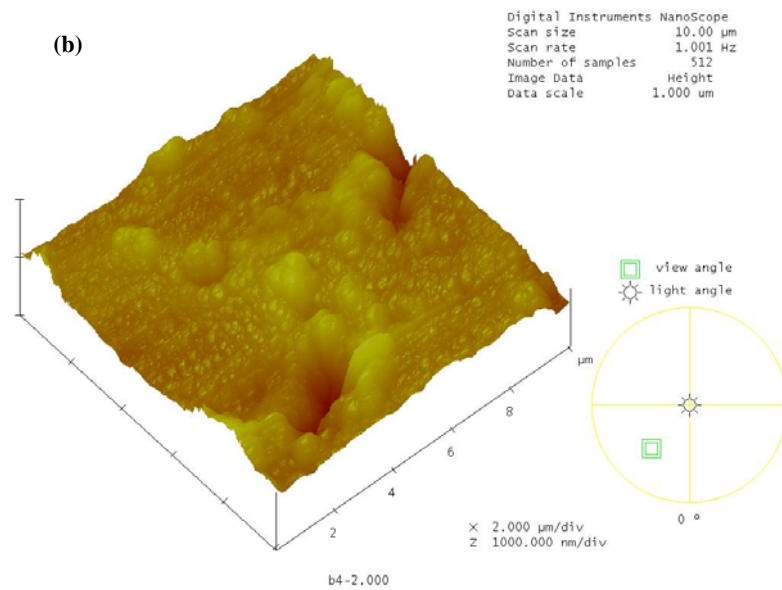
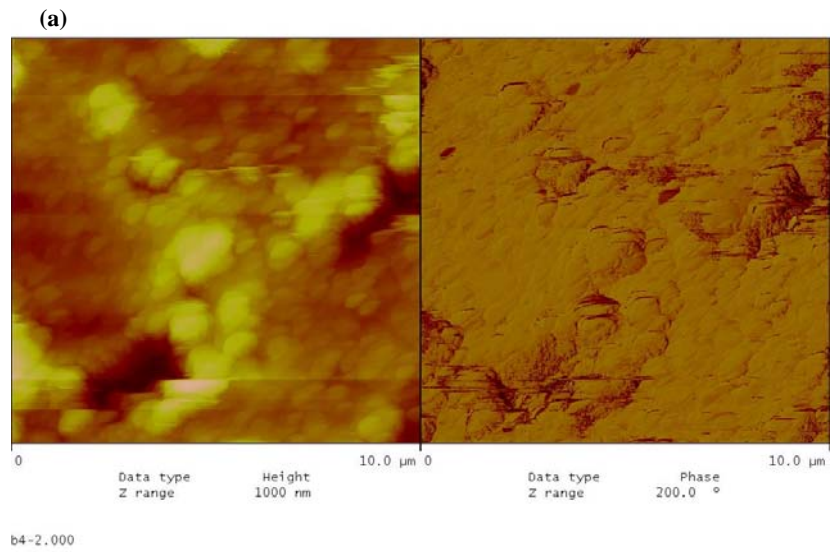


Figure 7.51. The AFM image of adsorbed BSA on c-HAp film on glass substrate (a) 2-dim. topographical and phase images $10 \times 10 \mu\text{m}$, (b) 3-dim. topographical image $10 \times 10 \mu\text{m}$, (c) 2-dim. topographical and phase images $1.84 \times 1.84 \mu\text{m}$, (d) 3-dim. topographical image $1.84 \times 1.84 \mu\text{m}$.

(cont. on next page)

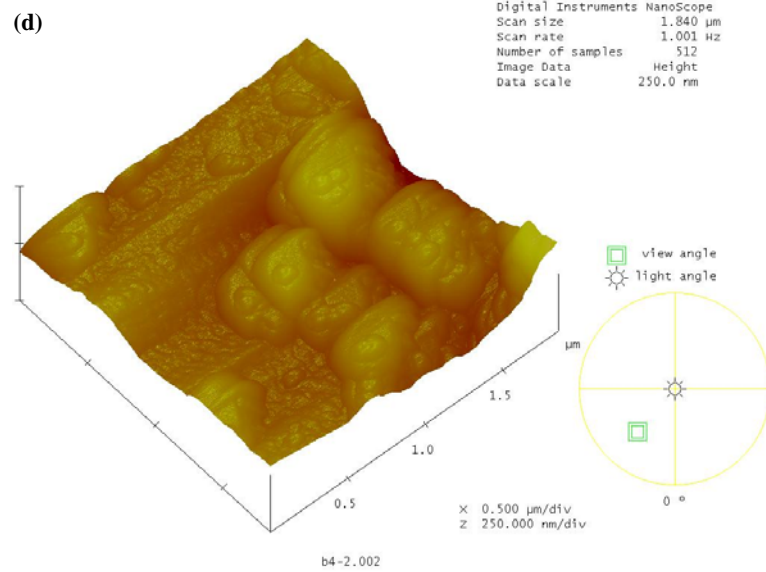
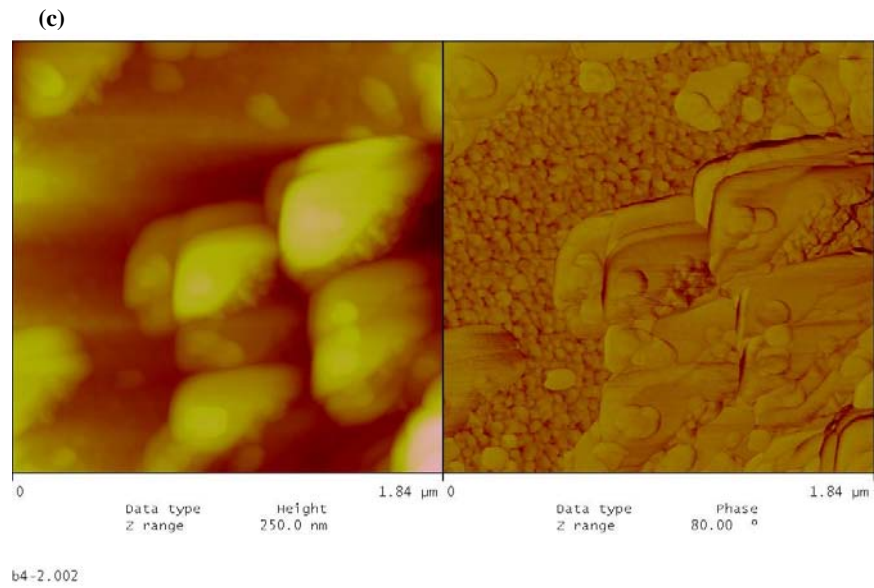


Figure 7.51. (cont.) The AFM image of adsorbed BSA on c-HAp film on glass substrate (a) 2-dim. topographical and phase images $10 \times 10 \mu\text{m}$, (b) 3-dim. topographical image $10 \times 10 \mu\text{m}$, (c) 2-dim. topographical and phase images $1.84 \times 1.84 \mu\text{m}$, (d) 3-dim. topographical image $1.84 \times 1.84 \mu\text{m}$.

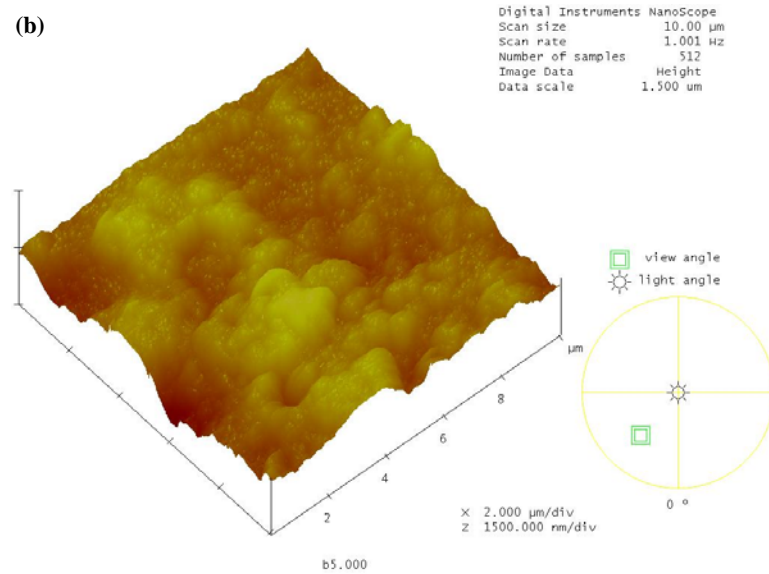
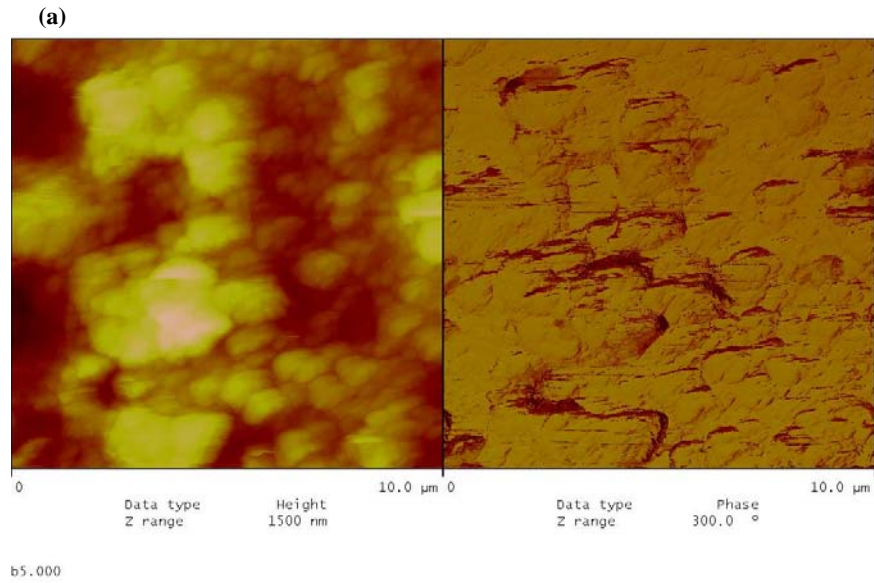


Figure 7.52. The AFM images of adsorbed BSA on m-HAp film on glass substrate (a) 2-dim. topographical and phase images $10 \times 10 \mu\text{m}$, (b) 3-dim. topographical image $10 \times 10 \mu\text{m}$, (c) 2-dim. topographical and phase images $1.84 \times 1.84 \mu\text{m}$, (d) 3-dim. topographical image $1.84 \times 1.84 \mu\text{m}$.

(cont. on next page)

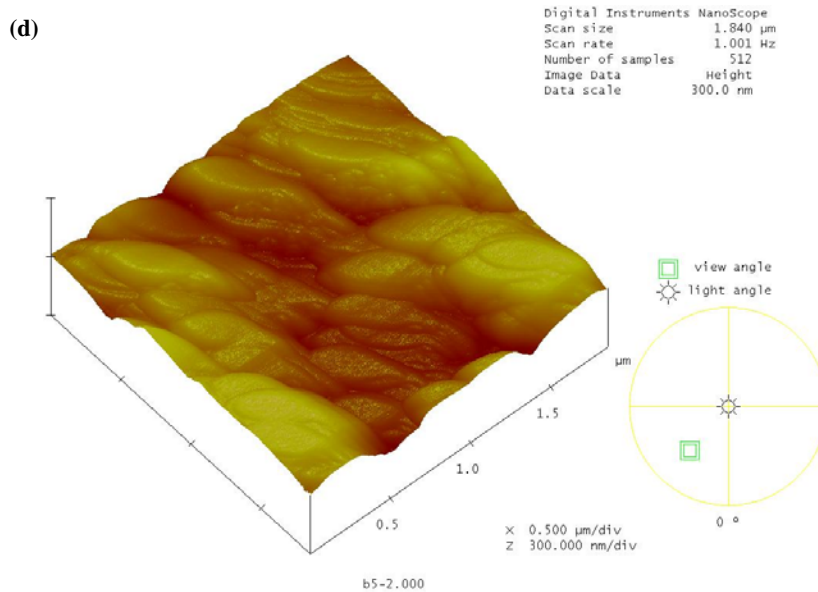
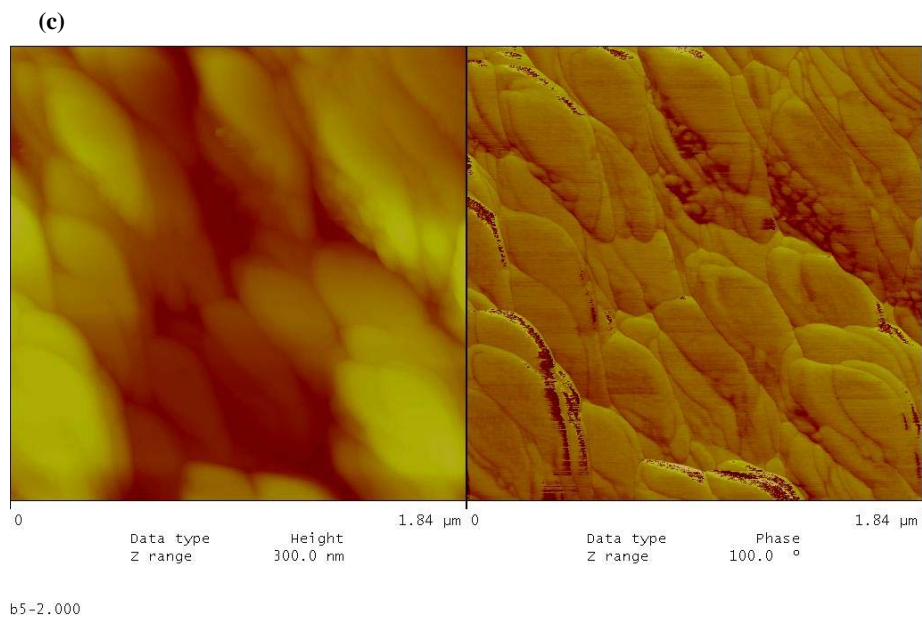


Figure 7.52. (cont.) The AFM images of adsorbed BSA on m-HAp film on glass substrate (a) 2-dim. topographical and phase images $10 \times 10 \mu\text{m}$, (b) 3-dim. topographical image $10 \times 10 \mu\text{m}$, (c) 2-dim. topographical and phase images $1.84 \times 1.84 \mu\text{m}$, (d) 3-dim. topographical image $1.84 \times 1.84 \mu\text{m}$.

The AFM images of the BSA adsorption on fibroin/c-HAp, and fibroin/m-HAp are shown in Figure 7.53 and 7.54, respectively. Again in the 10x10 μm scans it was not possible to discern whether the surface was covered with BSA or not. However, the higher resolution 1.84x1.84 μm scans, especially the phase images provided the answer. The fibroin/c-HAp film the surface coverage with the discernable BSA phase was approximately 85%. The BSA particles covered the HAp surface with agglomerates of 50-300 nm. On the fibroin/m-HAp film the surface coverage of the BSA phase reduced to approximately 25%, and on the average the BSA particles were of the size 50 nm.

The AFM images of the BSA adsorption on sericin/c-HAp, and sericin/m-HAp are given in Figure 7.55 and 7.56, respectively. In Figure 7.55, especially, the phase images gave an indication of BSA coverage of the sericin/c-HAp surface over 90%. The BSA particle agglomerate sizes ranged in 50-400 nm. In Figure 7.56 particularly 1.84x1.84 μm phase image indicated a BSA surface coverage of approximately 35% with BSA agglomerate sizes of 35-50 nm.

The glass/sericin/c-HAp provided the best coating for BSA adsorption. The glass/fibroin/c-HAp proved to be the next best for the BSA adsorption. The glass/sericin/m-HAp coating proved to be slightly better than its glass /fibroin/m-HAp counterpart for adsorbing BSA. However, the BSA adsorption affinity was drastically lower with the m-HAp films over sericin and fibroin surfaces. This indicated that the adsorbed BSA quantity reduced on the smaller particle size HAp films, glass/m-HAp, glass/fibroin/m-HAp and glass/sericin/m-HAp alike, most probably due to the extensive HAp particle agglomeration disrupting the regular surface charge distribution. The positive degree of cooperativity in the coulombic attraction driven adsorption process was therefore reduced. The adsorption process of protein molecules was affected by the topographical structure of the surface as well as the chemical structure.

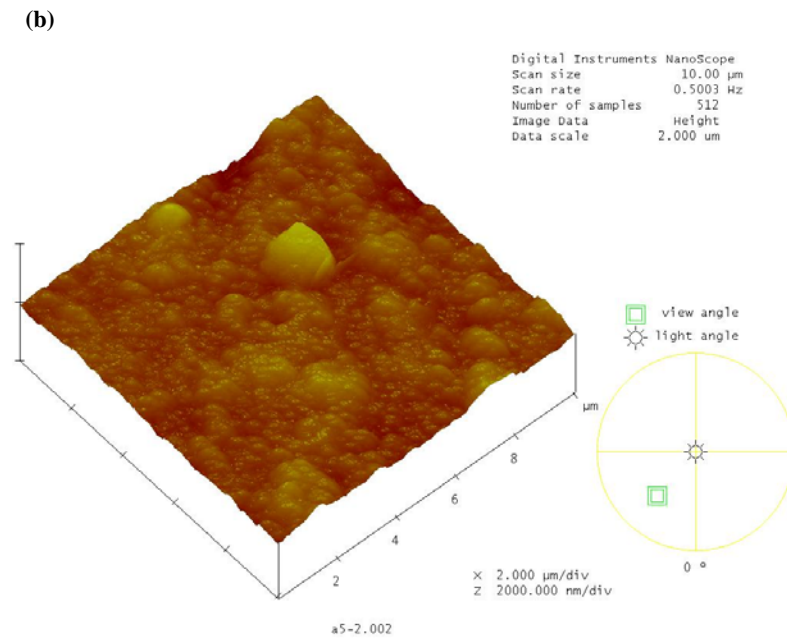
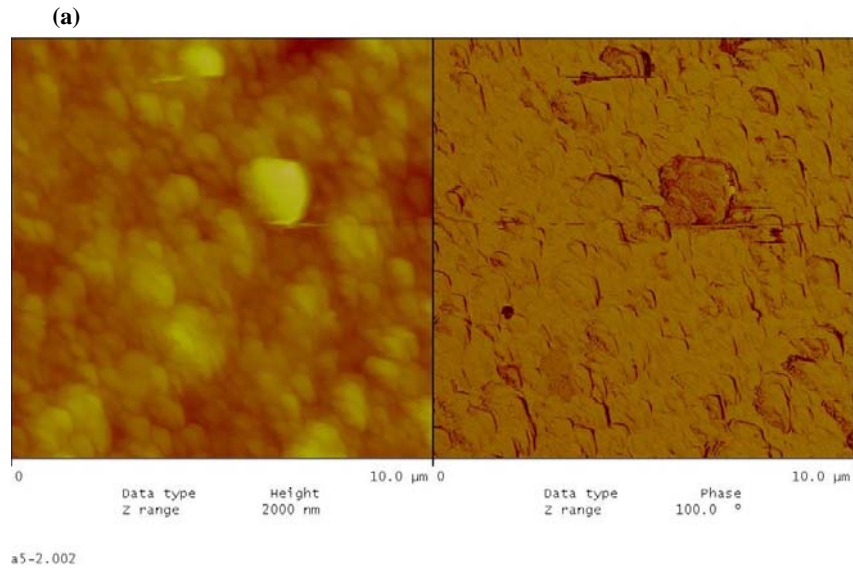


Figure 7.53. The AFM images of adsorbed BSA on glass/fibroin/c-HAp film, (a) 2-dim. topographical and phase images 10x10 μm, (b) 3-dim. topographical image 10x10 μm, (c) 2-dim. topographical and phase images 1.84x1.84 μm, (d) 3-dim. topographical image 1.84x1.84 μm.

(cont. on next page)

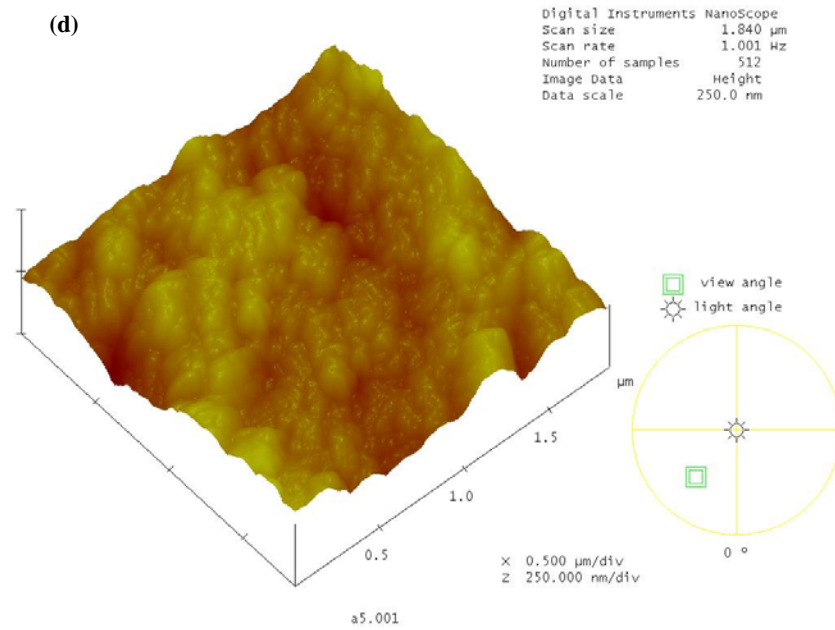
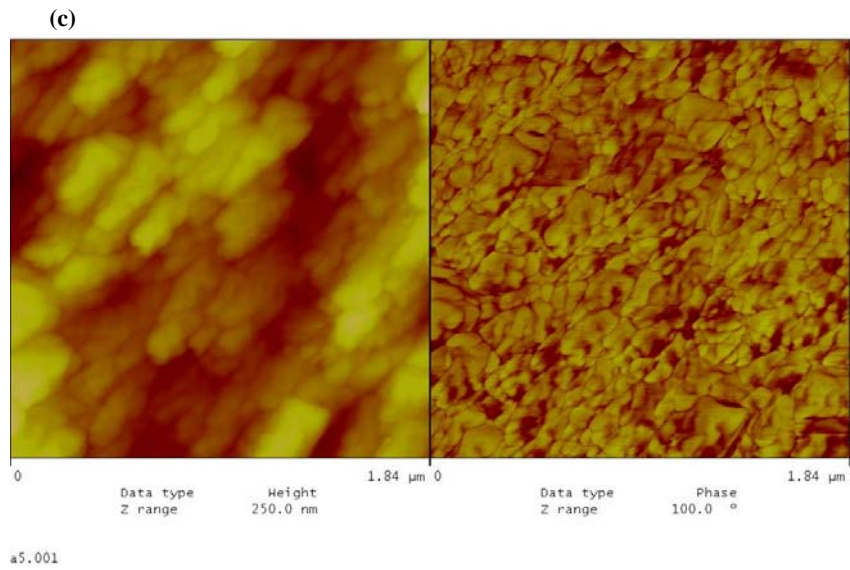


Figure 7.53. (cont.) The AFM images of adsorbed BSA on glass/fibroin/c-HAp film, (a) 2-dim. topographical and phase images $10 \times 10 \mu\text{m}$, (b) 3-dim. topographical image $10 \times 10 \mu\text{m}$, (c) 2-dim. topographical and phase images $1.84 \times 1.84 \mu\text{m}$, (d) 3-dim. topographical image $1.84 \times 1.84 \mu\text{m}$.

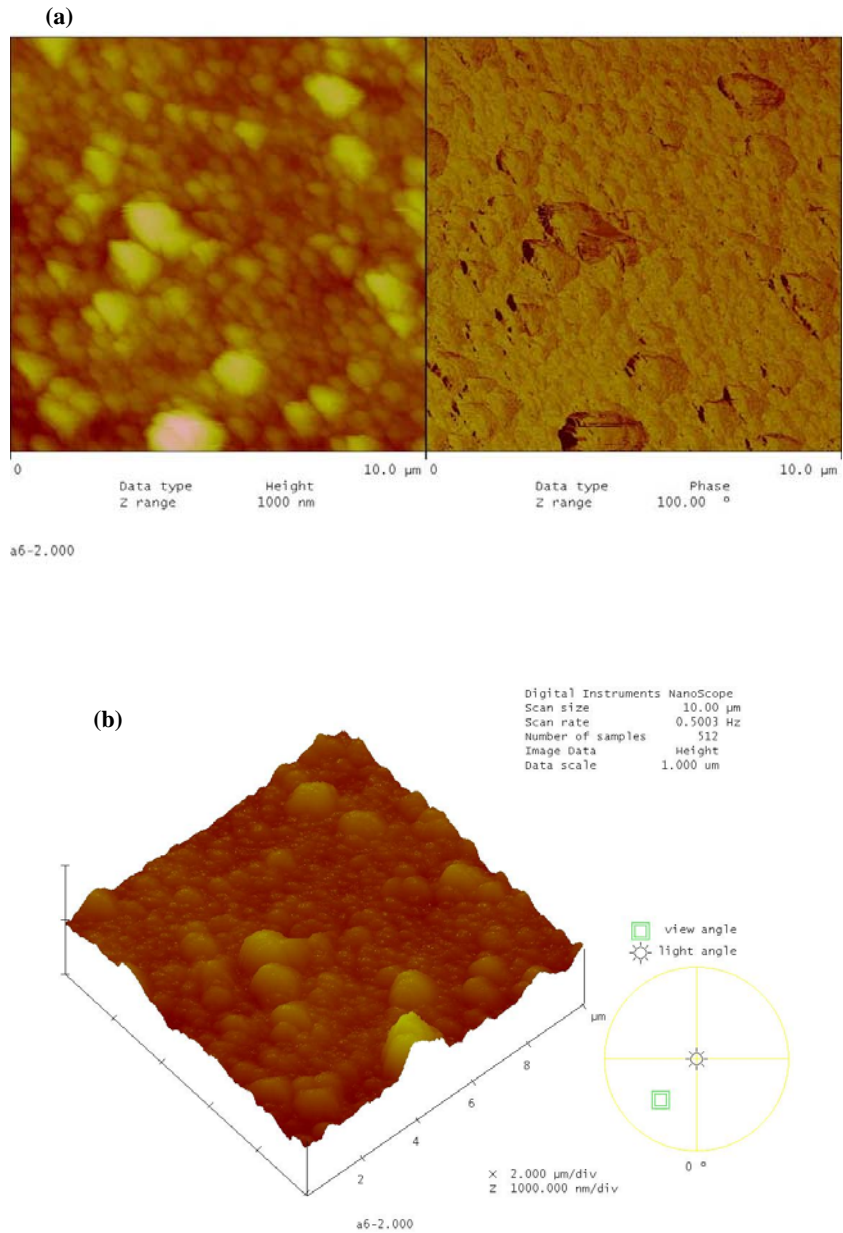


Figure 7.54. The AFM images of adsorbed BSA on glass/fibroin/m-HAp, (a) 2-dim. topographical and phase images $10 \times 10 \mu\text{m}$, (b) 3-dim. topographical image $10 \times 10 \mu\text{m}$, (c) 2-dim. topographical and phase images $1.84 \times 1.84 \mu\text{m}$, (d) 3-dim. topographical image $1.84 \times 1.84 \mu\text{m}$.

(cont. on next page)

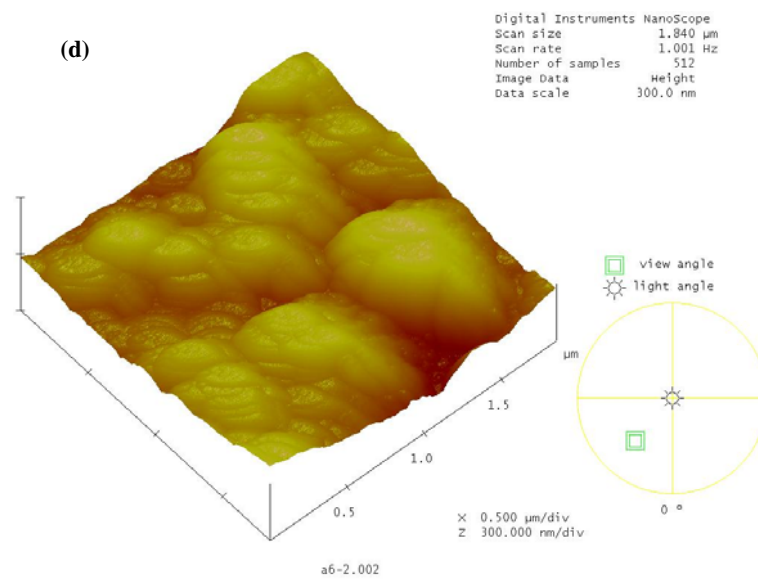
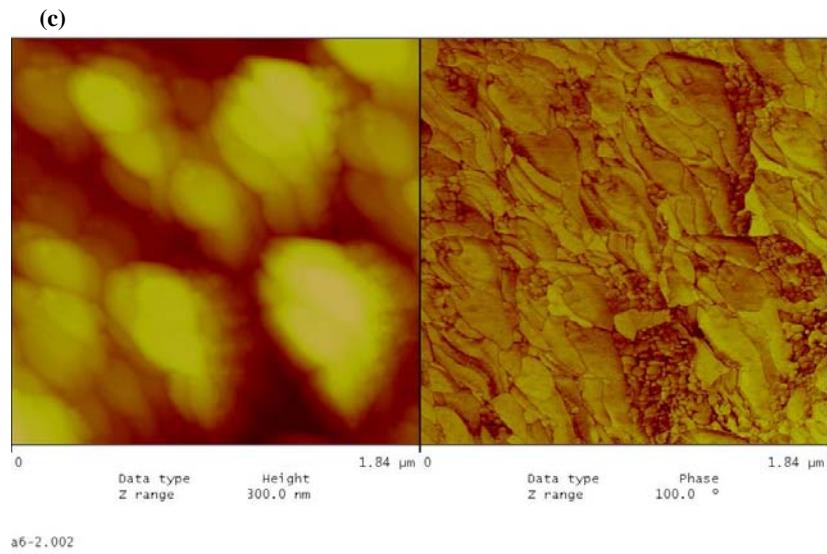


Figure 7.54. (cont.) The AFM images of adsorbed BSA on glass/fibroin/m-HAp, (a) 2-dim. topographical and phase images 10x10 μm, (b) 3-dim. topographical image 10x10 μm, (c) 2-dim. topographical and phase images 1.84x1.84 μm, (d) 3-dim. topographical image 1.84x1.84 μm.

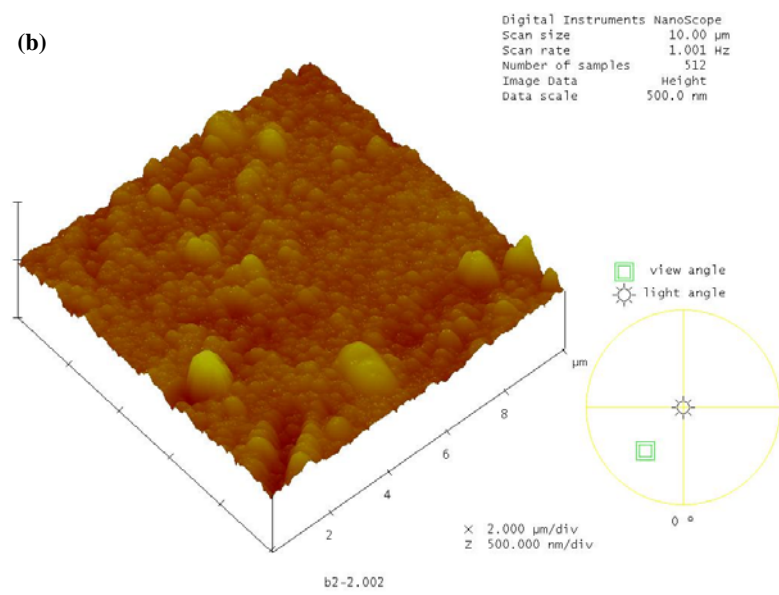
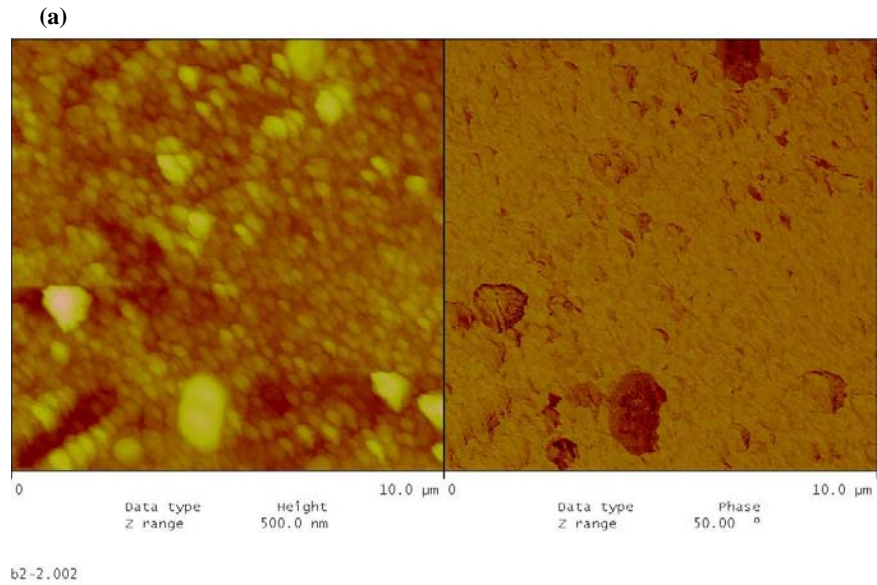


Figure 7.55. The AFM images of adsorbed BSA on glass/sericin/c-HAp, (a) 2-dim. topographical and phase images 10x10 μm , (b) 3-dim. topographical image 10x10 μm , (c) 2-dim. topographical and phase images 1.84x1.84 μm , (d) 3-dim. topographical image 1.84x1.84 μm .

(cont. on next page)

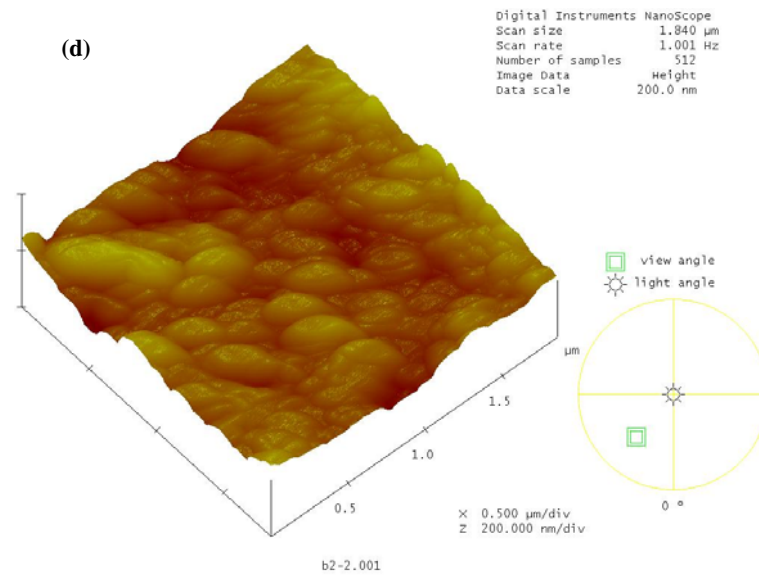
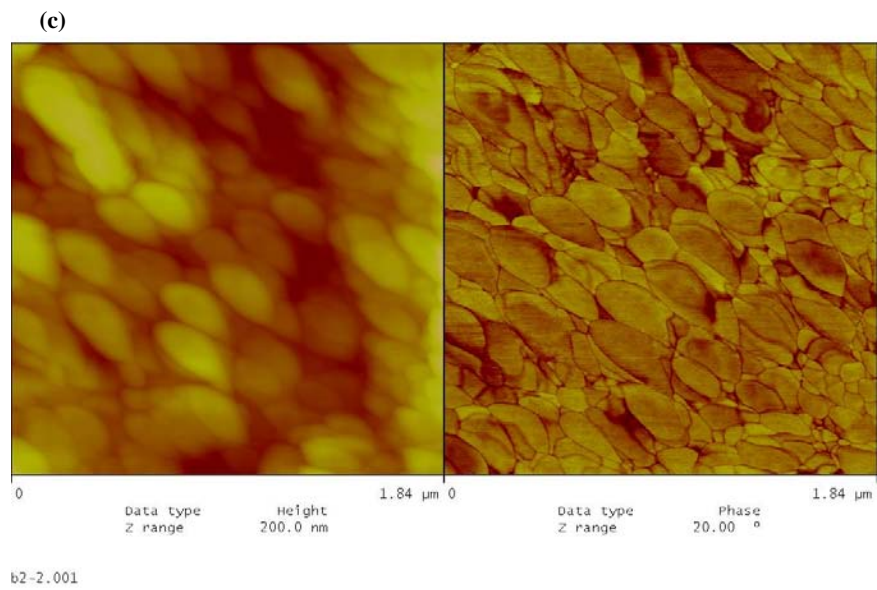


Figure 7.55. (cont.) The AFM images of adsorbed BSA on glass/sericin/c-HAp, (a) 2-dim. topographical and phase images 10x10 μm, (b) 3-dim. topographical image 10x10 μm, (c) 2-dim. topographical and phase images 1.84x1.84 μm, (d) 3-dim. topographical image 1.84x1.84 μm.

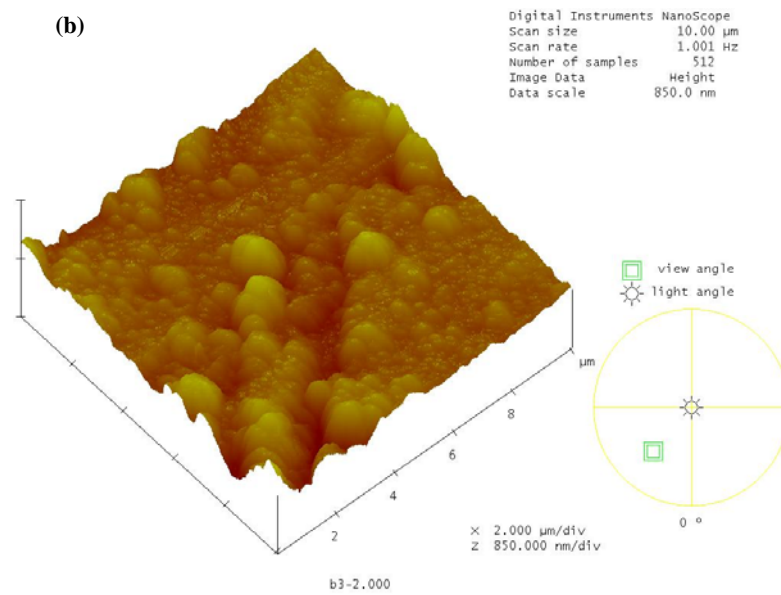
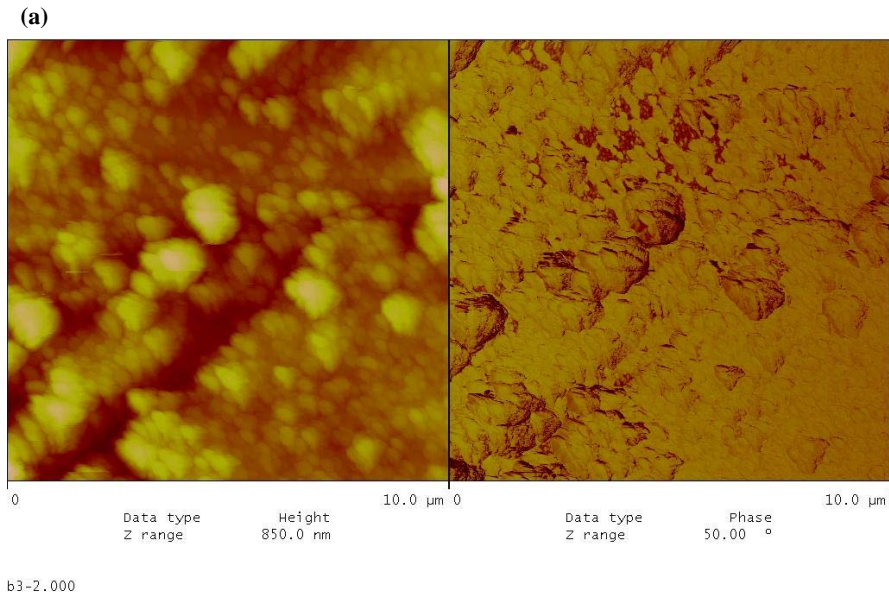


Figure 7.56. The AFM images of adsorbed BSA on glass/sericin/m-HAp, (a) 2-dim. topographical and phase images 10x10 μm , (b) 3-dim. topographical image 10x10 μm , (c) 2-dim. topographical and phase images 1.84x1.84 μm , (d) 3-dim. topographical image 1.84x1.84 μm .

(cont. on next page)

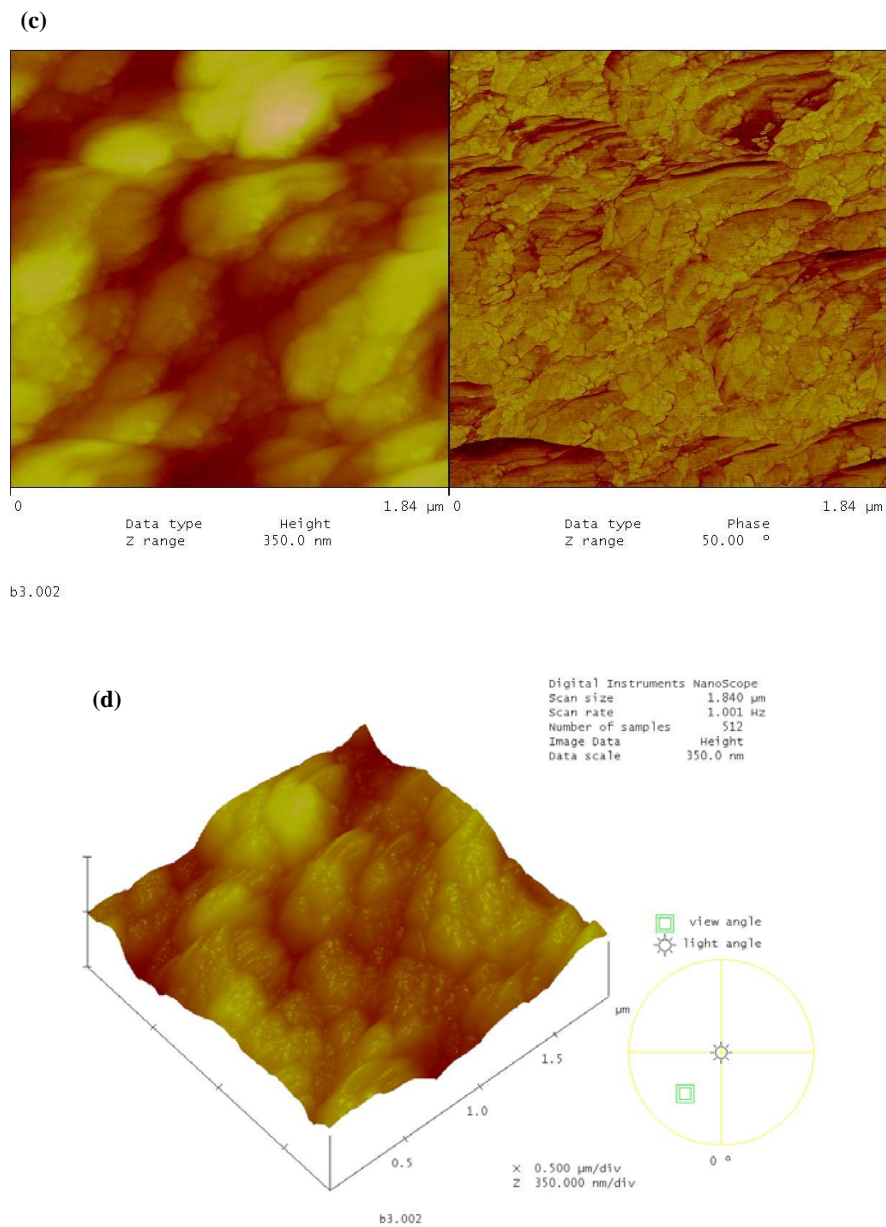


Figure 7.56. (cont.) The AFM images of adsorbed BSA on glass/sericin/m-HAp, (a) 2-dim. topographical and phase images $10 \times 10 \mu\text{m}$, (b) 3-dim. topographical image $10 \times 10 \mu\text{m}$, (c) 2-dim. topographical and phase images $1.84 \times 1.84 \mu\text{m}$, (d) 3-dim. topographical image $1.84 \times 1.84 \mu\text{m}$.

The AFM image of the collagen type I adsorbed on the glass surface is shown in Figure 7.57. The adsorption is weak with less than 5% surface coverage. The typical 64 nm striations of the collagen fiber (Darnel, et al. 1990) were visible in the phase image.

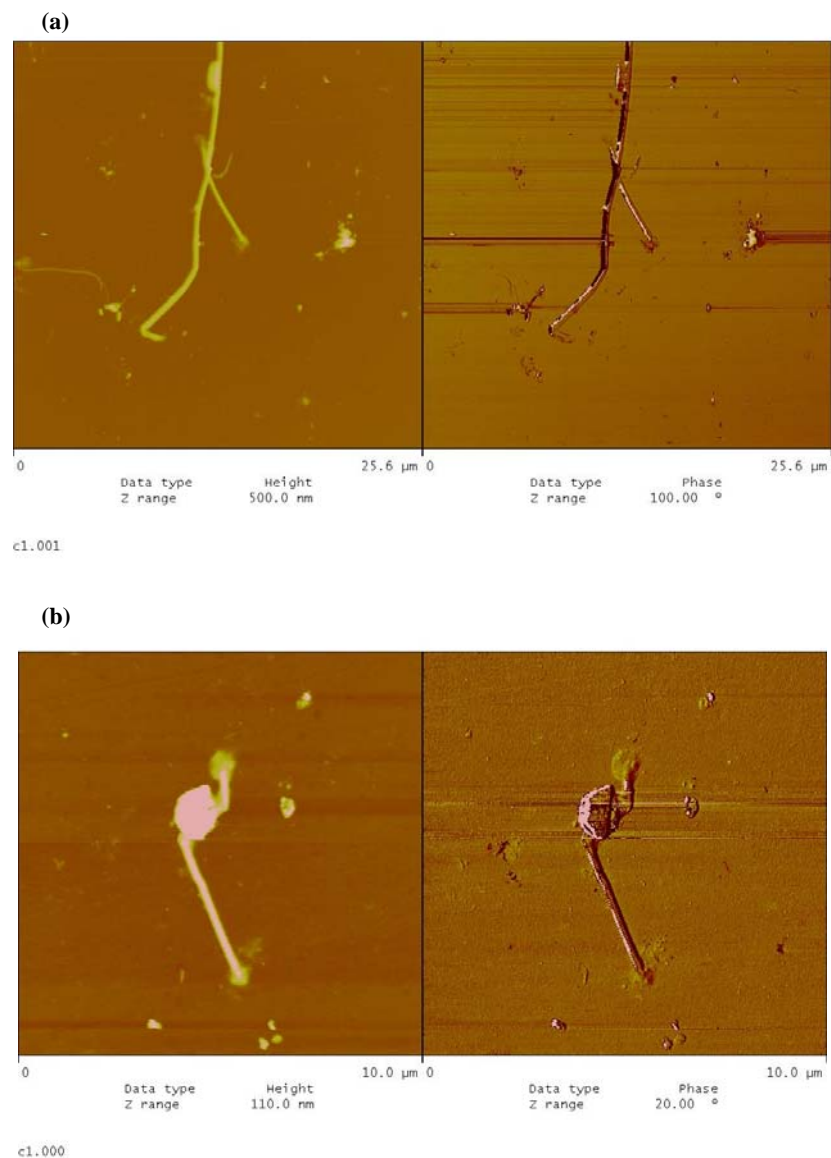


Figure 7.57. The AFM image of the collagen type I adsorption on glass surface, (a) 2-dim. topographical and phase images 25.6x25.6 μm , (b) 2-dim. topographical and phase images 10x10 μm .

Collagen type I adsorption on the fibroin film is shown in Figure 7.58. Again the adsorption showed a decisive increase in comparison to the glass substrate, the surface being covered approximately 40%. The collagen fibers were dispersed randomly, and intermingled extensively. Figure 7.59 shows collagen type I adsorption on the sericin film. Approximately 20% of the sericin surface was covered by the adsorbed collagen type I. The agglomeration of collagen fibers in the form of interminglings was not so excessive as it was on the fibroin film.

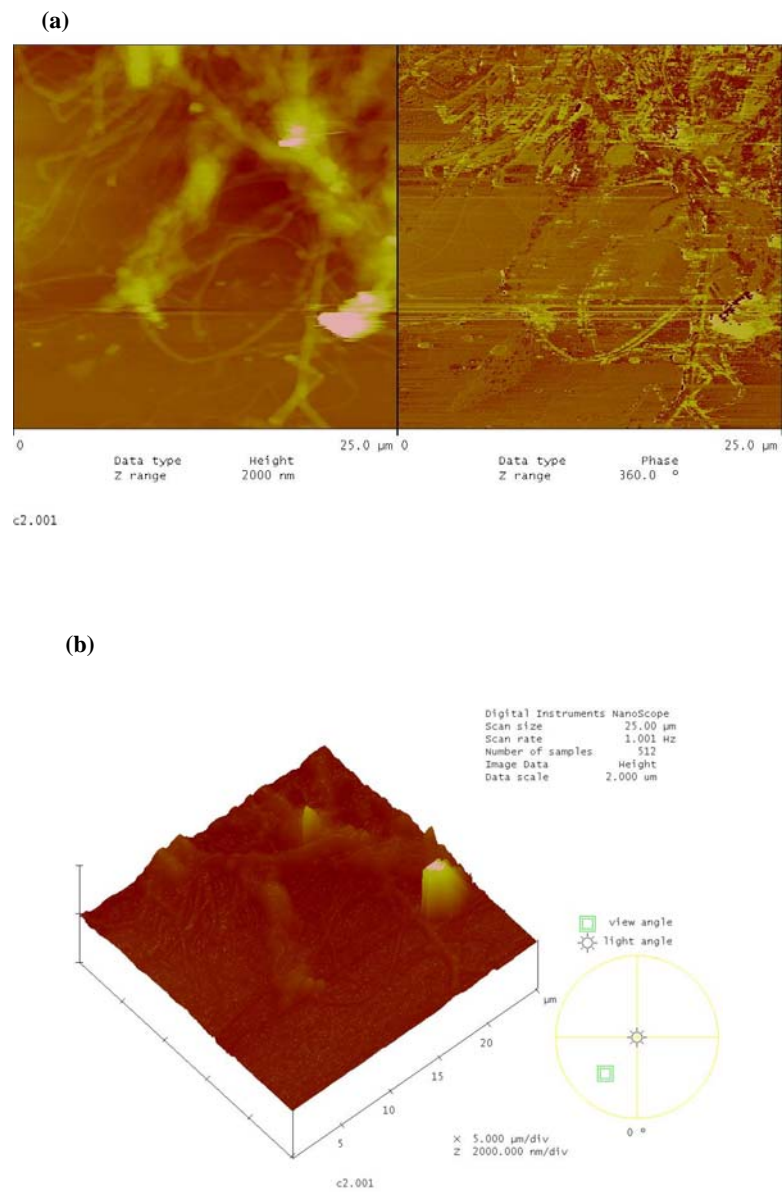


Figure 7.58. The AFM image of the collagen type I adsorption on fibroin film, (a) 2-dim. topographical and phase images 25x25 μm , (b) 3-dim. topographical image 25x25 μm .

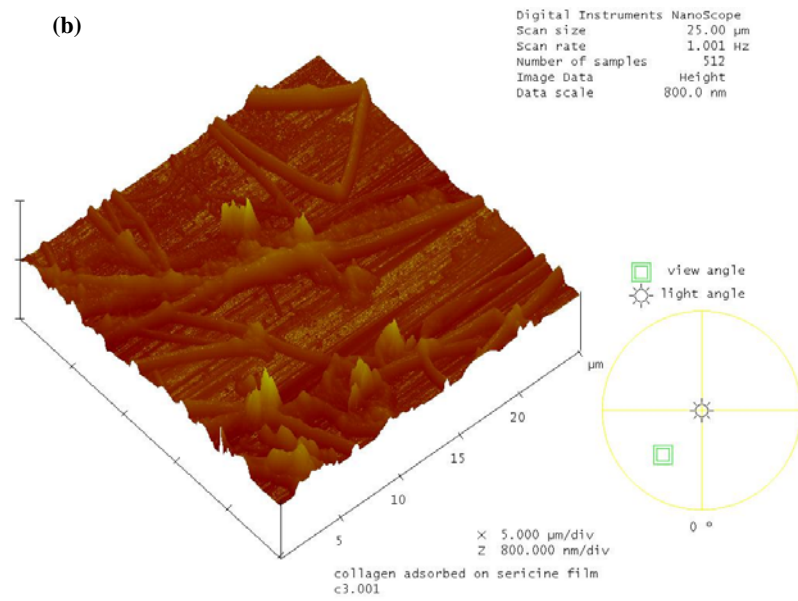
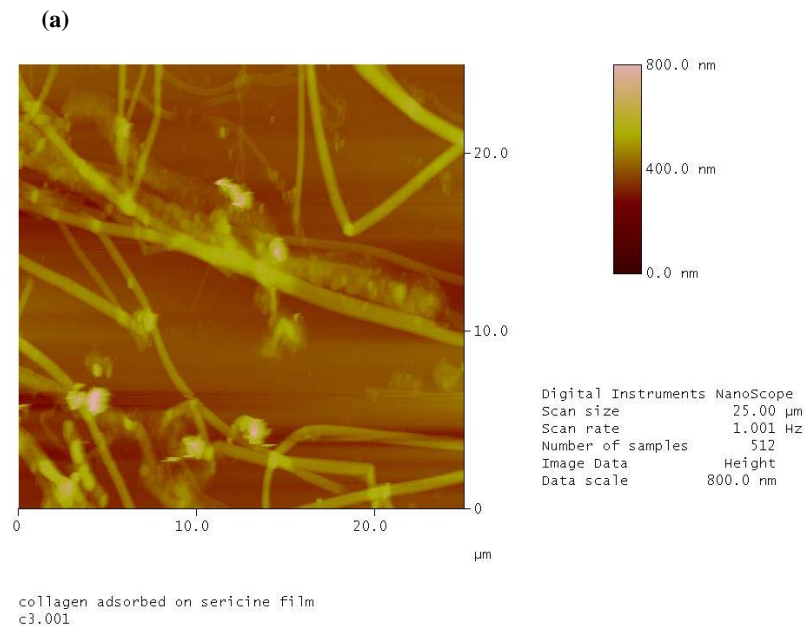


Figure 7.59. The AFM image of the collagen adsorption on sericin film, (a) 2-dim. topographical image 25x25 μm, (b) 3-dim. topographical image 25x25 μm.

The AFM images of the collagen type I adsorption on c-HAp, and m-HAp films on glass substrates, are given in Figure 7.60 and 7.61, respectively. Although on the c-HAp film collagen fibers roughly covered 15% of the surface, on the m-HAp surface there were not any collagen fibers observed.

The collagen type I adsorption on the glass/fibroin/c-HAp and glass/fibroin/m-HAp films are given in Figure 7.62 and 7.63, respectively. On the c-HAp film the collagen fiber adsorption was extensive with ~85% surface coverage, while on the m-HAp film the surface coverage was less than 10% on the average.

The collagen type I adsorption on the glass/sericin/c-HAp, and glass/sericin/m-HAp films are given in Figure 7.64 and 7.65, respectively. The collagen surface coverage of the c-HAp film was approximately 60% on the average evidencing an affinity less than for the glass/fibroin/c-HAp coating. On the m-HAp surface there were no observable collagen fiber adsorption at all. However, near the edge of the film where glass substrate was exposed directly to the collagen suspension little collagen fiber was observed.

Again these results for the collagen type I fibers indicated that surface topographic structure proves to be an important factor, as well as the chemical structure, determining adsorption affinity. The coatings with the intermediate fibroin layers provided a better adsorption affinity for the collagen type I fibers as compared to the coatings with the intermediate sericin layer, a phenomenon which was reverse for that of the BSA adsorption.

The collagen type I adsorption directly on the fibroin surface was greater than on the sericin surface on the other hand. This phenomenon might be due to the matching charge distributions of the collagen and fibroin fibers, increasing the degree of cooperativity in the coulombic attraction driven adsorption. Spatially matching hydrophobic groups on the collagen and fibroin fibrils may also contribute to the positive degree of cooperativity by hydrophobic interaction in the aqueous environment during adsorption.

The c-HAp particles might have been spatially distributed over the fibroin surface during their deposition, forming a charge distribution complementary and corresponding to that of the fibroin film underneath which might be considered as a template. Therefore, the collagen adsorption was also enhanced on the glass/fibroin/c-HAp coating, because of the matching surface charge of the c-HAp layer distributed in accordance with the fibroin film template. This phenomenon also pointed out that the

interaction between the fibroin film and collagen fibers was predominantly coulombic rather than hydrophobic, since the adsorption also enhanced on the c-HAp surface with the intermediate fibroin film acting as a template. The collagen type I fiber adsorptions on the m-HAp surfaces were much lower (or even non-existent) as compared to the c-HAp surfaces.

It is known that the first structure that is formed during peri-implant healing is the cementline which biochemically requires adsorbed growth factors on the implant surface, and mechanically requires a stable surface with micron scale roughness or porosity with nanoscale undercuts, reinforced with collagen fibers with which it can interdigitate and interlock for a strong adhesion. The subsequent anchorage and growth of bone tissue on the cementline is also accelerated by the availability of the growth factors on the healing site (Davies 2000). The enhanced adsorption affinity of the c-HAp films on the intermediate fibroin and sericin layers for the collagen type I and BSA (used as a model of bone morphogenetic proteins), respectively, indicates that such structures may greatly enhance the *in vivo* adsorption of collagen fibrils and growth factors on the implant surfaces, and provide a very convenient surface for osteoinduction and osteoconduction, facilitating the formation of an initial cementline interdigitating and interlocking with the implant surface and the subsequent development of an anchored bone tissue. For accelerated healing the implant surfaces can be loaded with the convenient growth factors before implantation for *in vivo* delivery of these proteins. On the other hand, the enhanced affinity of an implant surface for growth factors increases their concentration on the implant surface locally, again facilitating osteoinduction and osteoconduction at the peri-implant healing site.

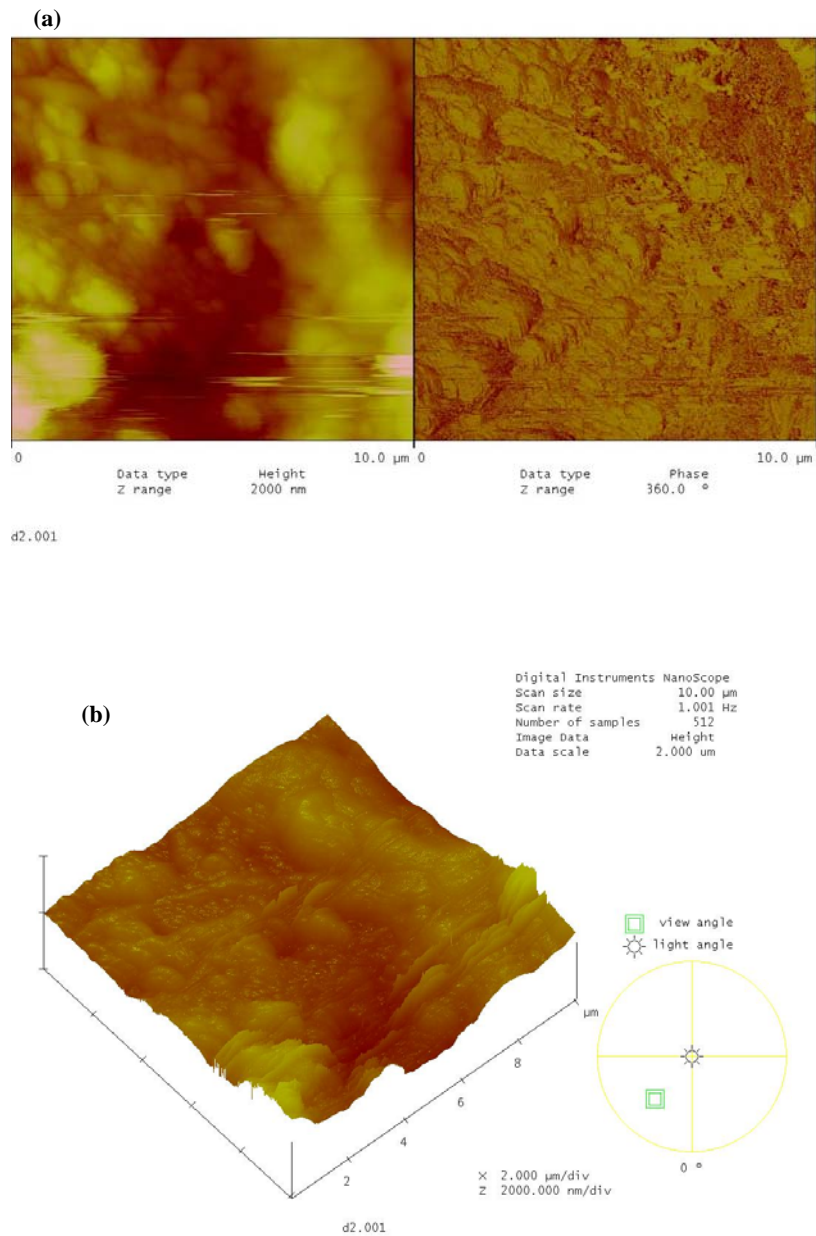


Figure 7.60. The AFM image of adsorbed collagen type I on c-HAp film on glass substrate (a) 2-dim. topographical and phase images 10x10 μm , (b) 3-dim. topographical image 10x10 μm .

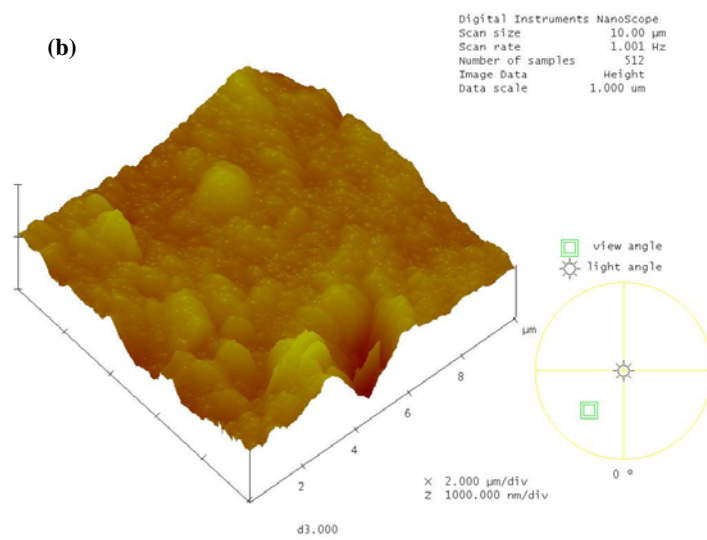
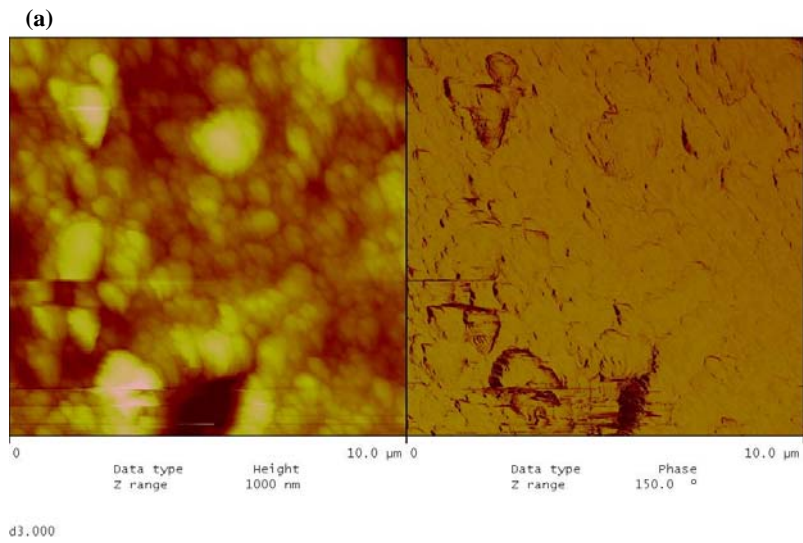


Figure 7.61. The AFM image of adsorbed collagen type I on m-HAp film on glass substrate (a) 2-dim. topographical and phase images 10x10 μm, (b) 3-dim. topographical image 10x10 μm.

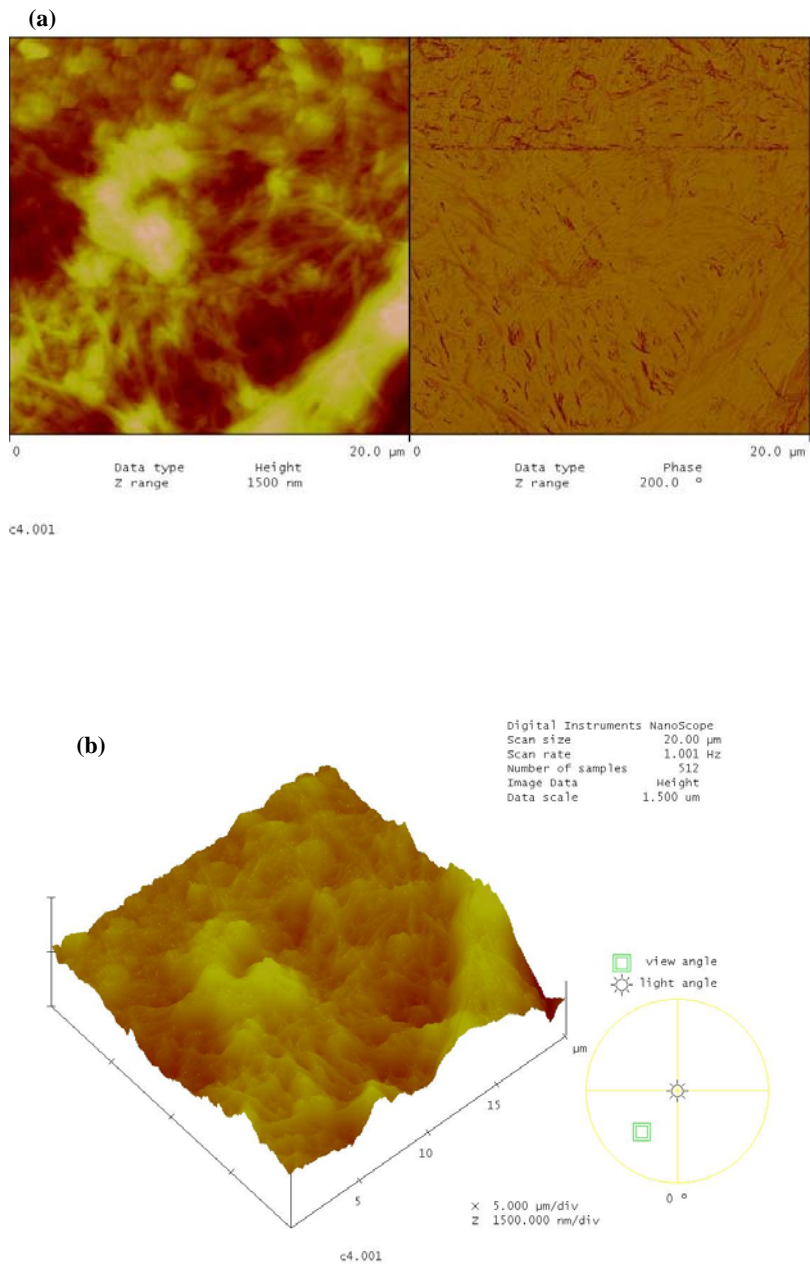


Figure 7.62. The AFM images of adsorbed collagen type I on glass/fibroin/c-HAp film, (a) 2-dim. topographical and phase images 20x20 μm , (b) 3-dim. topographical image 20x20 μm .

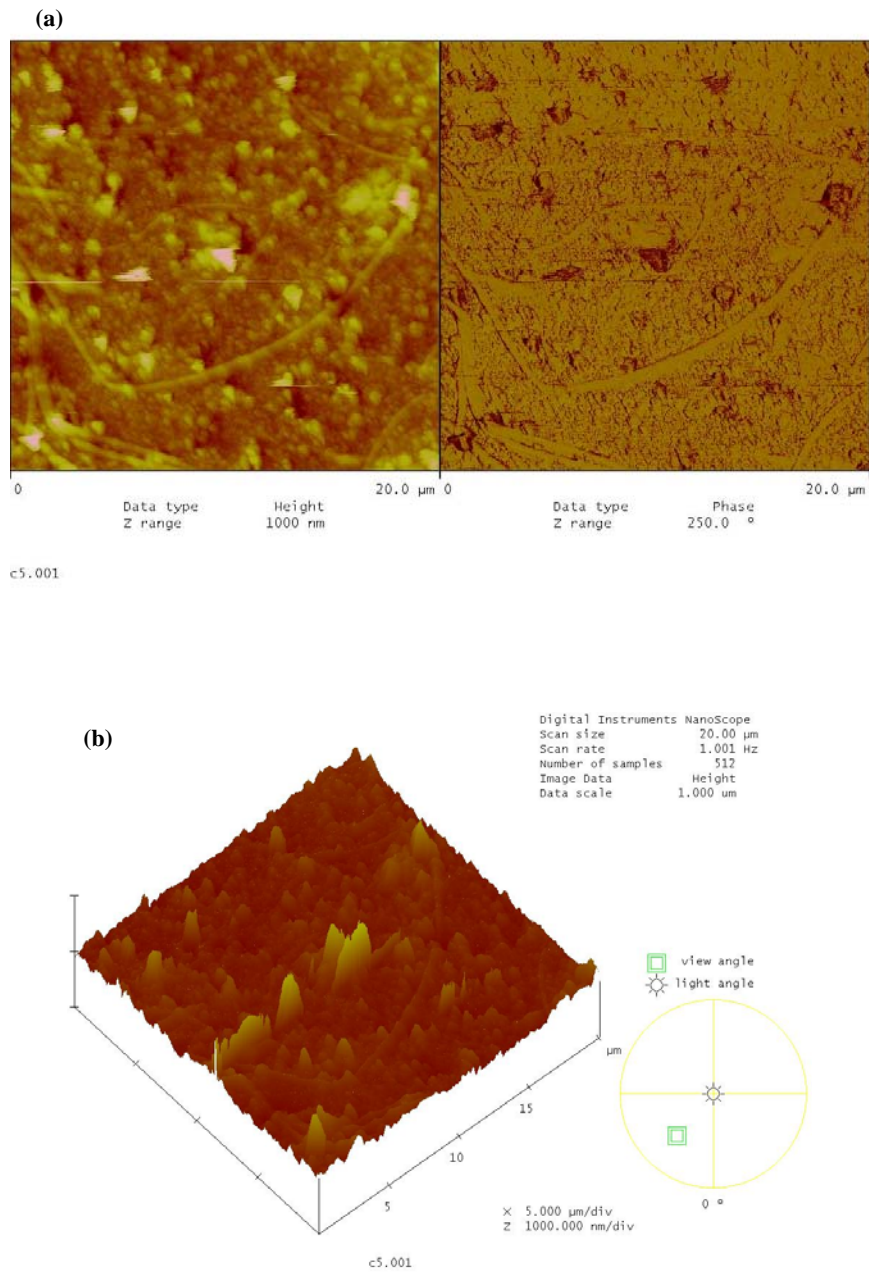


Figure 7.63. The AFM images of adsorbed collagen type I on glass/fibroin/m-HAp film, (a) 2-dim. topographical and phase images 20x20 μm , (b) 3-dim. topographical image 20x20 μm .

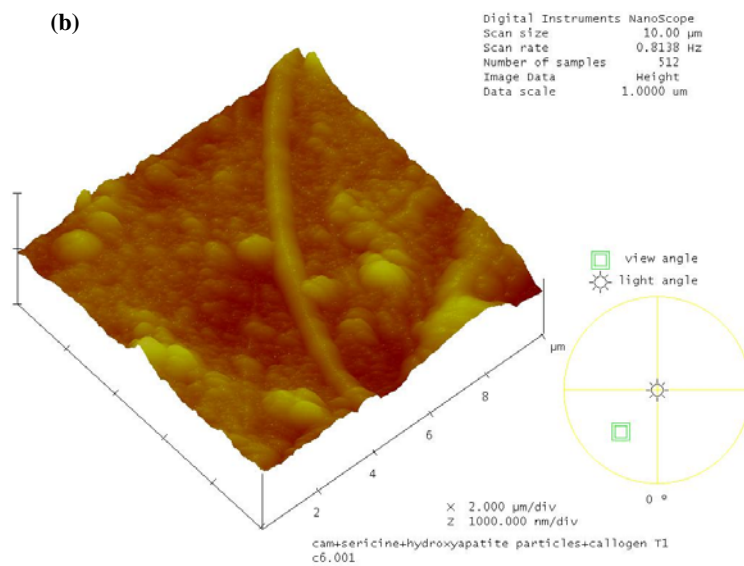
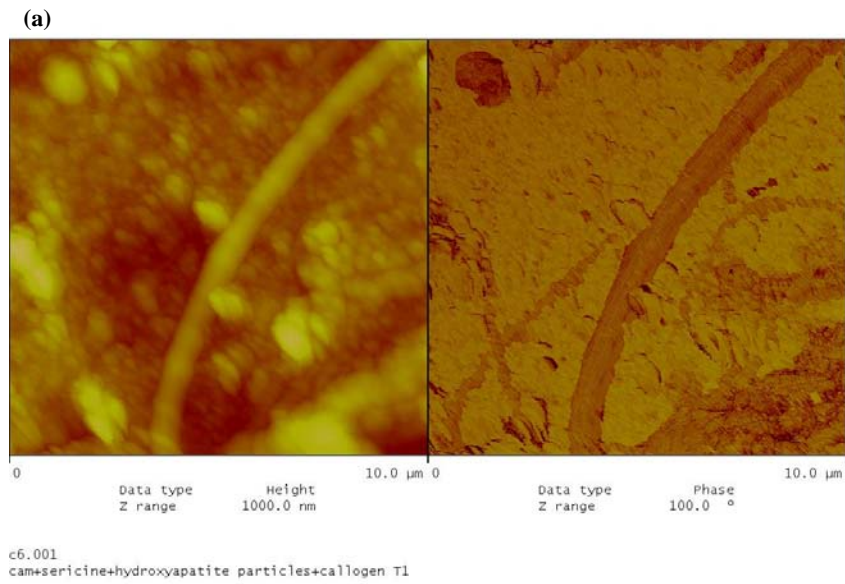


Figure 7.64. The AFM images of adsorbed collagen type I on glass/sericin/c-HAp film, (a) 2-dim. topographical and phase images 10x10 μm, (b) 3-dim. topographical image 10x10 μm, (c) 2-dim. topographical and phase images 10x10 μm, (d) 3-dim. topographical image 10x10 μm.

(cont. on next page)

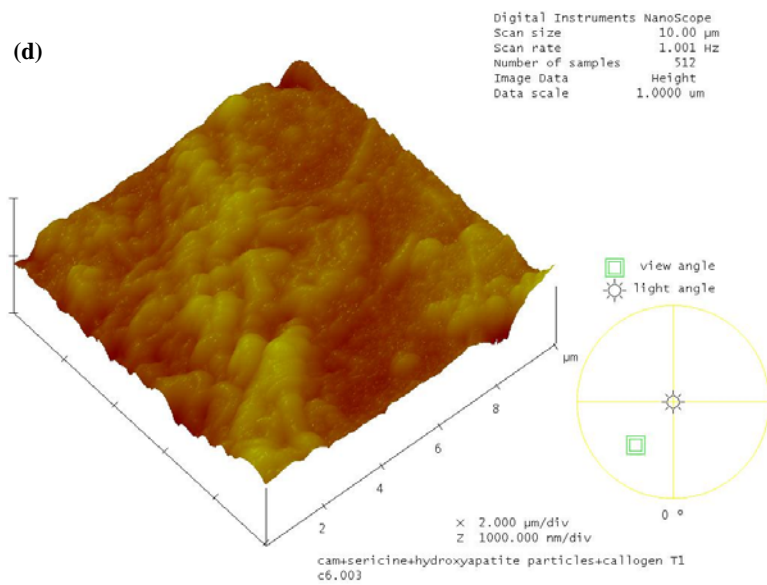
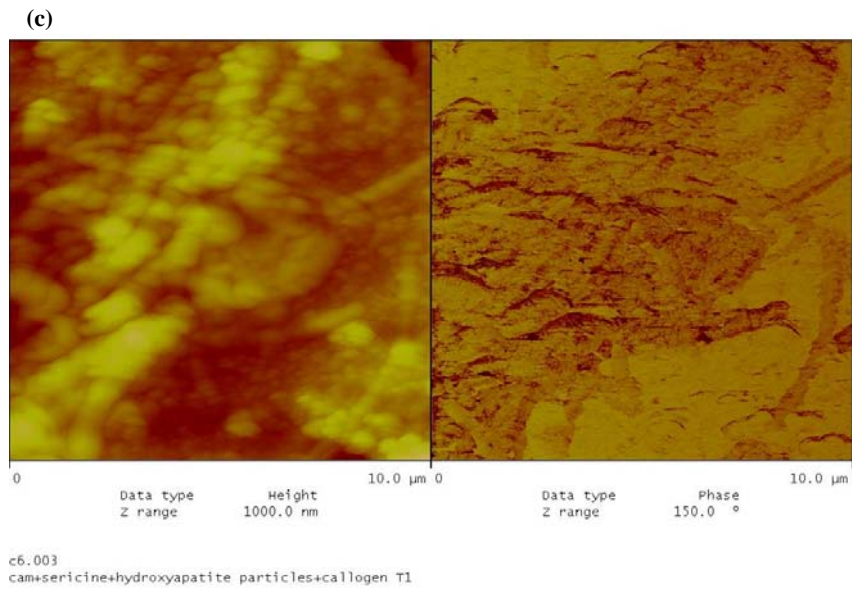


Figure 7.64. (cont.) The AFM images of adsorbed collagen type I on glass/sericin/c-HAp film, (a) 2-dim. topographical and phase images 10x10 μm, (b) 3-dim. topographical image 10x10 μm, (c) 2-dim. topographical and phase images 10x10 μm, (d) 3-dim. topographical image 10x10 μm.

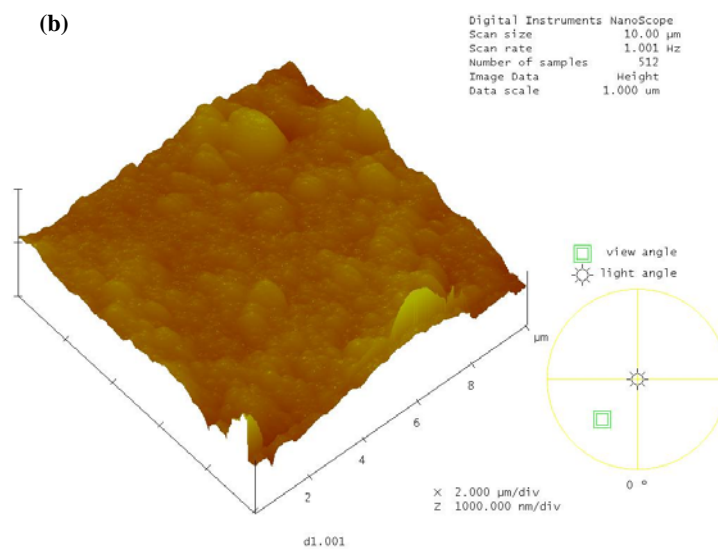
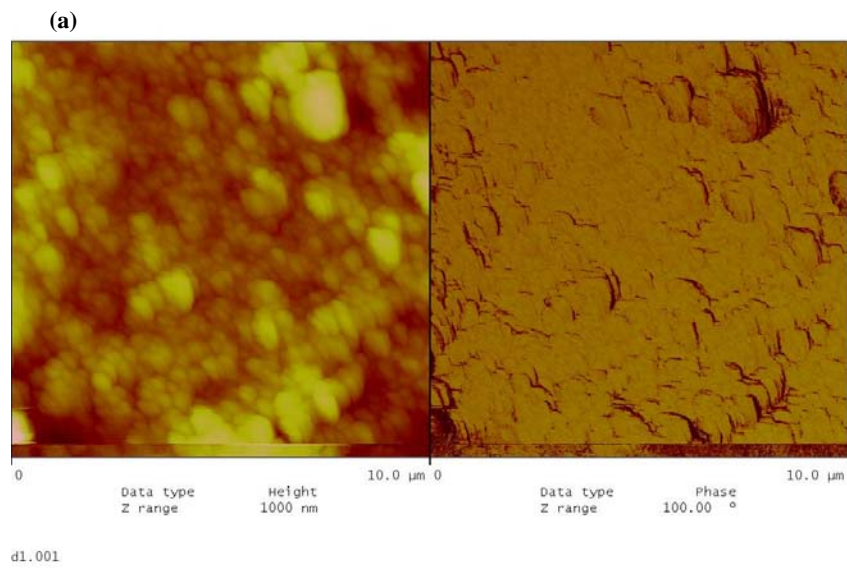


Figure 7.65. The AFM images of adsorbed collagen type I on glass/sericin/m-HAp film, (a) 2-dim. topographical and phase images $10 \times 10 \mu\text{m}$, (b) 3-dim. topographical image $10 \times 10 \mu\text{m}$, (c) 2-dim. topographical and phase images $10 \times 10 \mu\text{m}$, near the end of the film where glass substrate were exposed to the collagen suspension directly (d) 3-dim. topographical image $10 \times 10 \mu\text{m}$.

(cont. on next page)

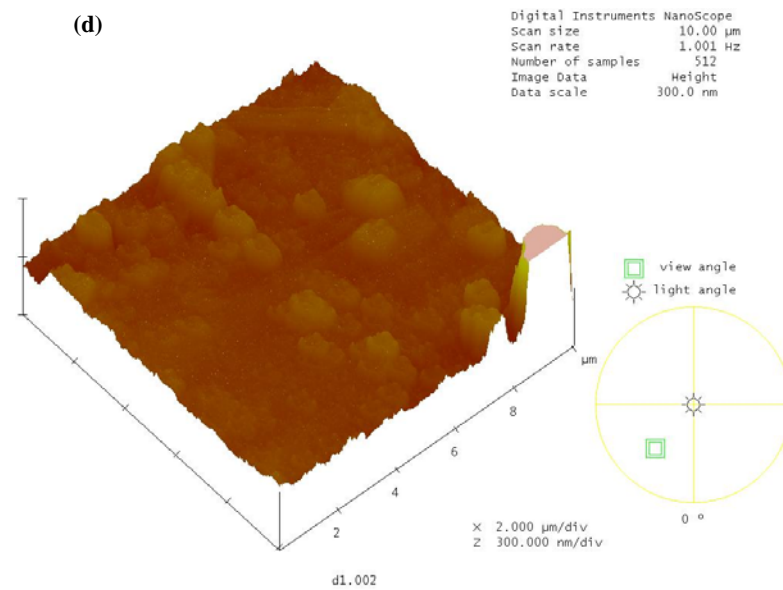
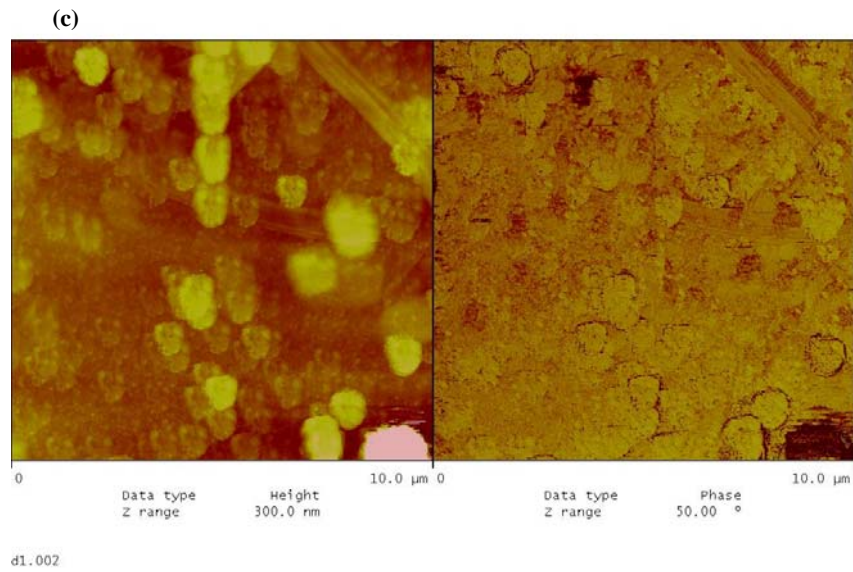


Figure 7.65. (cont.) The AFM images of adsorbed collagen type I on glass/sericin/m-HAp film, (a) 2-dim. topographical and phase images $10 \times 10 \mu\text{m}$, (b) 3-dim. topographical image $10 \times 10 \mu\text{m}$, (c) 2-dim. topographical and phase images $10 \times 10 \mu\text{m}$, near the end of the film where glass substrate were exposed to the collagen suspension directly (d) 3-dim. topographical image $10 \times 10 \mu\text{m}$.

The adsorption of BSA on the thin films of c-HAp and m-HAp on glass, and glass/sericin substrates was quantified. The BSA concentrations were measured by the HPLC size exclusion method, with 100 mM PBS solution as the mobile phase. The decrease in the BSA concentration was monitored as a function of time. The calibration curve obtained for the total BSA including its dimer is given in Figure 7.66.

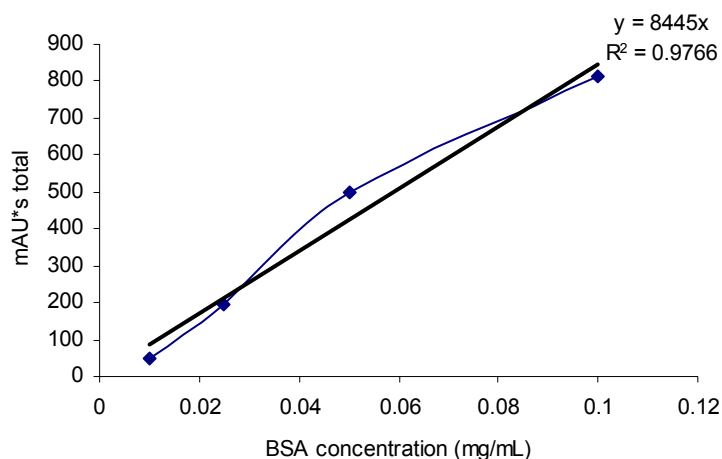


Figure 7.66. Calibration curve for BSA analysis by size exclusion HPLC; total peak area versus concentration.

The BSA adsorption on glass, glass/c-HAp, glass/m-HAp, glass/sericin/c-HAp, glass/sericin/m-HAp was studied. The change in BSA solution concentration with time is given in Figure 7.67. The glass substrates (blank 1, and blank 2) adsorbed BSA as well. The glass/c-HAp film did not show any enhanced adsorption over glass substrates. The BSA adsorption of glass/sericin/m-HAp substrate was nearly the same as glass/m-HAp substrate. The BSA concentration at 150 minutes was approximately 9% lower (a decrease from 43.8 $\mu\text{g/mL}$ for glass to 39.6 $\mu\text{g/mL}$ for glass/m-HAp) in comparison to glass substrate. The largest decrease in BSA concentration was for the glass/sericin/c-HAp film. The difference from glass substrate was around 30% (43.8 $\mu\text{g/mL}$ for glass, 33.6 $\mu\text{g/mL}$ for glass/sericin/c-HAp film) at 150 minutes. Therefore, the adsorption of BSA on glass/sericin/c-HAp film was the highest, a phenomenon supported by the AFM imaging results. Another feature of the adsorption curve was in that the time rate of concentration was fast until 20 minutes after which it decreased or even flattened.

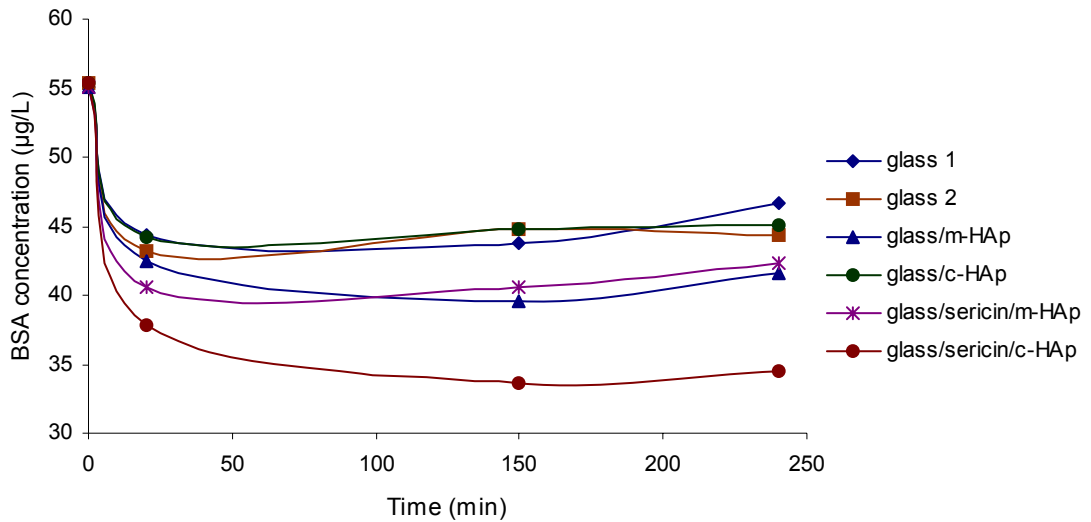


Figure 7.67. BSA adsorption on glass (blank), glass/c-HAp, glass/m-HAp, glass/sericin/c-HAp, and glass/sericin/m-HAp substrates, reported as decrease in BSA concentration versus time.

The adsorbed quantities per unit area are given in Figure 7.68-7.70. For the glass/m-HAp and glass/sericin/m-HAp films, the maximum adsorption was around $1 \mu\text{g}/\text{cm}^2$ and there was a tendency for the adsorbed amount to decrease at elongated times. The maximum adsorption of BSA was on glass/sericin/c-HAp film, $2.6 \mu\text{g}/\text{cm}^2$, a result evidencing the effectiveness of surface topographical structure as well as the chemical structure for BSA adsorption on hydroxyapatite surfaces.

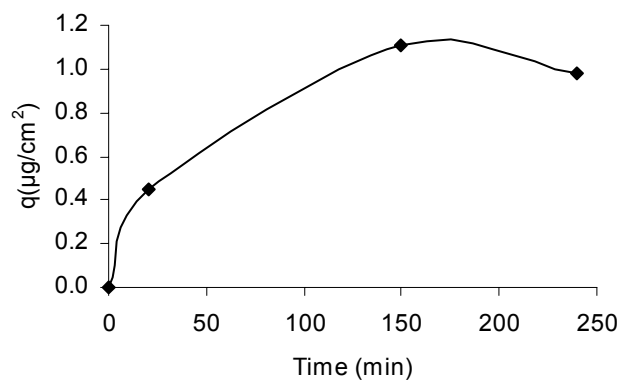


Figure 7.68. BSA adsorbed quantity on glass/m-HAp film as a function of time.

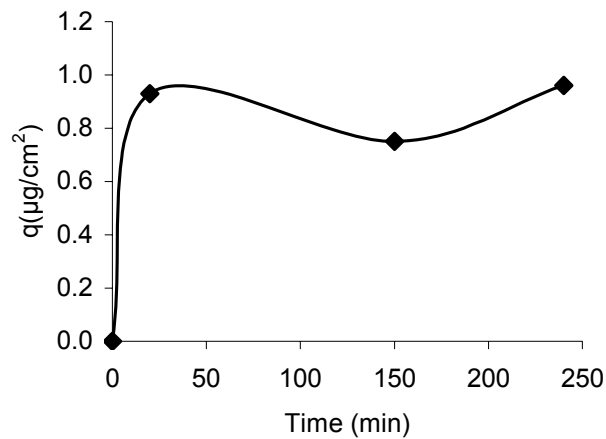


Figure 7.69. BSA adsorbed quantity on glass/sericin/m-HAp film as a function of time.

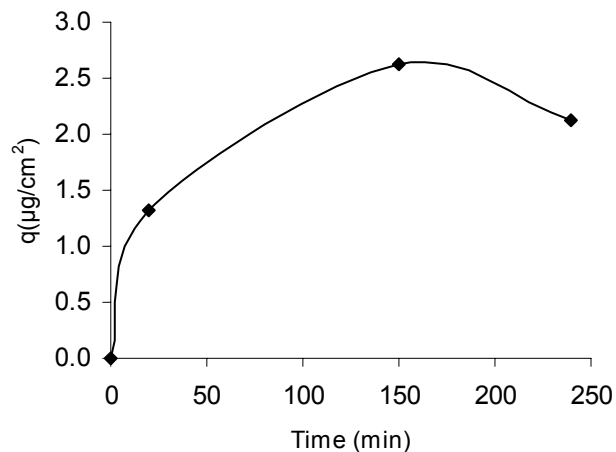


Figure 7.70. BSA adsorbed quantity on glass/sericin/c-HAp film as a function of time.

A regular surface charge distribution of the adsorbent (HAp) induces cooperative adsorption of the flexible BSA molecule (Luo and Andrade 1998). In section 7.2 the SEM and AFM images of the HAp coatings indicated much less agglomeration on the intermediate sericin films. The agglomeration is a factor that increases surface roughness and disrupts the regularity of surface charge zones, which in turn reduces the degree of cooperativity for coulombic attraction driven adsorption. The flexible structure, and charged side groups of BSA, together with the regular surface charge strips of the adsorbent HAp surface most probably provided a positive degree of cooperativity in adsorption and the adsorbed quantity of BSA increased when the surface topography was facilitating. This phenomenon was supported by the work of

Santos, et al. 2008, in which the nano topography of calcium phosphates (HAp, and β -TCP) strongly affected the protein adsorption (serum albumin), being more important than the surface chemistry. Similar results were obtained by them showing that albumin adsorption increased ~ 5 fold on a surface with a roughness of 32 ± 6 nm in comparison to a rougher surface of identical chemistry with surface roughness 142 ± 24 nm (Santos, et al. 2008). The charge distributions and surface topographical structures of the adsorbate and the adsorbent have to match for enhanced adsorption.

7.4. Microstructural and Mechanical Properties of Titania / Hydroxyapatite Films on Ti6Al4V Substrates

Microstructural evaluation of the electrochemically anodized substrates: Ti6Al4V alloy substrate surfaces were prepared at different surface roughnesses with grinding at different grits, and also polishing to $1 \mu\text{m}$. The substrates were electrochemically anodized at different voltages. The anodization current was kept approximately at 15 mA by limiting the ionic mobility with the solution viscosity. Various glycerol/H₂O mixtures were used for the purpose. The glycerol-H₂O ratio, for constant current of 15 mA, as a function of voltage is given in Figure 7.71.

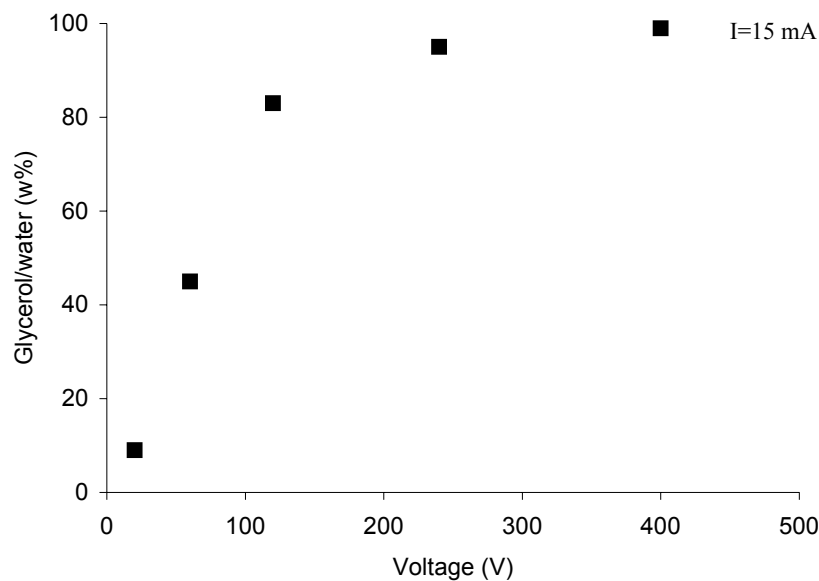


Figure 7.71. The glycerol/water ratio (weight %) for constant current of 15 mA as a function of voltage for electrochemical anodization of Ti6Al4V.

The surface roughness (R_q) was calculated as root mean square of the variations from the average, (Y_i), of the profile as in Equation 7.1. The baseline correction of the profile was done by Gaussian filter (Mitutoyo 2003).

$$R_q = \sqrt{\frac{1}{N} \sum_{i=1}^N Y_i^2} \quad (7.1)$$

The Ti6Al4V alloy surface roughness increased with the decreasing surface finish grit as expected (Figure 7.72). A steep increase in the surface roughness was observed for 120 grit samples. The anodized samples showed a cyclic surface roughness with respect to surface finish at all of the anodization voltage values. The smoothest surface was the alloy itself polished to 1 μm . The roughest surface belonged to the sample ground with 120 grit and anodized at 400 V.

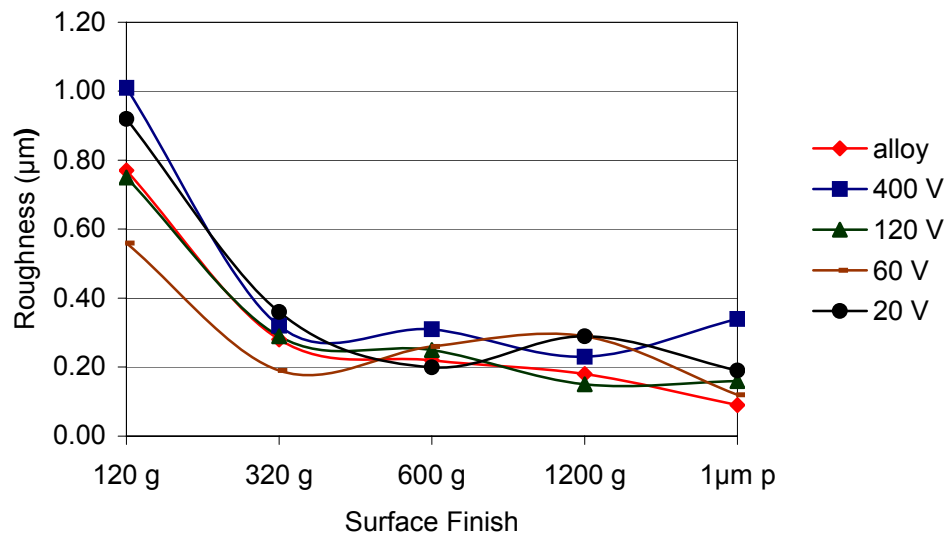


Figure 7.72. The surface roughness, R_q , of the Ti6Al4V alloy as it was, and as anodized at various voltages versus surface finish (grinding grit).

The Vickers hardnesses of the anodized alloys are given in Figure 7.73. The highest hardness value measured was HV 258 kg_f/mm^2 of the 120 grit surface ground and 20 V anodized sample. The hardnesses were the lowest for the 1 μm polished samples, HV 208 kg_f/mm^2 , and the highest for the 120 grit ground samples, HV 237 kg_f/mm^2 , on the average. The average of the Vickers hardness of the 320, 600, 1200

grits were 219. Since all the samples were ground gradually starting with the 120 grit, the variation of hardness of the substrates anodized at the same voltage, was not expected to arise from a depth property profile of the alloy near the surface. Most probably the source of the difference was the minute changes of the penetration depth of the micro indenter due to the surface topographical structure.

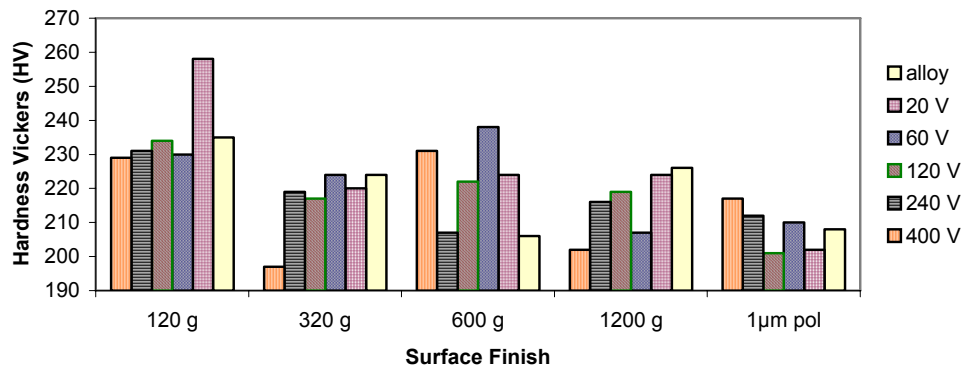


Figure 7.73. The surface hardness (HV) of the Ti6Al4V alloy with respect to surface finish grit and anodization voltage.

The change of Vickers hardness of the surface with respect to the anodization voltage averaged over surface roughness (grinding grit size) is illustrated in Figure 7.74. The hardness of the alloy was \sim HV 220 kg_f/mm^2 . The hardness decreased from \sim HV 226 kg_f/mm^2 of 20 V anodized sample to \sim HV 215 kg_f/mm^2 of the 400 V anodized sample. This might point out to phase and/or morphological changes with the changing anodization voltage.

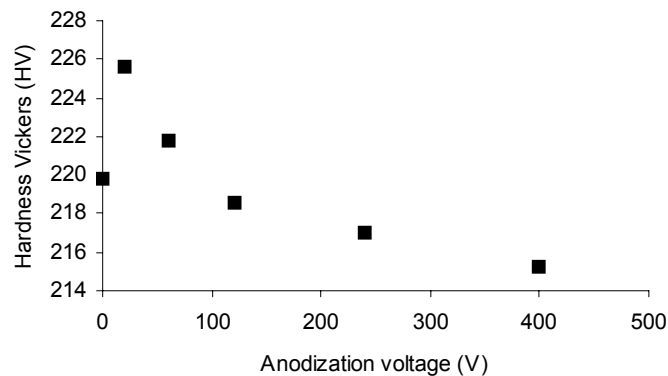


Figure 7.74. Ti6Al4V alloy surface hardness versus anodization voltage averaged over surface roughness; the alloy (without anodization) is shown as 0 volt.

The SEM image of the 20 V anodized (for 50 min), 1200 grit ground sample is shown in Figure 7.75. When compared to the optical micrograph of the etched alloy (Figure 3.5) the grain sizes of 10-15 μm coincided with the distance between the centers of the dispersed crest regions. This indicated that during anodization the oxidation reactions started on the grain boundaries where mass diffusion was to be highest. The EDX analysis results of the same sample are illustrated in Figure 7.76. In the crest region (Figure 7.76a) Ti/O atomic ratio was ~ 1 , while in the trough region Ti/O was 1.7. The crest region was richer in oxygen supporting the argument based on the SEM images of the crest and trough regions. The crest region (Figure 7.75c) was composed of fine TiO_2 particles majorly of size < 20 nm, while the trough, the metallic surface (Figure 7.75d) seemed featureless. The crest regions covered 35% of the anodized surface, hence, the weighted average of the Ti/O ratio of the 20 V anodized surface was taken as 1.48. The Ti/O ratios of the 60 V, 120 V, 240 V and 400 V anodized 1200 grit ground Ti6Al4V alloy surfaces were determined by the EDX analyses shown in Figure 7.77.

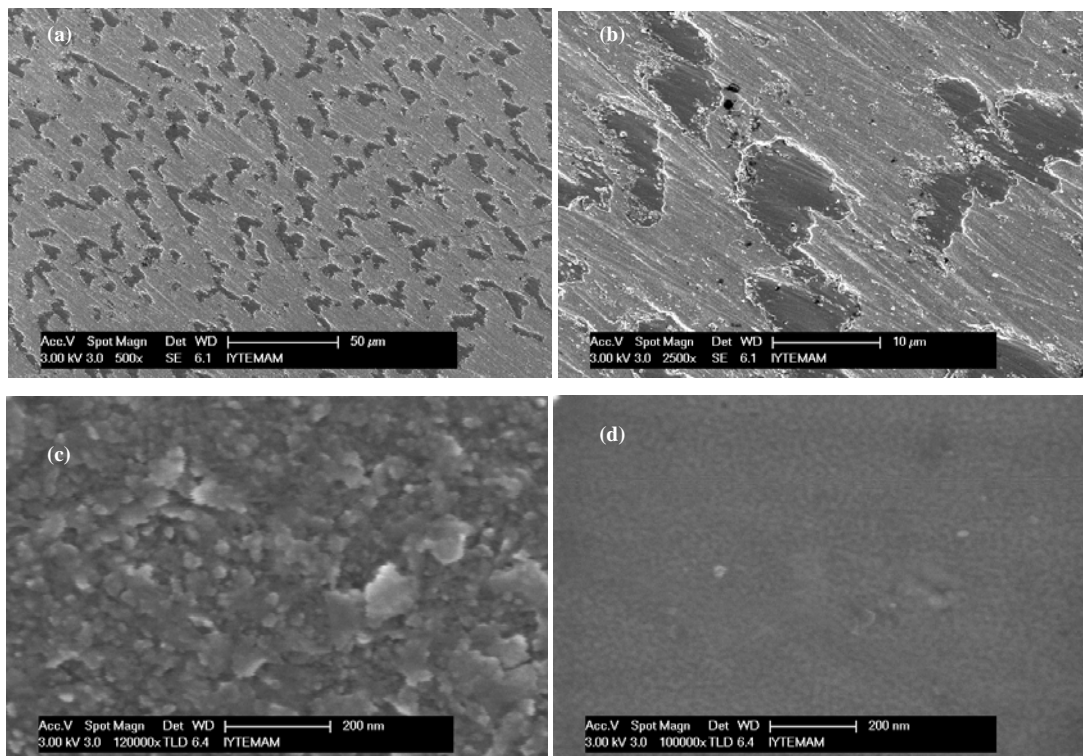


Figure 7.75. The SEM images of the 20 V anodized, 1200 grit ground Ti6Al4V alloy (a), (b) general view, (c) crest region, (d) trough region.

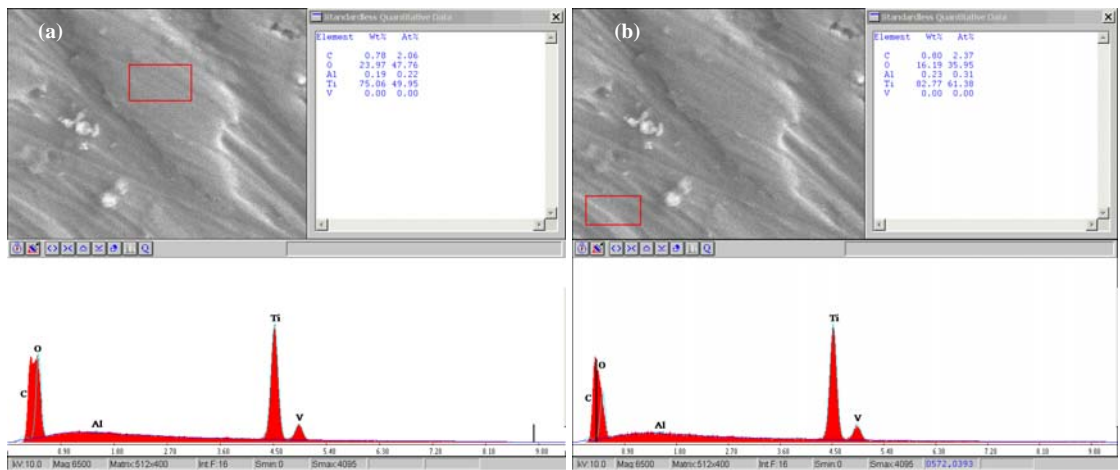


Figure 7.76. EDX analysis of 20 V anodized, 1200 grit ground Ti6Al4V alloy (a) crest region, (b) trough region.

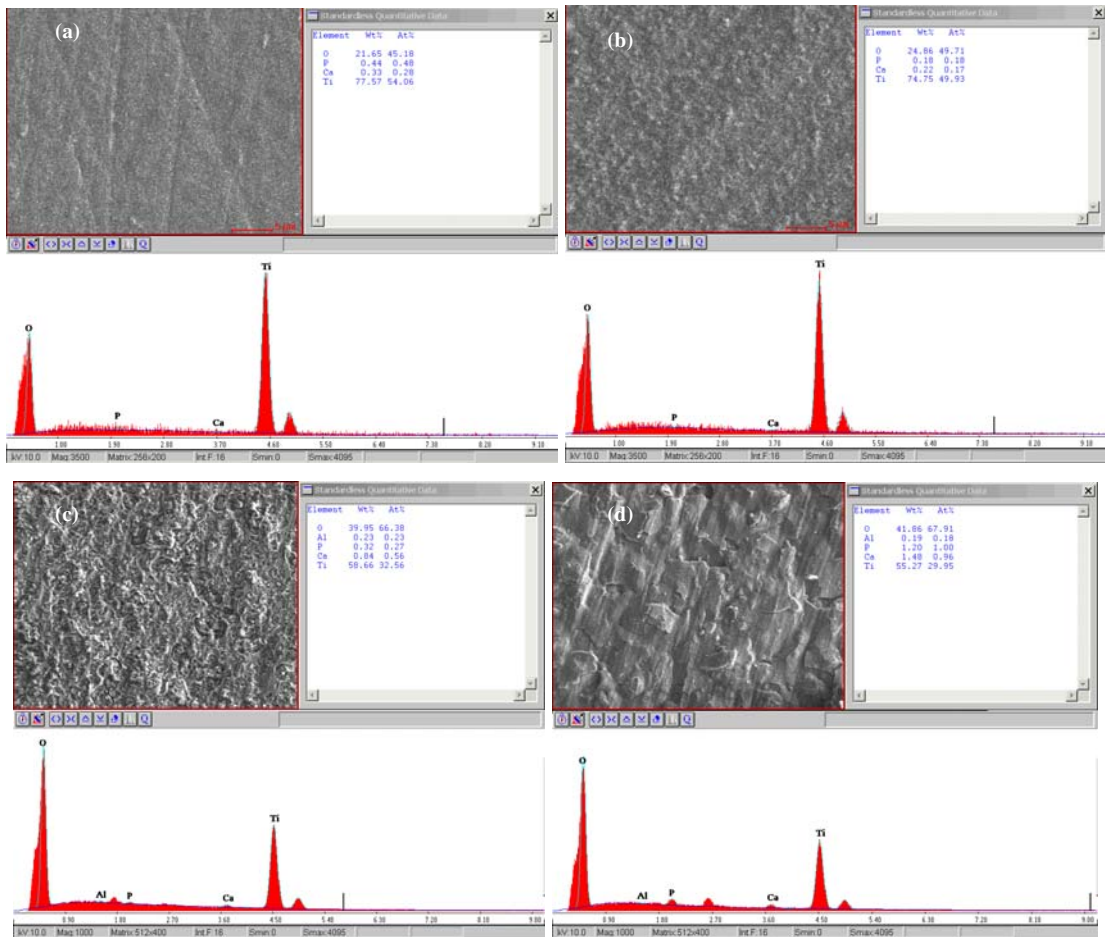


Figure 7.77. The EDX analysis of 1200 grit ground Ti6Al4V alloy anodized at (a) 60 V, (b) 120 V, (c) 240 V, (d) 400 V.

The Ti/O ratio versus anodization voltage for 1200 grit ground alloys is given in Figure 7.78. The Ti/O ratio decreased nearly linearly from 20 to 240 V, and flattened at higher voltages. Ti/O ratio versus Vickers hardness is plotted in Figure 7.79. The hardness decreased linearly with decreasing Ti/O ratio in the range 1.5-1.0, which corresponded to 20-120 V anodization. The XRD patterns of the anodized alloys are shown in Figure 7.80. The intensity of the titanium peaks (matching with Ti, syn, ICDD 05-0682) decreased at 400 V due to the increased thickness of the TiO₂ coating. The most intense peaks for anatase (ICDD 84-1286) at $2\theta=25.3^\circ$, and 48.1° were identified for 400 V and 120 V anodized samples.

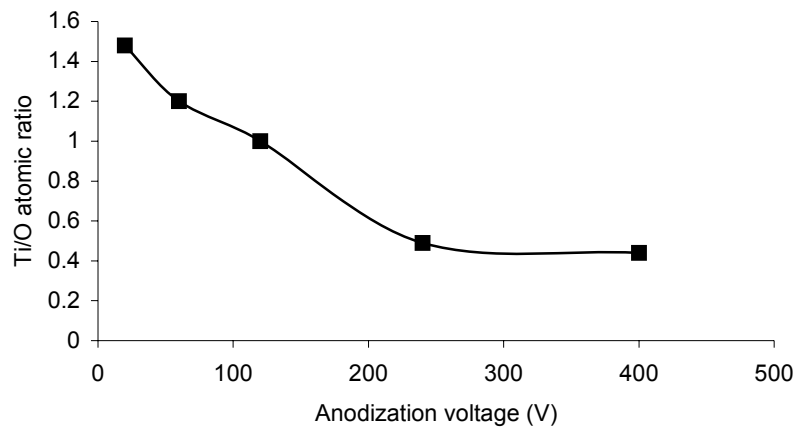


Figure 7.78. Ti/O ratio of the anodized 1200 grit ground alloys versus anodization voltage.

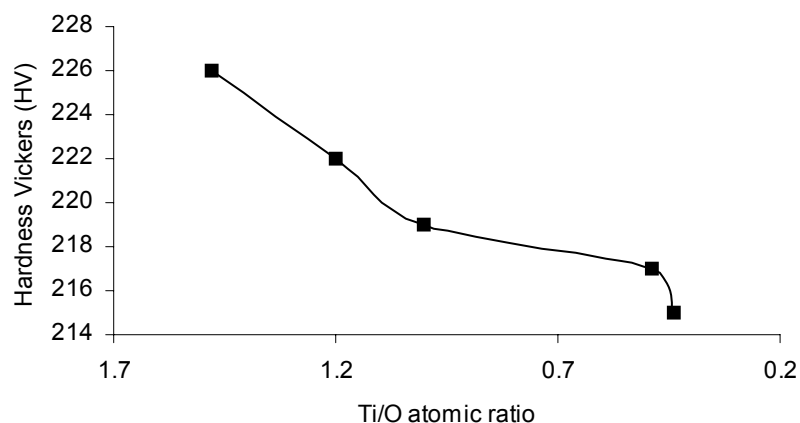


Figure 7.79. The Vickers hardness versus Ti/O atomic ratio of the 1200 grit ground alloys anodized at various voltages.

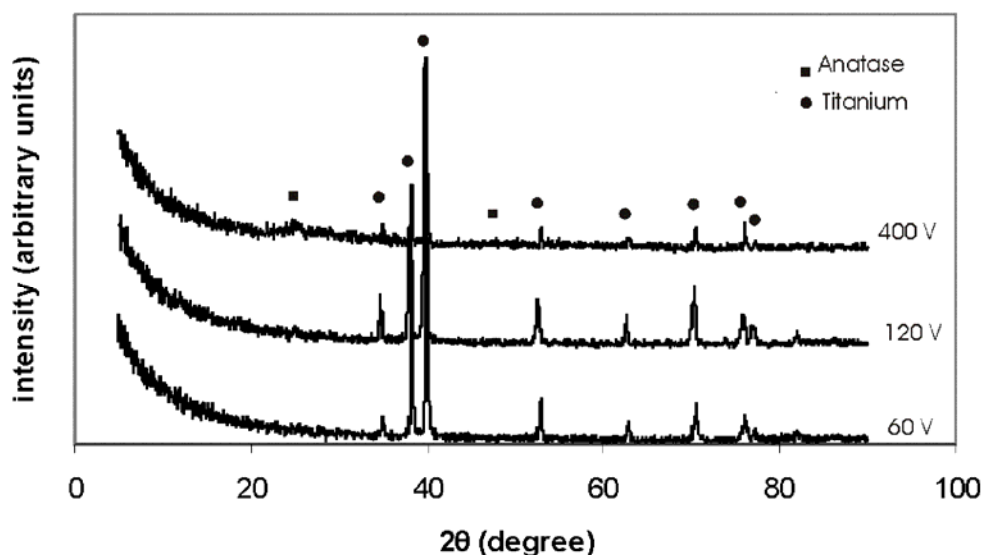


Figure 7.80. The XRD patterns of 1200 grit ground alloys anodized at various voltages.

The SEM images of the 1200 grit ground alloys anodized at voltages higher than 20 V are given in Figure 7.81. These showed that the surface morphology changed with the anodization voltage. The thickness of the only detected phase of Ti-O, namely anatase, increased with the increasing anodization voltage. At 20 V there were regions of high and low Ti/O atomic ratio. At 60 V major phase and morphological changes took place (as compared to 20 V substrates), and the thickness of the TiO₂ (anatase) increased and it covered the whole alloy surface. The growing TiO₂ grains were discernable in Figure 7.81b. The top of the crest regions seemed to be broken open reminiscent of breached hull as seen in Figure 7.81a, b. At 120 V the breached regions enlarged, and conjoined. They had discernable borders within which TiO₂ grain sizes grew to 100-300 nm (Figure 7.81c, d), and porosity increased. A second major morphological change occurred when the anodization voltage was raised to 240 V. Another breached hull picture was obtained. Outside the cracked crest top, the morphology was similar to that of 120 V substrates, however, inside the breach a totally different porous, sponge like morphology appeared (Figure 7.81e, f). At 400 V the porous, spongy morphology spread almost all over the surface (Figure 7-81g, h).

The phase and morphological changes that took place with various applied anodization voltages explains the changes in the patterns of the measured Ti/O atomic ratio and hardness values. The Ti/O ratio decreased with the increasing voltage, indicating that the surface coverage percentage and thickness of the Ti-O film increased. The hardness of the alloy increased when anodized at 20 V. The literature hardness

value of anatase is in the range HV_{100} 616-698 kg_f/mm^2 (Mineral Search 2009). Therefore, when the anatase film started to form on the Ti6Al4V alloy substrate (HV 220 kg_f/mm^2), the hardness of the surface increased. Although the thickness and surface coverage percentage of anatase film increased, the hardness gradually decreased due to the morphological changes with the increasing anodization voltage (Figure 7.74). As the anodization voltage increased in the range 20-240 V, the breached regions enlarged within which the particle size and porosity increased at the same time. The increasing porosity most probably caused the observed decrease in the hardness. At voltages surpassing 240 V the second major morphological change, the formation and enlarging of the highly porous, spongy film structure, caused the decrease in the hardness. Nevertheless, the rate of decrease in the hardness slowed, because within that voltage range the surface coverage of the new morphological structure was very rapid, and the effect of the increasing voltage was the increase in the thickness of the spongy film. The anodized alloy substrates were later used for spin coating of hydroxyapatite particles.

Microstructural evaluation of the spin-coated films: Commercial TiO_2 (c- TiO_2) powder suspensions (~15% solid content) in deionized water and ethanol, and c-HAp powder suspensions (~15% solid content) in deionized water and ethanol were used to prepare Ti6Al4V alloy substrate/c- TiO_2 , Ti6Al4V alloy substrate/c-HAp, and Ti6Al4V alloy substrate/c- TiO_2 /c-HAp films by spin coating, as described in Section 6.2.5.

In general, the films prepared with ethanol as the dispersing medium, were thicker in comparison to the films prepared with water, most probably due to the higher evaporation rate (higher vapor pressure) of ethanol that resulted in faster increase of suspension viscosity during the spin off and evaporation steps of the spin coating process. This in turn resulted in a thicker layer of compacted particles at the time the radial flow was counter balanced by the viscous resistance of a thicker fluid layer. The radial speed of spinning for H_2O , and EtOH suspensions were 4000 rpm and 3000 rpm, respectively. The spin speed for EtOH suspensions was selected lower due to their lower initial viscosity. The lower spin speed also contributed to the higher thickness of the films. The grinding paper grit size was a factor in the film thickness. The coarser surface finish gave rise to thicker films.

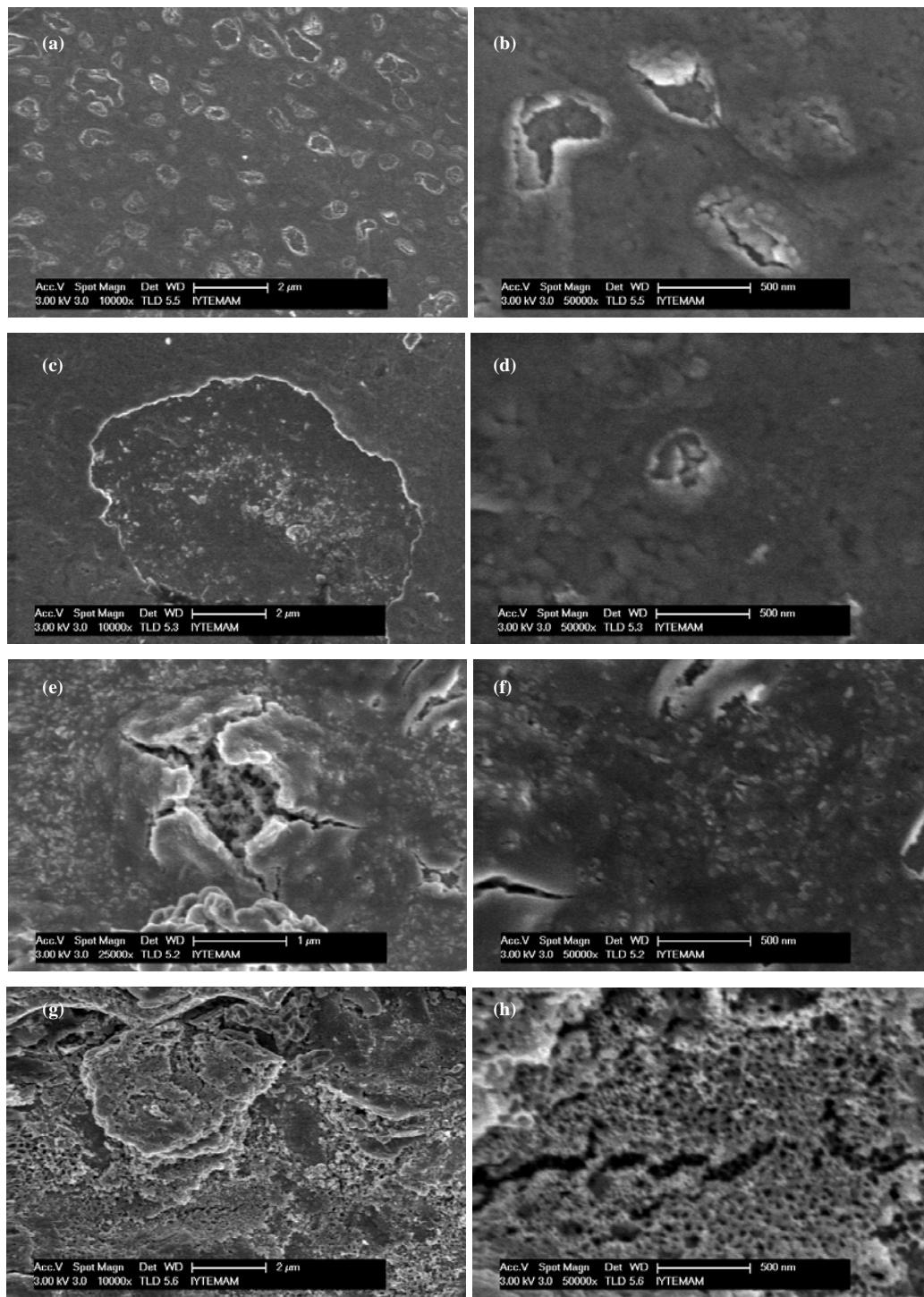


Figure 7.81. The SEM images of 1200 grit ground Ti6Al4V alloy anodized at (a), (b) 60V, (c), (d) 120 V, (e), (f) 240 V, and (g), (h) 400 V.

The SEM images of the Ti6Al4V (1200 grit)/c-TiO₂ (1 layer, H₂O suspension), and Ti6Al4V (180 grit)/c-TiO₂ (3 layers, EtOH suspension) films heat treated at 360°C are given in Figure 7.82, 7.83, respectively. The TiO₂ films prepared with the aqueous suspension contained large pores (or gaps) of sizes up to 400 nm distributed rather homogeneously over the surface. Many smaller pores in a wide size range down to ~20 nm also existed. In contrast, the TiO₂ films prepared with the EtOH suspension contained larger pores of sizes up to 1 μm distributed less homogeneously over the surface. This phenomenon was most probably the result of higher evaporation rate of ethanol which caused the viscosity of suspension to increase at a higher rate leaving less time for particles to migrate and distribute avoiding a more homogeneous film structure during the spin coating. The lower spin speed might have also contributed to larger size gaps with inhomogeneous distribution.

The SEM images of the Ti6Al4V (1200 grit)/c-TiO₂ (1 layer, H₂O suspension), and Ti6Al4V (180 grit)/c-TiO₂ (3 layers, EtOH suspension) films heat treated at 850°C are given in Figure 7.84, 7.85, respectively. The heat treatment at 850°C completely changed the surface morphology and microstructure of the Ti6Al4V/c-TiO₂ (1 layer, H₂O suspension) film (Figure 7.84). The SEM images might have indicated the TiO₂ layer was recrystallized. The film thickness was approximately 1 μm (1200 grit substrate, 1 layer, H₂O suspension). The thinner film, especially by the effect of radiative heat transfer in the muffle kiln might have reached temperatures higher than the set value of 850°C resulting in the above observation. In the polycrystalline film the crystallite sizes were in the range 100-200 nm, and the porosity seemed to be much lower in comparison to the granular structure of the same type of film heat treated at 360°C.

On the other hand, in the thicker film, Ti6Al4V/c-TiO₂ (3 layers, EtOH suspension), the TiO₂ particles sintered forming a three dimensional spongy structure (Figure 7.85). The film thickness was ~5 μm (180 grit substrate, 3 layers, EtOH suspension). The grain sizes increased as a result of the sintering and fell in the range 100-200 nm. The large gaps up to 1 μm still existed, but their number was less and they distributed more homogeneously compared to the same type of film heat treated at 360°C.

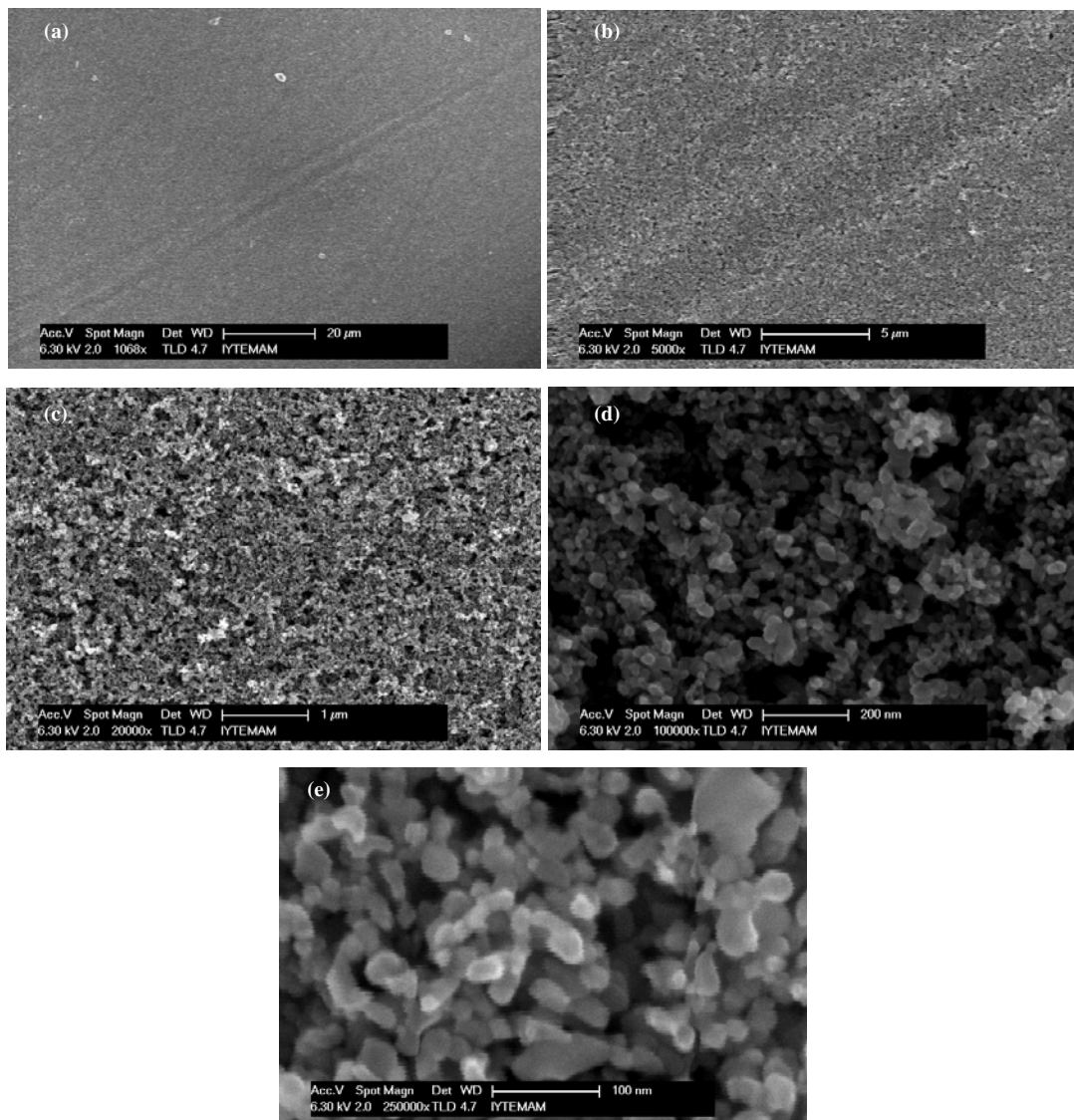


Figure 7.82. The SEM images of the Ti6Al4V alloy substrate (1200 grit)/ c-TiO₂ (H₂O suspension, 1 layer), spin coated, heat treated at 360°C at various magnifications.

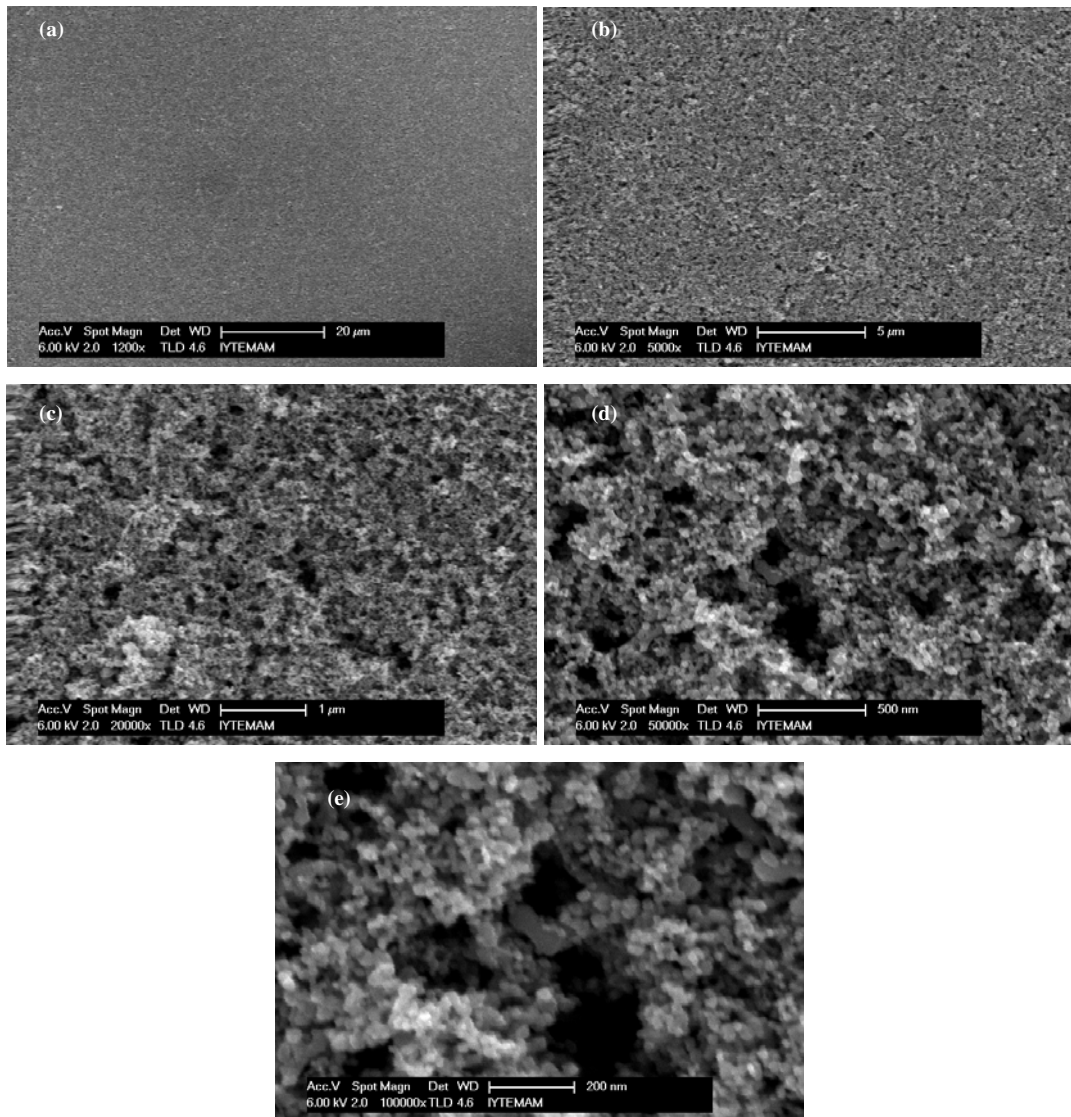


Figure 7.83. The SEM images of the Ti6Al4V alloy substrate (180 grit)/ c-TiO₂ (EtOH suspension, 3 layers), spin coated, heat treated at 360°C at various magnifications.

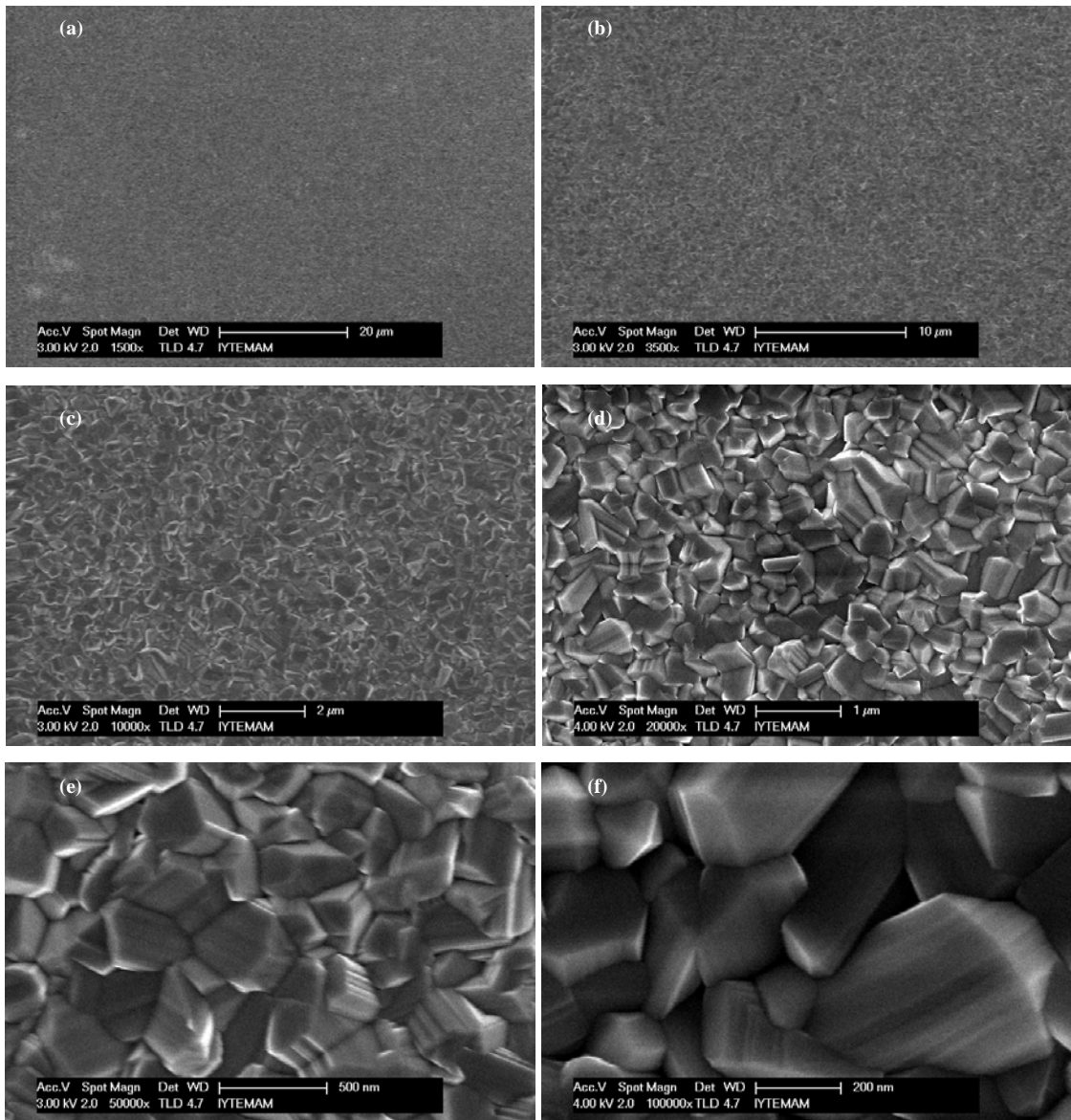


Figure 7.84. The SEM images of the Ti6Al4V alloy substrate (1200 grit)/ c-TiO₂ (H₂O suspension, 1 layer), spin coated, heat treated at 850°C at various magnifications.

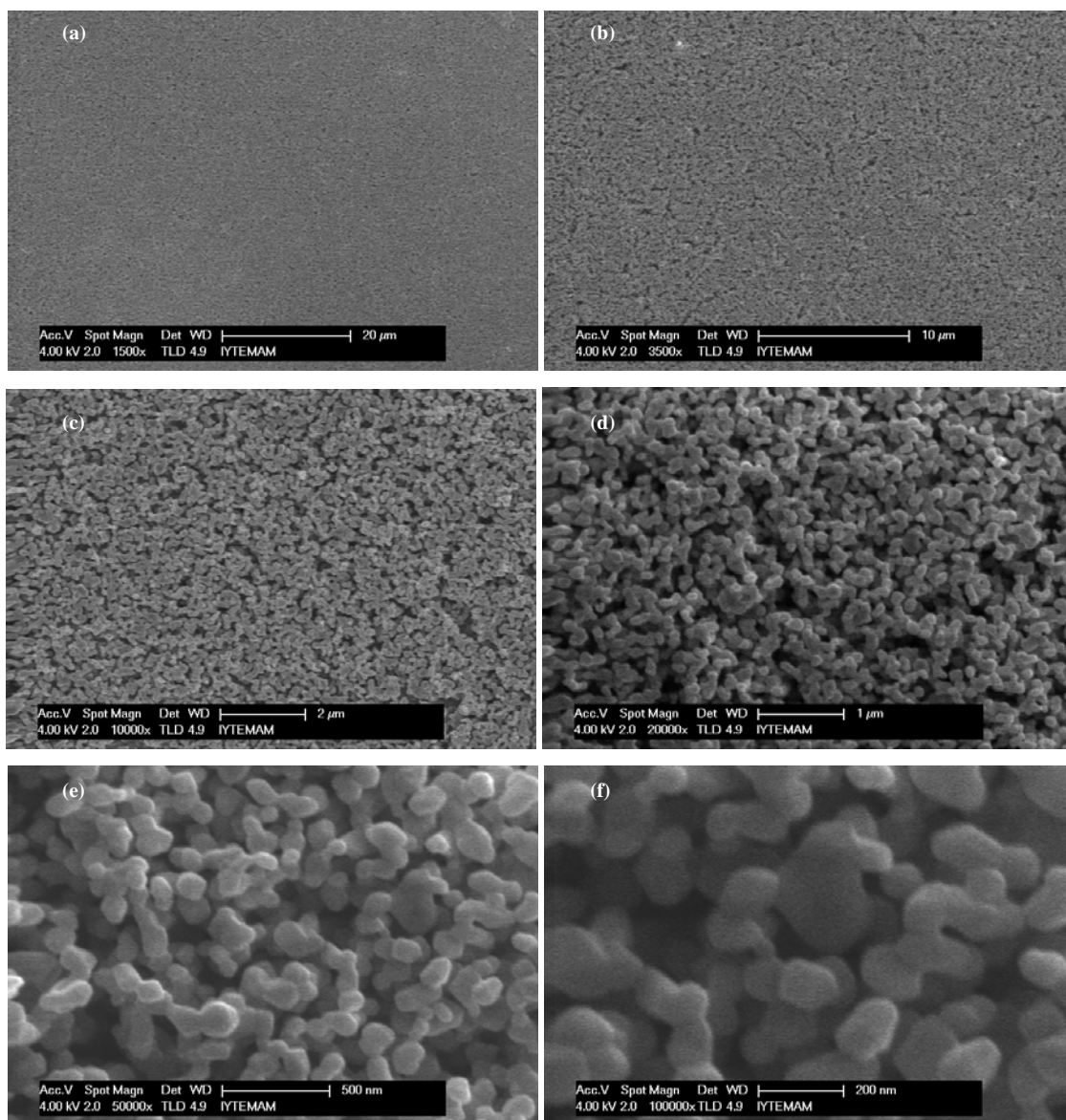


Figure 7.85. The SEM images of the Ti6Al4V alloy substrate (180 grit)/ c-TiO₂ (EtOH suspension, 3 layers), spin coated, heat treated at 850°C at various magnifications.

The XRD patterns of the Degussa P25 powder, Ti6Al4V alloy (1200 grit ground), Ti6Al4V (1200 grit)/c-TiO₂ (1 layer, H₂O suspension, heat treated at 850°C), and Ti6Al4V (180 grit)/c-TiO₂ (3 layers, EtOH suspension, heat treated at 850°C) films are shown in Figure 7.86. The P25 powder consisted of a mixture of anatase (ICDD 71-1169), and rutile phases (ICDD 76-0322), and rather pure, since all of the peaks belonged to either of the phases (Figure 7.86a). The rutile/anatase ratio was calculated by Eq 7.2 (Criado and Real 1983),

$$x_A = \frac{1}{1 + 2.18(I_R / I_A)} \pm 2\% \quad (7.2)$$

where x_A is the weight fraction of anatase, I_R is the intensity of the scattering from the (110) plane of the rutile, and I_A is the intensity of scattering from the (101) plane of the anatase. The relative intensities of the scattering from the (101) plane of the anatase, and the (110) plane of the rutile were 100, and 16.19, respectively. Hence, $x_A=74\pm2\%$, and $x_R=26\pm2\%$,

The major peaks of the Ti6Al4V alloy showed titanium (ICDD 44-1294). The minor peaks could not be identified but most probably was related to some Ti-Al-V compound (Figure 7.86b).

The XRD pattern of the Ti6Al4V (1200 grit)/c-TiO₂ (1 layer, H₂O suspension, heat treated at 850°C) film was identified as rutile (ICDD 76-1939) as the major phase (Figure 7.86c). It also contained a minor amount of Ti₃O (ICDD 76-1644). Since the original powder contained a mixture of anatase (74%) and rutile (26%) phases, this supported the argument that TiO₂ recrystallized at 850°C, transforming all of the anatase phase initially present to rutile. In fact, it was shown that, anatase to rutile transformation (Degussa P 25 powder) took place in the temperature range 500-900°C; at around 850°C after 1 hr heating the rutile ratio was ~90% by weight (Criado and Real, 1983). The peaks related to the Ti6Al4V substrate were attenuated to a great extent indicating the metallic substrate was oxidized at 850°C to a depth that scattering signal from the metal was insignificant.

The XRD pattern of the thicker Ti6Al4V (180 grit)/c-TiO₂ (3 layers, EtOH suspension at 850°C, ~5 μm thick) film was identified as rutile (ICDD 76-0322), and anatase (ICDD 71-1169) as the major phases (Figure 7.86d). A minor phase of Ti₃O₅ was also present. Again the peaks related to the Ti6Al4V were weak indicating deep

oxidation. The relative intensities of the scattering from the (110) plane of the rutile, and the (101) plane of the anatase were 100, and 22.81, respectively. Therefore, $x_A=10\pm 2\%$, and $x_R=90\pm 2\%$, and approximately 90% of the anatase initially present was transformed to rutile. This result was very close to the value obtained by Criado and Real. The greater thickness of the film avoided complete recrystallization, nevertheless, phase transformation reactions took place increasing the rutile fraction in the film, and sintering occurred changing the surface morphology.

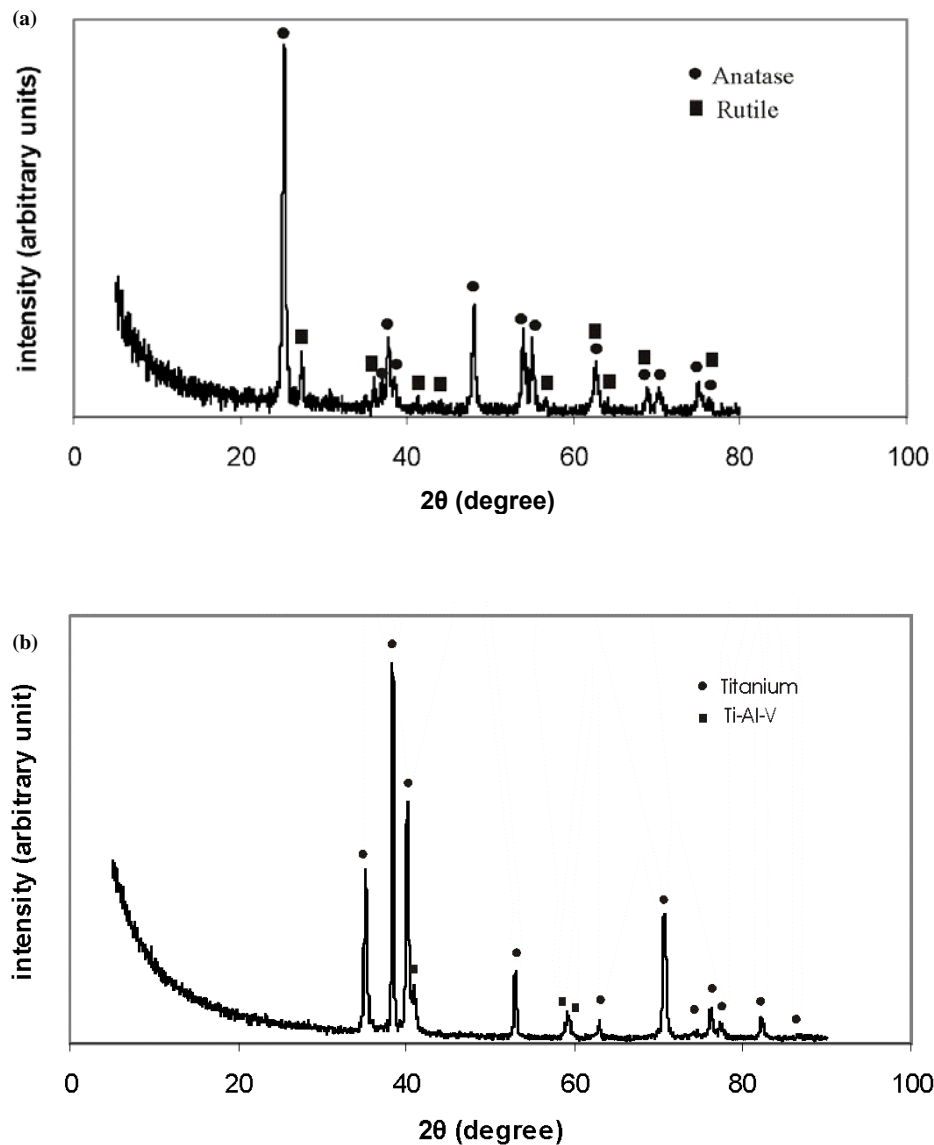


Figure 7.86. The XRD patterns of (a) Degussa P25 TiO₂ powder, (b) 1200 grit Ti6Al4V alloy, (c) 1200 grit Ti6Al4V/c-TiO₂ (1 layer, H₂O suspension) heat treated at 850°C, (d) 180 grit Ti6Al4V/c-TiO₂ (3 layers, EtOH suspension) heat treated at 850°C.

(cont. on next page)

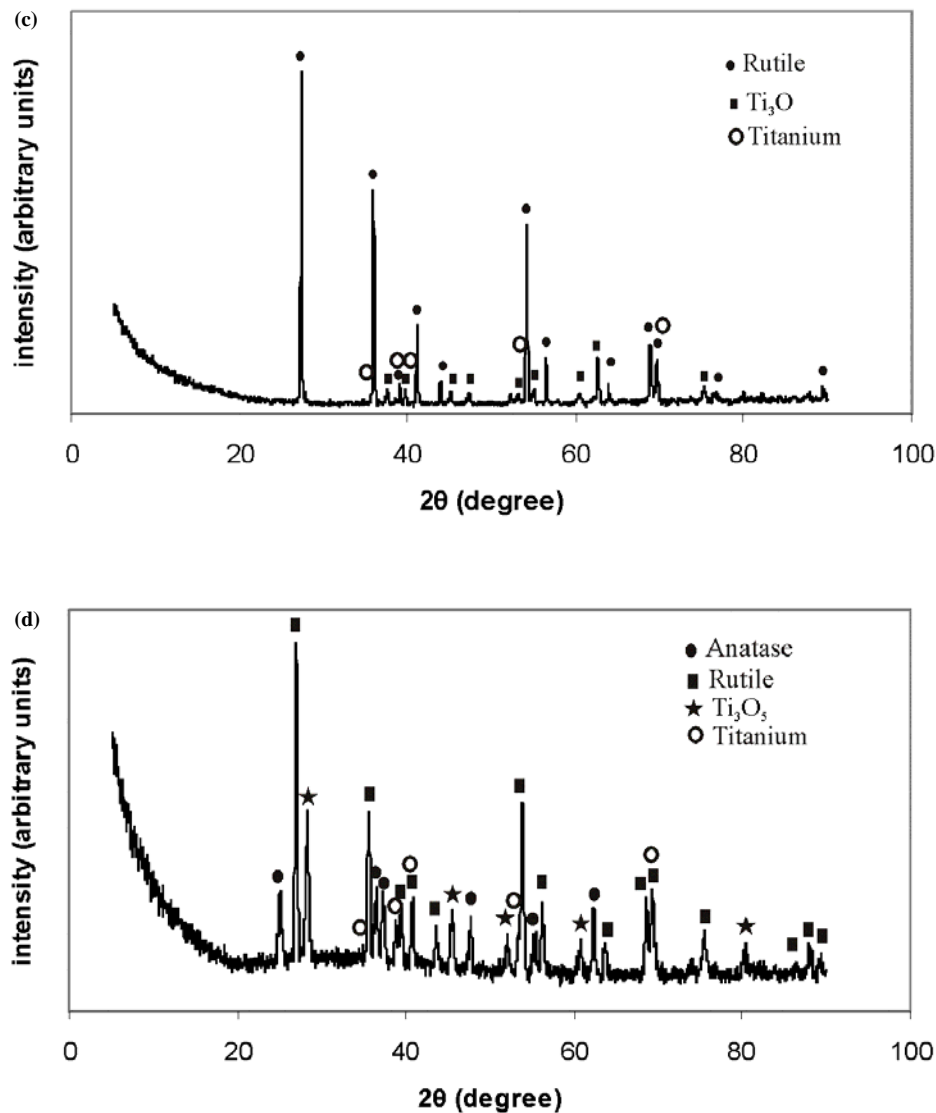


Figure 7.86. (cont.) The XRD patterns of (a) Degussa P25 TiO_2 powder, (b) 1200 grit Ti6Al4V alloy, (c) 1200 grit Ti6Al4V/c-TiO₂ (1 layer, H₂O suspension) heat treated at 850°C, (d) 180 grit Ti6Al4V/c-TiO₂ (3 layers, EtOH suspension) heat treated at 850°C.

The SEM images of the Ti6Al4V alloy (1200 grit)/c-HAp (1 layer, H₂O suspension) films heat treated at 360°C and 850°C are given in Figure 7.87, 7.88, respectively. The continuous film formed by 1 layer coating with the aqueous c-HAp suspension (~1 μm thick), heat treated at 360°C, was very homogeneous comprising mainly of primary HAp particles. The coating even repeated the underlying surface topography of the metallic alloy. When the same film was heat treated at 850°C the film morphology was totally changed. The primary particles of the homogeneous film were connected together in a three dimensional mesh forming a continuous structure of curls of 50-100 nm in diameter, reminiscent of an aerogel.

The SEM images of the Ti6Al4V alloy (1200 grit)/c-HAp (1 layer, EtOH suspension) films heat treated at 360°C, 700°C, and 850°C are given in Figure 7.89, 7.90 and 7.91, respectively. The HAp coating with the ethanol suspensions were again thicker (~1.5 µm) as compared to aqueous suspensions due to the reasons discussed above. The primary HAp particles comprised over 90% of the film surface; agglomerates of sizes up to 1.5 µm covered the rest of the surface. Unlike the aqueous suspensions, crack like openings of 50-150 nm wide, and 1 µm long appeared in the otherwise completely homogeneous film heat treated at 360°C (Fig 7.89). One reason for the crack formation was the higher evaporation rate of ethanol, not providing sufficient time for the particles to migrate and distribute evenly over the surface because of the high rate of increase in suspension viscosity during the spin off and drying steps. The shrinkage rate of a faster drying film was expected to be higher contributing to the crack formation. The increasing film thickness was also a factor for the crack formation. The higher agglomeration tendency of the HAp particles when they become in close proximity during the drying step, in ethanol suspension, in which pH was not adjusted and there was no organic dispersant, could be another reason. When the film was heat treated at 700°C, the onset of sintering could be seen. The surface morphology did not change appreciably. There were not any extensive film shrinkage and thus, crack sizes did not change. However, heat treatment at 850°C changed the surface morphology; the primary particles were connected in a three dimensional mesh of the same type and size of texture as in the case of aqueous suspensions. The agglomerates were transformed into plate like structures. The width and length of the cracks enlarged to 500 nm, and 5 µm, respectively, due to the film shrinkage.

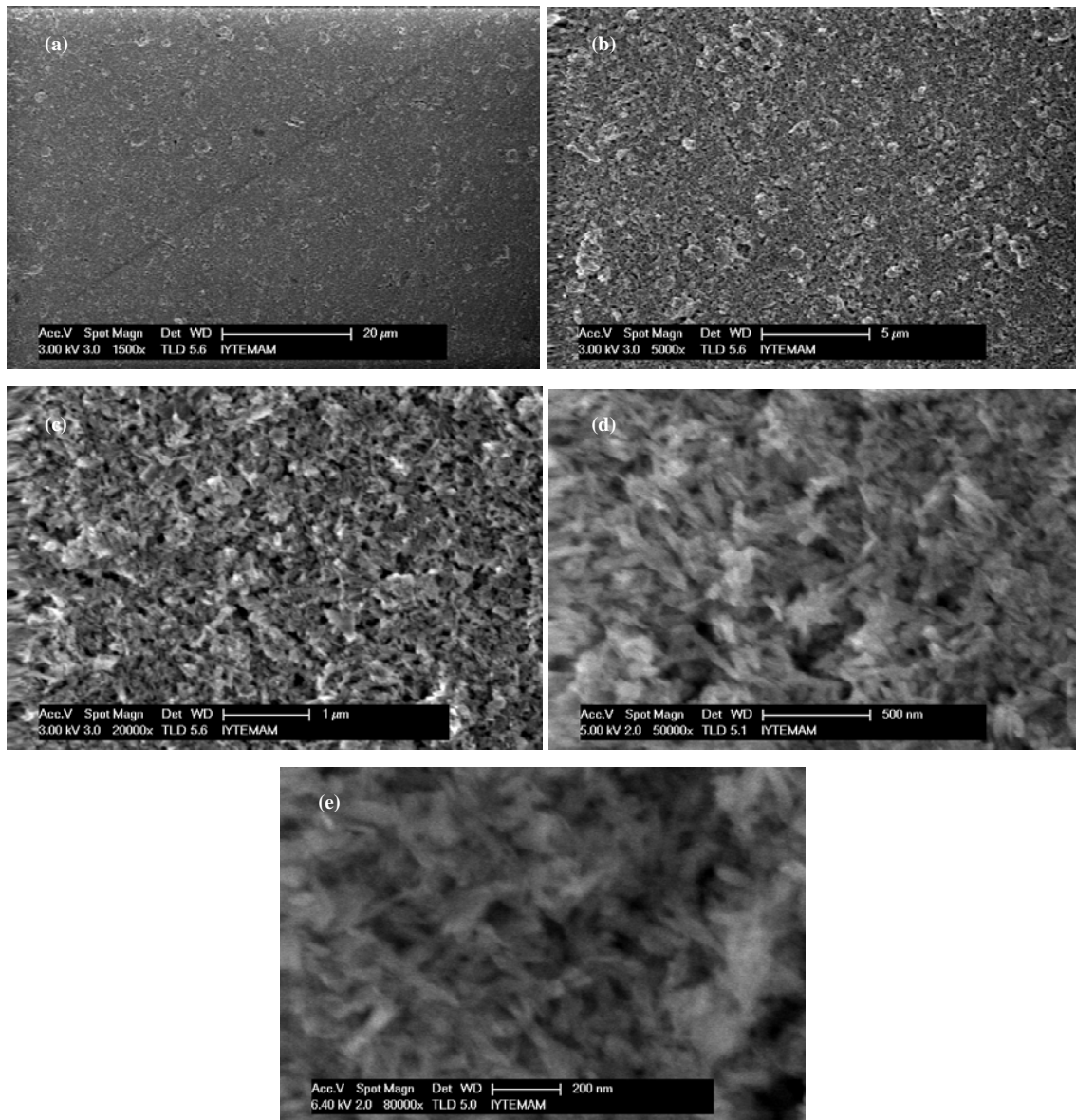


Figure 7.87. The SEM images of the Ti6Al4V alloy substrate (1200 grit)/c-HAp (H₂O suspension, 1 layer), spin coated, heat treated at 360°C at various magnifications.

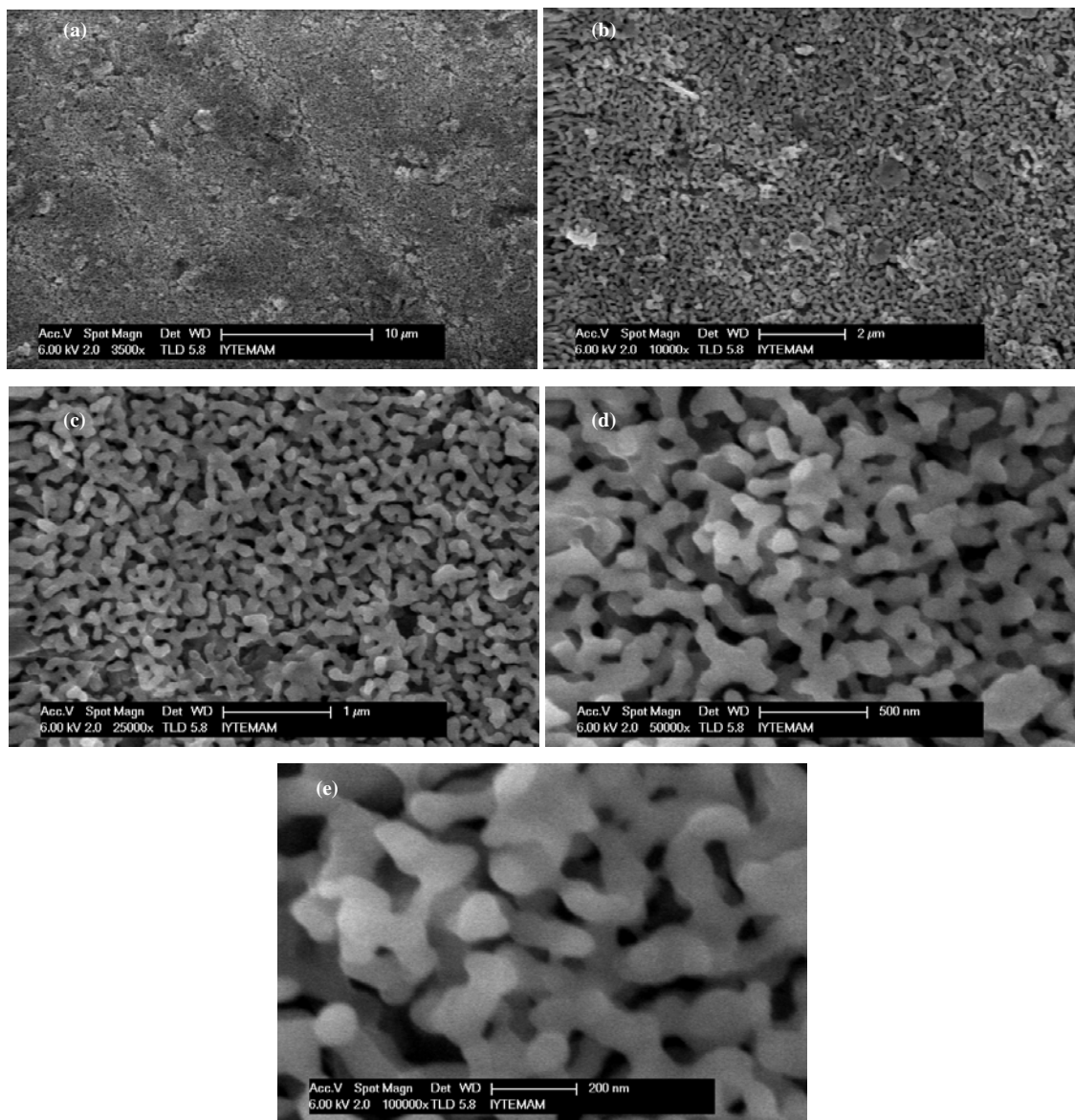


Figure 7.88. The SEM images of the Ti6Al4V alloy substrate (1200 grit)/c-HAp (H_2O suspension, 1 layer), spin coated, heat treated at 850°C at various magnifications.

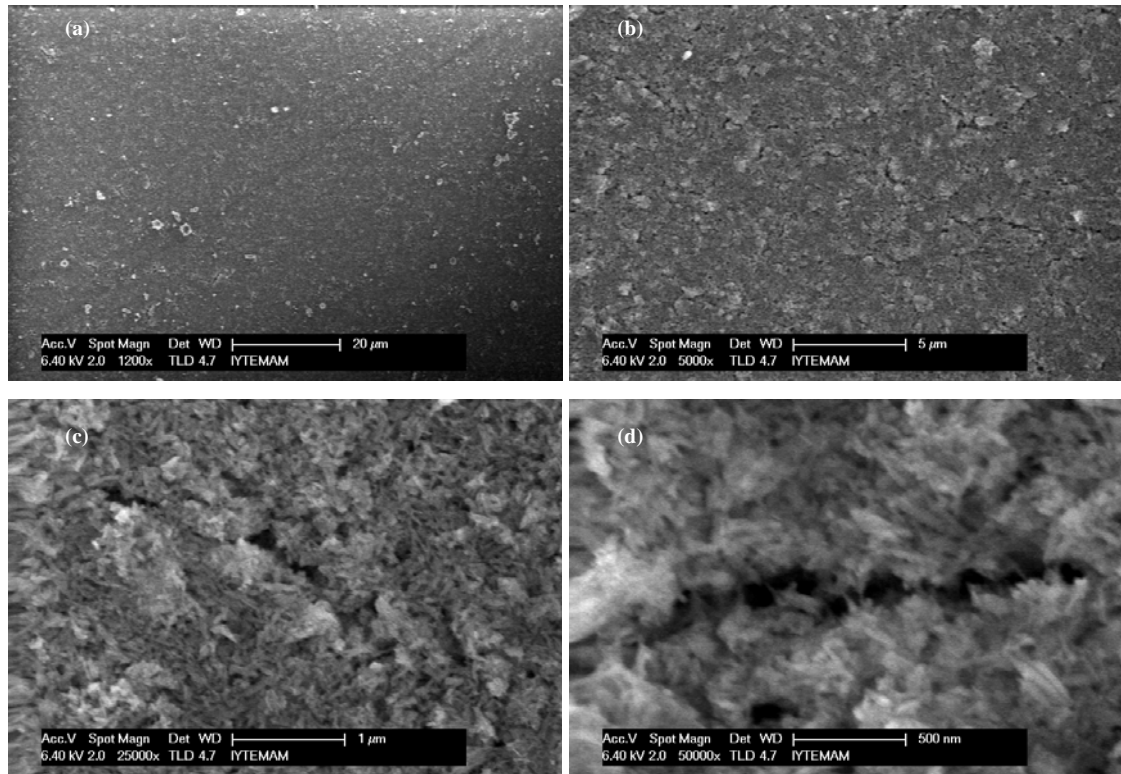


Figure 7.89. The SEM images of the Ti6Al4V alloy substrate (1200 grit)/c-HAp (EtOH suspension, 1 layer), spin coated, heat treated at 360°C at various magnifications.

The effect of multilayer HAp coatings is shown in Figure 7.92, and 7.93. The Ti6Al4V alloy (1200 grit)/c-HAp (3 layers, H₂O suspension) film, heat treated at 700°C, had a thickness of ~3 μm. The SEM images of the film (Figure 7.92) showed that agglomerates of sizes up to ~1.5 μm, covered 20% of the surface, and at the same time crack like gaps of 1.5 μm in length existed. The onset of sintering could be seen in Figure 7.92e. When compared to thinner, one layer films of the same type, the cause of the agglomerations was most probably the increased frictional resistance to flow of the rougher bottom HAp layers. This frictional resistance limited the migration and hence even distribution of the primary particles in the suspension, especially, during the increasing suspension viscosity of the drying step. The SEM images of same type of film, heat treated at 850°C, are given in Figure 7.93. Again the film morphology completely changed to the three dimensional mesh structure. The agglomerate sizes seemed to be lower (~1.2 μm max.), and cracks of length 1 to 5 μm appeared due to the film shrinkage.

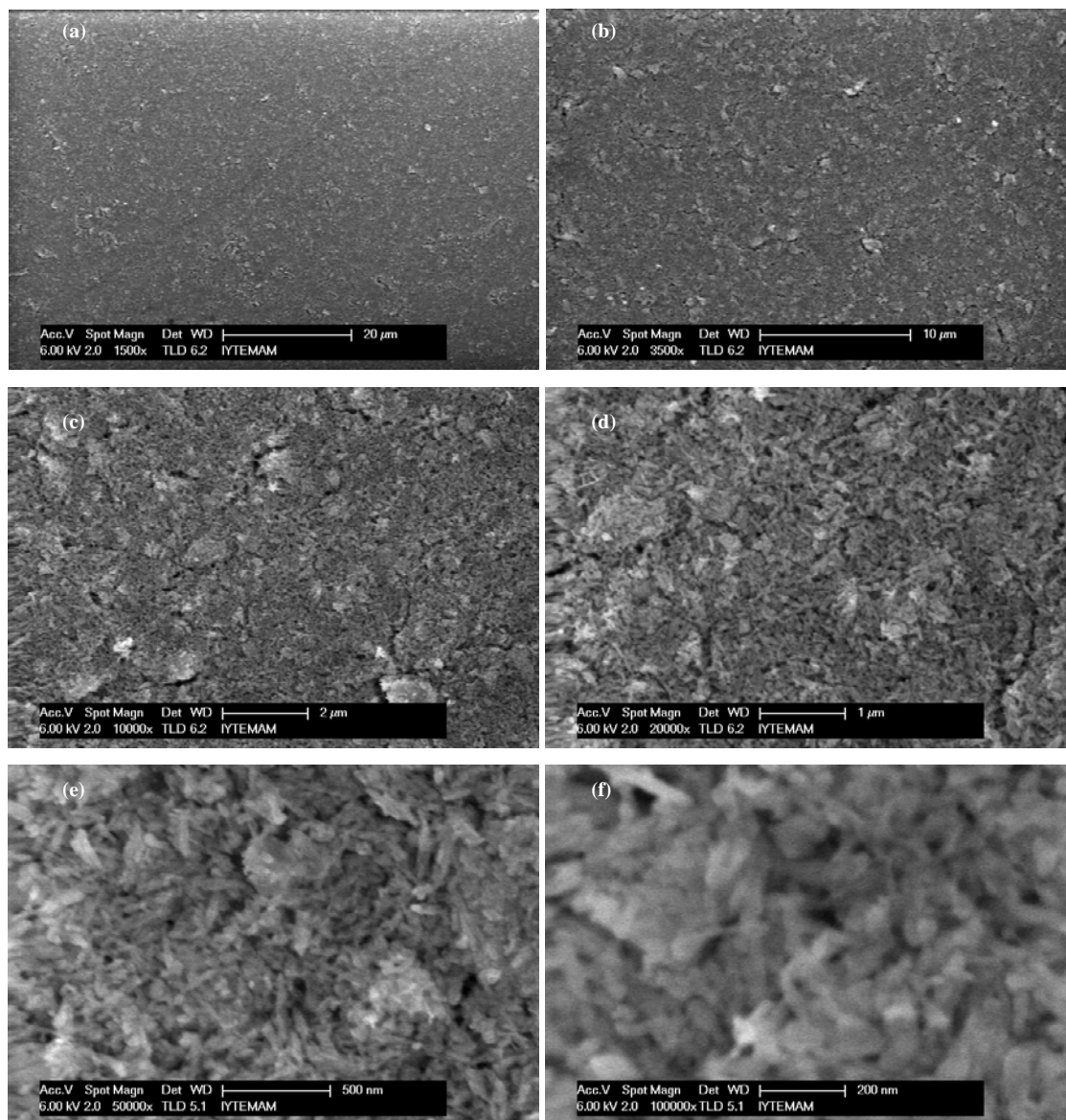


Figure 7.90. The SEM images of the Ti6Al4V alloy substrate (1200 grit)/c-HAp (EtOH suspension, 1 layer), spin coated, heat treated at 700°C at various magnifications.

However, when compared to the thinner films of the Ti6Al4V alloy (1200 grit)/c-HAp (1 layer, EtOH suspension) films (Figure 7.89, Figure 7.90, Figure 7.91) the cracks were less extensive in concentration and size. This phenomenon was most probably due to the film thickness threshold for crack formation for a single coating (Gan, et al. 2005). The single layer coatings prepared by EtOH suspension were thicker (1.5 μm on 1200 grit substrate) than the coatings prepared by H₂O suspension (1.0 μm on 1200 grit substrate). Hence it was possible to conclude that the threshold thickness for the films was in the range 1.0-1.5 μm for crack formation.

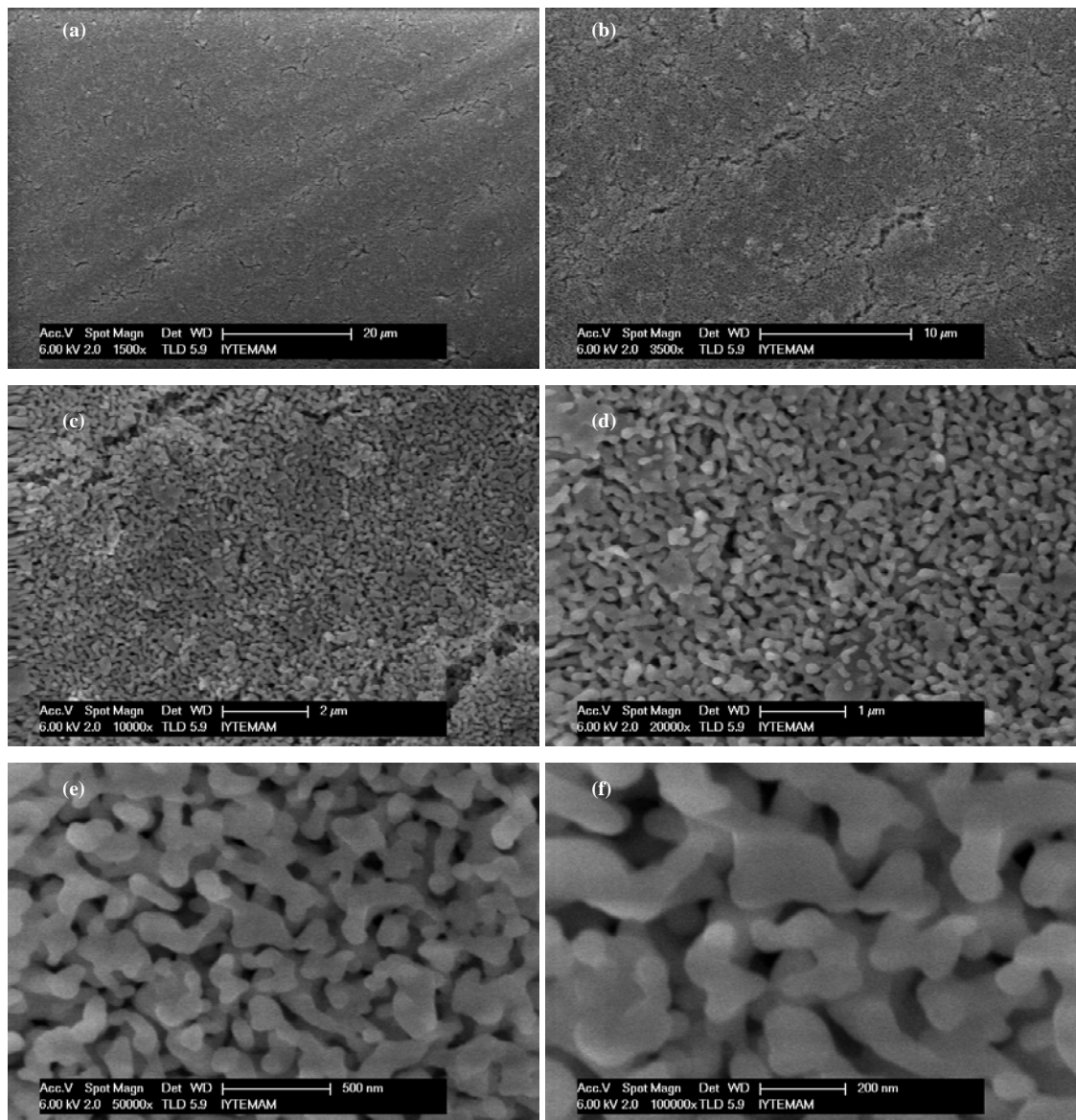


Figure 7.91. The SEM images of the Ti6Al4V alloy substrate (1200 grit)/c-HAp (EtOH suspension, 1 layer), spin coated, heat treated at 850°C at various magnifications.

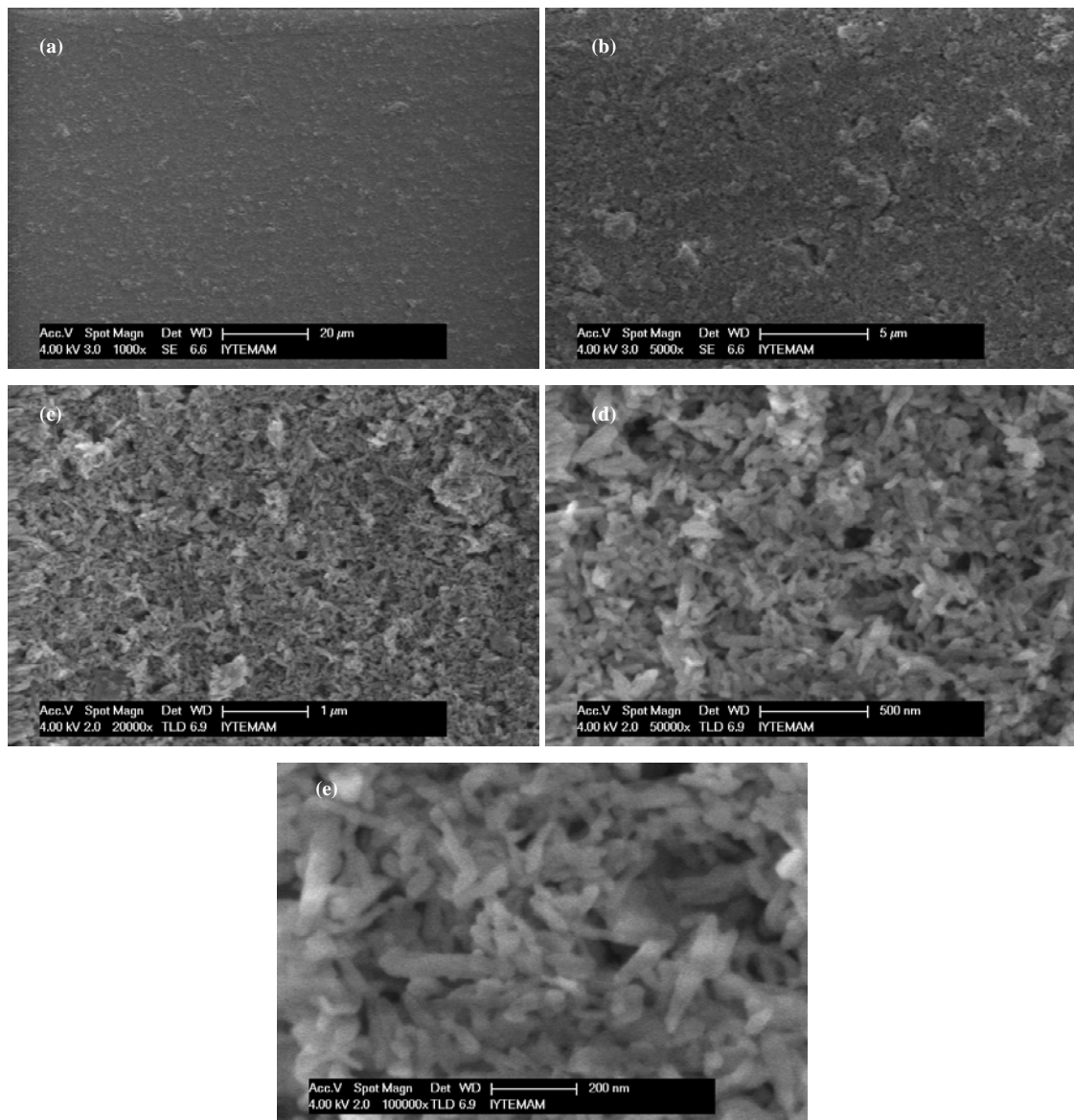


Figure 7.92. The SEM images of the Ti6Al4V alloy substrate (1200 grit)/c-HAp (H_2O suspension, 3 layers), spin coated, heat treated at 700°C at various magnifications.

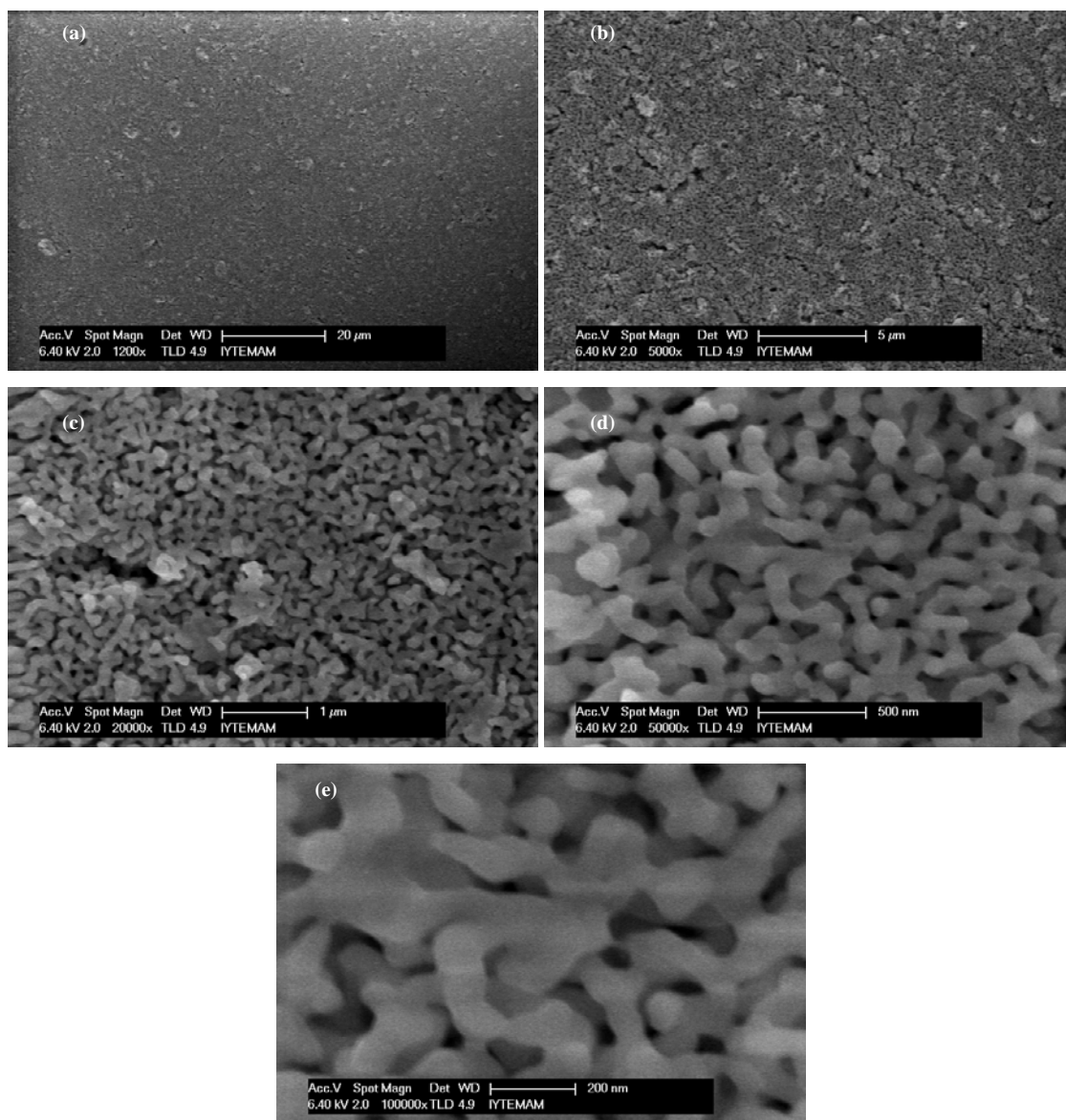


Figure 7.93. The SEM images of the Ti6Al4V alloy substrate (1200 grit)/c-HAp (H_2O suspension, 3 layers), spin coated, heat treated at 850°C at various magnifications.

The XRD patterns of the c-HAp powder, Ti6Al4V (180 grit)/c-HAp (3 layers, EtOH suspension) films heat treated at 360°C, 700°C, and 850°C are shown in Figure 7.94. The film thickness was ~5 μm . The c-HAp powder consisted of purely hydroxyapatite (ICDD 74-0565) since all of the peaks was accounted for hydroxyapatite (Figure 7.94a).

The XRD pattern of the Ti6Al4V (180 grit)/c-HAp (3 layers, EtOH suspension) film heat treated at 360°C (Fig 7.94b) was identified as hydroxyapatite and titanium substrate with a little amount of rutile. The existence of the rutile phase showed that the oxidation of titanium substrate started and a detectable layer of rutile formed. Interestingly enough, the most intense peaks of the hydroxyapatite coating were at 2θ values of 28.3° of (210) plane and 25.2° of (002) plane, which were different from the major peaks of the powder at 2θ values of 31.8° of (211) plane, 32.9° of (300) plane, and 32.2° of (112) plane. This most probably pointed out to a oriented crystal structure in the coating, which might be possible by the alignment of rod like c-HAp crystals, grown in a particular crystal direction during production, on the substrate. It was observed that the protein adsorption capacity of c-HAp films well surpassed that of m-HAp films on bioinert glass substrates prepared by dip coating. In the dip coated c-HAp films the grain orientation was the same as the spin coated films. However, in the m-HAp films the crystal orientation should have been random, since m-HAp powder consisted of equiaxed particles which were the crushed forms of the rod shaped grains of c-HAp. One of the causes of the observed phenomenon could be that the oriented crystal could provide a surface with a regular electrostatic potential distribution which might in turn increase the positive degree of cooperativity of protein adsorption on the HAp surface.

The XRD pattern of the Ti6Al4V (180 grit)/c-HAp (3 layers, EtOH suspension) film heat treated at 700°C (Figure 7.94c) was again identified as hydroxyapatite and titanium substrate. The peak intensities of the rutile phase increased a small quantity indicating that the depth of the oxidized layer of the substrate increased. The peak intensities of the titanium alloy substrate decreased correspondingly. The relative peak intensities of the HAp coating again indicated the same crystal orientation.

When the same type of Ti6Al4V (180 grit)/c-HAp (3 layers, EtOH suspension) film heat treated at 850°C, the XRD pattern (Figure 7.94d) showed hydroxyapatite, rutile, titanium phases. The peak intensities of the rutile phase increased drastically indicating the extensive substrate oxidation consuming the metal, and transformation of the titanium to rutile at an increased depth. The evident attenuation of the titanium

substrate peaks to a great extent also supported this. The same relative intensities of the hydroxyapatite still indicated the oriented crystal structure of the HAp coating.

The XRD patterns of the thinner films 1200 grit Ti6Al4V alloy/c-HAp (1 layer, H₂O suspension) (~1 μm) heat treated at 360°C, 700°C, and 850°C are given in Figure 7.95. The XRD pattern of the film heat treated at 360°C is given in Figure 7.95a, and the phases were identified as hydroxyapatite and titanium (from the substrate). Small peaks that belonged to rutile existed. The most intense peaks of hydroxyapatite were at 2θ values of 28.3° of (210) plane and 25.2° of (002) plane with significantly higher relative intensities as compared to the thicker films and as compared to the major peaks of the powder. In the thinner coatings of HAp, the crystal orientation was much more biased compared to the thicker films. Because the one layer films comprised of primary HAp particles distributed much more homogeneously and with much less agglomerations. This caused the crystal planes on different grains to align to the maximum possible degree. As the thickness increased by each added layer the homogeneous structure of the coating deteriorated to some degree and particle agglomerations became more extensive. This in turn disrupted the crystal plane alignment partially. As a matter of fact it was reported in literature that highly oriented polycrystalline thin films (that comprise of separate grains) were prepared by spin coating technique (Hwang and Kim 1999, Chen, et al. 2004).

When the same type of 1200 grit Ti6Al4V alloy/c-HAp (1 layer, H₂O suspension) film was heat treated at 700°C, the XRD pattern showed that (Figure 7.95b) the intensity of the rutile peaks increased which indicated an increasing thickness of the rutile layer by the oxidation of the Ti6Al4V substrate. The intensities of the titanium peaks decreased correspondingly. The relative intensities of the hydroxyapatite peaks did not change. When the heat treatment temperature was raised to 850°C, the XRD pattern (Figure 7.95c) showed that rutile was the major phase with its drastically increased relative peak intensities. Especially, the relative intensities of titanium peaks were very low indicating attenuation by the increased thickness of the rutile layer.

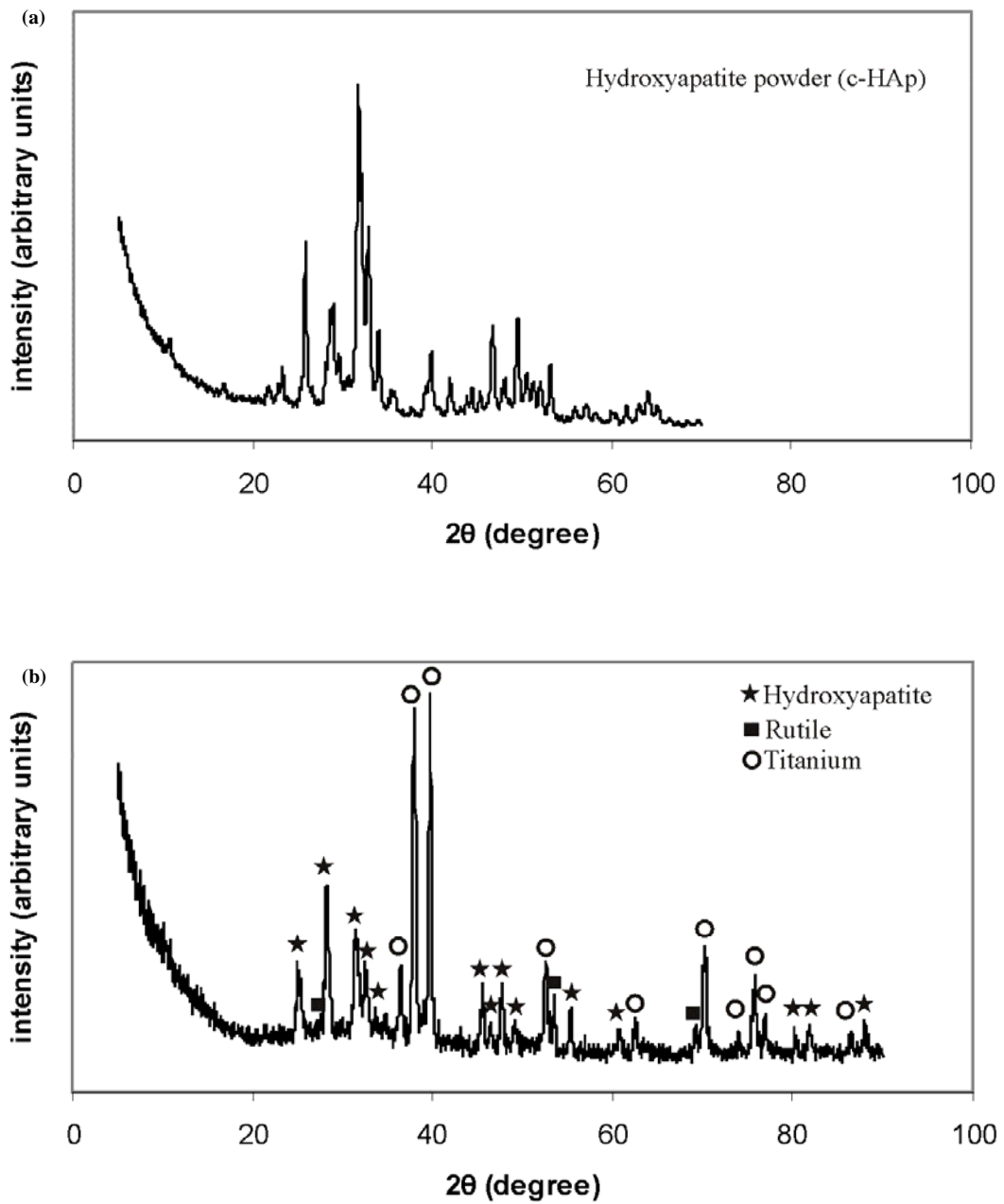


Figure 7.94. The XRD patterns of (a) c-HAp powder, (b) 180 grit Ti6Al4V alloy/c-HAp (3 layers, EtOH suspension) film heat treated at 360°C, (c) 180 grit Ti6Al4V/c-HAp (3 layers, EtOH suspension) film heat treated at 700°C, (d) 180 grit Ti6Al4V/c-HAp (3 layers, EtOH suspension) heat treated at 850°C.

(cont. on next page)

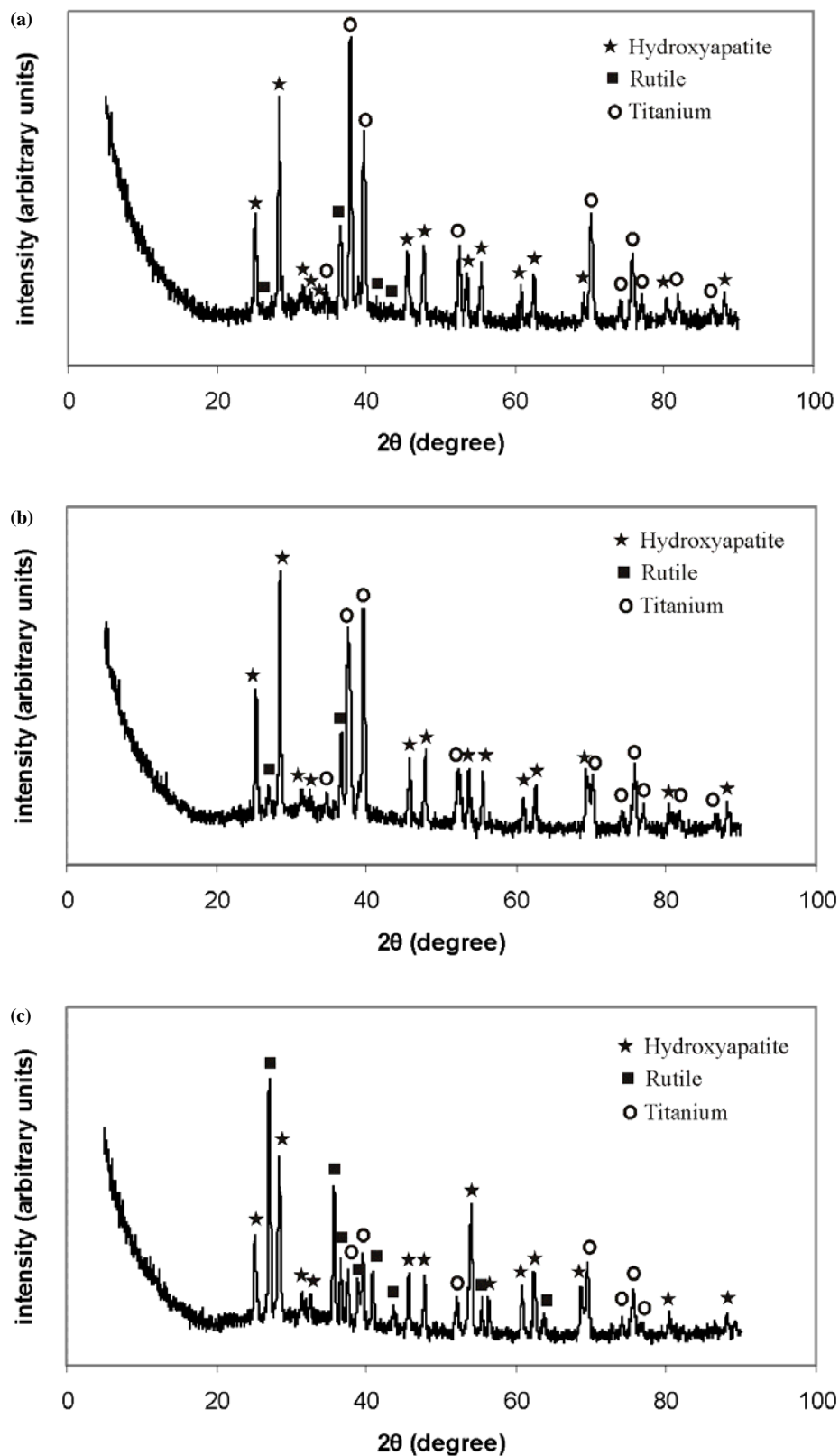


Figure 7.95. The XRD patterns of (a) 1200 grit Ti6Al4V alloy/c-HAp (1 layer, H₂O suspension) film heat treated at 360°C, (b) 1200 grit Ti6Al4V/c-HAp (1 layer, H₂O suspension) film heat treated at 700°C, (c) 1200 grit Ti6Al4V/c-HAp (1 layer, H₂O suspension) heat treated at 850°C.

The SEM images of the anodized alloy spin coated with c-HAp are given in Figure 7.96 and 7.97. The SEM images of the Ti6Al4V (1200 grit) anodized at 20 V/c-HAp (EtOH suspension, 3 layers), spin coated film, heat treated at 850°C (Figure 7.96), showed that the film surface was rough (the roughness values will be given later), most probably due to the rough and anisotropic anodized surface. The 20 V anodized surface consisted of 35% anatase and 65% metal, with different properties, that might have contributed the roughness of the c-HAp film. The HAp layer seemed to be consisted of scale like grains 1 to 2 μm in diameter, separated by crack like discontinuities. Although the film was treated at 850°C, the morphology was different from the three dimensional mesh like structures of the sole c-HAp coatings. Nevertheless, the primary particles fusing with plate like grains could be seen. (Figure 7.96f).

The SEM images of the Ti6Al4V (1200 grit) anodized at 60 V/ c-HAp (EtOH suspension, 3 layers), spin coated film, heat treated at 850°C (Figure 7.97), showed a more homogeneous microstructure in comparison to the 20 V anodized substrate. However, the film surface was ridden with cracks of up to 10 μm in length, and 1 μm in width, most probably due to film thickness (thickness of HAp layer was $\sim 5 \mu\text{m}$), and ethanol as the dispersing medium. The heat treatment at 850°C was expected to increase the size and formation of the cracks. The morphology was similar to the three dimensional continuous mesh structure of the alloy/c-HAp films.

The SEM images of the Ti6Al4V alloy/c-TiO₂/c-HAp films are shown in Figure 7.98, 7.99, 7.100. The SEM images of the Ti6Al4V alloy substrate (1200 grit)/c-TiO₂ (H₂O suspension, 3 layers)/c-HAp (H₂O suspension, 1 layer), spin coated, heat treated at 360°C (Figure 7.98), indicated a microstructure with agglomerates of sizes up to 1 μm in size, distributed homogeneously. The agglomerates covered $\sim 50\%$ of the surface. Thin cracks of up to 5 μm in length existed. The thickness of the TiO₂, and HAp layers was 3 μm , and 1 μm , respectively, hence the total thickness was $\sim 4 \mu\text{m}$. The increased thickness might have been effective in crack formation among the other factors discussed above.

When the same type of film, the Ti6Al4V alloy substrate (1200 grit)/c-TiO₂ (H₂O suspension, 3 layers)/c-HAp (H₂O suspension, 1 layer), spin coated, was heat treated at 850°C, the microstructure changed (Figure 7.99). The three dimensional mesh formed by the extensive sintering was apparent. The length and the number of cracks increased compared to the film treated at 360°C, due to the film shrinkage. The

agglomerates were converted to plate like fused structures, and this provided a homogeneous film appearance.

The SEM images given in Figure 7.100 showed the effect of increased thickness of the HAp layer. The total thickness of the Ti6Al4V alloy substrate (1200 grit)/c-TiO₂ (H₂O suspension, 2 layers)/c-HAp (H₂O suspension, 3 layers, spin coated, heat treated at 850°C) was 5 μm. The cracks of length up to 10 μm and width up to 300 nm were abundant. The plate like structures formed from the sintering of agglomerates, and their sizes were ~500 nm. The primary particles were connected by sintered, but they did not constitute a continuous mesh.

The XRD pattern of the Ti6Al4V alloy (1200 grit)/c-TiO₂ (H₂O suspension, 1 layer)/c-HAp (H₂O suspension, 1 layer), spin coated, heat treated at 850°C, is given in Figure 7.101. The identified phases were rutile, hydroxyapatite, and titanium. The anatase phase initially present in the TiO₂ coating were transformed to rutile by the heat treatment. The hydroxyapatite layer probably had the crystal orientation as previously discussed.

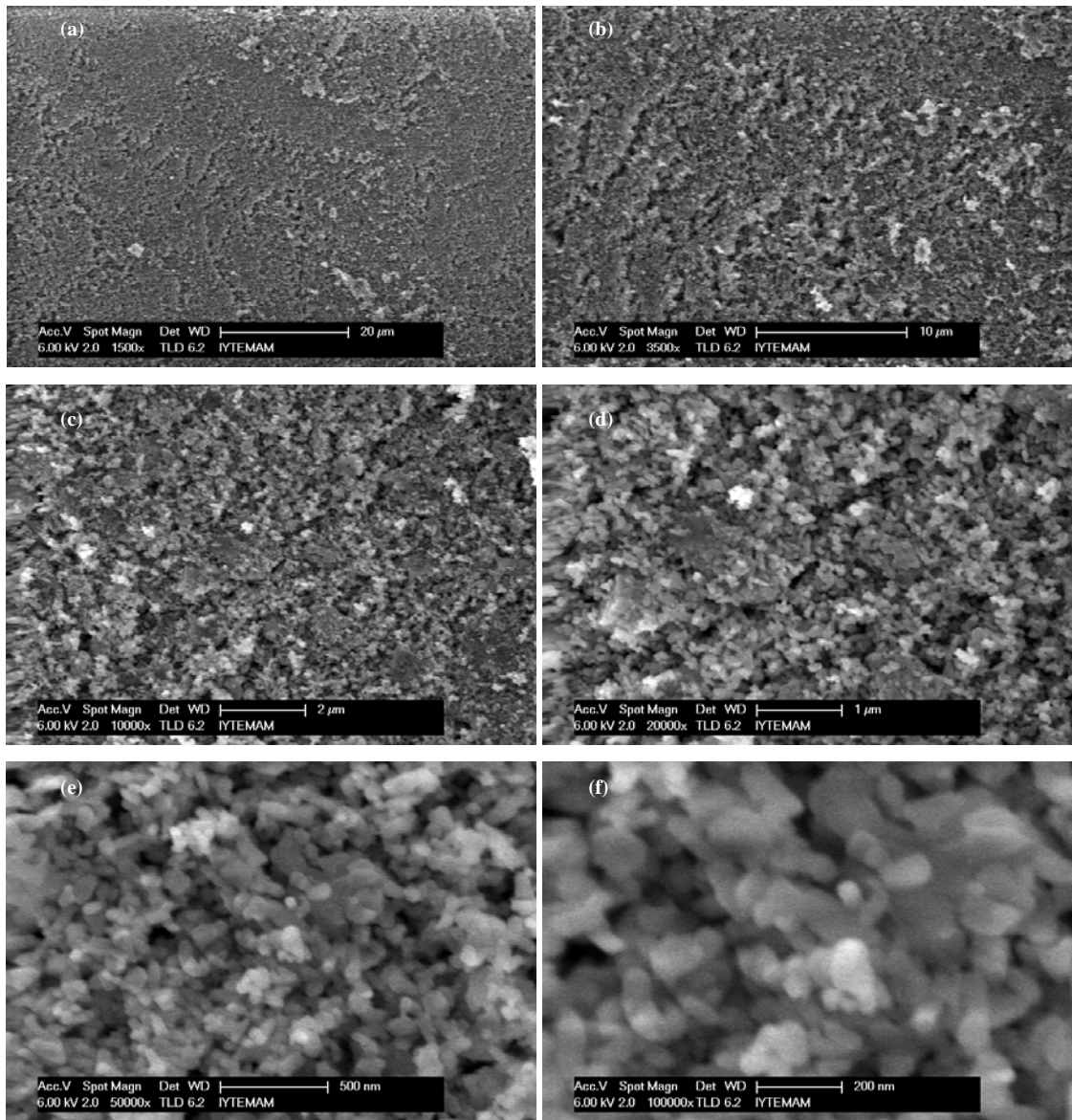


Figure 7.96. The SEM images of the Ti6Al4V alloy substrate (1200 grit) anodized at 20 V/c-HAp (EtOH suspension, 3 layers), spin coated, heat treated at 850°C at various magnifications.

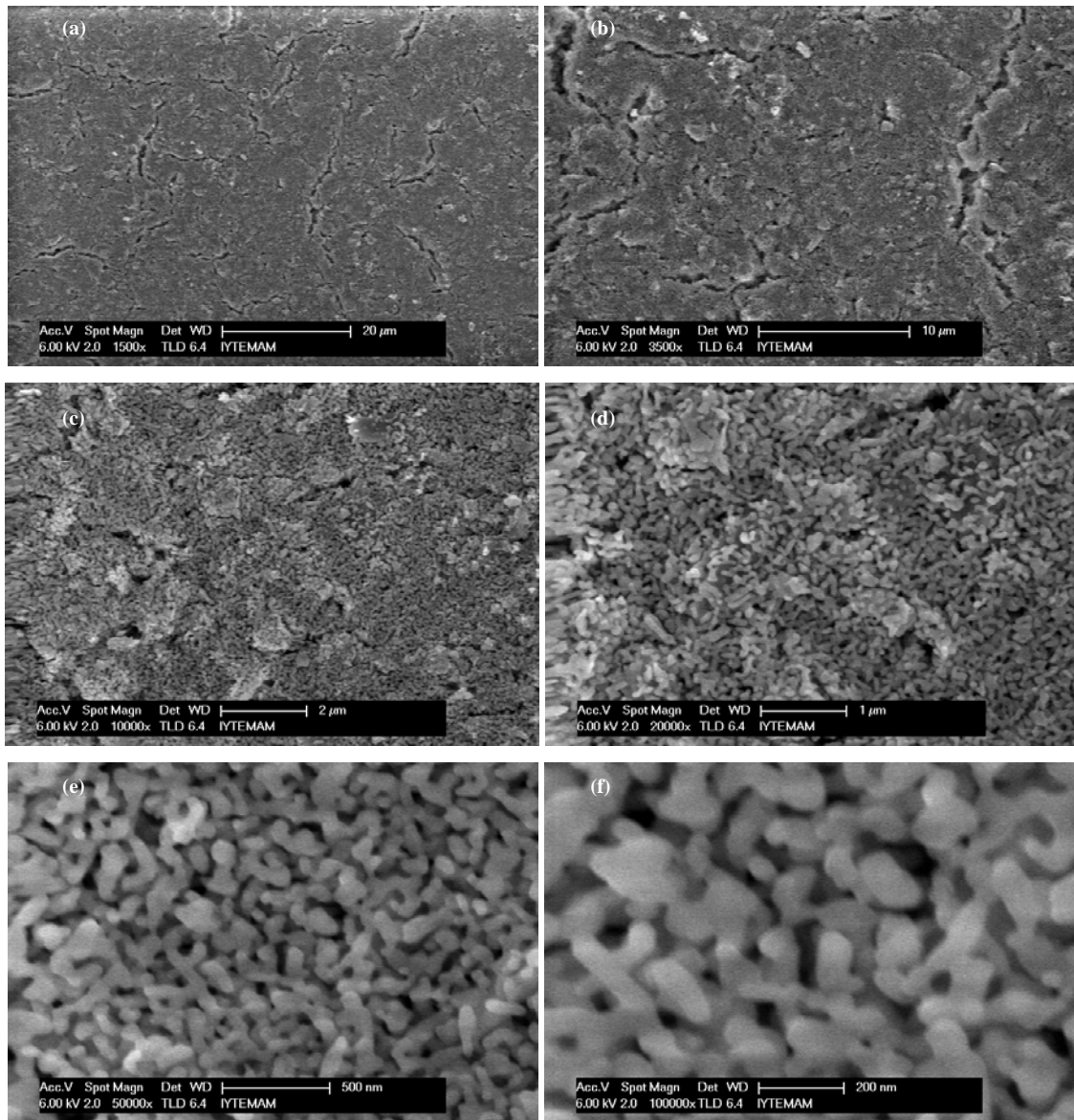


Figure 7.97. The SEM images of the Ti6Al4V alloy substrate (1200 grit) anodized at 60 V/c-HAp (EtOH suspension, 3 layers), spin coated, heat treated at 850°C at various magnifications.

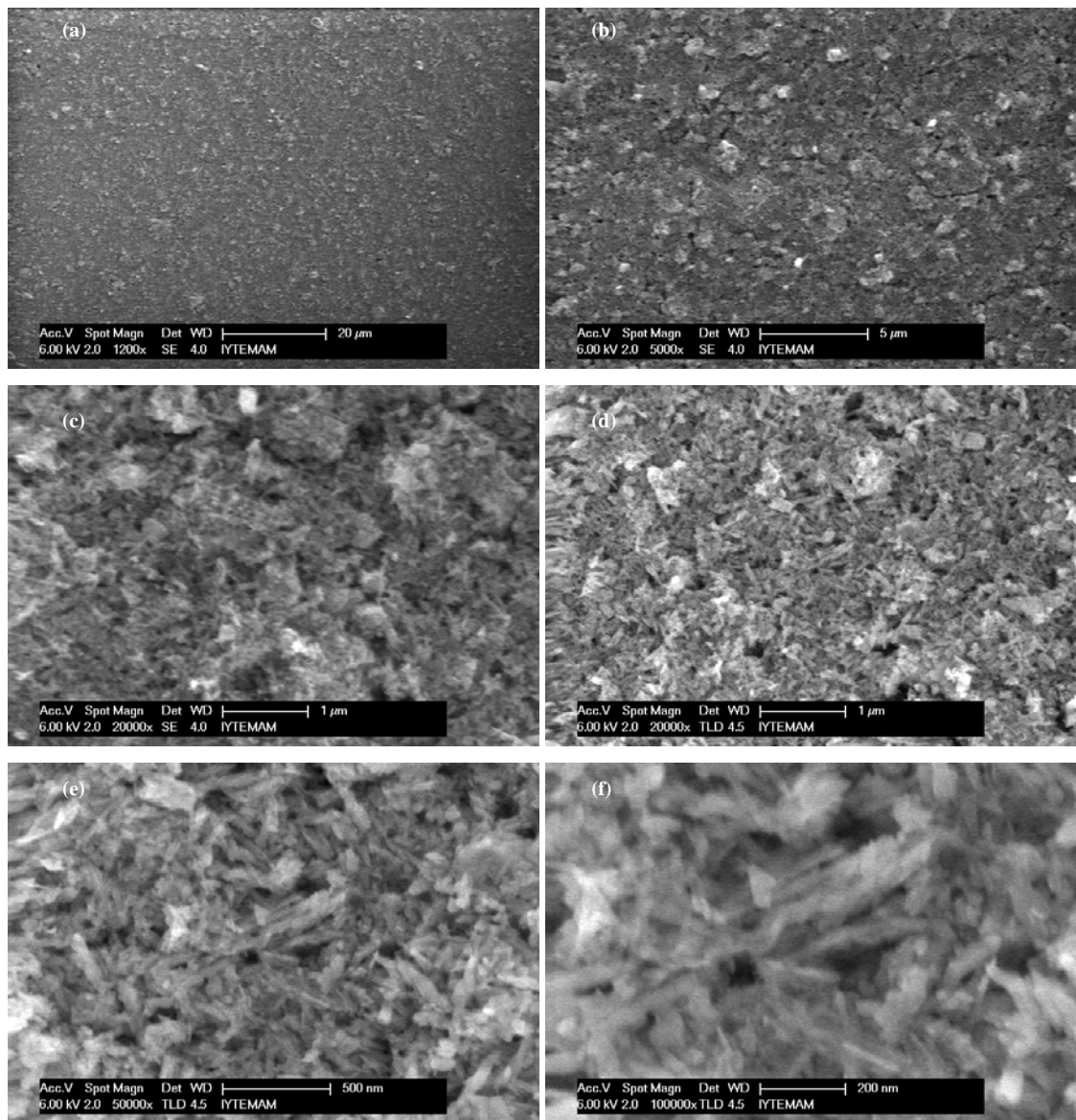


Figure 7.98. The SEM images of the Ti6Al4V alloy substrate (1200 grit)/c-TiO₂ (H₂O suspension, 3 layers)/c-HAp (H₂O suspension, 1 layer), spin coated, heat treated at 360°C at various magnifications.

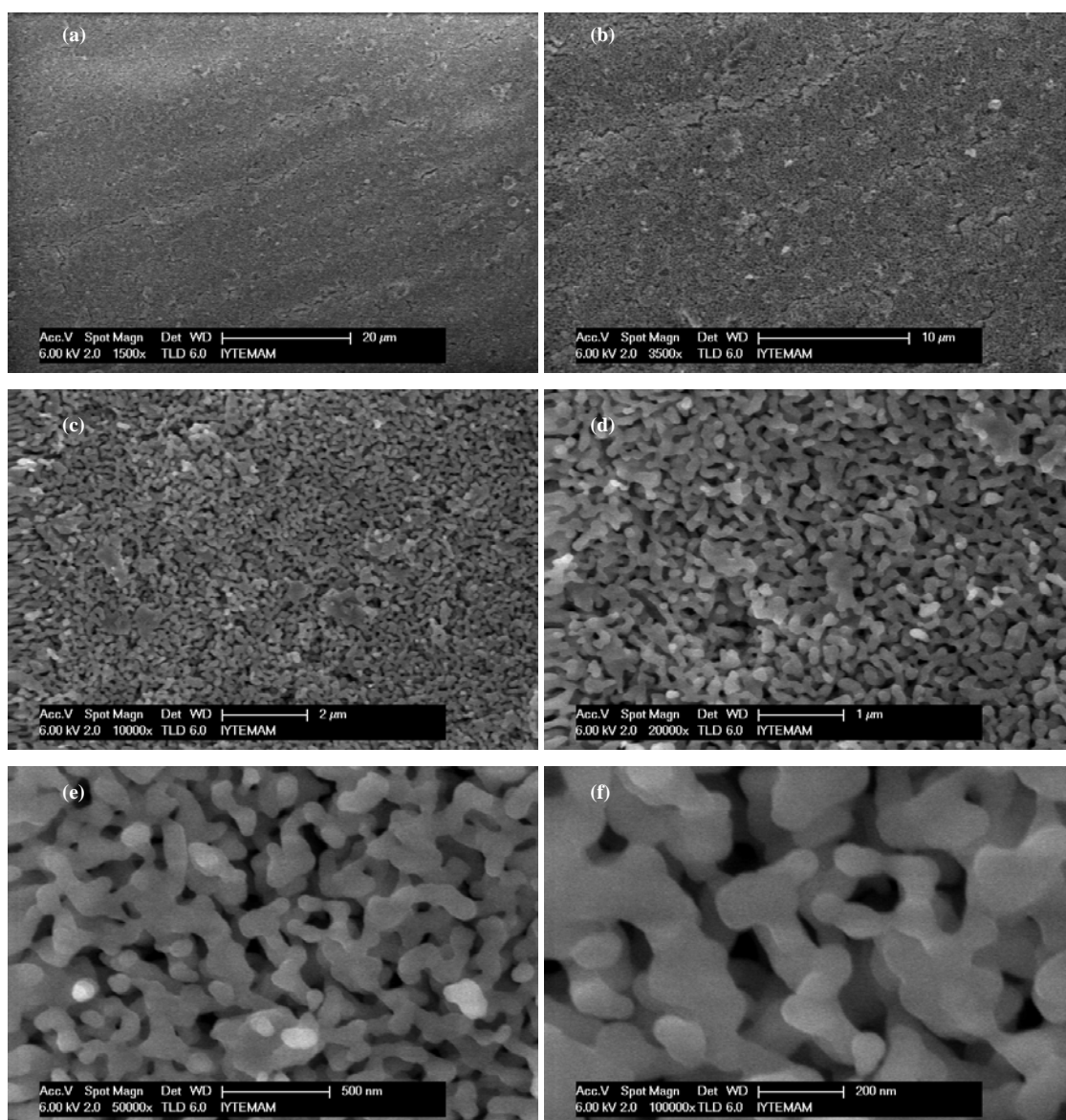


Figure 7.99. The SEM images of the Ti6Al4V alloy substrate (1200 grit)/c-TiO₂ (H₂O suspension, 3 layers)/c-HAp (H₂O suspension, 1 layer), spin coated, heat treated at 850°C at various magnifications.

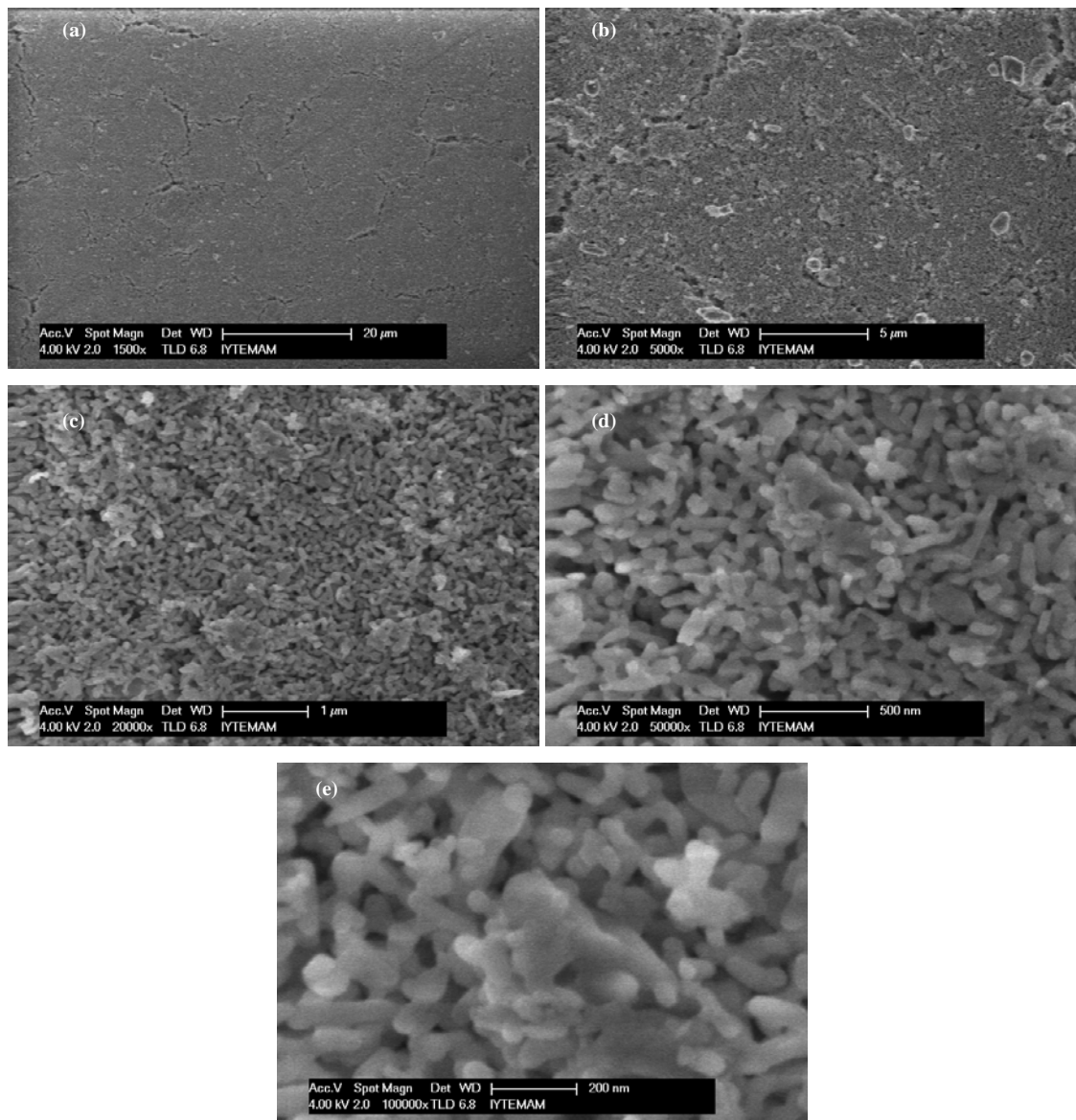


Figure 7.100. The SEM images of the Ti6Al4V alloy substrate (1200 grit)/c-TiO₂ (H₂O suspension, 2 layers)/c-HAp (H₂O suspension, 3 layers), spin coated, heat treated at 850°C at various magnifications.

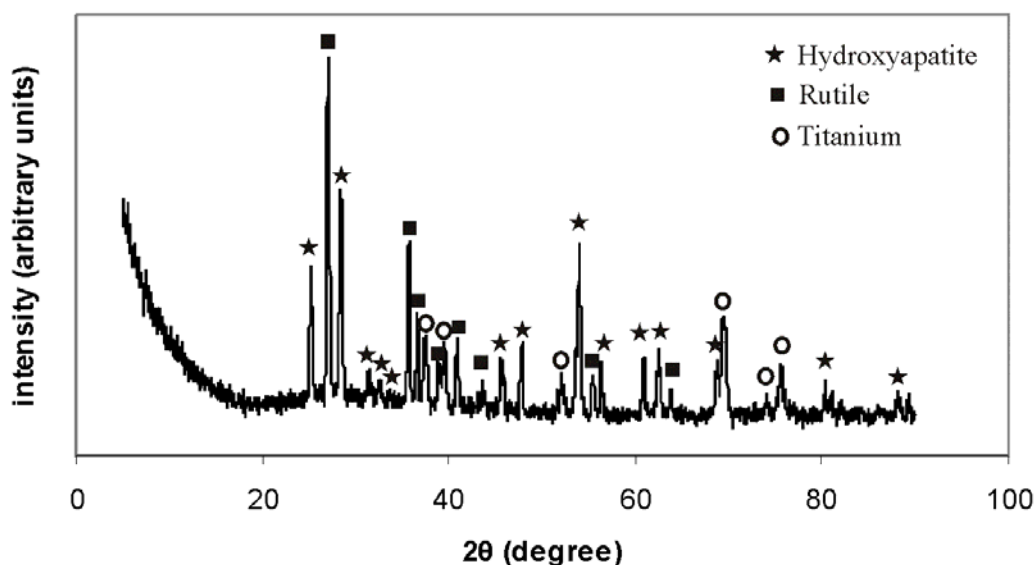


Figure 7.101. The XRD pattern of the film Ti6Al4V (1200 grit)/c-TiO₂ (H₂O suspension, 1 layer)/c-HAp (H₂O suspension, 1 layer), heat treated at 850°C.

The mechanical evaluation of the spin-coated films: The surface roughness, R_q of the TiO₂ coatings on the Ti6Al4V alloy substrate (1200 grit ground) as a function of the TiO₂ thickness (coated TiO₂ layers) is given in Figure 7.102. The surface roughnesses of the films heat treated at 850°C were rougher in comparison to the films heat treated at 360°C. The morphology changes associated with the heat treatment had an effect that increased the surface roughness. The surface roughness of the 1 layer coatings at 360°C and 850°C were at least ~50% greater than the thicker coatings. This corresponds to the microstructure of the thinnest TiO₂ coating given in Figure 7.84 in which the film was completely recrystallized and its morphology was completely different. As the film thickness increased the surface morphology was more like to the case given in Figure 7.85, and this corresponded to lower surface roughness values. The films that were prepared with the EtOH suspension were thicker and their roughness was lower (compared to aqueous suspension coatings. The roughness values decreased from 2 to 3 layer coatings for all of the cases which indicated that the surface roughness was decreased by the filling of the TiO₂ particles of sizes down to 20 nm, yielding a smoother surface.

The surface roughness of the c-HAp coatings on the Ti6Al4V alloy substrate (1200 grit ground) as a function of heat treatment temperature is given in Figure 7.103. The surface roughnesses of all of the coatings, thinner and thicker, that were heat treated

at 850°C, were greater than the lower temperature treated films. The increase in roughness at 850°C for the films prepared with H₂O suspension were much more prominent. The microstructure that corresponded to the drastically increased roughness, was the three-dimensional mesh structure reminiscent of an aerogel, given in Figure 7.88 (1 layer HAp, H₂O suspension) and Figure 7.93 (3 layers HAp, H₂O suspension). The 3 layers HAp coating had the most rough surface. The microstructure given in Figure 7.91 that belonged to the 850°C heat treated 1 layer HAp coating with the EtOH suspension corresponded to a lower surface roughness. Although the microstructure was similar to the 3 dimensional mesh structure of the aqueous coatings, most probably the initial agglomerates that were converted to plate or scale like structures reduced the roughness of the surface. The microstructures of the coatings at the lower temperatures which comprised the primary HAp particles and their agglomerates with only an onset of sintering at 700°C corresponded to lower surface roughness.

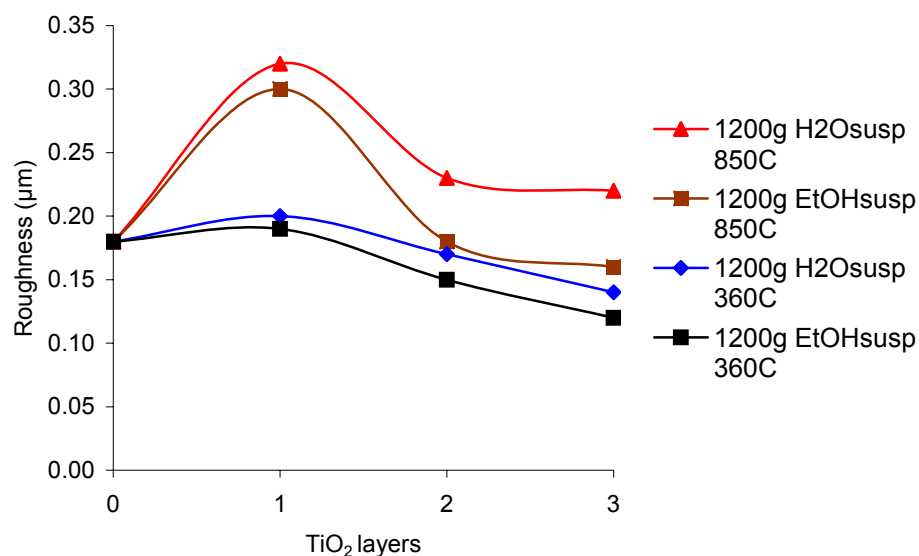


Figure 7.102. The surface roughness, R_q , of the Ti6Al4V alloy (1200 grit ground)/c-TiO₂; with different suspending medium and heat treatment temperatures as a function of coated TiO₂ thickness (coated layers).

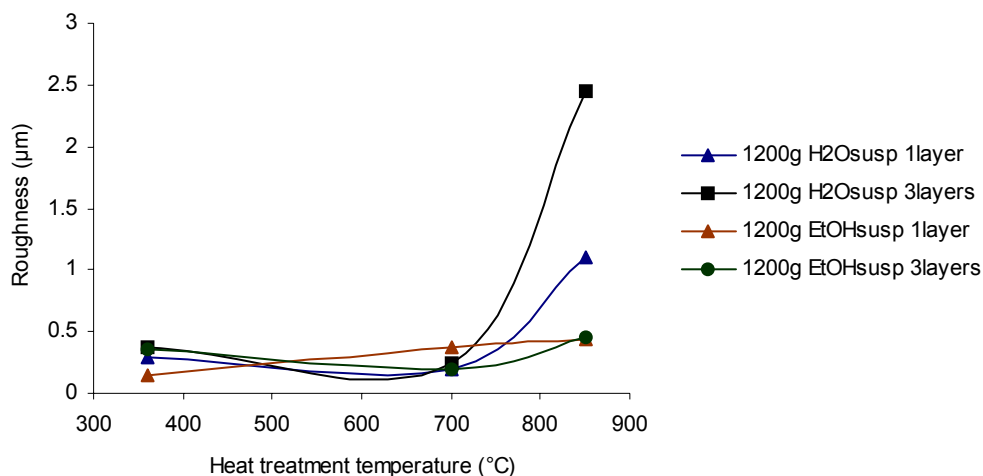


Figure 7.103. The surface roughness, R_q , of the Ti6Al4V alloy (1200 grit ground)/c-HAp; with different suspending medium, coated layers, as a function of heat treatment temperature.

The surface roughness, R_q of the anodized Ti6Al4V substrates coated with c-HAp heat treated at 850°C as a function of anodization voltage were given in Figure 7.104a and b. The substrates ground with the lower grit papers (rougher alloy surfaces) gave rise to rougher film surfaces for all of the anodization voltages, and suspending media, as expected. Interestingly, for both the aqueous and ethanol suspensions, the roughness decreased from 20V to 60V and was almost constant up to 120 V. At 400 V the roughness was the greatest for all of the coatings. The microstructures given in Figure 7.96 for 20 V and in Figure 7.97 for 60 V anodized substrates coated with c-HAp (EtOH suspension, 3 layers) heat treated at 850°C were in accord with the roughness values. The 20 V anodized substrate coating that appear rougher than the 60 V sample has a rougher microstructure resulting in a thicker film, and the roughness values of these coatings were 1.8 μm for the 20 V, and 1.0 μm for the 60 V case. The coatings with the EtOH suspensions were rougher, in general.

The surface roughness, R_q , Ti6Al4V alloy/c-TiO₂/c-HAp, with various substrate surface finish (grit), suspension medium, c-HAp layers, and heat treatment temperatures, as a function of intermediate TiO₂ layer thickness (coated layers) is given in Figure 105. The 180 grit ground substrate films were the roughest, and the substrate surface finish seemed to be the major parameter in determining the final surface roughness of the coatings. In general, the roughness of the 850°C heat treated films were greater. 2-3 layer intermediate TiO₂ coatings gave rise to higher roughness values.

The microstructure in Figure 7.98 of the Ti6Al4V substrate/c-TiO₂/c-HAp, heat treated at 360°C, corresponded to lower roughness values in comparison to the microstructures given in Figure 7.99 and 7.100 of the similar films heat treated at 850°C which had the 3 dimensional fused mesh structure. The more fused and continuous microstructure of the film in Figure 7.99 had greater surface roughness in comparison to the film in Figure 7.100 which has a less fused structure with discernable primary particles and a discontinuous mesh structure.

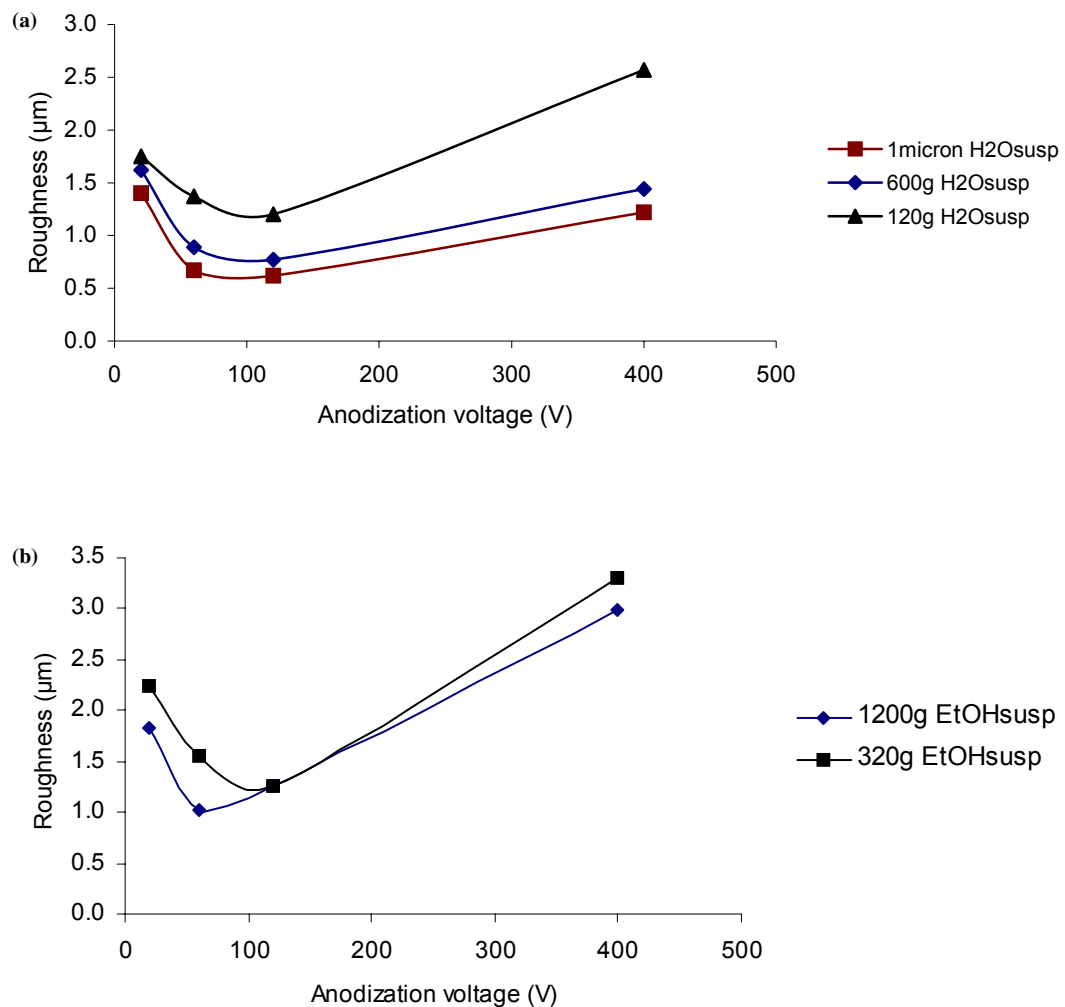


Figure 7.104. The surface roughness, R_q, of the (a) anodized Ti6Al4V alloy/c-HAp (H₂O suspension, 3 layers), (b) anodized Ti6Al4V alloy/c-HAp (EtOH suspension, 3 layers), heat treated at 850°C, with various substrate surface finish (grit), as a function of anodization voltage.

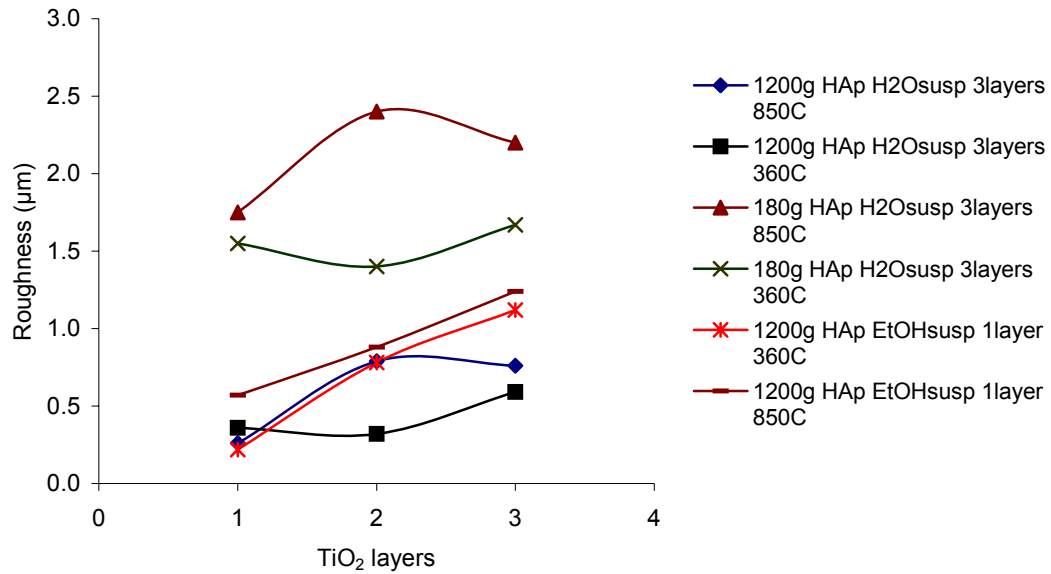


Figure 7.105. The surface roughness, R_q , Ti6Al4V alloy/c-TiO₂/c-HAp, with various substrate surface finish (grit), suspension medium, c-HAp layers, and heat treatment temperatures, as a function of intermediate TiO₂ layers coated.

The surface hardness (HV) of the TiO₂ coatings on the Ti6Al4V alloy substrate (1200 and 180 grit ground) as a function of the TiO₂ thickness (coated TiO₂ layers) is given in Figure 7.106. The surface hardness values of the films heat treated at 850°C showed a jump increase as compared to the films heat treated at 360°C. In general, the thinner the TiO₂ film the greater is the surface hardness; the greatest being the film on 1200 grit ground Ti6Al4V substrate, 1 layer of TiO₂ coating with H₂O suspension which is also the thinnest coating (1 μm). The microstructure of this film is given in Figure 7.84, which had a fused recrystallized morphology as different from the lower temperature treated and thicker films which more or less preserved the initial granular structure of the coating. The HV value of the coating was determined to be HV 760 kg_f/mm² which was between the literature values of rutile (HVN₁₀₀ 894-974 kg_f/mm²) and anatase (HVN₁₀₀ 616-698 kg_f/mm²) (Mineral Search 2009). As the thickness of the TiO₂ film decreased the hardness value increased at 850°C, most probably due to the microstructural changes (from granular to fused), and phase changes (from anatase to rutile). The trend for the films heat treated at 360°C was an increasing hardness with thickness for which none of the morphological and phase changes were applicable. For 850°C heat treated films, the coatings with the H₂O suspensions were thinner and the hardness were greater; the coatings with the 1200 grit substrates (H₂O suspension) were

thinner and the hardness were greater (for the EtOH suspensions the 1200 and 180 grit sample hardness were almost the same). In general, for the TiO₂ coatings the surface hardness and roughness followed similar trends of change with respect to the heat treatment temperature, coated layers, suspending media, and substrate finish.

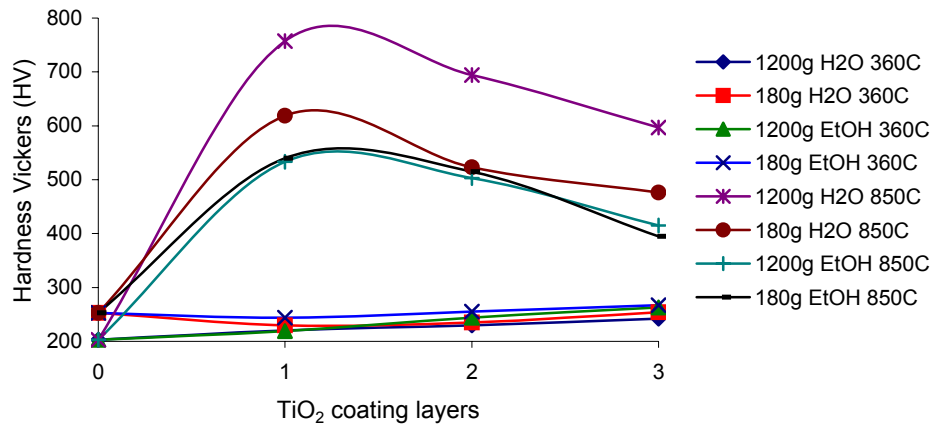


Figure 7.106. The surface hardness (HV) of the Ti6Al4V alloy/c-TiO₂; with various suspending medium, and heat treatment temperatures as a function of coated TiO₂ thickness (coated layers).

The Vickers hardness values of the Ti6Al4V alloy/c-HAp coatings are shown in Figure 7.107 a and b. The hardness values of the films heat treated at 850°C, especially the thicker ones, were exceedingly high because the indenter could not penetrate the films totally, instead elastically/plastically deformed them only partially penetrating (Figure 7.107a). Therefore, the values given at that temperature could only be taken as apparent hardness values which conveyed more information about the film thickness and deformability rather than hardness. It was beyond the scope of this work to correlate the measured hardness values with the film thickness and deformability. Nevertheless, the values, measured for the films, heat treated up to 700°C, most probably represented the real hardness, since the elastic or plastic deformability of these films was not an influential parameter on the measurements (Figure 7.107b). In general, the hardness values passed through a minimum for the samples treated at 360°C and were maximum at 700°C. The highest value that belonged to the thickest film used for the measurement was HV 644 kg_f/mm² (180 grit substrate, EtOH suspension, 3 layers); the next value of HV 594 kg_f/mm² belonged to the same type of film on a 1200 grit substrate. The hydroxyapatite pellet prepared by the commercial powder pressing and heated up to

1200°C (the dilatometer sample). Its hardness was measured to be HV 620 kg_f/mm² which was very close to the value of 611 kg_f/mm² given by Muralithran and Ramesh, 2000. The hardness value of HV 644 kg_f/mm² that was not much higher than value for the bulk c-HAp might point out only to a small degree of film deformation.

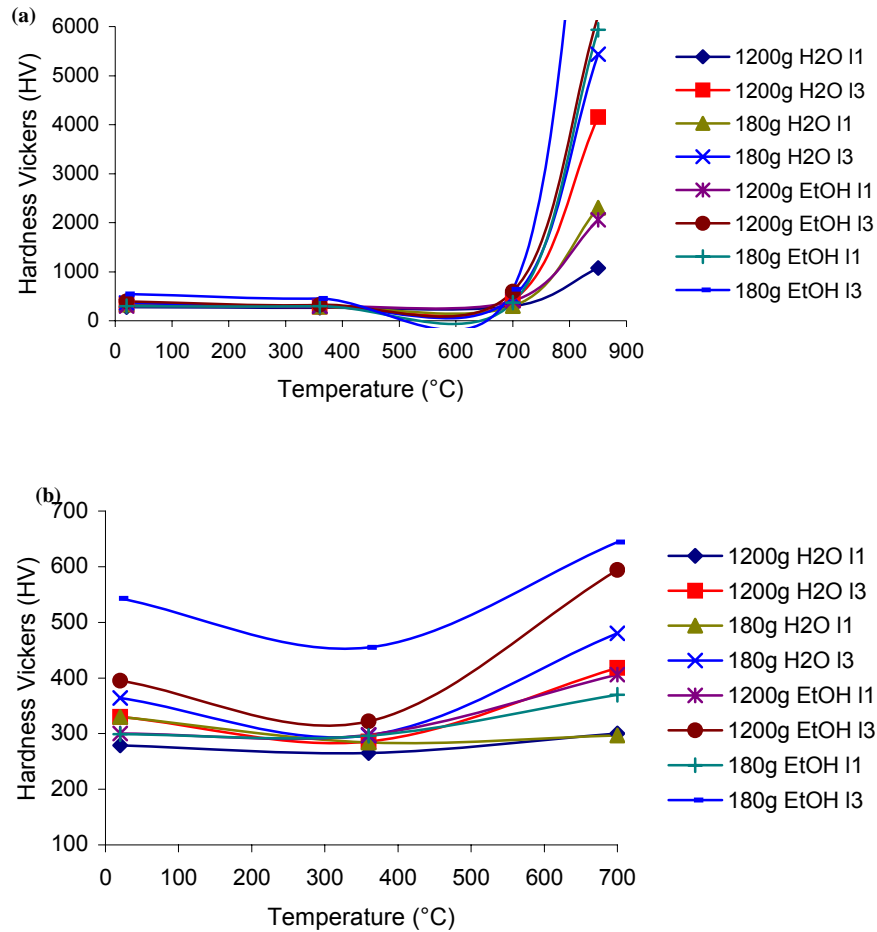


Figure 7.107. The surface hardness (HV) of the Ti6Al4V alloy/c-HAp; with various surface finish of the substrate (grit), suspending medium, HAp layers thickness (coated layers) as a function of heat treatment temperature (a) the hardness at 850°C as the apparent hardness values, (b) the detailed hardness values up to 700°C.

The film thickness of the anodized Ti6Al4V alloy/c-HAp coatings were over 10 μm , and the very high hardness values measured (over HV 1500 kg_f/mm²) were related to the film deformability and thickness, and hence were not reported.

The hardness values related to the films of Ti6Al4V alloy/c-TiO₂/c-HAp, with various surface finish of the substrate (grit), suspending medium, HAp thickness (coated layers) at 360°C as a function of TiO₂ thickness (coated layers) were given in Figure

7.108. The values for the same type of films heat treated at 850°C, again was exceedingly high indicating extensive film deformation. The values of HV 1121 kg_f/mm² and HV 1087 kg_f/mm² of the 180 grit and 1200 grit substrates, respectively, coated with 3 layers of EtOH suspension of TiO₂ and 3 layers of EtOH suspension of c-HAp (the thickest films; ~10 μm, and ~6 μm, respectively) were over the bulk Vickers hardness of the c-HAp (1200°C). Therefore, these values were regarded as the result of the film deformation. The next highest value was HV 629 kg_f/mm² close to the bulk hardness of c-HAp. The hardness values increased with the increasing total thickness of the film roughly within the range HV 300-450 kg_f/mm².

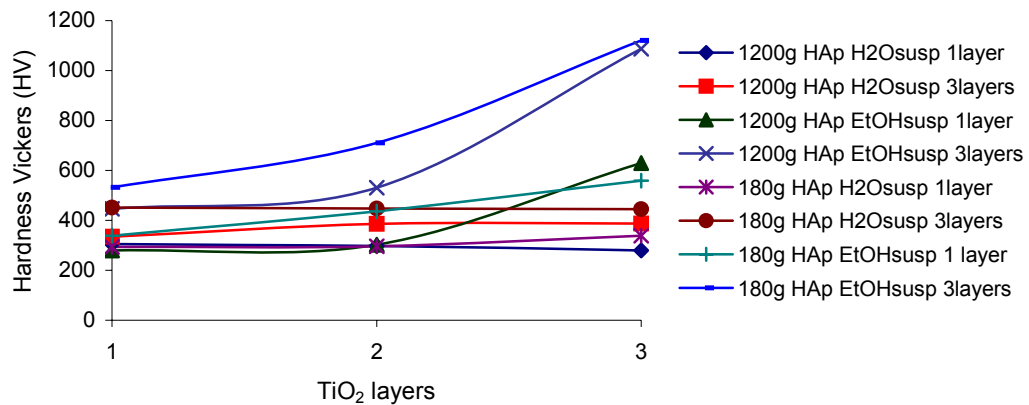


Figure 7.108. The surface hardness (HV) of the Ti6Al4V alloy/c-TiO₂/c-HAp; with various surface finish of the substrate (grit), suspending medium, HAp thickness (coated layers) at 360°C as a function of TiO₂ thickness (coated layers).

The adhesion strength of the Ti6Al4V substrate/c-TiO₂, Ti6Al4V substrate/c-HAp, and Ti6Al4V substrate/c-TiO₂/c-HAp films were measured using two different methods. The first method was the tensile test carried out by pulling apart the substrate and the film glued to stainless steel screw tops. A strong adhesion was achieved between the Ti6Al4V substrate and the stainless steel holder with curing at 70°C for 17 hours, and the breakage always took place at the film side. The second method was the scratch test the details of which were given in section 6.2.6.2. Eq. 6.1 was used to calculate the adhesion strength of the coating from the critical force value required to peel off the coating from the substrate (Culha, et al. 2009, Culha, et al. 2008, Celik, et al. 2006). In general, the strength values obtained by the tensile test method were lower than those obtained by the scratch test method. One reason could be that the tensile test

was related to the whole adhered surface. The peeling of the coating had to start on the weakest spot of adhesion and to continue catastrophically to complete breakage within a narrow increase of tensile force. Hence, the tensile test was more representative of the minimum adhesion strength of the whole film surface. On the other hand scratch test measured the peeling force at a particular spot on the surface, and the adhesion calculated was restricted to that particular spot.

The dilatometric curves of the c-HAp, c-TiO₂, mixtures of powders (50% c-HAp and 50% c-TiO₂), and layered c-HAp/c-TiO₂ pellets were obtained as given in Figure 7.109, in order to better understand the patterns in adhesion strength. The c-TiO₂ pellet (Degussa P25) underwent a linear shrinkage of 15% starting at 500°C and completed at 800°C. The linear shrinkage of c-HAp pellet started at 700°C and continued within the temperature range of interest (23% linear shrinkage to be completed at ~1300°C). The homogeneous mixtures of c-TiO₂ and c-HAp powder pellet started to shrink at the same temperature as c-HAp (700°C), but its temperature rate was lower. The layered c-TiO₂ and c-HAp pellet showed an irregular dilatometric curve. It expanded between 550°C and 700°C. After started to shrink, and the rate of shrinkage increased over 800°C. The most probable reason for the observed expansion was the breakage of interlocking bonding between the TiO₂ and HAp layers due to the shrinkage of TiO₂ layer that gave rise to two separate structures (pellets) with an air gap in between. The individual shrinkages of the separate structures later caused the overall observed shrinkage.

The adhesion strength (by tensile test) of Ti6Al4V substrate (1200 grit)/c-TiO₂ (H₂O suspension, 2 layers) as a function of temperature, is given in Figure 7.110. The adhesion of the film passed through a minimum at 700°C. The adhesion strength of 17 MPa occurred at 850°C. The dilatometric curve supported the adhesion strength pattern in Figure 7.110. The film shrank between the temperatures 500-800°C. The shrinkage was most probably associated with a decrease in adhesion strength. At temperatures above 800°C there was no considerable film shrinkage, and 850°C must have been a high enough temperature for the reconsolidation of the film on the substrate as also supported by the microstructure given in Figure 7.84. The microstructure of a similar but thinner film at 850°C indicated a fused structure, which also had the highest hardness, and roughness values. This implied a high adhesion strength.

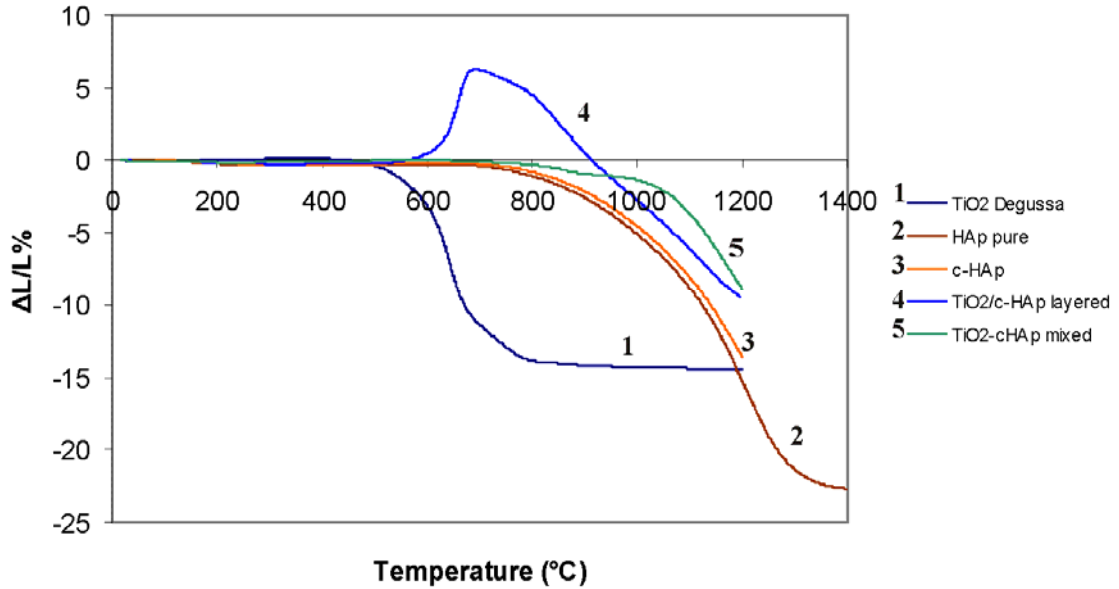


Figure 7.109. The dilatometric curves of the pellets prepared from the bulk powders of c-TiO₂, c-HAp, homogeneous mixture of c-TiO₂ and c-HAp, layered cTiO₂/c-HAp.

The adhesion strength (by scratch test) of the Ti6Al4V substrate (180g)/c-TiO₂ (EtOH suspension), heat treated at 850°C, as a function of TiO₂ thickness (coated layers) is given in Figure 7.111. The slight decrease of adhesion strength with the TiO₂ thickness was in accord with the microstructures given in Figure 7.84 and 7.85, which implied that the thinner the film the more fused was the microstructure. Probably the film reconsolidation at 850°C was closer to completion for thinner films providing a stronger adhesion between the film and the substrate.

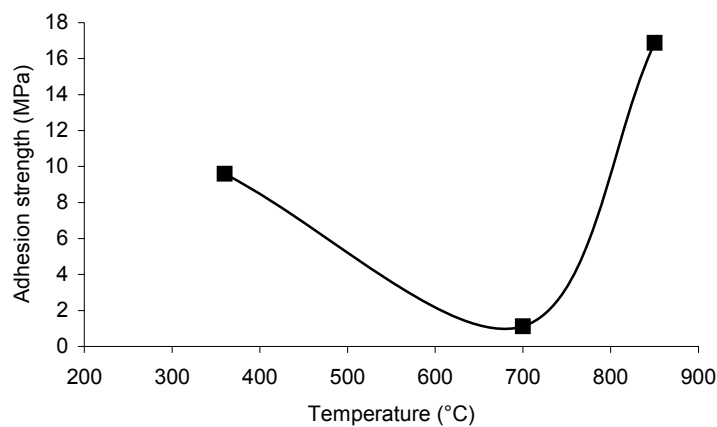


Figure 7.110. The adhesion strength (by tensile test) of Ti6Al4V substrate (1200 grit)/c-TiO₂ (H₂O suspension, 2 layers) as a function of temperature.

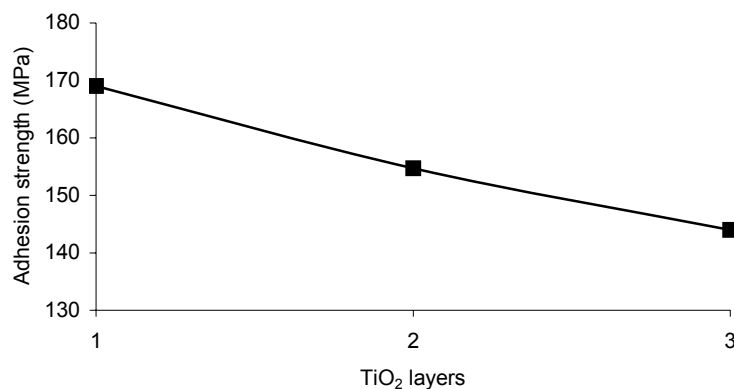


Figure 7.111. The adhesion strength (by scratch test) of the Ti6Al4V substrate (180g)/c-TiO₂ (EtOH suspension), heat treated at 850°C, as a function of TiO₂ thickness (coated layers).

The adhesion strength (by tensile test) of the Ti6Al4V/c-HAp films with various substrate surface finish (grit), suspending medium, and HAp thickness (coated layers) as a function of heat treatment temperature, is given in Figure 7.112. The patterns for all type of the films examined was similar and within a narrow range of adhesion strength values. The adhesion strength increased roughly 50% from 360°C to 700°C. The reason for the increase should be consolidation of the film by the onset of interparticle sintering which might also be effective in film interdigitation and interlocking with the substrate surface topographical features. It might have been expected that this effect even would yield a greater adhesion strength for the films heat treated at 850°C, also in the light of the corresponding microstructures given in Figure 7.88, 7.91 and 7.93. The three dimensional continuous mesh structure of the c-HAp film might have been instrumental in forming the necessary interdigitation and interlocking to provide a strong bond between the film and the substrate. However, in fact the adhesion strength values of the c-HAp films heat treated at 850°C were virtually zero. The dilatometric curve for c-HAp indicated that shrinkage started after 700°C and continued through 850°C. For temperatures up to 700°C film consolidation increased the adhesion strength, while for temperatures above 700°C extensive film shrinkage caused the breakage of the bonds between the film and the substrate. The shrinkage was also evident by the cracks forming and enlarging of the c-HAp films heat treated at 850°C (Figure 7.90-7.93). The adhesion strength (by scratch test) of the Ti6Al4V (180 grit)/c-HAp (EtOH suspension, 1 layer) as a function of heat treatment temperature is given in Figure 7.113.

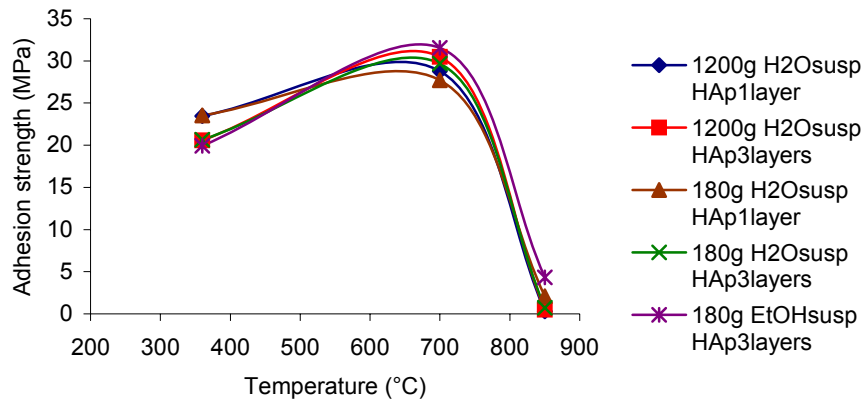


Figure 7.112. The adhesion strength (by tensile test) of the Ti6Al4V/c-HAp with various substrate surface finish (grit), suspending medium, and HAp thickness (coated layers) as a function of heat treatment temperature.

The pattern of change of adhesion strength with the heat treatment temperature was the same as the tensile test results (Figure 7.112); an increase in adhesion strength from 360°C to 700°C, and a larger decrease at 850°C. However, the adhesion strength values determined by the scratch test was almost an order of magnitude greater than the tensile test results. As discussed above this difference was inherent in the methods since the while value measured by tensile test was closer to the minimum value of adhesion over the whole surface, the scratch test measured a spot adhesion value. The adhesion strength at 850°C measured by the scratch test, although the lowest, was 114 MPa, much different from the virtual zero measured by the tensile test. Nevertheless, in predicting the failure behavior of such coatings tensile test might provide a better (more realistic) prediction.

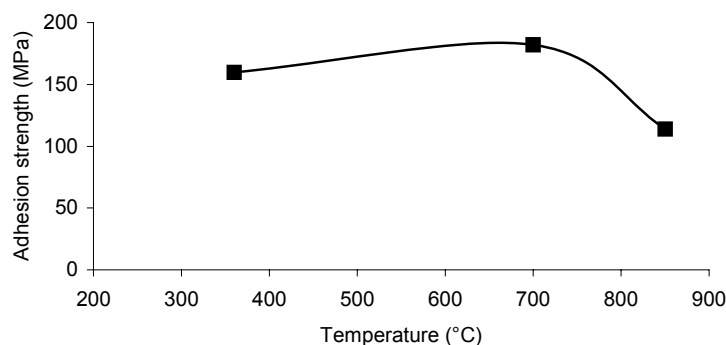


Figure 7.113. The adhesion strength (by scratch test) of the Ti6Al4V (180 grit)/c-HAp (EtOH suspension, 1 layer) as a function of heat treatment temperature.

In order to assess the effect of intermediate TiO₂ layer thickness on the adhesion strength of the Ti6Al4V alloy/TiO₂/c-HAp films the tests summarized in Figure 7.114-7.116 were performed. The anodization voltage changed the thickness of the TiO₂ (anatase before heat treatment) as well as the surface morphology and composition. The adhesion strength of the anodized Ti6Al4V (1200 grit)/c-HAp (H₂O suspension, 3 layers) heat treated at 850°C as a function of anodization voltage, is given in Figure 7.114. The adhesion strength of the c-HAp film on the 20 V anodized substrate was the lowest, similar to the values obtained for the Ti6Al4V/c-HAp films. At 20 V the TiO₂ coating on the alloy was not continuous, and most probably its thickness was not sufficient to reconsolidate the interlocking between the TiO₂ and c-HAp layers at 850°C. The maximum adhesion strength was achieved for the 60 V anodized substrate case. Probably the intermediate TiO₂ layer interdigitated and interlocked with the shrunk c-HAp layer reforming the bond between them by the morphological and phase transformation that was shown in Figure 7.84. The adhesion strength decreased with the increasing anodization voltage for the films on 120 V and 400 V anodized substrates. The increasing thickness of the intermediate TiO₂ layer most probably limited the necessary morphological and phase transformations that would rebond the weakened or detached c-HAp layer.

The adhesion strength (by tensile test) of Ti6Al4V substrate/c-TiO₂ (H₂O suspension, 2 layers)/c-HAp, with various substrate surface finish (grit), and suspending medium, as a function of temperature is given in Figure 7.115. The adhesion strength, alike the Ti6Al4V alloy/c-TiO₂ films, decreased from 360°C to 700°C (the minimum), and increased again at 850°C. This phenomenon could be explained by the behavior of the intermediate TiO₂ layer, since the dilatometric curve of TiO₂ showed a shrinkage between 500-800°C. Most probably, at 850°C the substrate-TiO₂, and TiO₂-c-HAp rebonding were achieved by the morphological and phase changes of the TiO₂ layer as described above.

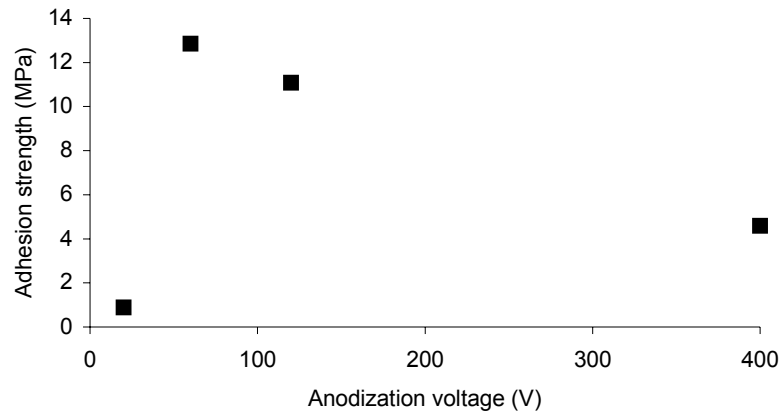


Figure 7.114. The adhesion strength (by tensile test) of the anodized Ti6Al4V (1200 grit)/c-HAp (H₂O suspension, 3 layers) heat treated at 850°C as a function of anodization voltage.

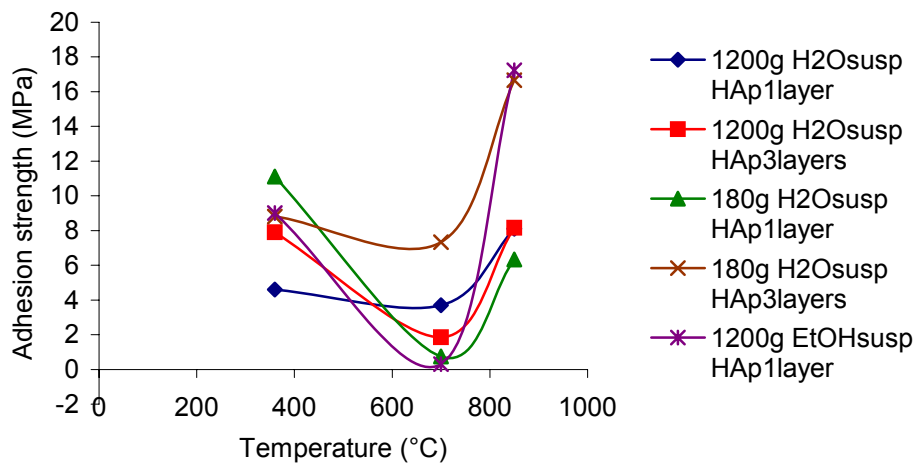


Figure 7.115. The adhesion strength (by tensile test) of Ti6Al4V substrate/c-TiO₂ (H₂O suspension, 2 layers)/c-HAp, with various substrate surface finish (grit), and suspending medium, as a function of temperature.

The adhesion strength (by scratch test) of the Ti6Al4V substrate (180 grit)/c-TiO₂ (EtOH suspension)/c-HAp (EtOH suspension, 3 layers), heat treated at 850°C as a function of TiO₂ thickness is given in Figure 7.116. As expected, these scratch test adhesion strength values were higher. The results for the films with 1 and 2 layers of intermediate TiO₂ (the total film thickness were 7 μm and 9 μm, respectively) were nearly the same, and lower with 3 layers of TiO₂ (11 μm). Most probably because of the increasing thickness limited the morphological and phase changes of intermediate TiO₂ necessary for the rebonding.

The effect of the intermediate TiO₂ layer in the Ti6Al4V/c-TiO₂/c-HAp film structures was the rebonding of the Ti6Al4V/c-TiO₂, and TiO₂/c-HAp at 850°C of the bonding broken at 700°C due to the TiO₂ shrinkage between 500-800°C. The bonding between the Ti6Al4V/c-HAp and TiO₂/c-HAp were broken above 700°C due to the c-HAp shrinkage. However, TiO₂/c-HAp layers were rebonded by the morphological and phase transformations in the TiO₂ layer.

The average linear thermal expansion coefficient of Ti6Al4V is $8.6 \times 10^{-6} \text{ K}^{-1}$ in the range 0-300°C (Azo Materials-1 2009), and of rutile is $9.2 \times 10^{-6} \text{ K}^{-1}$ in the range 0-1000°C (Azo Materials-2 2009). These values are close enough together that any appreciable metal/oxide interfacial thermal stresses do not occur in our study.

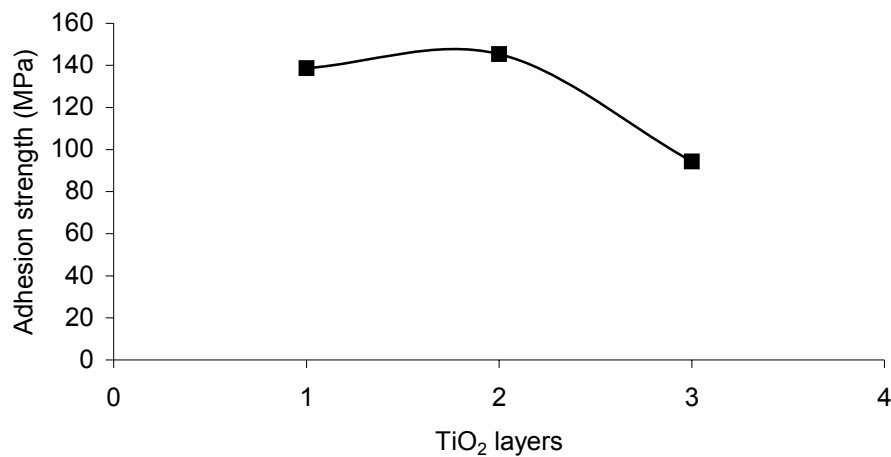


Figure 7.116. The adhesion strength (by scratch test) of the 180 grit Ti6Al4V substrate/c-TiO₂ (EtOH suspension)/c-HAp (EtOH suspension, 3 layers), heat treated at 850°C as a function of TiO₂ thickness (coated layers).

The interfacial shear strength of the inorganic, and organic route prepared hydroxyapatite films on Ti alloy substrates, annealed at 500°C, were measured to be $347 \pm 64 \text{ MPa}$, and $280 \pm 28 \text{ MPa}$ (Gan, et al. 2005). The adhesion strength of the hydroxyapatite coatings on Ti6Al4V alloy prepared by a sol gel method were reported as in excess of 14 MPa, which were within the same range with our results (Weng 1999). The adhesion strength values of colloidal-sol gel derived β -TCP, fluoridated hydroxyapatite biphasic coatings were reported as in between 430-500 mN by the scratch test (Cheng, et al. 2008). As a matter of fact adhesion strength could not be calculated since Eq. 6.1 yielded imaginary numerical values by these claimed too high

peeling forces. Probably these forces were high enough for the indenter tip to penetrate the Ti6Al4V alloy substrate. The adhesion strength of plasma sprayed hydroxyapatite coatings on grit blasted Ti and TiN (by laser gas-nitridation) substrates were 16 MPa and 30 MPa, respectively (Yang, et al. 2009).

7.5. The Surface Electrostatic Potential Distribution of Hydroxyapatite by Molecular Modeling

The surface electrostatic potential (ESP) distribution of hydroxyapatite was determined by molecular modeling methods. The geometry optimization of the ionic groups within the hydroxyapatite ($\text{Ca}_{10}(\text{PO}_4)_6(\text{OH})_2$) structure, namely, Ca^{2+} , PO_4^{3-} , and OH^- were carried out by density functional theory method (DFT), B3LYP, and with the basis set 6-31Gd. The results are given in Table 7.1.

Table 7.1. Geometry optimization job for the ionic species in hydroxyapatite

	Ca^{2+}	PO_4^{3-}	OH^-
Shape		tetrahedral	linear
Bond Angle		109.47122°	
Bond distance		P-O 1.599 Å O-O 2.611 Å	O-H 0.987 Å
Energy	-676.8669 hartrees*	-641.8124 hartrees	-75.7208 hartrees
Dipole moment	0	0	1.1726 Debye
Mulliken charges**	Ca=+2	P=+0.7136 O=-0.9284	O=-1.1394 H=+0.1394

*One hartree is the total energy of the electron in the first Bohr orbit (first circular orbit of Bohr model of hydrogen atom), and equals 4.35944×10^{-18} J or 627.51 kcal/mol.

**Mulliken charges are the partial atomic charges in molecules calculated by the Mulliken population analysis.

The hydroxyapatite unit cell was drawn utilizing crystal editor function (GaussView) with the parameters: hexagonal system, $P6_3/m$ space group, $a=b=9.4394$ Å, $c=6.8861$ Å, $\alpha=\beta=90^\circ$, $\gamma=120^\circ$ (Wilson, et al. 1999). The hydroxyapatite unit cell is depicted in Figure 7.117. One unit cell contains 44 atoms. Hydroxyapatite crystal structure of 9 unit cells together, is depicted in Figure 7.118.

The ESP distribution on the electron isodensity surface of the Ca^{2+} , PO_4^{3-} and OH^- fragments, and hydroxyapatite crystal composed of one and two unit cells were

calculated by the 3-21G basis set. The ESP on the electron isodensity surface calculation for hydroxyapatite was not possible with more than two unit cells, since the system would contain more than 100 atoms that the software could not solve. Electrostatic potential was mapped on the electron isodensity surface, $\delta=0.0004 \text{ e/Bohr}^3$ (Bohr is the radius of the first orbit in the Bohr atomic model and equals $5.29177249(24)\times 10^{-11} \text{ m}$).

The isodensity surface electrostatic potential distribution of Ca^{2+} , PO_4^{3-} and OH^- fragments are depicted in Figure 7.119. Ca^{2+} and PO_4^{3-} had homogeneous ESP distributions of +0.619 and $-0.592 \text{ hartrees}^3$ on the isovalue surfaces of the shapes given in Figure 7.119a and c, respectively. The ESP of OH^- changes in the range -0.362 to -0.080 hartrees on the isovalue surface of the shape depicted in Figure 7.119e. The ESP was color coded, from red-yellow up to green for negative potentials, red representing the most negative potentials, and from green to light blue-dark blue for positive potentials, dark blue representing the most positive potentials (green color represented neutral potential).

The ESP distribution of the hydroxyapatite unit cell, on the $\delta=0.0004 \text{ e/Bohr}^3$ isodensity surface, is given in Figure 7.120. The ESP on the isovalue surface was from +0.284 hartree (dark blue) to -0.284 hartree (red). The positive regions of ESP on the given isovalue surface was in the shape of a strips of roughly 10 \AA wide, and there existed two sharp tips of positive ESP due to Ca^{2+} on the (001) and (00-1) surfaces. On the other hand the negative ESP region was in the form of dull near globes.

The ESP distributions of the hydroxyapatite crystal that consisted of two unit cells, on the $\delta=0.0004 \text{ e/Bohr}^3$ isodensity surface are given in Figure 7-121 (ax2, bx1, cx1), 7.122 (ax1, bx2, cx1) and 7.123 (ax1, bx1, cx2) with the ESP potential maximums as 0.297, 0.290, 0.327 hartrees, respectively. Again especially, the positive ESP regions were in the shape of strips of roughly 10 \AA wide. This kind of potential distribution was quite different from that of, for example, NaCl crystal ESP distribution (on the same isovalue surface of $\delta=0.0004 \text{ e/Bohr}^3$; Figure 7.124) which was distributed as patches of sequentially changing positive and negative regions of 0.05897 hartree. The ESP distribution in the form of strips could induce positive cooperation in protein adsorption

³ Electrostatic potential is given as electric potential energy in hartrees (in some literature stated as e/Bohr or e/ \AA) of an electron (charge $1.6021\times 10^{-19} \text{ coul}$) located at the isovalue surface. 1 hartree is equivalent to 27.211 V ($=4.35944\times 10^{-18} \text{ J/hartree} / 1.6021\times 10^{-19} \text{ coul}$).

by providing consistent anchorage points or regions, particularly to flexible protein molecules.

The ESP mappings on various values of isosurfaces of electron density of the hydroxyapatite unit cell are shown in Figure 7.125, and the plots of ESP versus isovalue of the electron density surfaces of one and two unit cells of hydroxyapatite crystal are given in Figure 7.126. The ESP passes through a maximum with respect to electron isodensity surface. The ESP_{\max} was 0.402 hartree for the unit cell and 0.434 hartree for two unit cells at the same isovalue of 0.04-0.05 e/Bohr^3 of the electron density surface. These values might provide an indication of the minimum distance of approach which was roughly 1.5 Å. However, the real minimum distance of approach depends on also the adsorbate ESP and electron density values of the adsorbate and the degree of hydration as well as temperature and pH.

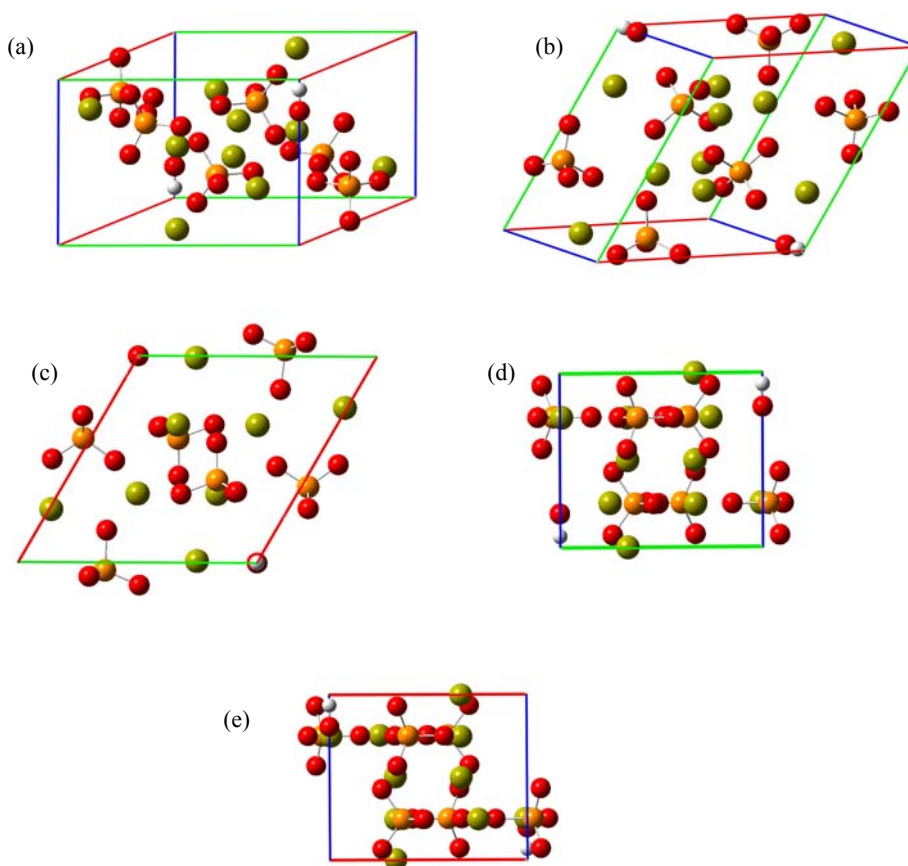


Figure 7.117. Hydroxyapatite unit cell; the color codes for axis are: a=red, b=green, c=blue; the color codes for atoms are: Ca=Khaki, P=orange, O=red, H=white; (a), (b) three dimensional views, (c) view through c-axis, (d) view through a-axis, (e) view through b-axis.

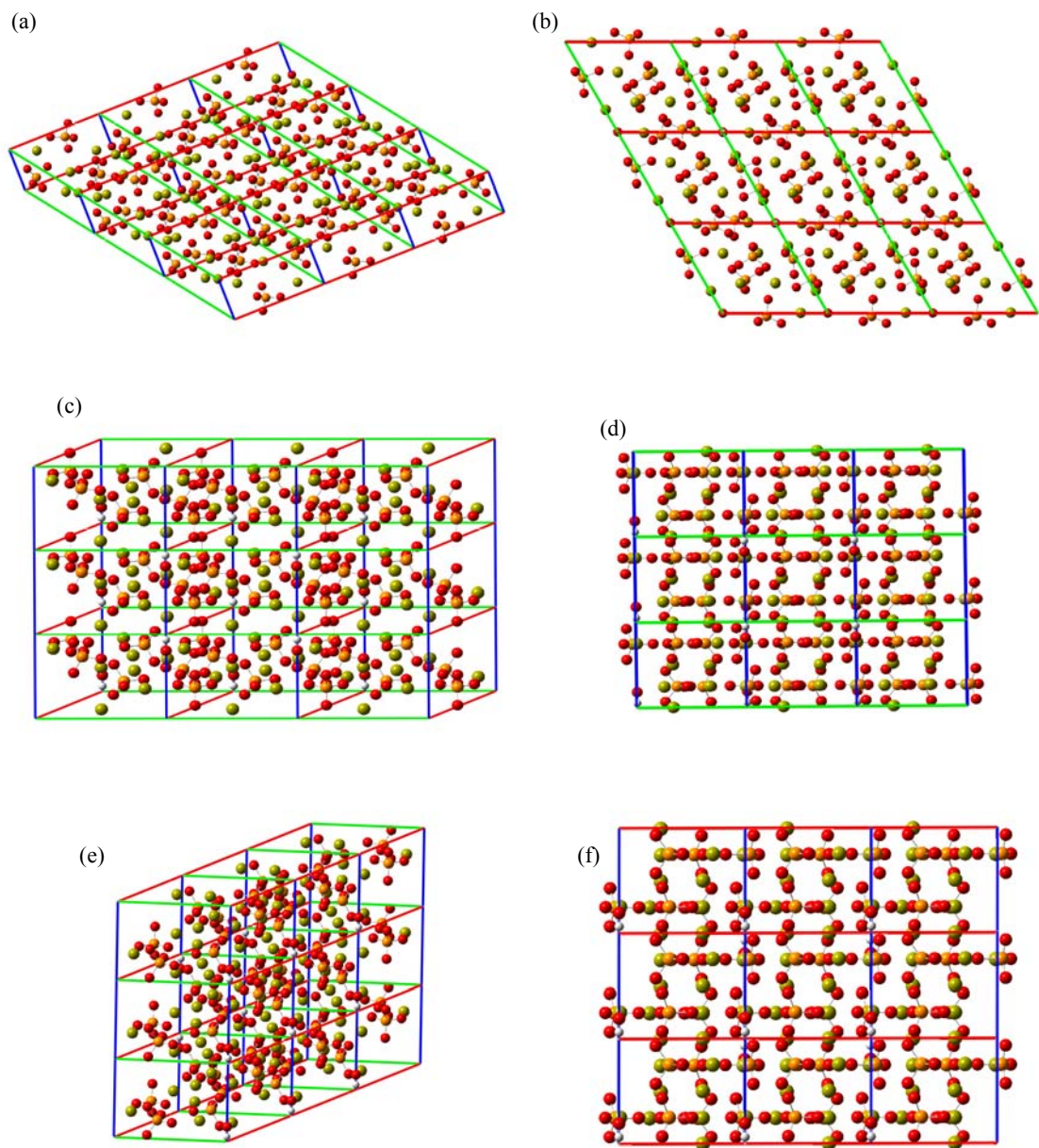


Figure 7.118. Hydroxyapatite crystal structure with 9 unit cells: (a), (b) ax_3, bx_3, cx_1 , (b) viewed through c-axis, (c), (d) ax_1, bx_3, cx_3 , (d) viewed through a-axis, (e), (f) ax_3, bx_1, cx_3 , (f) viewed through b-axis.

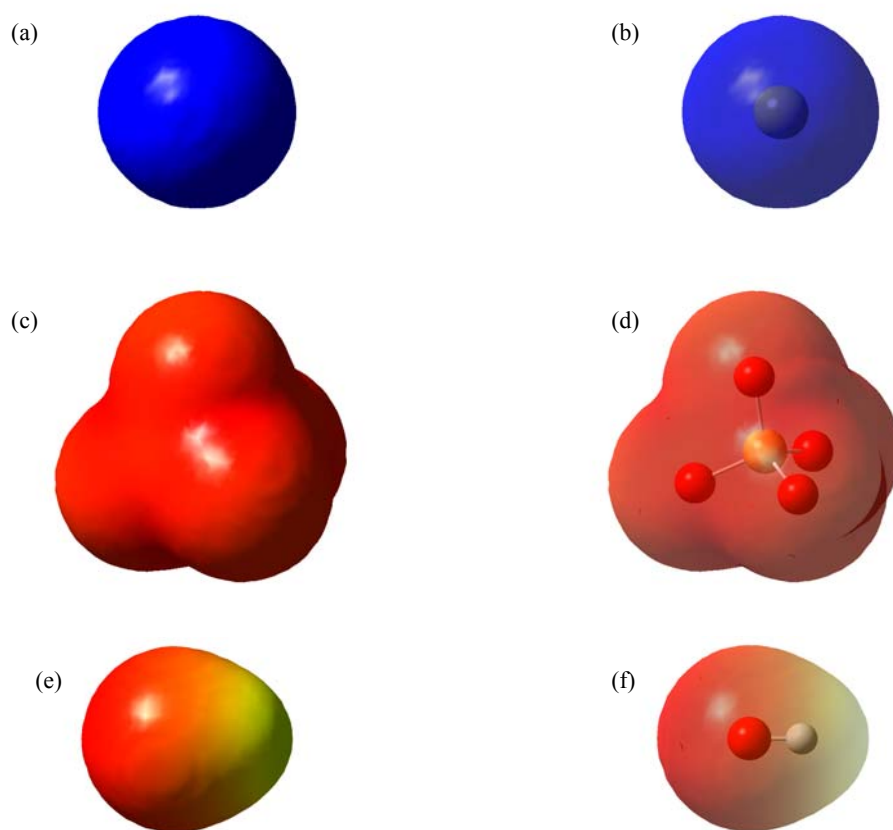


Figure 7.119. Solid and transparent views of the electrostatic potential mapped on the electron isodensity surface of 0.0004 e/Bohr^3 (blue color represents positive and red represents negative potentials) of (a) Ca^{2+} solid, $\text{ESP}=+0.619$ hartree, (b) Ca^{2+} transparent view, (c) PO_4^{3-} solid, $\text{ESP}=-0.592$ hartree, (d) PO_4^{3-} transparent view, (e) OH^- solid, $\text{ESP}=-0.362$ (red) to -0.080 (yellow-green) hartrees, (f) OH^- transparent view.

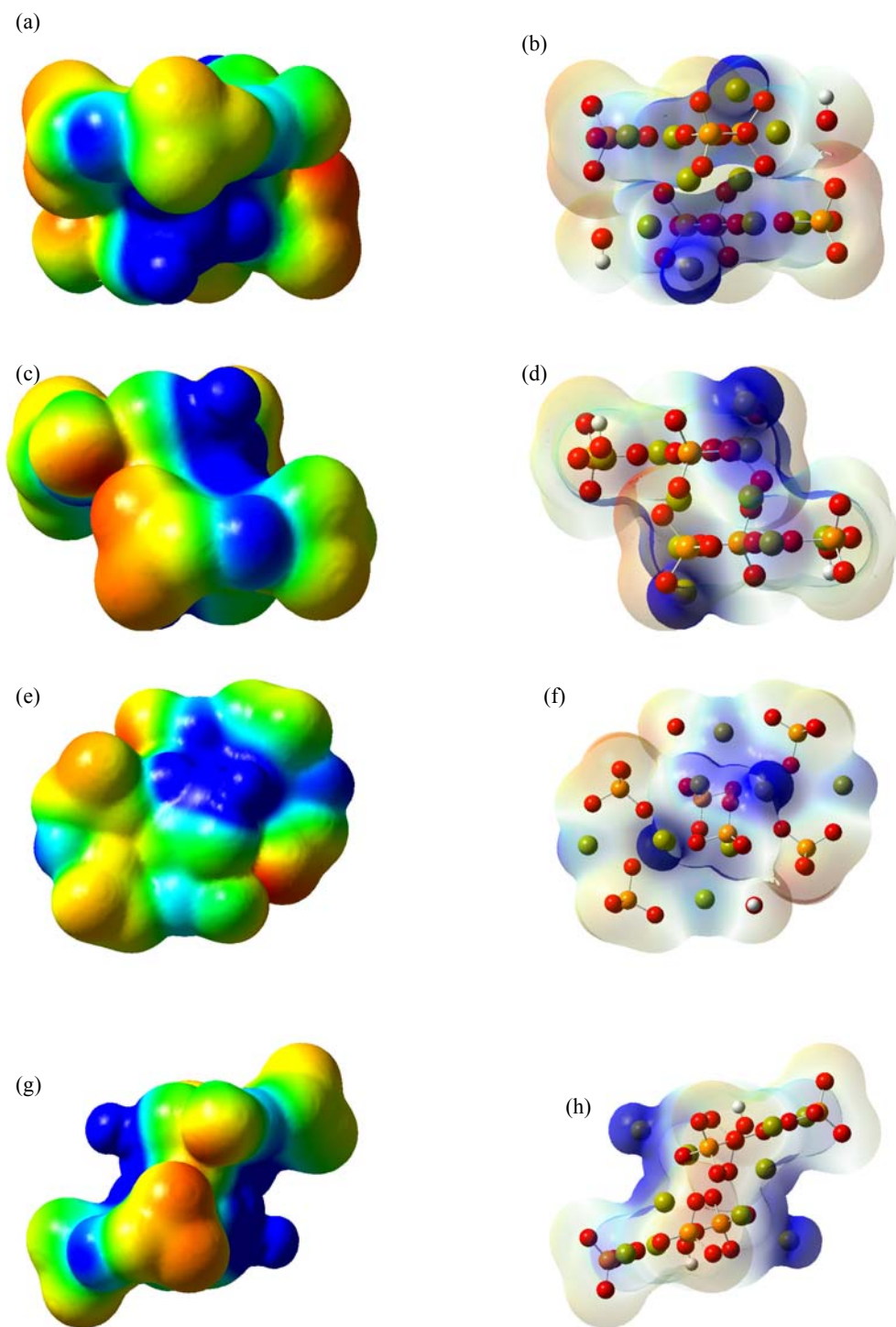


Figure 7.120. Solid and transparent views of the electrostatic potential mapped on the electron isodensity surface of 0.0004 e/Bohr^3 (color code: from blue $+0.284$ hartree to red -0.284 hartree) of HAp unit cell through (a), (b) a-axis, (c), (d), b-axis, (e), (f) c-axis, and (g), (h) random direction.

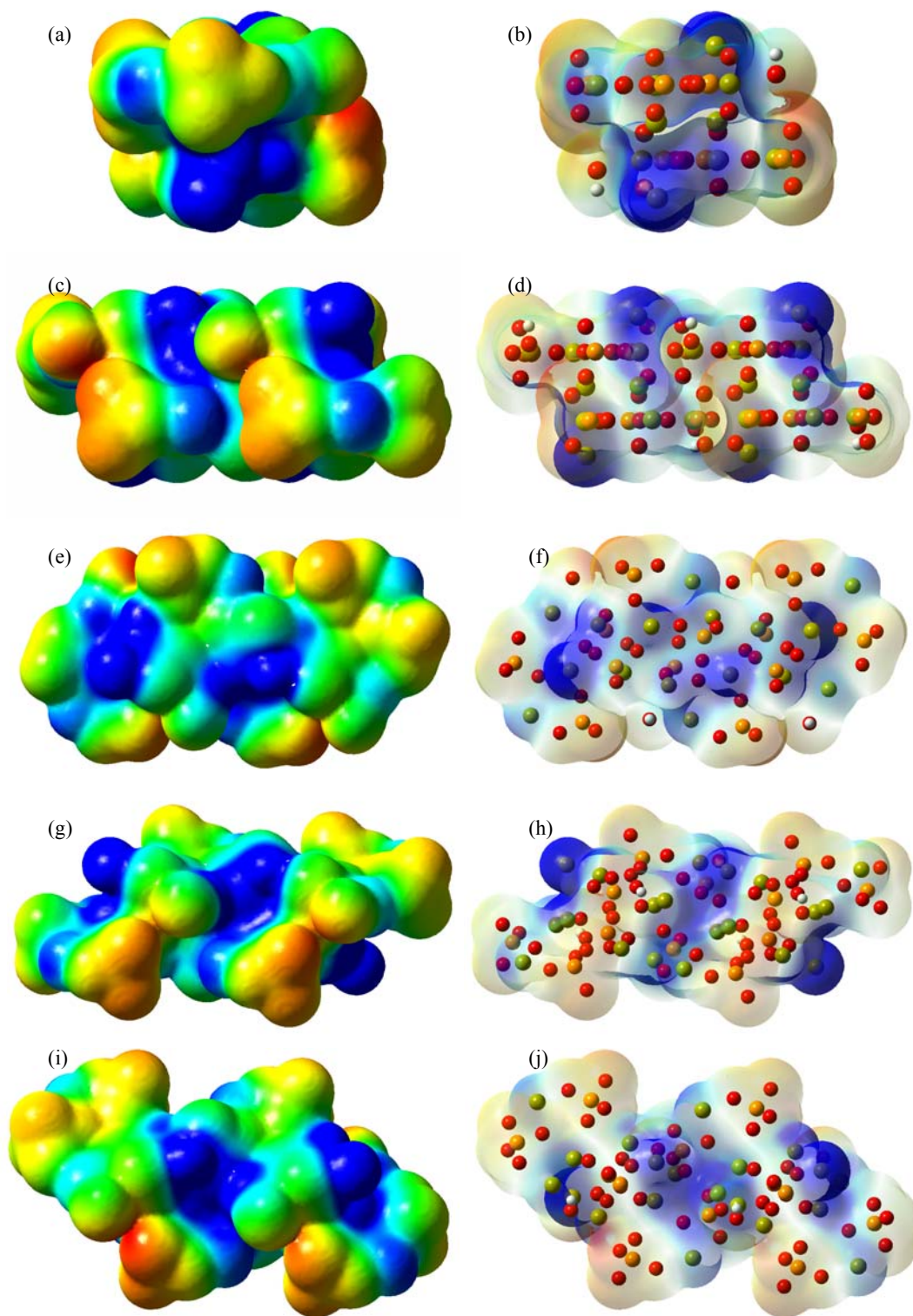


Figure 7.121. Solid and transparent views of the ESP mapped on the electron isodensity surface of 0.0004 e/Bohr^3 of two unit cells of HAp crystal, ax2, bx1, cx1, through (a), (b) a-axis, (c), (d), b-axis, (e), (f) c-axis, and (g), (h), (i), (j) random direction from -0.297 hartree (red) to $+0.297 \text{ hartree}$ (blue).

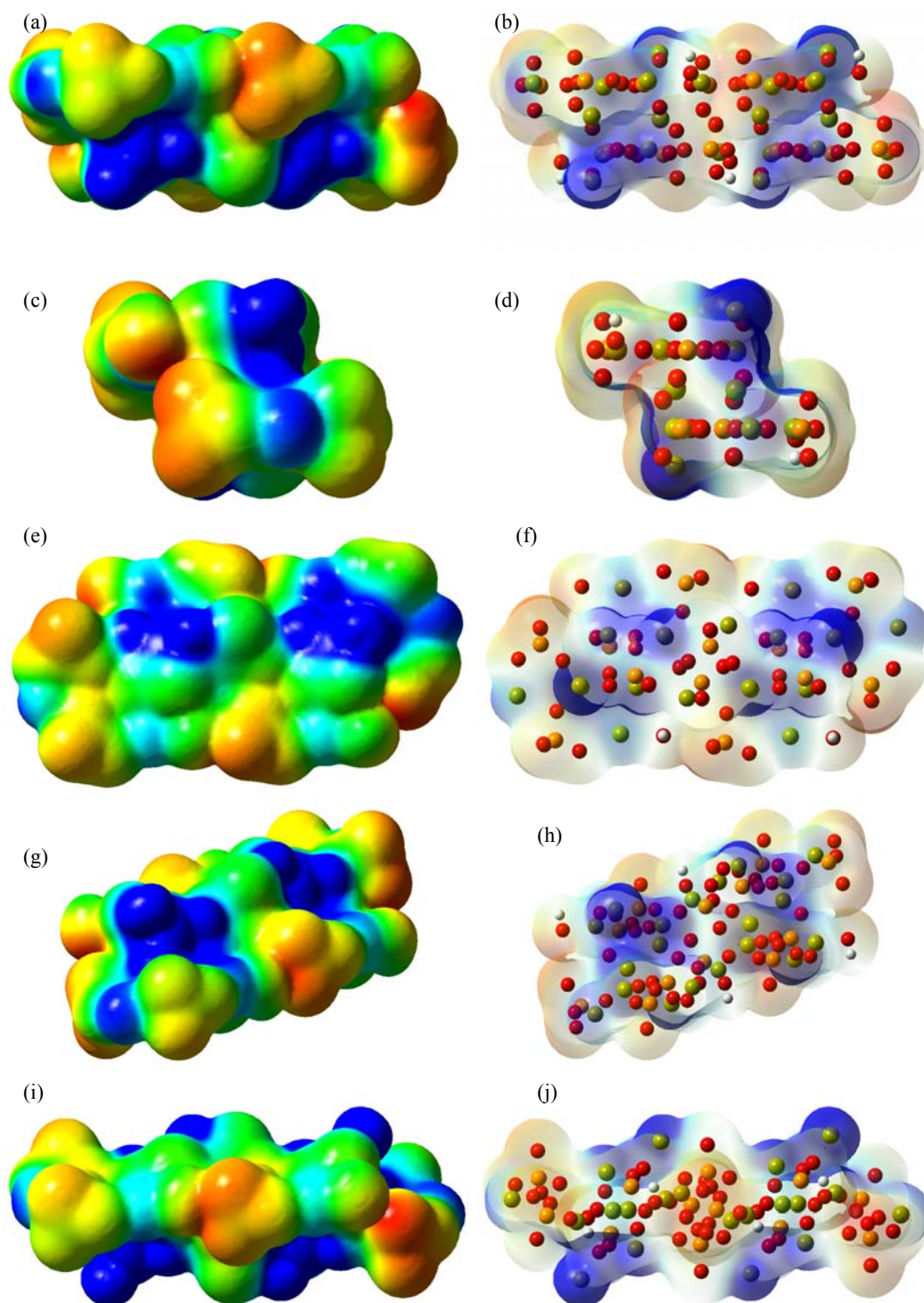


Figure 7.122. Solid and transparent views of the ESP mapped on the electron isodensity surface of 0.0004 e/Bohr^3 of two unit cells of HAp crystal, ax1, bx2, cx1, through (a), (b) a-axis, (c), (d), b-axis, (e), (f) c-axis, and (g), (h), (i), (j) random direction from -0.290 hartree (red) to $+0.290 \text{ hartree}$ (blue).

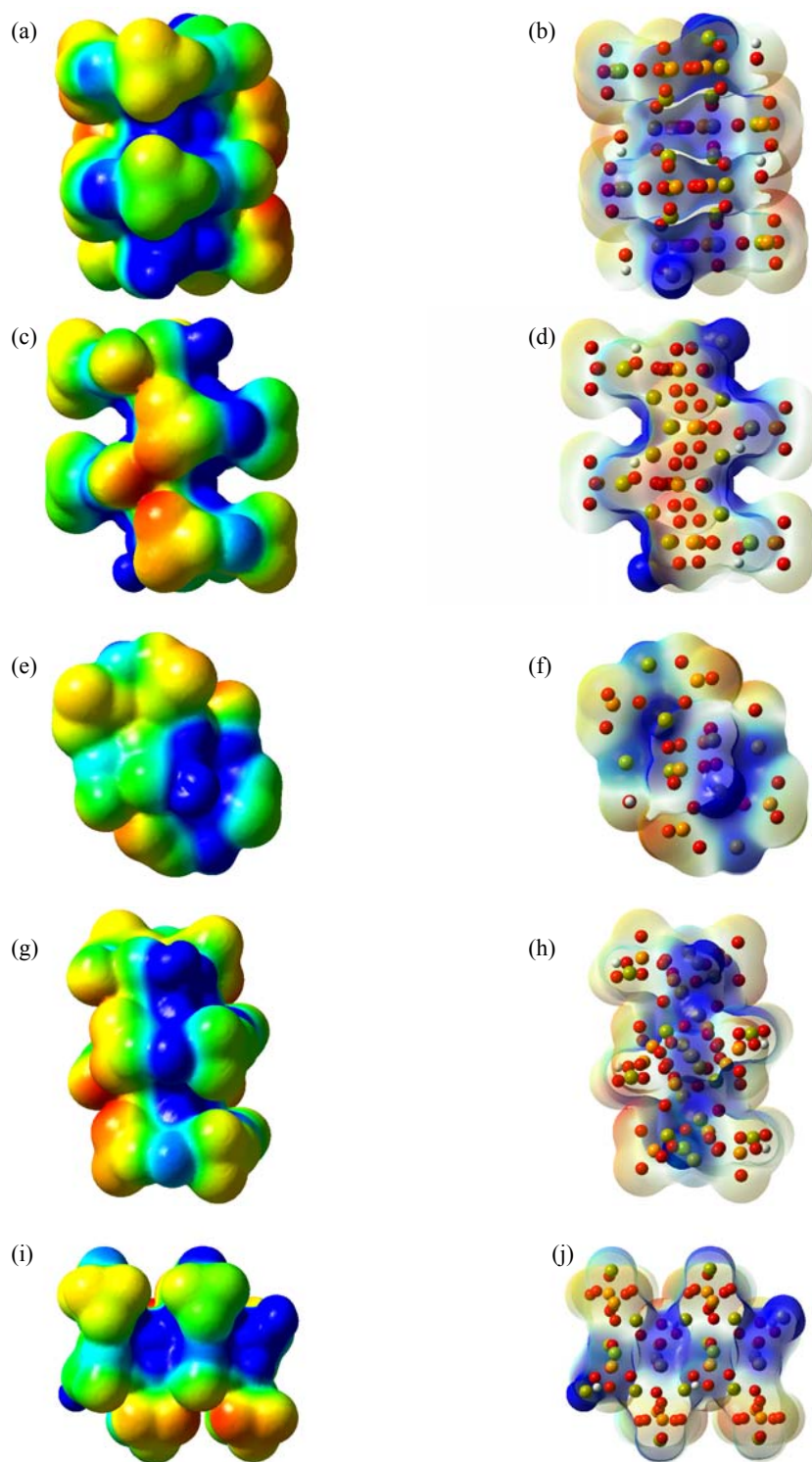


Figure 7.123. Solid and transparent views of the ESP mapped on the electron isodensity surface of 0.0004 e/Bohr^3 of two unit cells of HAp crystal, ax1, bx1, cx2, through (a), (b) a-axis, (c), (d), b-axis, (e), (f) c-axis, and (g), (h), (i), (j) random direction from -0.327 hartree (red) to $+0.327 \text{ hartree}$ (blue).

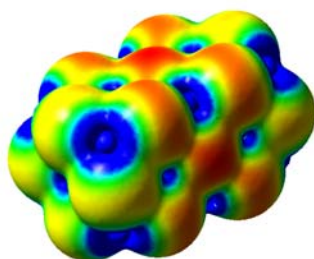


Figure 7.124. The ESP distribution of NaCl crystal of two unit cells mapped on the isovalue electron density surface of 0.0004 isovalue with maximum potential values as ± 0.05897 hartree.

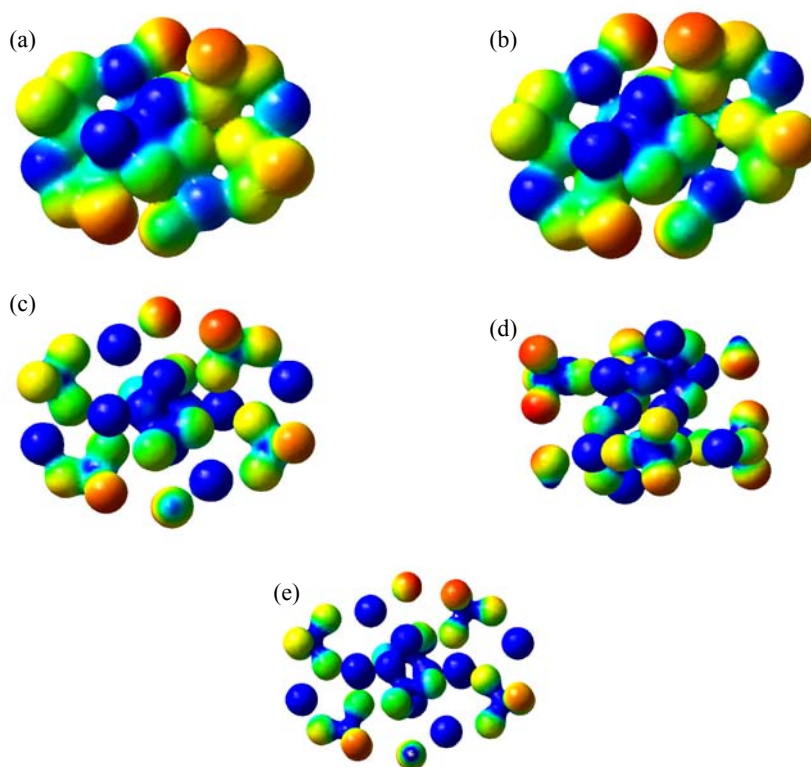


Figure 7.125. Solid views of the ESP mapped on various electron isodensity surfaces unit cells of HAp (a) $\delta=0.004$ e/Bohr³, c-axis, ESP=0.329 hartree, (b) $\delta=0.008$ e/Bohr³, c-axis, ESP=0.351 hartree, (c) $\delta=0.04$ e/Bohr³, c-axis, ESP=0.401 hartree, (d) $\delta=0.04$ e/Bohr³, a-axis, ESP=0.379 hartree, (e) $\delta=0.1$ e/Bohr³, c-axis, ESP=0.379 hartree.

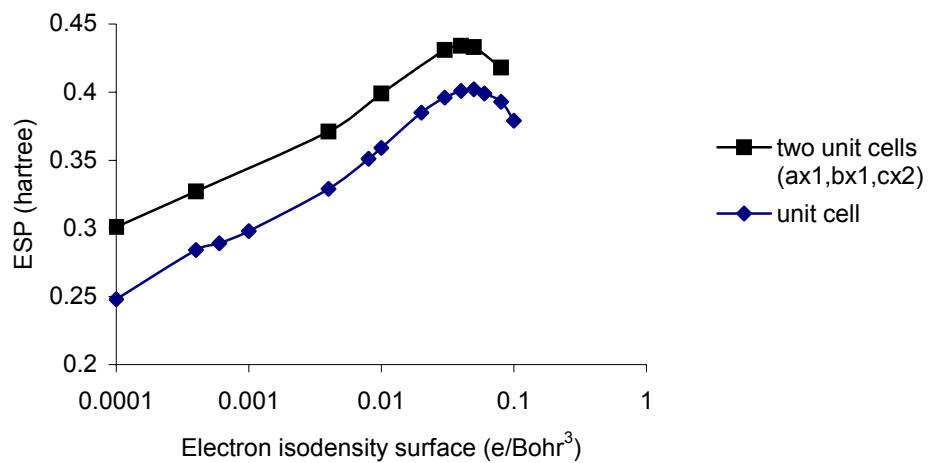


Figure 7.126. Electrostatic potential surface versus electron isodensity surface for one and two unit cells of hydroxyapatite crystal.

CHAPTER 8

CONCLUSIONS AND RECOMMENDATIONS

The purpose of this work was to prepare hydroxyapatite/silk protein thin film implant surfaces by a particulate sol method, and to investigate their microstructural properties and model protein interactions for enhanced osteoinduction.

The commercial hydroxyapatite powder was extensively dry milled resulting in the change of shape and size of the particles from rods of 150-250 nm in length and 50-80 nm in diameter to 20-100 nm equiaxed particles.

The aqueous suspensions of the commercial HAp powder as received, and in its dry ball milled form were used to prepare the thin films. For suspensions with the solid content of 7.6%, the deagglomeration effectiveness of double quenching with liquid N₂, wet ball milling for 2 hrs, single quenching with liquid N₂, fast mixing in baffled blender, thermal shock (all followed by ultrasonication except for fast mixing in blender) were in the given order. Hydropalate 64 (2w/w%) was determined to be a slightly better dispersant than calgon (1w/w%) for the system. Better deagglomerations were achieved with the increasing ultrasound bath treatment duration. Double quenching with liquid N₂, followed by 125 min of ultrasonication yielded a deagglomeration with ~79% of the agglomerates under 1 μm. The volume changes associated with the phase transformation of water, initiating intergranular gaps, were determined to be the major mechanism for particle deagglomeration for liquid nitrogen quenching. For the suspensions with 30% solid content, calgon and D-fructose was shown to be ineffective for deagglomeration. Wet ball milling for 2 hr followed by 125 min ultrasonication, with hydropalate as dispersant, was determined to be the most effective method to achieve a deagglomeration comparable to the case of lower solid content suspensions.

The optimum pH values for the dispersion of c-HAp and m-HAp powder suspensions were determined by the zeta sizer measurements as 10.2 for the c-HAp powder and 9.4 for the m-HAp powder (120 min dry milled). The PZC values of the c-HAp and m-HAp powders were measured as 5.71 and 5.47, and IEP values as 5.86 and 5.69, respectively. These results indicated that the decreasing particle size, or the

increasing particle surface area reduced the double layer repulsive barrier potential, because of the increased screening of the counter-ions within the slip layer of the surface charge, hence deteriorates the suspension stability. An increase in particle surface area of 23% (from 22 m²/gr of the c-HAp powder to 27 m²/gr of the m-HAp powder) brings about a 2.4 times increase in the slip layer charge. Direct measurements confirmed that $\zeta(c\text{-HAp, pH}=10.2)=-26.3$ mV, while $\zeta(m\text{-HAp, pH}=9.4)=-19.9$ mV. The steric dispersion effect of hydropalate 64 rapidly decreased the agglomerate sizes until about 1.2 % dispersant was added and higher quantities did not further help the deagglomeration.

By the SEM and AFM images, the minimum solid ratio of the suspensions was determined to be 15% for complete surface coverage of the glass substrates coated with c-HAp powder suspension; with the same solid ratio approximately 90% of the substrate surfaces were coated with the m-HAp powder suspension. The agglomerates larger in size and number in the coatings prepared from the dry milled powder proved to be an indication of the higher agglomeration tendency with increasing surface area, and hence, lower zeta potential of the crushed particles as discussed above. The thickness of the thin films prepared with the c-HAp powder was determined to be in the range 450 nm to 650 nm, while the ones with the m-HAp was in the range 500 nm to 750 nm. The multi layer coatings (5 layers) prepared with lower solid content suspensions increased the thickness of the already existing sporadic aggregates rather than coating the void area. The thickness of the thin films prepared with suspensions of 25%, was 2.4 μm , agglomeration was more intensive, and cracks of length over 1 μm existed. After heat treatment at 560°C there was not any new cracks forming or propagating in the films of 15% suspensions, however, the length and the width of the cracks increased in the films of 25% suspensions. The thin films before and after the heat treatment were identified as hydroxyapatite by the XRD and FTIR.

The c-HAp films on glass/sericin substrates were decisively more homogeneous as compared to their counterparts coated on glass substrates. Approximately 85% of the surface was covered with primary particles, and the agglomerate sizes were also less than 300 nm explaining the visible light transparency of the films. The thickness of the c-HAp layer on top of the sericin layer was measured to be 150-200 nm. The m-HAp films on glass/sericin substrates were also decisively more homogeneous as compared to glass substrates. The surface was covered predominantly by agglomerates, however, less than 400 nm in size, evidencing the increased agglomeration tendency of the higher

surface area particles, compared to c-HAp. Still the films were visible light transparent. The thickness of the m-HAp layer on top of the sericin layer was 150-200 nm. For both the c-HAp and the m-HAp films on glass/fibroin substrates the films were more homogeneous compared to glass substrates, and slightly scattered light with the predominant aggregate sizes of 400-500 nm; the maximum aggregate sizes reached 1-2 μm . The thickness of the c-HAp layer on glass/fibroin substrates were 150-200 nm, while m-HAp layer on the glass/fibroin substrate was 250-600 nm.

Apparently the effect of intermediate sericin and fibroin films was the selective deposition of primary HAp particles of the minimal available sizes. The regular arrangement of the carboxyl groups protruding from the β -sheet surfaces of the silk proteins provided a surface potential distribution that electrostatically bound Ca^{2+} . The regularity was expected to be delimited by the surface topography, and crystal size and shape could also be factors in determining the particle packing on the surface.

The high affinity of the silk proteins for BSA and collagen type I were confirmed by AFM imaging. The glass/sericin/c-HAp provided the best layered film for BSA adsorption. Glass/fibroin/c-HAp proved to be the next best for the BSA adsorption. The sericin film underlying the c-HAp proved to be slightly better than its fibroin counterpart for adsorbing BSA. However, the BSA adsorption affinity was found to be drastically lower with the m-HAp films over sericin and fibroin surfaces. The BSA adsorption was quantified by the HPLC analysis. For the glass/m-HAp and glass/sericin/m-HAp films, the maximum adsorption was around 1 $\mu\text{g}/\text{cm}^2$. The maximum adsorption of BSA was on glass/sericin/c-HAp film, 2.6 $\mu\text{g}/\text{cm}^2$, a result evidencing the effectiveness of surface topographical structure as well as the chemical structure. Likewise collagen type I adsorption was drastically lower on the glass/sericin/m-HAp and glass/fibroin/m-HAp films compared to glass/sericin/c-HAp and glass/fibroin/c-HAp films. Again indicating the surface topography to be effective on the protein adsorption affinity of the HAp films.

Ti6Al4V alloy substrates were anodized or spin coated with c-TiO₂ followed by subsequent spin coating with c-HAp suspensions in water and ethanol. As a result of anodization anatase formed on the alloy surface as determined by XRD. The thickness of anatase increased with the anodization voltage and two major morphological changes took place with their onset at 60 V and 240 V. The first change was prominent with grain growth while the second change was in the form of a spongy surface. The Ti/O ratio decreased with the increasing voltage, indicating that the surface coverage

percentage and thickness of Ti-O film increased. When the anatase film started to form on the Ti6Al4V alloy substrate, the hardness of the surface increased at 20 V. Although the thickness and surface coverage percentage of anatase film increased, the hardness gradually decreased due to the morphological changes with the increasing anodization voltage.

The c-TiO₂ and c-HAp films coated with the ethanol suspension were thicker due to its higher evaporation rate in comparison to water. The grinding grit size and spin speed were other factors affecting the film thickness. The thickness of the spin coated, layered films were obtained in the range 1 μm to over 10 μm. All of the films showed a very homogeneous structure and consisted almost totally of the primary particles. When the c-TiO₂ films of thickness 1 μm (the thinnest films) were heat treated at 850°C their morphology was totally changed. They had the appearance of recrystallized structure, and the initially present anatase phase was completely transformed to rutile. In the films of thickness 5 μm, ~10% of the anatase remained unconverted. When the c-HAp films heat treated at 850°C a three dimensional mesh of a continuous structure of curlings of 50-100 nm in diameter, reminiscent of an aerogel, were formed without any detectable phase change. In the c-HAp films prepared with EtOH suspension there were cracks of 50-150 nm wide, and 1 μm long. The higher shrinkage rate of a faster drying film most probably contributed to the crack formation besides increased film thickness. The width and length of the cracks enlarged to 500 nm, and 5 μm, respectively, after heat treatment at 850°C.

The XRD patterns of c-HAp films most probably indicated an oriented crystal since the peaks at 2θ values of 28.3° of (210) and 25.2° of (002) planes were biased as compared to the major peaks of the powder. This was possible by the alignment of rod shape grains (most probably grown in one crystal direction during production) on the substrate. It was observed that the protein adsorption capability of c-HAp well surpassed that of m-HAp films. In the m-HAp films the equiaxed particles were the crushed forms of the rod like grains of c-HAp, and there could not be any particular crystal orientation in these films which might constitute one of the causes of the observed phenomenon.

In the layered films Ti6Al4V/c-TiO₂/c-HAp heat treated at 850°C, the anatase-rutile transformation in TiO₂ layer, and the kind morphological change in the c-HAp layer described above took place. As the thickness of the films increased the same crystal orientation bias in the XRD patterns was preserved.

In general, the roughness of the films increased with the heat treatment temperature and the substrate roughness. The hardness of the films increased with the heat treatment temperature. The adhesion strength of the films could be explained by the dilatometric curves of the c-TiO₂ and c-HAp. The adhesion strength of the c-TiO₂ films was reduced to a minimum at 700°C, while that of c-HAp films reached a maximum. The adhesion strength of the layered c-TiO₂/c-HAp was minimum at 700°C, and maximum at 850°C heat treatment. The tensile test yielded adhesion strength values up to roughly 30 MPa, while scratch test yielded values up to roughly 170 MPa. The tensile test was representative of the whole surface and limited with the weakest adhesion zone on the surface, while the scratch test represented the adhesion strength of particular points on the surface. The adhesion strength of the c-HAp films on anodized substrates was maximum at 60 V, most probably due to the surface morphological features of the substrate, and in general, lower in comparison the spin coated c-TiO₂ intermediate films.

The ESP distribution on the electron isodensity surface of the HAp crystal was mapped with molecular modeling methods. The ESP was in the form of strips that could induce positive cooperation in protein adsorption by providing consistent anchorage points or regions, through out the surface, particularly for flexible protein molecules.

The study conducted carries the potential of developing novel fabrication methods of thin hydroxyapatite films on implant devices, in a exceedingly practical, and fixed capital cost effective manner. The developed microstructures of the HAp films can prove effective in the delivery of bone morphogenetic proteins (BMP) in vivo for accelerated hard tissue regeneration by enhanced osteoinduction. The morphology of the films can provide a surface topography convenient for cell and collagen anchorage with undercuts in the nanoscale range through which the developing bone tissue could interdigitate and interlock for enhanced osteoconduction. The study can be expanded by investigating the effects of collagen films for developing HAp thin film microstructures for in vitro and in vivo BMP delivering and osteoconduction capabilities.

REFERENCES

- Addison, W.N., F. Azari, E.S. Sorensen, M.T. Kaartinen and M.D. McKee. 2007. Pyrophosphate Inhibits Mineralization of Osteoblast Cultures by Binding to Mineral, Up-regulating Osteopontin, and Inhibiting Alkaline Phosphatase Activity. *The Journal of Biological Chemistry* 282(21): 15872-15883.
- Ajisawa, A. 1998. Dissolution of silk fibroin with calcium chloride/ethanol aqueous solution. *The Journal of Sericultural Science of Japan* 67(2): 91-94.
- Akkus, O. 2008. Purdue University, College of Engineering, Biomedical Engineering, BIOE 4710, Mechanics of Soft and Hard Tissues. <http://bmew.ecn.purdue.edu/akkus/Lecture1.ppt> (accessed November 11, 2008).
- Albayrak, O., O. El-Atwani and S. Altintas. 2008. Hydroxyapatite coatings on titanium substrate by electrophoretic deposition method: Effects of titanium inner layer on adhesion strength and hydroxyapatite decomposition. *Surface and Coatings Technology* 202(11): 2482-2487.
- Albrektsson, T. and C. Johansson. 2001. Osteoinduction, Osteoconduction and Osseointegration, *European Spine Journal*. 10(Supp.2): S96-S101.
- Altman, G.H., F. Diaz, J. Jakuba, T. Calabro, R.L. Horan, J. Chen, H. Lu, J. Richmond and D.L. Kaplan. 2003. Silk-based biomaterials. *Biomaterials* 24(3): 401-416.
- Ascenzi, A. and A. Benvenuti. 1986. Orientation of Collagen Fibers at the Boundary between Two Successive Osteonic Lamellae and Its Mechanical Interpretation. *Journal of Biomechanics* 19: 455-463.
- Azo Materials-1. 2009. <http://www.azom.com/Details.asp?ArticleID=1547> (accessed January 3, 2009).
- Azo Materials-2. 2009. <http://www.azom.com/Details.asp?ArticleID=1179> (accessed January 3, 2009).
- Babu, N.R., S. Manwatkar, K.P. Rao and T.S. Kumar. 2004. Bioactive Coatings on 316L Stainless Steel Implants. *Trends in Biomaterials and Artificial Organs* 17(2): 43-47.
- Ban, S. and S. Maruno. 1998. Hydrothermal-electrochemical deposition of hydroxyapatite. *Journal of Biomedical Materials Research* 42(3): 387-395.
- Bansal, G., J.E. Wright, S. Zhang, R.F. Zernicke and H. Uludag. 2005. Imparting mineral affinity to proteins with thiol-labile disulfide linkages. *Journal of Biomedical Materials Research Part A* 74A(4): 618-628.
- Bessa, P.C., M. Casal and R.L. Reis. 2008. Bone morphogenetic proteins in tissue engineering: the road from laboratory to the clinic, part I (basic concepts), *Journal of Tissue Engineering and Regenerative Medicine* 2(1): 1-13.

- Best, S.M., E.A. Porter, E.S. Thian and J. Huang. 2008. Bioceramics: Past, present and for the future. *Journal of the European Ceramic Society* 28(7): 1319-1327.
- Bloch, B. and G.W. Hastings. 1972. *Plastics Materials in Surgery*. 2nd ed. Springfield: Thomas.
- Brinker, C.J. and G.W. Scherer. 1990. *Sol-Gel Science - the Physics and Chemistry of Sol-Gel Processing*, San Diego: Academic Press, Inc.
- Cane, V., G. Marotti, G. Volpi, D. Zaffe, S. Palazzini, F. Remaggi and M.A. Muglia. 1982. Size and density of osteocyte lacunae in different regions of long bones. *Calcified Tissue International* 34(1): 558-563.
- Cavalli, M., G. Gnappi, A. Montenero, D. Bersani, P.P. Lottici, S. Kaciuli and G. Mattogno. 2001. Hydroxy and fluorapatite films on Ti Alloy substrates: Sol-gel preparation and characterization. *Journal of Material Science* 36(13): 3253-3260.
- Celik, E., O. Culha, B. Uyulgan, N.F. Ak Azem, I. Ozdemir and A. Turk. 2006. Assessment of microstructural and mechanical properties of HVOF sprayed WC-based cermet coatings for a roller cylinder. *Surface and Coatings Technology* 200: 4320-4328.
- Ceschini, L., E. Lanzoni, C. Martini, D. Prandstraller and G. Sambogna. 2008. Comparison of dry sliding friction and wear of Ti6Al4V alloy treated by plasma electrolytic oxidation and PVD coating. *Wear* 264: 86-95.
- Chang, M. C., C.C. Ko and W.H. Douglas. 2003. Preparation of hydroxyapatite-gelatin nanocomposite. *Biomaterials* 24(17): 2853-2862.
- Chen, Y.C., Y.M. Sun, C.P. Lin and J.Y. Gan. 2004. Enhanced a-axis oriented crystal growth of Nd substituted bismuth titanate thin films with layer by layer crystallization. *Journal of Crystal Growth* 268(1-2): 210-214.
- Cheng, K., S. Zhang, W. Weng, K.A. Khor, S. Miao and Y. Wang. 2008. The adhesion strength and residual stress of colloidal-sol gel derived β -tricalcium-phosphate/fluoridated hydroxyapatite biphasic coatings. *Thin Solid Films* 516: 3251-3255.
- Christel, P., C. Cerf and A. Pilla. 1981. Time Evolution of the Mechanical Properties of the Callus of Fresh Fractures. *Annals of Biomedical Engineering* 9: 383-391.
- Christoffersen, M.R., T. Balic-Zunic, S. Pehrson and J. Christoffersen. 2000. Growth and precipitation of a monoclinic calcium pyrophosphate tetrahydrate indicating auto-inhibition at pH 7. *Journal of Crystal Growth* 212: 500-506.
- Cirilli, F., S. Kaciulis, G. Mattogno, G. Righini and F. Ferrari. 1997. Surface analysis of biocompatible hydroxyapatite coatings on titanium. *ECASIA 97*. eds. J. Olefjord, L. Nyborg, D. Briggs. 151-154. Chichester: John Wiley and Sons.

- Clokie, C.M.L., R. Coulson R., A.A.F. Peel and G.K.B. Sandor. 2000. Approaches to bone regeneration in oral and maxillofacial surgery. *Bone Engineering*. ed. J. E. Davies. Chapter 53: 558-576. Toronto: Em Squared Inc.
- Cotell, C.M. 1993. Pulsed Laser Deposition and Processing of Biocompatible Hydroxyapatite Thin Films. *Applied Surface Science* 69(1-4): 140-148.
- Criado, C. and C. Real. 1983. Mechanism of the inhibiting effect of phosphate on the anatase-rutile transformation induced by thermal and mechanical treatment of TiO₂, *Journal of the Chemical Society, Faraday Transactions 1: Physical Chemistry in Condensed Phases* 79(12): 2765-2771.
- Culha, O., M. Zor, M.A. Gungor, Y. Arman and M. Toparlı. 2009. Evaluating the bond strength of opaque material on porcelain fused to metal restorations (PFM) alloys by scratch test method. *Materials and Design*: Article in Press.
- Culha, O., E. Celik, N.F. Ak Azem, I. Birlik, M. Toparlı and A. Turk. 2008. Microstructural, thermal and mechanical properties of HVOF sprayed Ni-Al based bond coatings on stainless-steel substrate. *Journal of Materials Processing Technology* 204: 221-230.
- Daculsi, G., O. Laboux and R. Le Geros. 2002. Outcome and perspectives in bioactive coatings: What's new, what's coming, *ITBM-RBM* 23: 317-325.
- Damien, C.J., J.R. Parsons, A.B. Prewett, D.C. Rietveld and M.C. Zimmerman. 1994. Investigation of an organic delivery system for demineralized bone matrix in a delayed-healing cranial defect model. *Journal of Biomedical Materials Research* 28: 553-561.
- Darnel, J., H. Lodish and D. Baltimore. 1990. *Molecular Cell Biology*. 2nd ed. Chapter 23. New York: Scientific American Books.
- Davies, J. E. 2007. Bone bonding at natural and biomaterial surfaces. *Biomaterials* 28: 5058-5067.
- Davies, J.E. and M.M. Hosseini. 2000. Histodynamics of Endosseous Wound Healing. *Bone Engineering*. ed. J.E. Davies. Chapter 1: 1-14. Toronto: Em Squared Inc.
- Delecrin, J., G. Daculsi, N. Passuti and B. Duquet. Specific resorbable calcium phosphate coating to enhance osteoconduction. *Cells and Materials* 4: 51-62.
- Deng, X.M., J.Y. Hao and C.S. Wang. 2001. Preparation and mechanical properties of nanocomposites of poly(D,L-lactide) with Ca-deficient hydroxyapatite nanocrystals. *Biomaterials* 22(21): 2867-2873.
- Ducheyne, P., A. El-Ghannam and I. Shapiro. 1994. Effect of bioactive glass templates on osteoblast proliferation and in vitro synthesis of bone-like tissue. *Journal of Cell. Biochemistry* 56: 162-167.

- Foresman, J.B. and A. Frisch. 1996. *Exploring Chemistry with Electronic Structure Methods*. 2nd ed. Pittsburgh: Gaussian Inc.
- Gan, L. and R. Pilliar. 2004. Calcium phosphate sol-gel derived thin films on porous-surfaced implants for enhanced osteoconductivity. Part I: Synthesis and characterization. *Biomaterials* 25: 5303-5312.
- Gan, L., J. Wang and M. Pilliar. 2005. Evaluating interface strength of calcium phosphate sol-gel derived thin films to Ti6Al4V substrates. *Biomaterials* 26: 189-196.
- Giraud-Guille, M.M. 1988. Twisted plywood architecture of collagen fibrils in human compact bone osteons. *Calcified Tissue International* 42: 167-180.
- Guyton, A.C. 1991. *Textbook of Medical Physiology*. 8th ed., Chapter. 79. Philadelphia: W. B. Saunders Company.
- Gyorgi, E., P. Toricelli, G. Socol, M. Iliescu, L. Mayer, N.I. Mihailescu, A. Bigi and J. Werckman. 2004. Biocompatible Mn doped carbonated hydroxyapatite thin film grown by pulsed laser deposition. *Journal of Biomedical Materials Research Part A* 71A(2): 353-358.
- Hehre, W.J. 2003. *A Guide to Molecular Mechanics and Quantum Chemical Calculations*. Irvine: Wavefunction Inc.
- Heimann, R.B. 2006. Thermal spraying of biomaterials. *Surface & Coatings Technology* 201: 2012–2019.
- Helmus. M.N., 1991. Overview of Biomedical Materials. *MRS Bulletin* September: 33-38.
- Hench L L. 1998. Bioceramics. *Journal of the American Ceramic Society* 81(7): 1705-1728.
- Hench L.L. and J. Wilson. 1991. Bioceramics, *MRS Bulletin* September: 62-74.
- Hench L.L., R. J. Splinter, W.C. Allen and T.K. Greenlee Jr. 1971. Bonding mechanisms at the interface of ceramic prosthetic materials, *Journal of Biomedical Materials Research* 2(1): 117–141.
- Hille G.H. 1966. Titanium for surgical implants. *Jornal of Materials* 1: 373–383.
- Histology-World-1. 2008. Histology Photo Album, Bone Histology, page 10, file 119. <http://histology-world.com/photoalbum/displayimage.php?album=8&pos=118> (accessed November 11, 2008).
- Histology-World-2. 2008. Histology Photo Album, Bone Histology, page 10, file 118. <http://histology-world.com/photoalbum/displayimage.php?album=8&pos=117> (accessed November 11, 2008).

- Hofmann, S., C.T. Wong Po Foo, F. Rossetti, M. Textor, G. Vunjak-Novakovic, D.L. Kaplan, H.P. Merkle and L. Meinel. 2006. Silk fibroin as an organic polymer for controlled drug delivery. *Journal of Controlled Release* 111(1-2): 219-227.
- Hollinger, J.O. and K. Leong. 1996. Poly(a-hydroxy acids): Carriers for osteoinductive biomaterials, bone morphogenetic proteins. *Biomaterials* 17(2): 187-194.
- Hossain, K.S., E. Ohyama, A. Ochi, J. Magoshi and N. Nemoto. 2003. Dilute Solution Properties of Regenerated Silk Fibroin. *Journal of Physical Chemistry B* 107: 8066-8073.
- Hwang, K.S. and B.H. Kim. 1999. Preparation of highly oriented LaNiO₃ thin films by spin-coating technique. *Journal of Sol-Gel Science and Technology* 14: 203-207.
- Kandori K., A. Fujiwara, M. Mukai, A. Yasukawa and T. Ishikawa. 1998. Evaluation of the adsorption affinity of proteins to calcium hydroxyapatite by desorption and pre-adsorption methods. *Colloids and Surfaces B: Biointerfaces* 11: 313-320.
- Keaveny, T.M., E.F. Morgan, G.L. Niebur and O.C. Yeh. 2001. Biomechanics of Trabecular Bone, *Annual Review of Biomedical Engineering* 3: 307-333.
- Kim, H-W., J.C. Knowles, V. Salih, H-E. Kim. 2004. Hydroxyapatite and Fluor-Hydroxyapatite Layered Film on Titanium Processed by a Sol-Gel Route for Hard Tissue Implants. *Journal of Biomedical Materials Research Part B: Applied Biomaterials* 71B: 66-76.
- Komatsu, K. 2000. Chemical and structural characteristics of wild cocoon and silk. *Structure of Silk Yarn, Part B, Chemical Structure and Processing of Silk Yarn.* ed. N. Hojo. 21-46. Enfield: Science Publishers Inc.
- Kong, X.D., X. Sun, F. Cui and C. Ma. 2006. Effect of Solute Concentration on Fibroin Regulated Biomineralization of Calcium Phosphate. *Materials Science and Engineering C* 26: 639-643.
- Kong, X.D., F. Cui, X.M. Wang, M. Zhang and W. Zhang. 2004. Silk fibroin regulated mineralization of hydroxyapatite nanocrystals. *Journal of Crystal Growth* 270: 197-202.
- Kraus, K.H. and C. Kirker-Head C. 2006. Mesenchymal Stem Cells and Bone Regeneration. *Veterinary Surgery* 35: 232-242.
- Kuroda, K., R. Ichino, M. Okido and O. Takai. 2002. Hydroxyapatite coating on titanium by thermal substrate method in aqueous solution. *Journal of Biomedical Materials Research* 59: 390-397.
- Laurencin, C.T., M.E. Norman, H.M. Elgendy, S.F. El-Amin, S. Pucher, A. Ambrosio and H.R. Alcock. 1993. Polyphosphozanes-a novel biocompatible bioerodible polymer for bone regeneration. *Transactions - Orthopaedic Research Society* 18: 480-487.

- Lee, K.G., H.Y. Kweona, J.Y. Yeo, S.O. Woo, Y.W. Lee, C-S. Chob, K.H. Kim and Y.H. Park. 2003. Effect of methyl alcohol on the morphology and conformational characteristics of silk sericin. *International Journal of Biological Macromolecules* 33: 75–80.
- Lind, M., S. Overgaard, C. Bunger and K. Soballe. 1999. Improved bone anchorage of hydroxyapatite coated implants compared with tricalcium phosphate coated implants in trabecular bones in dogs. *Biomaterials* 20: 803-808.
- Liu, D-M., Q. Yang and T. Troczynski. 2002. Sol-gel hydroxyapatite coatings on stainless steel substrates. *Biomaterials* 23: 691-698.
- Lucas, P.A., C. Laurencin, G.T. Syftestad, A. Domb, V.M. Goldberg, A.I. Caplan and R. Langer. 1990. Ectopic induction of cartilage and bone by water soluble proteins from bovine bone using a polyanhydride delivery vehicle. *Journal of Biomedical Materials Research* 24: 901-911.
- Luo, Q. and J.D. Andrade. 1998. Cooperative Adsorption of Proteins on Hydroxyapatite. *Journal of Colloid and Interface Science* 200: 104-113.
- Magoshi, J., Y. Magoshi, M.A. Becker, M. Kato, Z. Han, T. Tanak, S.I. Inoue, and S. Nakamura. 2000. Crystallization of Silk Fibroin from Solution. *Thermochimica Acta* 352-353: 165-169.
- Manso-Silvan, M., M. Langlet, J. Jimenez, M. Fernandez and J.M. Martinez-Duart. 2003. Calcium phosphate coating prepared by aerosol-gel. *Journal of the European Ceramic Society* 23: 234-246.
- Marotti, G. and M.A. Muglia. 1988. A Scanning Electron Microscope Study of Human Bone lamellae: Proposal for a New Model of Collagen Lamellar Organization. *Archivio Italiano di Anatomia e di Embriologia (Italian Journal of Anatomy and Embryology)* 93: 163-175.
- Martin, R. B. and D.B. Burr. 1998. *Skeletal Tissue Mechanics*. New York: Springer-Verlag.
- Mavis, B. and C. Tas. 2000. Dip Coating of Calcium Hydroxyapatite on Ti-6Al-4V Substrates. *Journal of the American Ceramic Society* 84(4): 989-991.
- McQuarrie, D. A. 1983. *Quantum Chemistry*. Mill Valley: University Science Books.
- Mikos, A. G., Y. Bao, L.G. Cima, D.E. Ingber, J.P. Vacanti and R. Langer. 1993. Preparation of poly(glycolic acid) bonded structures for cell attachment and transplantation. *Journal of Biomedical Materials Research* 27: 183–189.
- Miller, J. 2006. A comparison of optical and SEM BSE imaging techniques for quantifying alpha-beta titanium alloy microstructures (preprint). *AFRL-ML-WP-TP-2006-432*.

- Miller, E.J. and R.K. Rhodes. 1982. Preparation and characterization of different types of collagen. *Methods in Enzymology* 82A: 33–64.
- Mineral Search. 2009. mindat.org.
<http://www.mindat.org/min-213.html> (accessed January 3, 2009).
- Mitutoyo. 2003. *SJ-301, Surface Roughness Tester, User's Manual*. Chapter 14, Reference Information. Tokyo: Mitutoyo.
- Moreno, E.C., M. Kresak and A. Gaffar. 1994. Adsorption of peroxydiphosphate onto hydroxyapatite: Kinetics, thermodynamics, and crystal growth inhibition. *Journal of Colloidal and Interface Science* 168(1): 173-182.
- Muralithran, G. and S. Ramesh. 2000. The effects of sintering temperature on the properties of hydroxyapatite. *Ceramics International* 26: 221-230.
- Nam J. and Y.H. Park. 2001. Morphology of regenerated silk fibroin: Effects of freezing temperature, alcohol addition, and molecular weight. *Journal of Applied Polymer Science* 81(12): 3008-3021.
- Narasaraju, T.S.B. and D.E. Phebe. 1996. Some physico-chemical aspects of hydroxyapatite. *Journal of Materials Science* 31: 1-21.
- Nemoto, R., L. Wand, M. Aoshima, M. Senna and T. Ikoma. 2004. Increasing the Crystallinity of Hydroxyapatite Nanoparticles in Composites Containing Bioaffinitive Organic Polymers by Mechanical Stressing. *Journal of the American Ceramic Society* 87(6): 1014-1017.
- Ohgushi, H., M. Okumura, S. Tamai, E.C. Shors and A.I. Caplan. 1993. Marrow cell-induced osteogenesis in porous hydroxyapatite and tricalcium phosphate: A comparative histomorphometric study of ectopic bone formation. *Journal of Biomedical Materials Research* 24: 1563–1570.
- Ombelli, M., R.J. Composto, Q.C. Men and D.M. Eckmann. 2005. A Quantitative and Selective Chromatography for Determining Coverages of Multiple Proteins on Surfaces. *Journal of Chromatography B* 826: 198-205.
- Park, J. and R.S. Lakes R. S. 2007. *Biomaterials An Introduction*. 3rd ed.. New York: Springer Science and Business Media, LLC.
- Peroos, S., Z. Du and N.H. de Leeuw. 2006. A Computer Modeling Study of the Uptake, Structure and Distribution of Carbonate Defects in Hydroxyapatite. *Biomaterials* 27: 2150-2161.
- Putthanarat, S., S. Zakoob, J. Magoshi, J.A. Chen, R.K. Eby, M. Stone and W.W. Adams. 2002. Effect of processing temperature on the morphology of silk membranes. *Polymer* 43: 3405-3413.
- Qiu, S., R.D. Soloway and R.S. Crowther. 1992. Interaction of bile salts with calcium hydroxyapatite: Inhibitors of apatite formation exhibit high-affinity pre-micellar binding. *Hepatology* 16(5): 1280-1289.

- Radin, S.R., and P. Ducheyne. 1992. Plasma spraying induced changes of calcium phosphate ceramic characteristics and the effect on in vitro stability. *The Journal of Materials Science: Materials in Medicine* 3(1): 33-42.
- Rahaman, M.N. and A. Yao. 2007. Ceramics for Prosthetic Hip and Knee Joint Replacement. *Journal of the American Ceramic Society* 90(7): 1965-1988.
- Raja, K.S., M. Misra M. and K. Paramguru. 2005. Deposition of Calcium Phosphate Coating on Nanotubular Anodized Titanium. *Material Letters* 59: 2137-2141.
- Renier, M.L. and D.H. Kohn. 1997. Development and characterization of a biodegradable polyphosphate. *Journal of Biomedical Materials Research* 34: 95-104.
- Rhee, S.H., Y. Suetsugu and J. Tanka. 2001. Biomimetic configurational arrays of hydroxyapatite nanocrystals on bio-organics. *Biomaterials* 22(21): 2843, 2001
- Sahai, N. and J.A. Tossell. 2000. Molecular orbital study of apatite ($\text{Ca}_5(\text{PO}_4)_3\text{OH}$) nucleation at silica bioceramic surfaces. *Journal of Physical Chemistry B* 104: 4322-4341.
- Santos, E.A., M. Farina and G.A. Soares. 2008. Surface energy of hydroxyapatite and β -tricalcium phosphate ceramics driving serum protein adsorption and osteoblast adhesion. *The Journal of Materials Science: Materials in Medicine* 19: 2307-2316.
- Schaffler, M.B., D.B. Burr and R.G. Fredrickson. 1987. Morphology of the Cement Line in Human Bone. *The Anatomical Record* 217: 223-228.
- Shashidhar, V.M. 2006. Bone Histology and Fracture Healing. Fiji School of Medicine. <http://www.scribd.com/doc/2562740/Bone-Histology-Healing-iBooktk> (accessed November 11, 2008).
- Shen, J.W., T. Wu, Q. Wang and H.H. Pan. 2008. Molecular simulation of protein adsorption and desorption on hydroxyapatite surfaces. *Biomaterials* 29: 513-532.
- Stupp, S.L. and G.W. Ciegler. 1992. Organoapatites: Materials for dogs: Artificial bone. I: Synthesis and microstructure. *Journal of Biomedical Materials Research* 26: 169-183.
- Takeuchi, A., C. Ohsuki, T. Miyazaki, M. Kamitakahara, S. Ogata, M. Yamazaki, Y. Furutani, H. Kinoshita and M. Tanihara. 2005. Heterogeneous Nucleation of Hydroxyapatite on Protein: Structural Effect of Silk Sericin. *Journal of the Royal Society Interface* 2: 373-378.
- Tanahashi M. and T. Matsuda. 1997. Surface functional group dependence on apatite formation on assembled monolayers in a simulated body fluid. *Journal of Biomedical Materials Research* 34: 305-315.

- Teramoto, H., A. Kakazu, K. Yamauchi and T. Asakura. 2007. Role of hydroxyl side chains in *bombyx mori* silk sericin in stabilizing its solid structure. *Macromolecules* 40: 1562-1569.
- Torrise, L. and G. Foti. 1993. Ion Sputtering of Hydroxyapatite. *Applied Physics Letters* 62(3): 237-239.
- University of Michigan. 2008. Engineering Faculty, BME/ME 456 Biomechanics, Bone Structure.
<http://www.engin.umich.edu/class/bme456/bonestructure/bonestructure.htm>
 (accessed December 11, 2008).
- Varma H.K., Y. Yokogawa, F.F. Espinosa, Y. Kawamoto, K. Nishizawa, F. Nagata and T. Kameyama. 1999. Porous calcium phosphate coating over phosphorylated chitosan film by a biomimetic method. *Biomaterials* 20: 879-884.
- Vashishth, D. 2007. Hierarchy of bone microdamage at multiple length scales. *International Journal of Fatigue* 29: 1024-1033.
- Wang D. and C. Chen. 2008. Hydroxyapatite Coating on Ti6Al4V Alloy by a Sol-Gel Method. *The Journal of Materials Science: Materials in Medicine* 19: 2281-2286.
- Wassell, D.T.H., R.C. Hall and G. Embery. 1995. Adsorption of bovine serum albumin onto hydroxyapatite. *Biomaterials* 16: 697-702.
- Weng, W. 1999. Preparation and Characterization of Hydroxyapatite Coatings on Ti6Al4V Alloy by a Sol-Gel Method. *Journal of the American Ceramic Society* 82(1): 27-32.
- Weng, W. and J.L. Baptista. 1998. Alkoxide route for preparing hydroxyapatite and its coatings. *Biomaterials* 19: 125-131.
- Weiner, S. and W. Traub. 1992. Bone Structure: from Angstrom to Microns. *The FASEB Journal* 6: 879-885.
- Wierzbicki, A. and H.S. Cheung. 2000. Molecular modeling of inhibition of hydroxyapatite by phosphocitrate. *Journal of Molecular Structure (Theochem)* 529: 73-82.
- Wilson, R.M., J.C. Elliot and S.E.P. Dowker. 1999. Retrieved refinements of the crystallographic structure of human dental enamel apatites. *American Mineralogist* 84: 1406-1414.
<http://rruff.geo.arizona.edu/AMS/result.php>, sample: H6G, synthetic
 (accessed January 3, 2009).
- Winn, S.R., H. Uludag H. and J.O. Hollinger. 1998. Sustained release emphasizing recombinant human bone morphogenetic protein-2. *Advanced Drug Delivery Reviews* 31: 303-318.

- Yamada, H., H. Nakao, Y. Takasu and K. Tsubouchi. 2001. Preparation of Undegraded Native Molecular Fibroin Solution from Silkworm Cocoons. *Materials Science and Engineering C* 14: 41-46.
- Yang, S., H.C. Man, W. Xing and X. Zheng. 2009. Adhesion strength of plasma sprayed hydroxyapatite coatings on laser gas-nitrided pure titanium. *Surface and Coatings Technology* online available.
- Ying, P., Y. Yu, G. Jin and Z. Tao. 2003. Competitive protein adsorption studied with atomic force microscopy and imaging ellipsometry. *Colloids and Surfaces B: Biointerfaces* 32: 1-10.
- Zhao, F., Y.J. Yin, W.W. Lu, J.C. Leong and W.Y. Zhang. 2002. Preparation and histological evaluation of biomimetic three-dimensional hydroxyapatite/chitosan-gelatin network composite scaffolds. *Biomaterials* 23(15): 3227-3234.
- Zhitomirsky, I. 2000. Electrophoretic Hydroxyapatite Coatings and Fibers. *Materials Letters* 42: 262-271.

CURRICULUM VITAE
OF

SELÇUK ÖZCAN

80/10 sokak, 3/3,
Sevgi Mah., Gaziemir,
Izmir, 35410

Residence: ++90 232 274 3624
Mobile: ++90 542 674 3685
E-mail: selcukozcan@iyte.edu.tr
tthinc@yahoo.com

Date of Birth: March 20, 1962

Place of Birth: Izmir

EDUCATION:

- 2002- Ph.D. candidate in Chemical Engineering, Izmir Institute of Technology (Izmir, Turkey); G.P.A.: 3.93/4.00;
Thesis: Preparation of Hydroxyapatite/Silk Protein Thin Film Implant Surfaces, Investigation of their Microstructural Properties and Model Protein Interactions
- 1991 **M.A.Sc. Chemical Engineering and Applied Chemistry**, University of Toronto (Ontario, Canada); G.G.P.A.: 4.00/4.00
Thesis: "Recovery Boiler Fireside Deposit Thermal Shock Resistance and Thermal Conductivity"
- 1988-1989 Middle East Technical University (Ankara, Turkey); M.Sc. Program; course work completed; G.P.A.: 4.00/4.00
- 1983 **Chemical Engineering**, Hacettepe University (Ankara, Turkey)
G.G.P.A.: 3.70/4.00;

PUBLICATIONS:

1. Selçuk Özcan, Honghi Tran, "Evaluation of the Effectiveness of the Bulk Thermal Stresses for Kraft Recovery Boiler Fireside Deposit Cleaning", *Tappi J*, **5** [4], 3-9,(2006)
2. Selçuk Özcan ve Sedat Akkurt, "Microstructural Analysis of Corroded Frit Kiln Refractories", I. Industrial Kilns and Refractories Symposium Proceedings, TMMOB (Turkish Association of Architects and Engineers), Turkish Chamber of Metallurgical Engineers, 58-68, (2005)
3. Sedat Akkurt and Selcuk Ozcan, "ANN Model Predicts Floor Tile Properties", *American Ceramic Society Bulletin*, **83** [2], 9101-9109, (2004)

WORK EXPERIENCE:

- 2003- Research Assistant; Izmir Institute of Technology
- 1998-2003 Assistant General Manager; Tamsa Seramik San ve Tic. A. Ş.
- 1994-1998 Head of Research and Development (R&D Manager)
Exports and Imports Manager; Anatolia Seramik San. Tic. A. Ş.
- 1992-1993 Research Assistant; Ege University, Izmir
- 1988-1991 Teaching Assistant and Research Asssitant; University of Toronto, Ontario, Canada
- 1988-1989 Research Assistant; Middle East Technical University, Ankara, Turkey
- 1984-1986 Military Service; Second Lieutenant